Lights, Camera, Molecules: Developing Fluorescence Methods to Investigate Chemical Reactions.

By

Veronica K. Krasecki

A dissertation submitted in partial fulfillment of the
requirements for the degree of

Doctor of Philosophy

(Chemistry)

at the

UNIVERSITY OF WISCONSIN-MADISON

2023

Date of final oral examination: May 19th, 2023

This dissertation is approved by the following members of the Final Oral Committee:

Randall H. Goldsmith, Professor, Physical Chemistry
John F. Berry, Professor, Inorganic Chemistry
Ive Hermans, Professor, Inorganic Chemistry
AJ Boydston, Professor, Materials Chemistry

Table of Contents

Table of Figures

Table of Tables

Abstract

Chemical reactions feature complex mechanisms with molecules undergoing multiple transformations going from starting materials to products. To better understand chemical reactions, one investigates the reaction mechanism. Fluorescence microscopy can provide a way to optically probe chemical reactions. Optical microscopy, specifically fluorescence microscopy, can provide a real-time, *in situ* measurement of a chemical reaction with inherently high signal-to-background, providing glimpses into a reaction as it occurs. Fluorescence microscopy has been used extensively in the biological field, contributing to our overall understanding of various biological molecules and functions. However, the use of fluorescence microscopy to understand chemistry and chemical reactions is still relatively new. Many fluorescence microscopy techniques have been designed and developed with aqueous biological systems in mind, which does not always translate to an organic chemical reaction. Therefore, the development of new methods is necessary to study chemical systems using fluorescence microscopy.

In this thesis I focus on three major applications of fluorescence microscopy, going from large scale bulk measurements down to a single molecule. The first application focuses on the development of a hybrid classical-molecular computer. The hybrid classical-molecular computer consists of an electrochemical reaction on top of an array of discrete electrodes. In this project, a ratiometric fluorescence pH sensitive readout and input is used in combination with a classical computer to generate a feedback loop to solve computational problems. In particular, the fluctuations within the optical signal are investigated and found to aid in solving combinatorial optimization problems. The second application focuses on the development of a technique to monitor polymerizations catalyzed by homogenous catalysts within droplets. This project uses droplets around 0.5 mm in diameter to encapsulate and immobilize a polymerization. Fluorescence anisotropy and aggregation-induced emission are used to monitor the progress of the polymerization. This dual readout method provides a greater temporal dynamic range than either method alone. Then, the size of the droplets is reduced, as I attempt to monitor fluorescence anisotropy changes from single catalysts within attoliter droplets. Preliminary results show increases in anisotropy in droplets less than 1 µm in diameter. Finally, I begin an investigation into surface chemistry and using fluorous surfaces as a noncovalent immobilization technique for single molecules. This project features single particle tracking along with fluorescence recovery after photobleaching as the fluorescence methods of choice. Preliminary data here is inconclusive and points to the need for further development of homogeneous fluorous surfaces. Collectively, there is a combination of techniques and methods to study interesting chemical processes using fluorescence.

Acknowledgements

A thesis would not be complete without acknowledging all of the amazing people who have come into my life and supported me throughout this Ph.D. First off, thank you to Randy. Your guidance, leadership and mentorship have shaped me into the scientist that I have become. Your enthusiasm about science is something I hope I can bring to every project I take on in the future. Thank you for the opportunity to do some really insane science and for letting me be me.

I feel incredibly lucky to have joined the Goldsmith group. The camaraderie within the group was pivotal in building my confidence as a scientist. I have been so lucky to overlap with *almost* every graduate student whose been in the Goldsmith group, and every single member has left a lasting impact on me. Whether it be through teaching me the wide variety of skills necessary to tackle this Ph.D., showing me kindness through some of the most difficult times, or teaching me the importance of asking the most thought-provoking questions, like is a hot dog really a sandwich? A few specific mentions include: Angela and Daniel, taught me all there is about fluorophore synthesis. Katie, James and Andrew guided me through all things related to microscopy and fluorescence. Prior to graduate school I couldn't

even look through a microscope correctly and now I find joy in aligning optics setups. Additionally, Andrew thank you for showing me the importance in finding my voice and confidence within all of the incredibly complex projects we took on. Alex (Foote), showed me that snark and sass are critical to any Ph.D. Erik, you created the most top-tier presentations I have ever seen, and I strive to meet your standards with every presentation I make. Morgan, you are one of the most amazing scientists I have ever known, and I feel so lucky to have been your coworker and desk buddy. You are one of the strongest people I know and showed such consideration and kindness to others while always staying true to yourself. Lydia, showed me how to be a truly great leader. Ceci, we came in this together and I'm so happy we've been able to get through it side-by-side, thank you for your conversations and support, there's no one else who I'd want to go through graduate school with. Katherine, your optimism, kindness, and warmth are just a few of the wonderful qualities that you possess and bring to all those around you. Brendan, you're absolutely hilarious and genuinely one of the best people to come from New Jersey (probably #1). Mackinsey and Ray, you're both such talented and creative scientists, and I'm lucky to have worked with both of you and I'm so excited for all that you will accomplish. The catalysis side is in the best hands with both of you. Beau, you have excellent taste in sci-fi movies (Godzilla (1997) forever). Brandon, you keep snark and sass high and that's important in any office and in any friendship, you're genuinely incredibly kind and considerate and such a wonderful friend (even though I'm sure you would hate reading that). Alex (Fairhall), you're such a kind person and you always look out for others, and one day we'll finally see the end of AoT. Julia, you have strong convictions and great opinions, you're strong and smart, never change. Simi, you're absolutely amazing, you're hilarious, and your baking skills are next-level. Sam, I really value that we've been able to become closer friends, I know you'll accomplish great things and your style has always been excellent.

Thank you to all of the amazing friendships I've formed while in Madison, you all have made the Midwest feel a little less lonely. Thank you to Lisa-Maria. You're an amazing scientist and friend. You work incredibly hard, have such a love for life, and have really helped me through some incredibly difficult moments. Thank you to Kate. Kate you were truly my New York away from New York. You are also one of the hardest workers I know, and an absolute rock star. I'm so grateful to call you my best friend, I love you so much.

Thank you to my family, particularly my parents. All that you have given and done for me has allowed me to be where I am today. Thank you for always visiting, always calling, always checking in on me, and always supporting me and being by my side. I love you dearly.

Finally, Cole, or I guess I should say Dr. Cole, Ph.D. Your support, encouragement, and belief in me are what truly pushed me to pursue this degree. You are the reason that I believe in myself. I'm thankful for the opportunity to learn and grow together in Madison (including teaching me how to ride a bike). Thank you for always being there for me, and thank you for being someone I can truly depend on. Thank you for all of the amazing memories and experiences. I know that regardless of which city we're in, what challenges come our way, or how many cats are in our life, I can handle it all as long as you're by my side. Thank you and I love you.

Thesis Outline

A wide variety of topics and applications will be discussed in this thesis, with fluorescence microscopy as the main technique linking them all. Chapter 1 begins with an overview of the basic concepts of fluorescence, written as an initial guide for anyone who is not familiar with fluorescence. I also provide general overviews of each technique that is featured in the various projects within this thesis, along with their concepts and applications.

Chapter 2 uses ratiometric pH sensitive fluorescence as a readout and input for a hybrid classical-molecular computer. This project was a collaborative effort between UW-Madison, Northwestern, University of Toronto, and University of Glasgow, focusing on the implementation of a physical hybrid computer. The fluctuations in fluorescence signal inherent in optical measurements were found useful to help solve computational problems.

Chapter 3 investigates the polymerization of norbornene to polynorbornene within droplets using fluorescence anisotropy and aggregation-induced emission. These two separate emission signals combined provided a larger temporal dynamic range than was possible with just either alone, providing a unique method for monitoring polymerization.

Chapter 4 focuses on a project that I began which is inspired by the work accomplished in Chapter 3. Here, still using fluorescence anisotropy, the polymerization of norbornene to polynorbornene is scaled down to investigate the polymer growth catalyzed by a single molecular catalyst. I provide preliminary data showing increases in anisotropy in small (<1 µm diameter) droplets. As this project is not finished, I also hope this chapter can act as a resource for anyone continuing this project.

Chapter 5 is another project with preliminary data. This project focused on fluorous-functionalized surfaces and molecules, with the goal of understanding the interactions between them. More specifically, whether this concept could be used as an immobilization technique for single-molecule fluorescence microscopy measurements. This chapter shows very preliminary data both in terms of fluorescence measurements as well as characterization of surfaces. Again, I hope this chapter can be used as a resource for anyone who takes this project next.

Chapter 1 Introduction to Fluorescence

1.1 Basics of Fluorescence

Fluorescence is a very powerful technique. It has an inherently high sensitivity due to the high signal-to-background nature of the experiment. This comes from fluorescence depending on collecting emitted photons as opposed to measuring small changes in transmitted light in an absorption experiment. The high sensitivity has even allowed the imaging of light emitted from single molecules.[1,2] A brief overview of the concept of fluorescence is provided below. If interested in going deeper into these topics, please refer to the Principles of Fluorescence Spectroscopy by Joseph Lakowicz.[3]

Fluorescence is a radiative relaxation process, that is, the emission of light from a molecule in an excited state. A fluorophore (can be referred to as emitter or dye) is a molecule which can fluoresce. After a fluorophore has absorbed light, which typically occurs on the femtosecond timescale, it will be excited a higher energy vibrational level of an excited electronic state. Molecules will then usually relax down to the lowest vibrational level of the excited electronic state on the picosecond timescale *via* internal conversion and maintain the same molecular spin. The molecule then can relax to the ground electronic state by spontaneous emission, otherwise known as fluorescence, which usually occurs on the nanosecond timescale. This process is illustrated in **Figure 1-1** via a Jablonski diagram, which highlights that the energy of fluorescence will be lower than the absorbed energy. This change in energy is observed by the fluorescence shifting to longer wavelengths of light compared to the absorbed light (also known as being red-shifted). The difference between the maximum absorbance wavelength and maximum emission wavelength is known as a Stokes Shift.

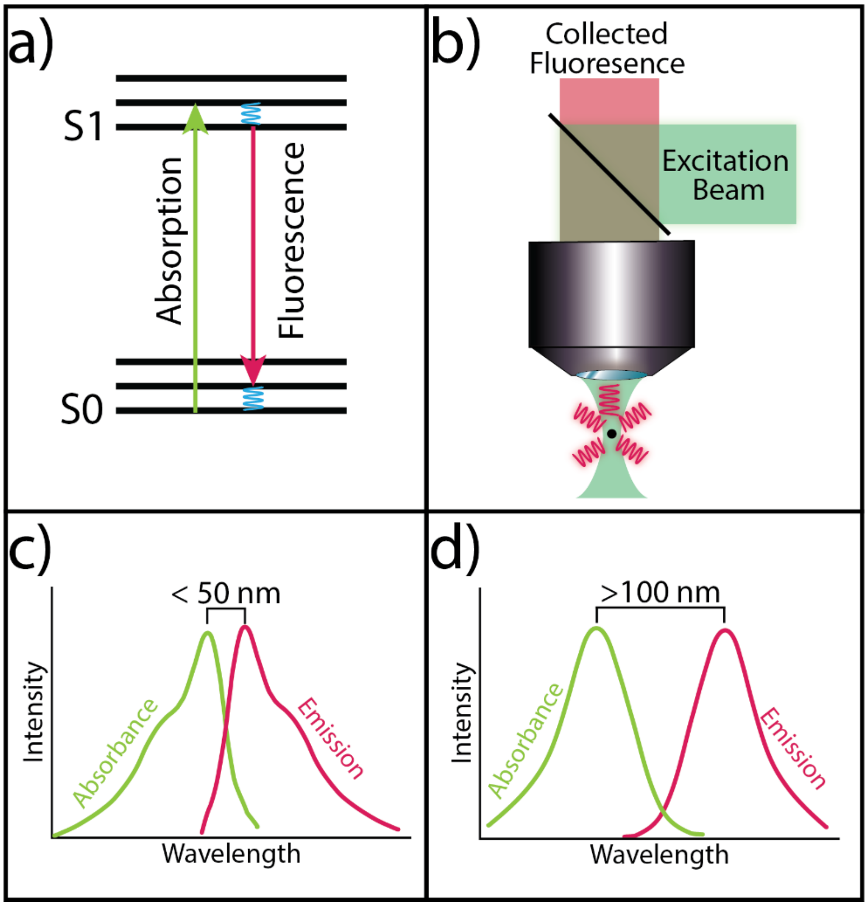

Figure 1-1. Example of Jablonski Diagram, Illustration of Fluorescence Process and Stokes Shift. (a) Absorption (green arrow) of a photon excites the molecule to an excited vibrational state in S1, then internal conversion (blue) relaxes to a lower excited vibrational state resulting in a lower energy fluorescence emission (red) to a vibrational state in S0, and then final internal conversion relaxing down to the ground vibrational state. (b) Excitation (green) of a single emitter (not to scale) and then collection of red-shifted emission using spectral filtering. Example absorbance and emission spectra with (c) a relatively small Stokes shift and (d) large Stokes shift.

The Stokes shift between excitation and emission for a fluorophore allows for fluorescence measurements to produce an isolated signal. By using spectral filters, it’s possible to remove excitation light and only collect the fluorescence from the molecule. The larger the Stokes shift, the easier it is to remove the excitation light while maintaining high fluorescence signal. The Stokes shift gives insight into the degree of relaxation in the excited state, with rigid ring systems experiencing smaller Stokes shifts. Interactions with solvent can also causes changes to this shift.

Fluorescence occurs within the singlet ground and excited electronic states. However, intersystem crossing can populate triplet states of the molecule, which is a spin-forbidden process, with timescales typically much longer for accessing these states. In fluorescence experiments, these longer timescales result in dark states, which is observed as blinking when investigating single fluorophores. Photon emission from these triplet excited states is known as phosphorescence.

A fluorophore's performance is quantified by its extinction coefficient, fluorescence quantum yield, and fluorescence lifetime. The extinction coefficient is a measure for how much light is attenuated by the fluorophore. Quantum yield refers to the number of photons emitted relative to the number of photons absorbed, where a quantum yield approaching 100% is an incredibly bright chromophore. For example, fluorescein and rhodamine 6G are two bright fluorophores and in certain solvents are able to achieve quantum yields of 92.5% and 95% respectively.[4] Quantum yield (ϕ) can be expressed as a ratio of the number of photons emitted divided by the number of photons absorbed. It can also be expressed by the rate of emission (Γ) and rate of non-radiative decay (k_{nr}) for the molecule:[3,5,6]

$$\phi = \frac{\Gamma}{\Gamma + k_{nr}} \tag{1.1}$$

Fluorescence lifetime is the amount of time a fluorophore spends in the excited state before emitting a photon, indicating the stability of the excited state of the fluorophore. The relationship between time-dependent fluorescence intensity ($I(t)$) and fluorescence lifetime (τ) is denoted by the following equation,[5] where I_0 is the intensity at t = 0:

$$I(t) = I_0 e^{-(t/\tau)} \tag{1.2}$$

The loss of fluorescence is known as quenching, which can occur through various routes. One is collisional quenching, where an excited-state fluorophore relaxes through contact with another molecule, which is aptly referred to as a quencher. Molecular oxygen is one of the most well-known quenchers. It is important to note that collisional quenching does not chemically alter the fluorophore. However, there are instances during a fluorophore's excited state lifetime where it can be susceptible to degradation. With high intensity illumination, a fluorophore can undergo a chemical or structural change that results in the loss of fluorescence permanently, known as photobleaching. A highly photostable dye is one that can maintain a high percentage of fluorescence emission for the duration of the measurement.

How fluorescence is used in an experiment is very important. As not all molecules can fluoresce, experimental design includes incorporation of a fluorophore either as a label to a molecule of interest or as a sensor to the changes in the environment. The ideal fluorescence experiment includes a fluorophore that does not change the reactivity of the molecules, so as not to obscure or alter the dynamics observed. Fluorescence is a fundamental phenomenon utilized in a myriad of techniques, all which can grant different information. Descriptions of the techniques used in this thesis are found below.

1.2 Wavelength-Ratiometric Fluorescence

Wavelength-ratiometric fluorescence is a technique that measures either the fluorescence intensity or excitation strength at two spectrally separated wavelengths to detect changes within a local environment.[7] Ratiometric fluorescence is most commonly used to detect intracellular pH changes,[8] though it has also been applied to detect changes in ion concentration.[9,10] Wavelength ratiometric probes exhibit two spectrally separated peaks, either in their excitation or emission spectrum. These peaks would be sensitive to the measured property. In **Figure 1-2**, a hypothetical emission spectrum of an emission-wavelength ratiometric probe is shown, with two emission peaks, **A** and **B**, whose intensities are sensitive to pH. The emission spectrum also shows an isosbestic point, **C**, which can be used to determine the wavelength of spectral filters needed to separate the emission into two separate collection channels. The first channel would capture the emission from wavelengths corresponding to peak A, and the second channel would collect the emission from wavelengths of light corresponding to peak B. As the pH changes from acidic to basic, there is a shift in the emission wavelength. This causes a change in the intensity in both peaks. As the pH becomes more basic the intensity of the emission at wavelength A decreases and the intensity at wavelength B increases. The ratio of these peaks can be calculated and will directly correlate to pH.

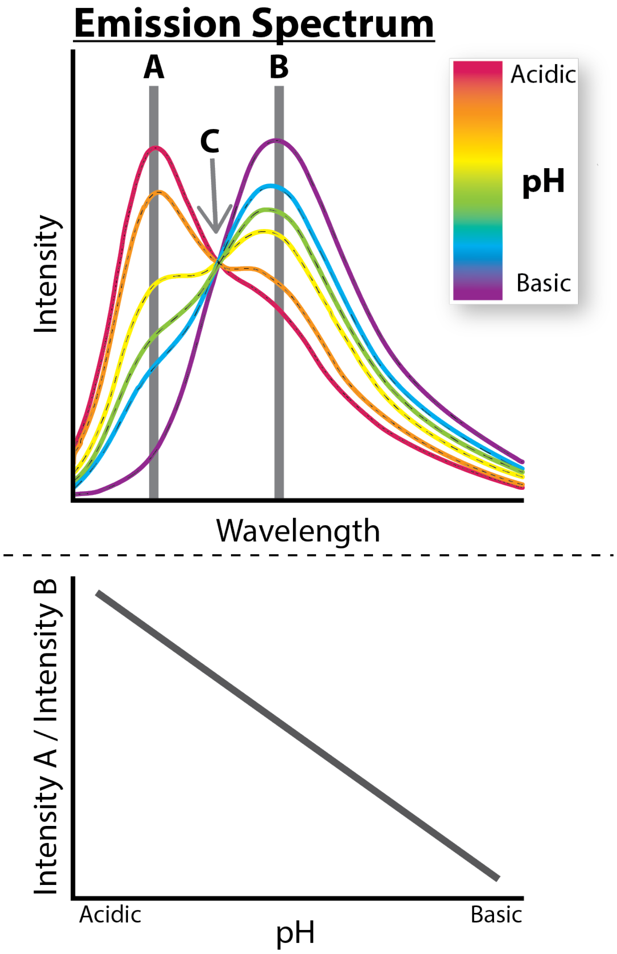

Figure 1-2. Principle of pH sensitive ratiometric fluorescence.
(Top) Emission spectra of ratiometric fluorophore, where A and B are pH sensitive peaks, and C is the isosbestic point. (Bottom) The intensity ratio between peaks A and B forms a linear relationship with pH.

Ratiometric fluorescence is used in Chapter 2, with Carboxy-SNARF-1, whose protonated and deprotonated states exhibit changes in the fluorescence emission. It has been used in the literature to determine intracellular pH.[11–15] The ratiometric signal from SNARF-based fluorophores is not dependent on fluorophore concentration nor is it affected by photobleaching. These qualities make SNARF an excellent choice for pH sensing over long term measurements. Measuring pH with SNARF (or any other ratiometric fluorophore) requires a calibration curve. The calibration curve should be performed at the same experimental conditions as the intended measurement, as the response from the fluorophore can change depending on the environment.

1.3 Fluorescence Anisotropy

Fluorescence anisotropy is a measure of a molecule's rotational diffusion based on the polarization of its emission. This technique provides insight into the rigidity or viscosity of a molecular environment. To measure fluorescence anisotropy, fluorophores are selectively excited using linearly polarized light. Fluorophores preferentially absorb photons whose electric field components are oriented parallel to the transition dipole moment of the molecule. The transition dipole moment of a fluorophore has a defined orientation with respect to its molecular axis.

In solution, you would expect the molecules to be oriented randomly. Therefore, when linearly polarized light excites the solution, the fluorophores with transition dipole moments parallel to the excitation light would absorb the most. Molecules oriented offset from the polarized excitation will have a much weaker absorption, with molecules oriented perpendicular to the excitation axis not absorbing at all. This results in photoselective excitation, **Figure 1-3**. The emission from the molecules will also be polarized and collected in two separate polarization channels, one parallel to the excitation and one perpendicular. Anisotropy (r) is calculated using the intensities from both channels ($I_{\parallel}$ and $I_{\perp}$) in the following equation:

$$r = \frac{I_{\parallel} - GI_{\perp}}{I_{\parallel} + 2GI_{\perp}} \tag{1.3}$$

In the equation above there is a correction factor, G, which is referred to as a G factor. The G factor is used to account for properties of the detection system which can affect the anisotropy measurement or induce a bias in the anisotropy. The G factor can be determined by measuring the anisotropy of a well-studied system and correcting the experimentally determined anisotropy with the literature value for that fluorophore. A G factor of 1 means that the system detects polarized light evenly in both channels.

The denominator in the equation is the total intensity of the sample and features a factor of $2I_{\perp}$. To understand this factor, consider the three axes present for a molecule: x, y, and z. If the excitation polarization and transition dipole are both parallel to the z-axis, then the intensity in the parallel channel is described along the z-axis. Therefore, for the intensity in the perpendicular channel, we can expect contributions resulting from polarized emission along the x- and y-axes, resulting in a multiple of 2.

The theoretical maximum anisotropy of a homogeneous solution is 0.4. This is determined based on the probability distribution of molecules that can be excited by vertically polarized light.[3] As previously mentioned, while fluorophores aligned exactly parallel to the light polarization absorb strongest, perfect alignment is not needed to absorb the light. The distribution of angles at which a fluorophore can absorb light relative to the excitation polarization can be used to determine the maximum anisotropy possible. Full derivations can be found in Lakowicz.[3] When measuring the anisotropy for a single molecule that is oriented parallel to the excitation, it's possible to observe values above 0.4, approaching r = 1. In instances of aggregation or highly concentrated solutions, fluorophores can transfer energy between molecules, resulting in depolarization and in some cases negative anisotropy values ($r < 0$). This is dependent on the spectral properties of the fluorophores, particularly if the spectral overlay between excitation and emission can result in energy transfer.

Rotational diffusion can cause deviations from the theoretical maximum of anisotropy. If the rotational diffusion of the molecule is faster than emission lifetime of the excited state, then the transition dipole of the molecule will be changed before it emits. In solution, most fluorophores can rotate on the picosecond time scale, which is much faster than the 10s of nanoseconds excited state lifetime of a fluorophore. If the fluorophore can rotate freely, the polarized emission will be randomized, i.e. depolarized, resulting in anisotropy values close to $r = 0$, **Figure 1-3**. The rotational diffusion of the molecule can be affected by the microenvironment present, slowing down the rotation and causing an increase in anisotropy approaching the theoretical maximum.

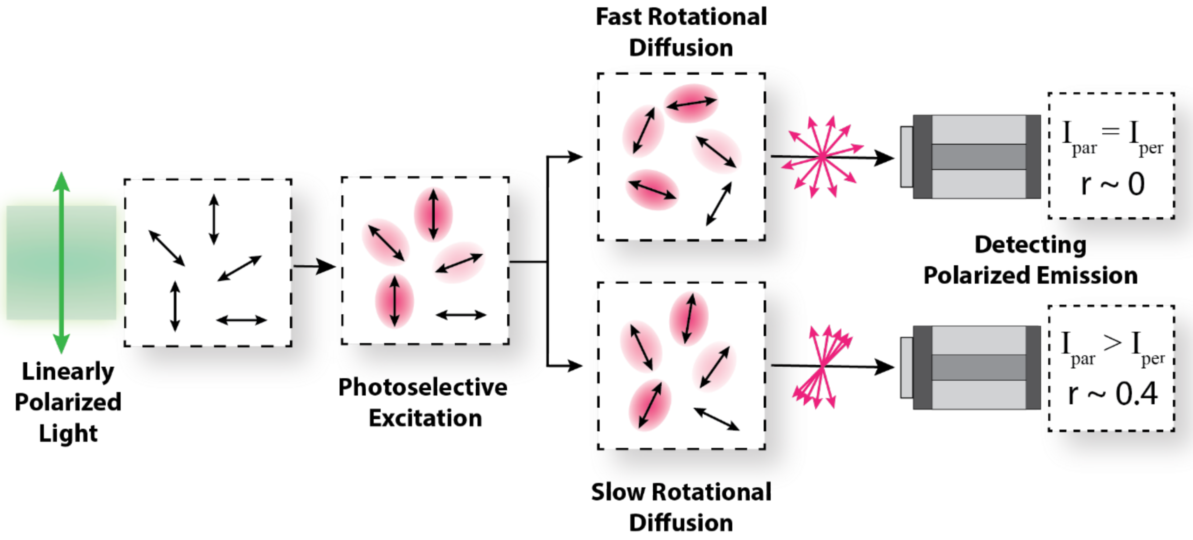

Figure 1-3. Principle of Fluorescence Anisotropy.
(Top) Fast rotational diffusion of molecules causes depolarization, resulting in low anisotropy (approaching 0). (Bottom) Slow rotational diffusion causes emission to maintain excitation polarization, resulting in high anisotropy (approaching 0.4).

Fluorescence anisotropy has been used in the literature on the single-molecule level investigating DNA and protein conformations, binding interactions between biomolecules, and aggregation within cells.[16,17] Fluorescence anisotropy has also been used to determine the orientation of dye molecules within aqueous microdroplets.[18] This versatile technique is used in Chapters 3 and 4 to monitor the progress of a polymerization by measuring the rotational diffusion of a perylene diimide-labeled norbornene (PDI-NB) monomers. At the beginning of the polymerization, with the PDI-NB molecule freely diffusing, a low anisotropy value is expected. As the monomers are incorporated into the polymer, the rotational diffusion of the dyes is restricted resulting in anisotropy increases, until reaching the maximum of 0.4, **Figure 1-4**.

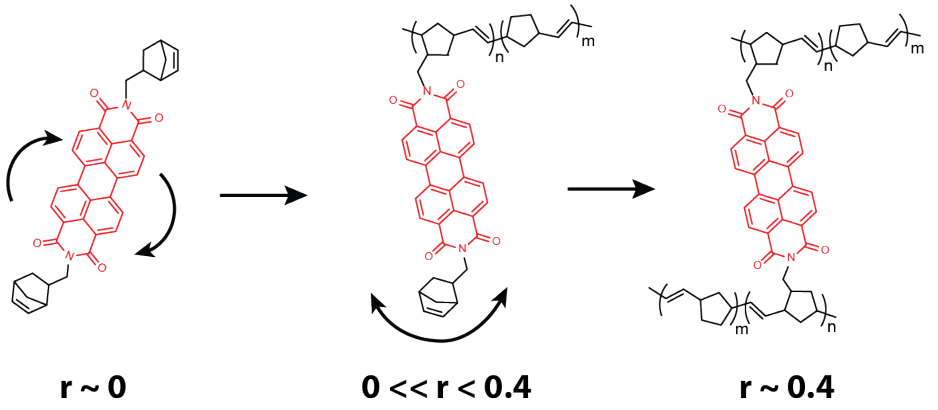

Figure 1-4. Expected fluorescence anisotropy response during polymerization.

1.4 Aggregation-Induced Emission

Aggregation of fluorophores can result in quenching of emission, where intermolecular $\pi - \pi$ stacking results in a decrease of fluorescence intensity. Fluorophores consist of conjugated aromatic ring systems, which can have a reduced solubility and make them prone to aggregate in certain solvents, thereby reducing their overall fluorescence intensity. This can be circumvented by utilizing alternative or co-solvents and working in dilute solutions. However, there are some instances where non-emissive molecules in solution become emissive (turn on) after aggregating, referred to as aggregation-induced emission (AIE). This phenomenon is attributed to the restriction of intramolecular motions which include intramolecular rotations and vibrations.[19–21] When dissolved in solution, molecules such as tetraphenylethylene (TPE) relax via non-radiative pathways by intramolecular rotations, however when rotations are restrained, like in the cases of increased microenvironment viscosity, the radiative relaxation becomes more favorable, and the molecule becomes emissive, **Figure 1-5**. Signal obtained from an AIE measurement is usually presented as normalized fluorescence intensity. Experiments using AIE fluorophores[22] include sensing of biological molecules such as DNA[23–28] and proteins.[29,30] AIE-based fluorophores have even been used for super-resolution imaging of mitochondrion.[31] AIE polymers have also been developed with potential applications such as optoelectronics and fluorescent sensors for both biological and chemical molecules.[32–35] In addition AIE has been used prior to monitor polymerizations in bulk.[36–39] In Chapter 3, AIE is used to monitor the polymerization progress using a TPE-labeled norbornene monomer (TPE-NB), however uniquely, this will be applied to polymerization within a novel environment of droplets. It is expected that at the beginning of the polymerization the TPE-NB will be non-emissive, and as the monomers are incorporated and the local viscosity increases, the TPE-NB should increase in fluorescence.

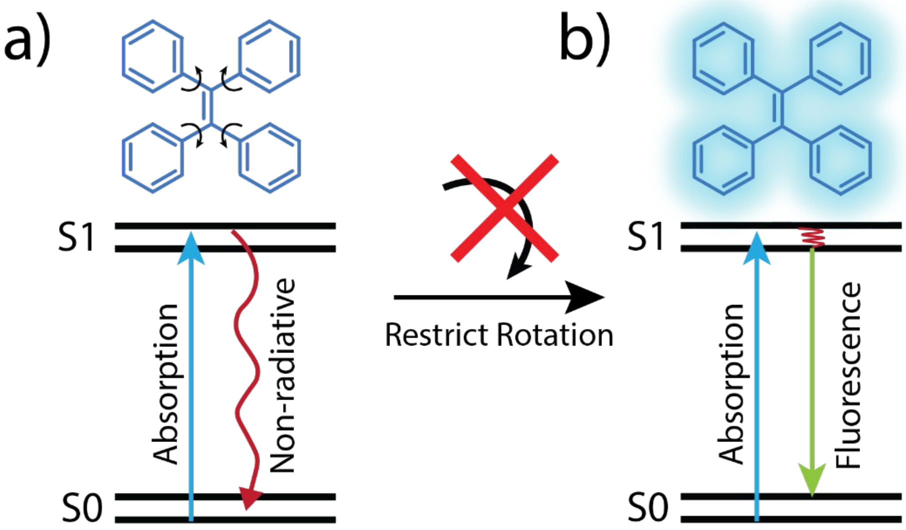

Figure 1-5. Principle of Aggregation-Induced Emission featuring tetraphenylethylene (TPE).
(a) TPE relaxes via non-radiative pathways by intramolecular rotations when in solution. (b) When the rotations are restricted via aggregation or increased local viscosity, fluorescence is then the preferential relaxation pathway.

1.5 Fluorescence Recovery After Photobleaching

Fluorescence recovery after photobleaching (FRAP) is a technique to determine diffusion kinetics. A sample is covered in a thin film (carpet) of fluorescent molecules. Laser light is focused to form a high intensity spot, photobleaching the fluorophores within an area. The laser intensity is then lowered to optically monitor the emission from the same area. Recovery of fluorescence is observed when unbleached molecules diffuse into the photobleached area, **Figure 1-6**. The rate of recovery can be used to determine diffusion coefficients for the fluorescent molecules. FRAP is most often used to study the mobility of molecules within cell membranes.[40,41] In this thesis, FRAP is used to probe the interactions between a fluorous-labeled BODIPY fluorophore and a fluorous-functionalized glass surface.

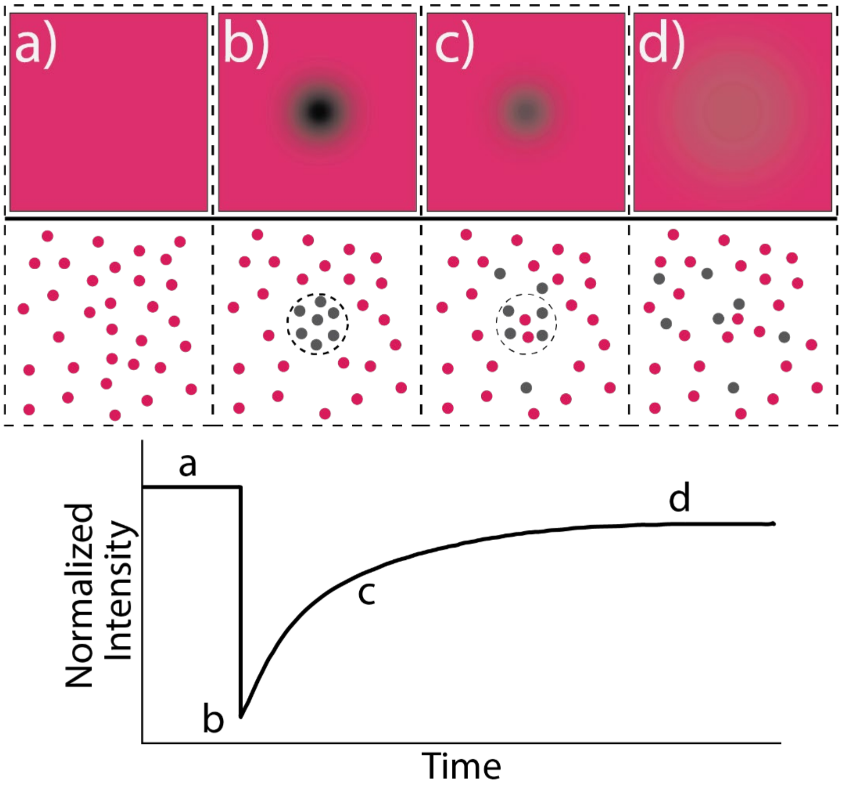

Figure 1-6. Illustration of Fluorescence Recovery after Photobleaching.
(top) Images representing fluorescence images captured by cameras, (center) images representing the position of molecules on the surface, and (bottom) Intensity vs. Time trace depicting four steps (a) prior to photobleaching, (b) photobleaching (c) initial recovery (d) end of recovery.

1.6 Single Particle Tracking

Another technique to monitor diffusion kinetics is single particle tracking (SPT). SPT is a single-molecule microscopy technique, where the fluorescence from an individual molecule is recorded and used to obtain a trajectory of its motion, **Figure 1-7**. The trajectory is then analyzed which can provide insight into diffusion dynamics. Images are taken at exposure times fast enough to capture the motions of the molecules. In contrast to FRAP, SPT requires spatially resolved fluorophores, as particle or molecule identification and localization is an important step to determining accurate trajectories. A microscope has a limit in the resolution it can distinguish two fluorescent spots by, known as the diffraction limit, Equation 1.4.

$$d = \frac{\lambda}{2NA} \tag{1.4}$$

Where λ is the wavelength of light, and NA is the numerical aperture of the objective. In a dense sample, it would not be possible to distinguish the trajectory of each molecule if the space between them is smaller than the diffraction limit.

Many algorithms and programs are available to perform single particle tracking analysis of data which includes localization of molecules, connecting molecules from separate frames to form trajectories, and then analyzing those trajectories to determine the type of diffusion present.[42–46] The trajectory of a molecule can be related to diffusion using mean-squared displacement curves and fit to different types of motions such as pure diffusion (Brownian motion), anomalous subdiffusion, confined motion, immobile and directed motion. The usefulness of the information obtained by this measurement relies on the spatial localization accuracy of the emitters, the temporal resolution of the instrument, including detector speed and integration times, and finally the total experimental observation time.

Along with investigating diffusion, SPT has also been used to investigate adsorption-desorption dynamics, folding-unfolding dynamics, and trapping.[47,48] In Chapter 5, in addition to FRAP, we aim to use SPT to investigate the diffusion of fluorous-labeled BODIPY fluorophores interacting or embedded within a fluorous-functionalized surface.

Figure 1-7. Illustration of Single Particle Tracking.
(Left) Examples of single molecule tracking trajectories created from multiple images (right) example of analysis such as mean-squared displacement.

1.7 Single-Molecule Fluorescence for Chemical Reactions

Single-molecule (SM) microscopy has been as a powerful technique to study biological molecules since the 1980s.[2] SM microscopy has the advantages of being an *in situ* real time measurement, while also providing the benefit of not being limited by ensemble averaging. Ensemble averaging is a result of a bulk technique, which can obscure unsynchronized dynamics. These unsynchronized events can be critical to fully understand mechanisms of catalysts.

Applications of SM fluorescence to study catalysis has primarily been used for heterogeneous catalysis.[49,50] SM techniques have been pivotal in monitoring catalysis on single nanoparticles, uncovering interesting dynamics such as single-turnover detection using fluorogenic molecules[51–53] as well as uncovering mechanisms hidden by ensemble measurements.[54,55] SM techniques have also been used to optically image and understand reactivity of surface catalysts.[56]

SM fluorescence has also been used to investigate homogeneous catalysis.[57] Ring opening metathesis polymerizations have been investigated using SM techniques, identifying interesting growth chain dynamics[58] as well as the selectivity of the molecular catalyst.[59] Within the Goldsmith group, we have investigated molecular catalyst initiation[60] and the heterogeneity of silane bonds on glass surfaces.[61]

The techniques described in Sections 1.2-1.4 can be performed on the single-molecule level, where the major difficulty is resolving the signal from individual molecules, as described in section 1.6. This can be done by either limiting the concentration of the fluorophores or by limiting the excitation volume of the laser beam. Oil objectives with high numerical apertures are used to obtain high collection efficiencies, which is critical to obtain the necessary sensitivity to single emitters. Additionally, freely diffusing non-interacting molecules move too quickly to be able to obtain useful information about a chemical reaction. One route for immobilization is to “heterogenize” molecules by synthetically attaching them to surfaces, but this can result in unwanted interactions between the surface and the molecule of interest, potentially changing the dynamics observed. Another route, which is used in this thesis in Chapters 3 and 4, is through encapsulation of droplets, where the reaction droplet is placed onto a surface and immobilized using surface tension. Finally, fluorescent impurities are a large issue for experiments of single molecules. Fluorescent “dirt” is surprisingly photostable and can appear as small as individual fluorophores. Therefore, it is critical to ensure robust and thorough cleaning procedures so that the fluorescence in any measurement is indeed from the fluorophore of interest and not an impurity.

1.8 Considerations for Experimental Methods

When using any of the above techniques to investigate chemical reactions there are a few considerations that need to be made, as these techniques have been established and tuned to work in aqueous environments. The first is the fluorophore choice, as commercially available fluorophores are often for biological applications their photophysical properties are tuned for aqueous environments. Additionally, these fluorophores are also often only provided with options for labeling of or attaching to biological molecules. Therefore, experiments in organic solvents can often require novel synthesis of the fluorophore-labeled molecule of interest. In the Goldsmith group, the 4,4-difluoro-4-bora-3a,4a-diaza-*s*-indacene (BODIPY) is the fluorophore of choice. With its established synthetic procedures, photostability, and ability to be labeled in the meso-position of the core without affecting the spectroscopic properties,[62,63] BODIPY has been used in many experiments within the Goldsmith group.[60,61]

Another consideration is the material of supplies and items used. For biological applications, imaging in solution is possible with silicon-based wells which can easily be stuck to glass coverslips. When working in organic solvents, plastics and glues can dissolve or swell. This can cause leaking and can introduce unwanted fluorescent impurities. Within the group, we have established a way of making all-glass chambers to perform solution measurements. This features a glass ring which is annealed to glass coverslip using sodium silicate, a procedure for chamber construction can be found in Section 3.4.b.

The final consideration is fluorescent impurities, Millipore water is often free of fluorescent impurities, however organic solvents often are not. Many aromatic organic compounds are fluorescent and dissolve in organic solvents. Blanks of neat solvent should be taken prior to experiments to ensure the cleanliness of a solvent. Purification of solvents can be performed, such as distillations and filtering, to reduce fluorescent impurities, a descriptor of solvent purification is provided in Section 3.4.a.

Chapter 2 The Role of Experimental Noise in a Hybrid Classical-Molecular Computer to Solve Combinatorial Optimization Problems[i]

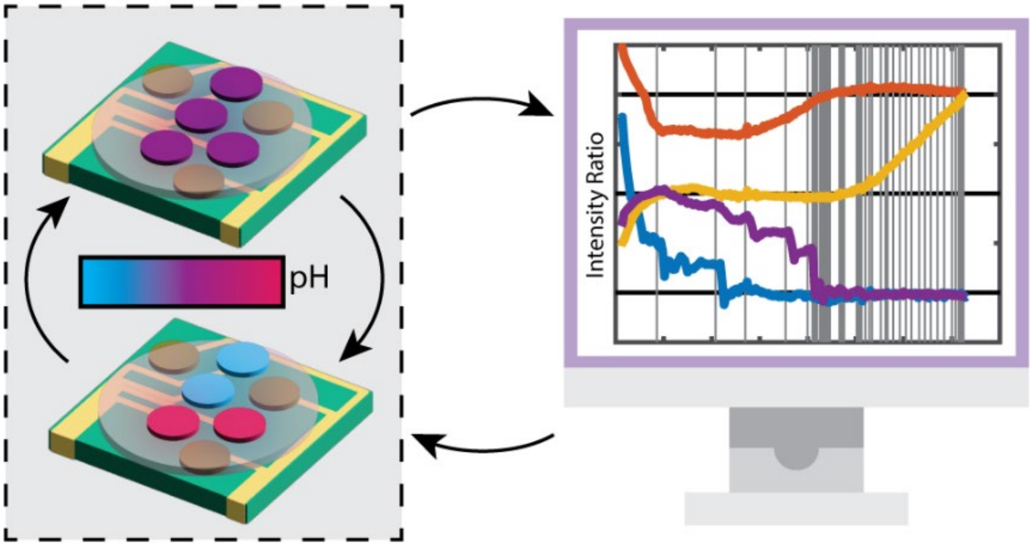

---

[i] Submitted for publication. **Authors:** Veronica K. Krasecki[a], Abhishek Sharma[b], Andrew C. Cavell[a], Christopher Forman[c], Si Yue Guo[d], Evan Thomas Jensen[a], Mackinsey A. Smith[a], Rachel Czerwinski[a], Pascal Friederich[d], Riley J. Hickman[d], Nathan Gianneschi[c], Alán Aspuru-Guzik[d], Leroy Cronin[b]*, Randall H. Goldsmith[a]*

[a] Department of Chemistry, University of Wisconsin-Madison
[b] Department of Chemistry, University of Glasgow, United Kingdom
[c] Department of Chemistry, Northwestern University
[d] Department of Chemistry, University of Toronto, Canada

This chapter has been submitted for publication, it has been reformatted to fit the style of this thesis. I have omitted SI sections regarding coding and simulations of pH.

Abstract

Novel forms of computing are necessary to overcome the impending limitations of modern silicon-based computers. Chemical and molecular-based computers are promising alternatives, and in particular, hybrid systems, where tasks are split between a chemical medium and traditional silicon components, may provide a means to access and demonstrate chemical advantages such as scalability, low power dissipation and genuine randomness. This work describes the development and execution of a hybrid classical-molecular computer (HCMC) featuring an electrochemical reaction on top of an array of discrete electrodes with a fluorescent readout. The chemical medium, optical readout, and electrode interface work in combination with a classical computer to generate a feedback loop to solve several canonical optimization problems in computer science, such as number partitioning and prime factorization. Importantly, the HCMC makes constructive use of the experimental noise, with the optical readout introducing stochasticity that is utilized in a gradient descent to solve these optimization problems, as opposed to in silico random number generation. Specifically, we show that calculations stranded in local minima are able to consistently converge to a global minimum in the presence of experimental noise. Scalability of the hybrid computer is demonstrated by expanding the number of variables from 4 to 7, which increases the number of possible solutions by an order of magnitude. This work provides a steppingstone to fully molecular approaches to solving complex computational problems using chemistry.

2.1 Introduction

The approaching limits of modern silicon computing motivate research into alternative computing paradigms. Silicon-based computers following a von Neumann architecture can be inefficient for some processes due to a limit on data throughput caused by the inherent separation of the memory and processing units. The number of transistors within a device has greatly increased allowing for the execution of more complex tasks. However, high heat dissipation and power constraints,[64–66] along with increasing costs and complexity in manufacturing, limit further increases of transistor density.[67] Molecular or chemical-based computers are one attractive family of alternative computing systems. Chemical computers have been developed based on reaction-diffusion systems and oscillating chemical reactions such as the Belousov-Zhabotinsky (BZ) reaction,[68–75] while molecular computers have historically utilized DNA or other biological molecules to assist in computations.[76–80] More broadly, molecular approaches to a variety of critical computational subsystems, including memory,[69,81–86] image processing and recognition,[87,88] digital circuits,[89] and logic gates,[90–94] are being pursued to investigate the nature of any perceived molecular advantage.

A hybrid classical-molecular computer (HCMC)[95] couples chemical and digital analogues of a set of state variables. Having some tasks performed within a chemical medium and other tasks performed by traditional silicon components can allow certain advantages of molecular information processing to be accessed, such as scalability, low power dissipation, and genuine randomness. Hybrid computing frameworks are designed with intent to go beyond their individual computing components.[96–98] For example, our HCMC can allow for programmability, which is a current limitation of purely chemical computing systems. Taken together, a demonstrative HCMC can provide substantial value as a steppingstone to evaluate molecular approaches to key computing subsystems, even though the approach is not fully molecular. Here, we present the implementation of an HCMC that consists of spatially-distinct sites (we will refer to these “sites” throughout this paper) in an aqueous gel containing a payload of chemical reagents on top of a two-dimensional (2D) lattice of electrodes. To design and evaluate the HCMC, we have tested the hybrid computer on several well studied problems in computer science, including problems that are representative of a nondeterministic polynomial time (NP)-complete class such as Boolean satisfiability problems specifically 3-satisfiability (3-SAT) and number partitioning, as well as non-NP problems such as 2-satisfiability (2-SAT) and factorization. Importantly, we show that this architecture allows the chemical and electronic noise based in the physical infrastructure to directly and constructively influence complex algorithms in well-defined ways that may otherwise be expensive or sub-optimal to achieve using a digital computer alone.

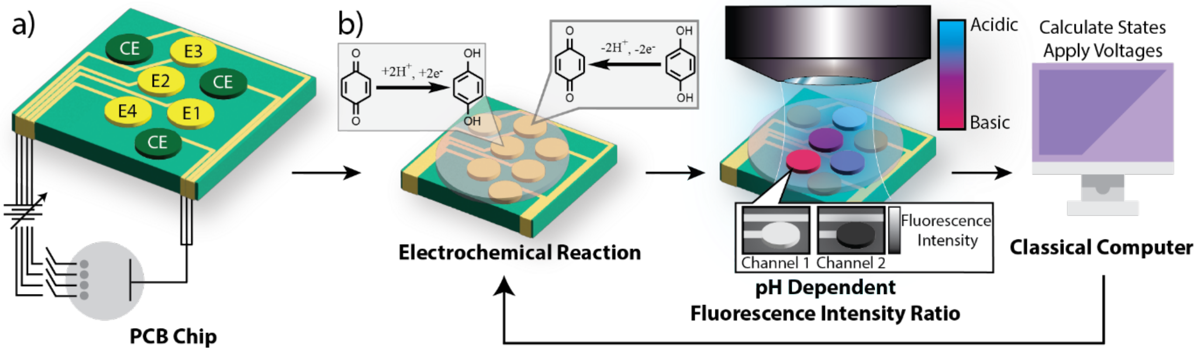

Figure 2-1. Concept of HCMC.
a) Electronic schematic diagram of printed circuit board (PCB) chip featuring four individually addressable working electrodes (E1-4), and three counter electrodes (CE) connected to a programmable power supply. b) General concept of hybrid classical-molecular computer (HCMC) electrode chip with electrochemical redox reaction of benzoquinone and hydroquinone resulting in changes to [H+] concentration. The pH changes are then measured optically using the fluorescence emission from a pH sensitive dye, which is spectrally separated to collect the ratio of the two emission peaks. The intensity ratio is then used in the classical computer to calculate the computational states of each variable and apply potentials at the electrode surface. This feedback loop is repeated until the computation converges.

The generalized HCMC architecture is shown in **Figure 2-1** and consists of a simple feedback loop that couples information processing from a classical computer together with a chemical system. This autonomous feedback loop forces the chemical and digital versions of a given variable to stay synchronous, enabling either physicochemical or digital events to dynamically update the information stored in both the digital and chemical registers, which are copies of each other. The chemical matrix, a gel, sits on top of a printed circuit board (PCB) chip with individually addressable electrodes that define the chemically active sites, **Figure 2-1a**. Importantly, the chemical variables encode information among the ensemble of molecules at the site proximal to each electrode. The chemical information comprised of the states of the molecules over the working electrode sites, is passed to the classical computer to manipulate the digital variables for processing, leading to output as potentials applied at the electrodes coupled to the chemical components, **Figure 2-1b**. Combined, the chemical and digital variables work together to solve computational problems, using properties unique to the digital and chemical environments to aid in processing.

For the chemical variables to be computationally useful, the chemical properties must be tunable in a manner that is reversible and responsive to electrochemical input signals and must themselves be capable of providing a robust signal which can be measured during readout. For this demonstrative HCMC, a simple redox reaction capable of bringing about reversible pH changes is employed, with a pH sensitive fluorophore, carboxy-SNARF-1, added to allow optical readout of the system states. The fluorescence readout is captured by cameras and is then processed by the classical computer, which converts the fluorescence reading into a digital state variable. The chemical and digital manifestations of each variable are interchangeable with a full two-way commuting relationship. Information is transferred from chemical to classical computer by fluorescence detection and from the classical computer to the chemical system by electrochemical control.

To use the chemical variables for problem solving, the HCMC must construct a many-to-one mapping between the microstates of the chemical system and an abstract mathematical formalism.[99] For this purpose, we define the pH of the site to be analogous to the two spin states of an *idealized* Ising model,[100] or equivalently, quadratic (two-local) unconstrained Boolean optimization (QUBO). The Ising model is a paradigm that can be used to solve hard combinatorial optimization problems, with a wide range of applications including logistical operation, biomolecule structural optimization,[101–103] circuit design,[102,104] and machine learning.[105,106] Simulated annealing processors have previously been shown to be able to solve NP-Hard combinatorial optimization problems. Various types of digital and simulated annealers and Ising solvers have been developed,[107–114] but our system uniquely utilizes a molecular fluorescent response both as an input to couple to the digital representation and as a readout of the final or interim states.

A given combinatorial optimization problem can be represented as a problem Hamiltonian which then can be mapped onto the Ising Hamiltonian. A general Ising Hamiltonian for a two-state system of binary variables is defined as:

$$H_g = \sum_{i=1}^{N} \alpha_i s_i + \sum_{i<j}^{N} \beta_{ij} s_i s_j \tag{2.1}$$

where, s_i and s_j represent spins (+1 or -1) for variables i and j , while α and β are problem specific coupling coefficients. The problem of choice is encoded into these coefficients, with α_i representing the local field for an individual variable as a vector, and β_{ij} denoting the interaction energy or coupling between two variables as a matrix. To find the solution, one must find the optimal spin configuration such that the overall scalar value of H_g reaches a minimum given a specific α and β.

The HCMC has two distinct overall inputs: the problem Hamiltonian that defines the external relationships between the sites as a function of the state that each site maintains, and the initial values of the states, which can be any value between (-1, +1). The Hamiltonian matrix defines the sign and strength with which a pair of sites interact, represented by the β coupling coefficient. The interactions between the states along with the local field for the individual state, represented by the α term, are used in combination to yield a continuous scalar field over the space spanned by the state vectors. These couplings are a direct analogy to the mechanical linkages in a historical differential analyzer,[115,116] which constrain the relationships between the variables of the mechanical analogue computer. The classical computer part of the HCMC also generates outputs used to induce couplings between the individual variables by actuating the electrodes. Specifically, the classical computer controls a potentiostat to apply voltages at the electrodes, inducing an electrochemical reaction and thereby changing the local pH. As the system evolves the pH is measured and read out using a ratiometric fluorescent dye. The dye, carboxy-SNARF-1, allows for the ratio of its two fluorescence emission peaks to be linearly converted to pH, and in turn converted to a numerical state value ranging from +1 to -1. By using a classical computer to host the information about site interactions virtually, interactions are not limited to nearest neighbors, and the difficult engineering problem of creating tunable physical interconnects between sites is sidestepped. This version allows for full connectivity between all the variables encoded in the problem Hamiltonian. This arrangement expands the types of computational problems which can be tackled by this demonstrative HCMC.[95]

A gradient descent algorithm is applied in the classical computer to the computational representation of the state at each site so that the entire system moves towards a minimum or a solution to the computational problem. Gradient descent algorithms find minima by taking steps based on the steepness of the gradient, with each step's direction being dependent on the current state and the value of the function's instantaneous gradient at that point. The step size is a scaling factor for how far the algorithm can move down the gradient at each step and is tuned by the user to optimize performance. For the HCMC, the position or gradient at each step uses the state value derived from the fluorescent output. The algorithm uses the slope of the scalar cost function for each problem, rather than calculating absolute values, which allows us to solve problems whose global minima have a non-zero absolute value. However, this approach is susceptible to converging on local minima.

The cost function for a problem can be rugged, with multiple, sometimes near degenerate, low energy local minima. For the HCMC to successfully solve the problem, it must identify and converge (halt) on the configuration corresponding to the lowest scalar value, the global minimum. Importantly, the HCMC can get trapped in local minima during the gradient descent and converge on the wrong solution. One common way to combat this process is to perform multiple initializations at different starting states to obtain a distribution of all converged states thereby increasing the probability of convergence towards the global minimum. Additionally, it has been shown that stochastic noise or random perturbations added to the optimizer, resulting in a stochastic gradient descent, can speed up the calculation by reducing the probability of being trapped in local minima.[114,117–119] However, the way noise is generated is not always ideal. For example, all digital number generators are pseudo-random, meaning they can be predicted. An alternative can be found in the experimental measurements themselves. Intrinsic hardware noise has been reported as beneficial in solving combinatorial optimization problems using a memristor-based neural network system.[120] Additionally, sensor noise for an optical cavity has also been theorized as a resource to increase sensitivity in low-power or noisy conditions.[121] This phenomenon is true both for classical and quantum systems.[122]

By designing computational paradigms that take advantage of the inherent experimental noise instead of deterring it, new chemical processes and designs can be used for chemical and molecular computing. The effect of noise on the computational efficacy inspired questions about how the inherent experimental noise could aid or limit the annealing process in a HCMC.

2.2 Results and Discussion

2.2.a Optical Experimental Setup

The HCMC includes a purpose-built microscope**, Figure 2-2a**, with widefield illumination provided by a 488 nm laser. Fluorescence is collected using a 1X air objective and directed toward cameras, passing through a 505 nm long pass dichroic mirror and a 532 nm long pass filter to remove excitation light. The fluorescence is spectrally resolved into two color channels using a 610 nm long pass dichroic mirror and focused onto two separate cameras which capture the emission from the two fluorescence peaks of the pH indicator.

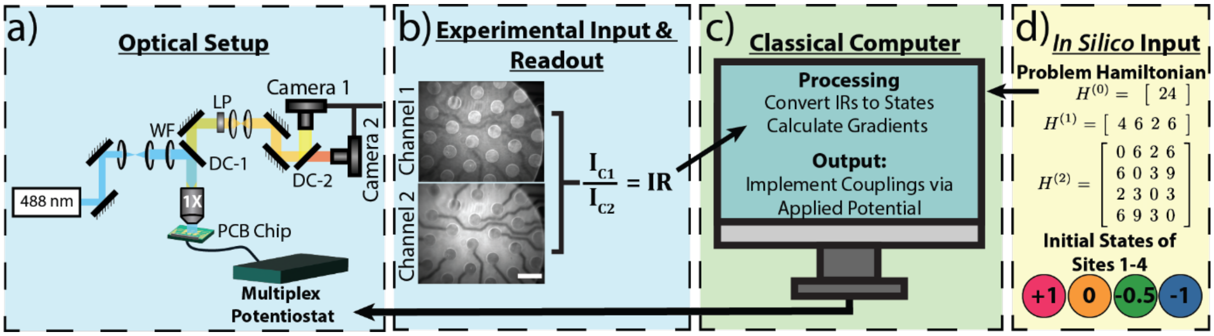

Figure 2-2. Experimental Design of Feedback Loop for HCMC.
a) Experimental optical set up for monitoring pH changes in chemical reaction gel on the 2D electrode array. b) Fluorescence images of reaction gel used to calculate an intensity ratio (IR) which is used as an experimental input to the c) classical computer to use in the gradient descent along with d) the *in silico* inputs, such as the Ising Hamiltonian for the problem as well as the initial states for the sites at the first step of the computation. The classical computer outputs a potential at the electrode chip via a multi-channel potentiostat to induce pH changes monitored via the experimental readout, IR. (2 mm scale bar, WF – Widefield lens, DC-1 – 505 nm dichroic mirror, DC-2 – 610 nm dichroic mirror, 1X Objective, LP – 532 nm long pass filter and 540 nm long pass filter)

2.2.b Electrode Array Design

We use a simple and cost-effective custom-made electrode array with an electrode size of 1 mm placed in a hexagonal grid to maximize the connectivity of multiple working electrodes with the counter electrodes. All electrodes were gold plated by the PCB manufacturer. The electrode arrays were fabricated using standard PCB manufacturing, see Section 2.6.a for details.

2.2.c Chemical Encoding, Input, and Readout

The chemical system for encoding information in the HCMC is a hydroquinone/benzoquinone redox couple dissolved in an aqueous buffered Pluronic gel containing a fluorescent reporter. The gel is placed onto a PCB-based electrode chip.[123] The Pluronic gel allows for a solid-like matrix reducing diffusion across the electrode chip, which keeps the chemical changes localized over the specific electrode surface but does not hinder electrophoretic motion. The quinone redox couple allows for a reversible way to manipulate pH when paired with applied potential from the electrodes. There is around a 1 pH difference between the -1 state and $+1$ state for each site participating in the computation. The formulations and specific pH values for each site corresponding to the computational states are described in Section 2.7.

Readout is provided by fluorescence, which optically assesses the pH of the gel region over each electrode, and thereby conveys the computational state of each variable. These fluorescent measurements allow for a real-time, in-situ readout.[124] To optically monitor pH, we used a ratiometric pH sensitive fluorophore with a pH-dependent emission spectrum,[125,126] Carboxy-SNARF-1, which has previously been used to measured intracellular pH.[11,13,14,127,128] The fluorescence emission has two peaks at 580 nm and 640 nm, and the ratio between these two peaks can be calibrated to read out pH. The use of a ratiometric pH sensor is critical, as a pure intensity readout can be changed by interference from electric field-induced concentration fluctuations, aggregation, and photobleaching. The intensity ratio (IR) between these two channels, which is proportional to pH, is passed to the classical computer and converted into a state value, **Figure 2-2(b-c)**. The fluorescence signal is therefore not only used as a readout of the chemical information, but also as an input to the classical computer.

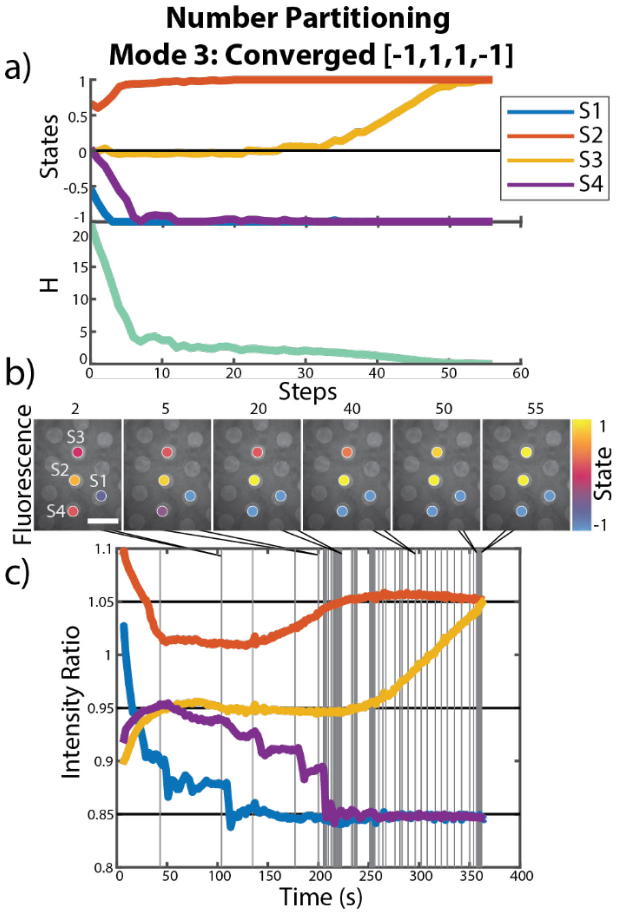

Figure 2-3. Progression of the hybrid classical-chemical computer solving a Number Partitioning problem using Mode 3 (see text for details).

a) Evolution of states throughout the computation, where S1-S4 represent the four sites, and the value of the problem Hamiltonian (H) at each step of the computation. b) Fluorescence images of the reaction gel on the electrode chip with artificially colored circles depicting the state value at various steps, scale bar is 2 mm. c) The value of the intensity ratios over time during the computation, where vertical lines represent each step of the computation.

2.2.d Classical Processing and Output

To process the ratiometric responses from these images, the coarse location and approximate size of electrodes participating in the computation are initially determined manually and refined using image segmentation that employs a watershed algorithm[129] to identify the electrode region, **Figure 2-3b**, all before the computation begins. The state values, converted from the experimental IRs, are used as the input in the gradient descent calculation performed by the classical computer, **Figure 2-3**. As previously mentioned, the gradient descent algorithm uses the state values along with the user-determined step size to determine the target state values for the next step. Alternatively, a stochastic gradient descent algorithm can be utilized through the addition of random computer-generated noise to the target states. This noise will be referred to as *in silico* noise and can be optionally added. To achieve the determined target state, a potential is applied at the electrodes via a multiplexed potentiostat, which allows independent iterative control of up to 7 electrodes, **Figure 2-2b**. A proportional-integral-derivative (PID) algorithm is used to reach the target IR corresponding to the target state, with the PID gains tuned to avoid overshooting by the potentiostat. The PID loop consists of the potentiostat manipulating the potentials over the electrodes while the changing IRs are monitored using the optical setup, **Figure 2-3c**. Once the IR values at all participating sites are within a set threshold of the target, the PID loop for that step in the gradient descent is finished and the next step can be taken. This is illustrated by the vertical lines shown in **Figure 2-3c**. The user-set threshold determines how close the experimental IR needs to be to the targeted set point before proceeding to the next step. This PID loop is performed for each step of the gradient until the minimum is found. A movie of the fluorescence response is provided in the supporting information of the published manuscript, showing the HCMC using 7 sites (working electrodes) where the PID gains were set to induce an exaggerated fluorescence response. Combining all these parts, the HCMC can be successfully run starting at either random or specific initial states and converging on the global minima, thus solving various optimization problems, including number partitioning, **Figure 2-3**, and 2-SAT, **Figure 2-11**.

An accompanying numerical simulation engine was developed describing the computation using the HCMC process. The simulation engine creates a generalized electrode array network by combining Kirchhoff's equations coupled with a Secondary current distribution model. The calculated time-dependent current profiles are then combined with a buffer dynamics model to describe localized pH changes over the electrodes (see SI of published manuscript). Combined with a stochastic gradient descent algorithm, this supporting simulation shows convergence, as well as hallmarks of experimental non-idealities, such as ringing in the experimental PID loops, and can aid in parameter optimization as well as instantiating a large-scale problem on an electronic chip.

2.2.e Evaluating the Role of Experimental Noise

The HCMC is designed to solve quadratic combinatorial optimization problems using a gradient descent algorithm with a fluorescent molecular signal as input and readout. As previously mentioned, added stochastic noise aids convergence to a global minimum by preventing getting stuck in local minima, saddle points, or plateaus. Importantly, we examined the impact of the HCMC's intrinsic noise when solving computations.

Three operational modes of the HCMC were investigated: Mode 1 uses what have been termed "idealized states," where the states in each step of the gradient are identical to the set points determined by the classical computer; Mode 2 uses "*in silico* states," which are idealized states, but with an added stochastic *in silico* noise component, resulting in a stochastic gradient descent; Mode 3 uses "measured states," which converts the experimentally achieved IR signal into the state for the computation with no added *in silico* noise. As Mode 1 does not include any noise component, the HCMC is expected to either not be able to progress through the computation, in contrast to the run displayed in **Figure 2-3**, or be more likely to get trapped in local minima, resulting in convergence on incorrect answers. Mode 3 also does not include an *in silico* noise component, however the experimental noise within the measurement is expected to be a beneficial source of stochasticity with potentially large enough fluctuations to avoid repeating the failed trajectories observed in Mode 1.

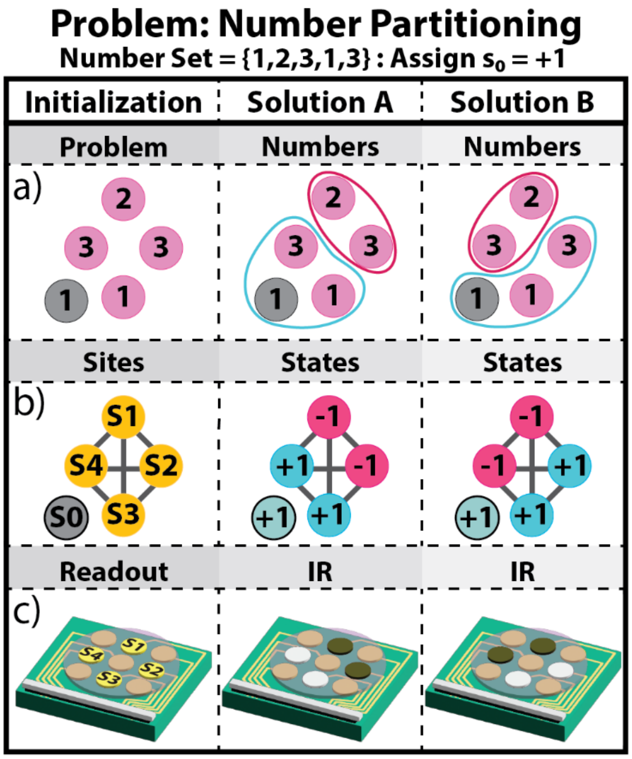

Figure 2-4. A visual depiction of the number partitioning problem and the two solutions. The general form of the Ising Hamiltonian is shown at the top. The three columns correspond to the numbers in the problem (left), the grouping for solution A (center) and solution B (right). a) The problem represented by the numbers in the problem, b) the state values at the Sites S1-S4 and c) depiction of changes observed on the electrode chip via fluorescence.

To investigate the role of experimental noise, multiple complementary experiments involving number partitioning problems were performed. Number partitioning is a NP-complete problem, which asks, for a given set of numbers, how can they be divided into disjoint subsets with equal sums? Number partitioning has been called the “easiest hard problem”[130] in terms of its complexity. For the purpose of investigating the role of noise, we have selected a simple problem consisting of a small number of variables that still produced a non-trivial cost function with multiple solutions. The number set {1,2,3,1,3} was selected and an Ising Hamiltonian for the problem was generated, **Figure 2-2d**, see SI of manuscript for details regarding Hamiltonian generation. The Hamiltonian corresponding to this problem is non-negative and minimized at H=0, when the sums of the two sets are equal. This five-number set was expressed using four variables with the first number {1} automatically assigned to a +1 state (s_0)

without loss of generality. The other four numbers are assigned to the spatially distinct gel areas over individual electrodes, referred to as sites. The state values (s_i) for the remaining numbers {2,3,1,3} describe which subset each number belongs to and will be defined by the fluorescence IR values at Sites 1, 2, 3, and 4. A depiction of this problem can be seen in **Figure 2-4**. The correct partition solution (H=0) for this problem is {1,1,3} and {2,3}. However, as the number three is repeated twice in the set for our problem, there are two different ways this partition can be expressed using our sites. One solution, Solution A, is where the number two associated with Site 1 would be paired with the number three associated with Site 2, **Figure 2-4a-Solution A**. The second solution, Solution B, has the number two associated with Site 1 paired with the number three on Site 4 instead, **Figure 2-4a-Solution B**. To express that these numbers are grouped together, the state values of these sites must be the same, **Figure 2-4b**.

Starting with Solution A, the state values for Sites 1 and 2 should be the same, meaning that both sites should either be +1 or -1. However, there is an additional constraint: the first number in the number set is already assigned a +1 state. Consequently, Sites 1 and 2 are unable to take the +1 state, as this would result in the partitioning of {1,2,3} and {1,3}, which is incorrect. Therefore, Site 1 and Site 2 must take a -1 state, which gives Solution A [-1,-1,1,1], visually depicted in **Figure 2-4-Solution A**. For the second solution, Site 1 is paired with Site 4, both will take the -1 state, resulting in Solution B [-1,1,1,-1], **Figure 2-4-Solution B**.

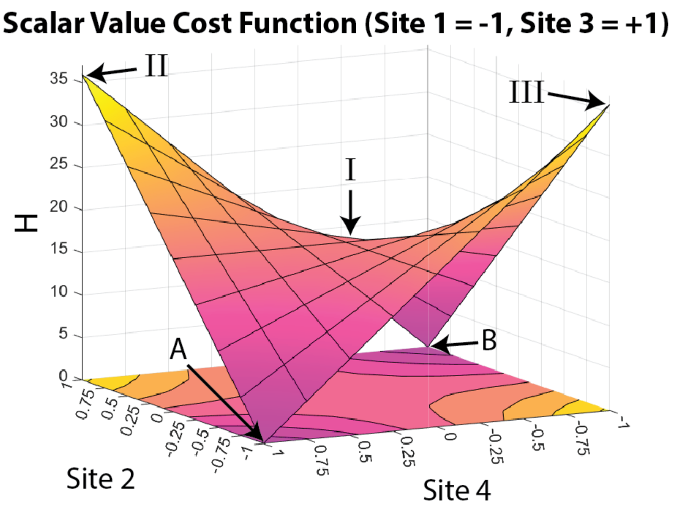

Figure 2-5. Scalar value cost function for the Number Partition Hamiltonian when Sites 1 and 3 are kept constant at -1 and +1, respectively, and Sites 2 and 4 are varied from -1 to +1 states.
Labeled states correspond to: I) Saddle point [-1,0,1,0], II) first maxima point [-1,1,1,1], III) second maxima point [-1,-1,1,-1], and Solution A) [-1,-1,1,1] and Solution B) [-1,1,1,-1].

Interestingly, Solutions A and B differ by two variables, the second and fourth, both of which have oppositely signed values of 1. When plotting the cost function for this problem with respect to Sites 2 and 4, and with Sites 1 and 3 at constant solution state values (-1 and +1 respectively), a symmetric saddle shape emerges, **Figure 2-5.** The flat saddle point is located at [-1,0,1,0], **Figure 2-5-I**. The value 0 here represents the midpoint state value between the two extreme state values, -1 and +1. There are two maxima located at **Figure 2-5-II** at the states [-1,1,1,1], and **Figure 2-5-III** at states [-1,-1,1,-1], with equal values for the problem Hamiltonian. The landscape also shows the two solutions, **Figure 2-5-A** [-1,-1,1,1] and **Figure 2-5-B** [-1,1,1,-1], both with the problem Hamiltonian equal to 0. Based on this function, three separate initial states were selected as starting points to explore how noise affects system evolution: [-1,0,1,0] (Initial State I, **Figure 2-5**-I), [-1,1,1,1] (Initial State II, **Figure 2-5**-II), and [-1,-1,1,-1] (Initial State III, **Figure 2-5**-III).

For these experiments, the HCMC was run using each of the 3 operational modes described above, Mode 1 using idealized states, Mode 2 using *in silico* states and Mode 3 using measured states. 20

repeats were performed for each mode at each of the three initial states, resulting in a dataset of 180 runs, see **Table 2-1**. The distribution of converged states is shown in **Figure 2-6**.

Table 2-1. Distribution of Solutions from Number Partitioning Computations

	Mode 1 – Idealized States	Mode 2 – *in silico* States	Mode 3 – Measured States
Initial State I	A: 0/20 B: 0/20 Initial State I: 20/20	A: 8/20 B: 12/20	A: 5/20 B: 15/20
Initial State II	A: 0/20 B: 20/20	A: 9/20 B: 11/20	A: 8/20 B: 12/20
Initial State III	A: 0/20 B: 0/20 LM: 20/20	A: 8/20 B: 8/20 LM: 4/20	A: 11/20 B: 8/20 LM: 1/20

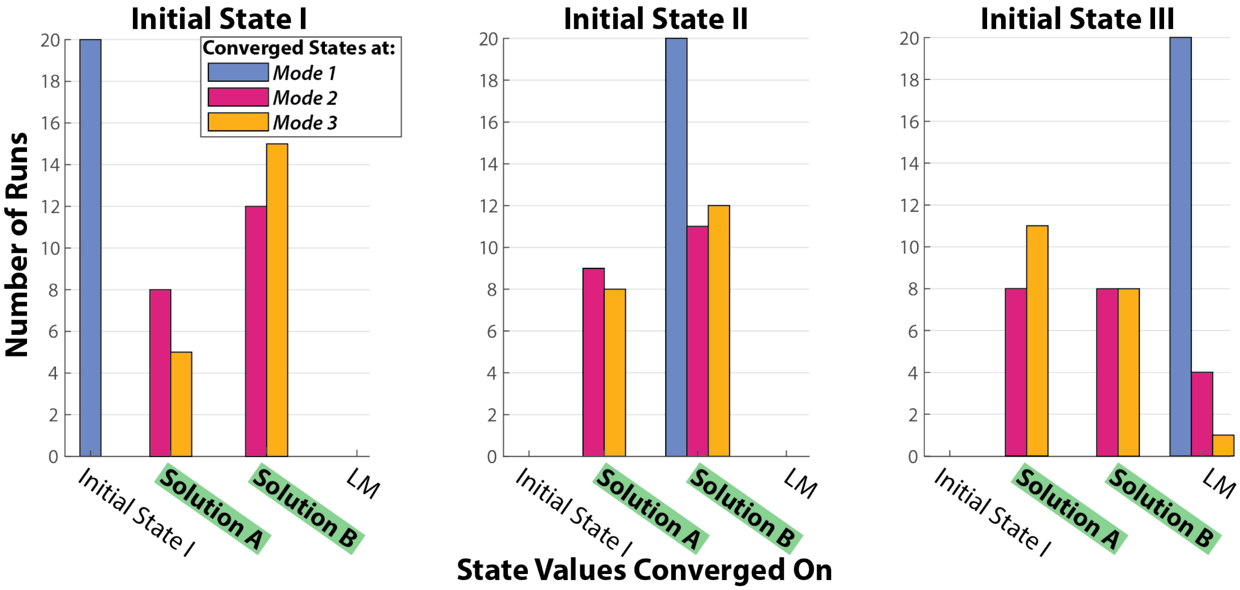

Figure 2-6. Distribution of converged answers.
Bar graphs showing the distribution of converged answers, where each graph corresponds to a separate initial state, with Initial State I (left), Initial State II (center), and Initial State III (right). The states converged on by our system correspond to the Initial State I, the two solutions A and B, and a local minimum (LM). Colors correspond to the three different operational modes for the HCMC.

When starting at the saddle point (**Figure 2-5-I**) and using Mode 1, the idealized states, the computation immediately and erroneously converges on the initial states [-1,0,1,0] for all the runs carried out in this mode (100%), **Figure 2-6**. Here, with the starting point at the saddle and without the addition of any stochastic *in silico* noise, the gradient experiences a flat slope and incorrectly determines this scenario to be a minimum, as expected. When repeating the computation starting from the same initial state but with Mode 2, *in silico* states with noise, the computation was always able to converge on one of the two correct solutions, with a 40:60 split between Solutions A and B. Excitingly, with Mode 3, which uses the experimentally determined measured states, the computation is once again able to run smoothly and converge to both global solutions, resulting in a 25:75 split between Solution A and B across all runs, a similar distribution of converged states as when using Mode 2. This result is important, as it clearly shows that the experimental noise inherent to the empirical measurement in the chemical system is significant enough to allow the HCMC to leave this flat portion of the energy landscape while not impeding convergence.

We then switched to an alternate starting point: one of the maxima on the cost function **Figure 2-5-II**. Without any additional noise at Mode 1, the HCMC is only able to find one of the two correct solutions (100%). In contrast, runs at both Modes 2 and 3 were able to converge on both solutions with similar distributions, see **Table 2-1**.

Finally, when starting at the second maximum, **Figure 2-5-III**, runs at Mode 1 all converged on states [1,-1,1,-1] (100%), which does not match either of the two solutions nor the initial state. For this set of converged states, the state value for the first site has flipped, from -1 to +1. When plotting the cost function for this case, it is illustrative to switch to Site 1 and Site 2 as the independent variables, **Figure 2-7.** We see another saddle but this time it is asymmetric, with the global minimum at one of the correct solutions, Solution B, **Figure 2-7-B** and a new local minimum at states [1,-1,1,-1], **Figure 2-7-LM**. When using Mode 2 we see a split of 40:40:20 between solutions A, B, and the LM. Excitingly, runs at Mode 3 also demonstrate a distribution of the converged states, with a 55:40:5 split between Solutions A, B and LM. This again supports that the intrinsic experimental noise is beneficial to the HCMC to solve computations, seen previously with experiments starting at Initial State I. Additionally, the magnitude of the noise present also shows a benefit in reducing convergence at local minima, with similar statistical results compared to Mode 2, using the *in silico* states. Therefore, it is reasonable to run the HCMC using the measured states with the experimental noise in lieu of the *in silico* noise.

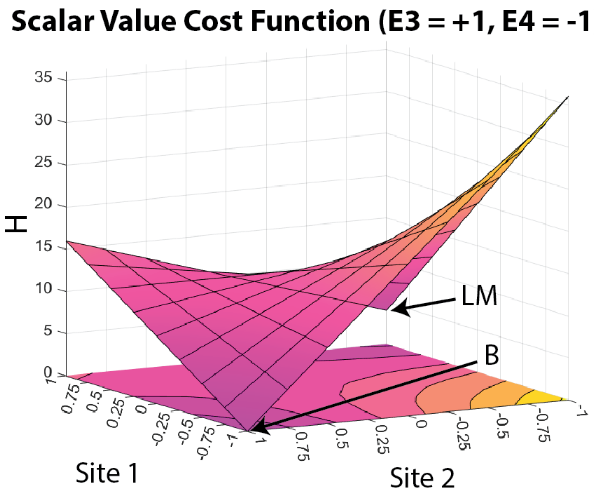

Figure 2-7. Energy landscape for number partition problem where Sites 3 and 4 are kept constant at +1 and -1 respectively, and Sites 1 and 2 and varied from +1 to -1.
Two minima are observed, B) a global minimum at state values [-1,1,1,-1] corresponding to Solution B, and LM) a local minimum at state values [1,-1,1,-1].

2.2.f Sources and Magnitude of Experimental Noise

While the above results show how experimental noise benefits the HCMC's function, there are still unanswered questions about the origins and magnitude of the experimental noise. As the complexity of computational problems changes, the amount of noise that is beneficial *vs*. inhibitive changes as well. By identifying the sources of experimental noise within the HCMC, it becomes possible to program or tune the noise depending on the complexity of the problem. As mentioned earlier, the optimal noise to carry out a stochastic process has been heavily studied in the context of classical and quantum dynamics.[122]

For the experimental noise to impact the computational ability of the computer, it must be present in the experimental input used in the gradient descent. The experimental input originates in the measured fluorescence-detected IRs, which are based on the electrochemically generated pH changes. Therefore, the magnitude of fluctuations in the optical measurements of fluorescence or the electrochemical components responsible for changing pH must be determined. As these fluctuations will be quantified in terms of intensity ratios, it is possible to convert the noise to state variables and obtain the relative scale of the noise in state space. Said another way, the conversion allows us to compare the experimental noise to the *in silico* noise added in the previous section when running the HCMC at Mode 2.

Before investigating the experimental noise, it is necessary to discuss what exactly qualifies as *in silico* noise. The *in silico* noise in the HCMC is a randomly selected number from a normal Gaussian distribution generated via Python. The Gaussian distribution is centered over the integer zero, with the standard deviation or width of the distribution specified by the user. The randomly selected number is applied to the state value, after the next step in the gradient is calculated but before it is executed. As the offset applied at each step changes, the standard deviation selected by the user is what will be broadly referred to as the *in silico* noise. For the experiments above, runs at Mode 1 had a standard deviation of 0 selected, while at Mode 2 a standard deviation of 0.1 was selected.

Runs at Mode 3, using measured states, had a standard deviation of 0, meaning no *in silico* noise was added. Importantly however there is experimental noise present that allows the HCMC to perform successfully. To determine the magnitude of experimental noise, the noise in the optical measurements was first quantified. A reaction gel containing SNARF-1 dye was examined under the same conditions used in the computational runs. The reaction gel was imaged for 5 minutes without an applied potential, and the standard deviation in the average fluorescence IR signal over the electrodes was quantified. This measurement includes noise from the imaging setup, such as the read noise of the cameras and the noise in the intensity of the laser, as well as any background fluorescence from the electrode chip. The standard deviation was converted into an effective *in silico* noise value by using the linear relationship between IR and state. The percent standard deviation, along with the calculated equivalent *in silico* noise value are shown in **Table 2-2**. The equivalent *in silico* noise value calculated is an order of magnitude smaller than what was used at Mode 2.

Table 2-2. Quantified experimental noise.

Description	Percent Standard Deviation (%)	Calculated Relative *in silico* Noise
Noise from Optical Measurement	0.22 (±0.05)	0.02
Noise from Electrochemical Measurement	0.0010 (±0.0002)	0.0001
Noise from Complete Experimental Measurement	0.25 (± 0.05)	0.02

For the electrochemical apparatus, the noise in the current at each electrode was measured under a variety of conditions. This measurement includes noise in the potential applied on the electrode surface, fluctuations in current caused by interactions at the electrode surface, and noise in the measurement of the current itself. The current was measured by the potentiostat while performing a controlled potential chronoamperometry experiment. A gel was placed onto the electrode chip and imaged in the same way as described above, but with various constant applied potentials. The potential in each case was held constant for 5 minutes while the current was measured. The noise in applied potential alone was also measured independently but was found to be insignificant, see Section 2.10.a. The measured current traces were converted to charge traces, which were used to determine the gain or loss of protons over time due to the oxidation or reduction of the quinone couple. By assuming 100% Faradaic efficiency, a maximum possible contribution from current noise can be determined, as each fluctuation in the measured current is assumed to reflect changes in the production or loss of protons in solution at the electrode. After accounting for buffering, these fluctuations in proton concentration (and thus in pH) can be equated to a change in the IR over time. As shown in **Table 2-2**, the maximum contribution to the experimental noise from the electrochemical apparatus is significantly less than the contribution from the optical measurement.

Finally, to investigate how the optical and electrochemical components of the noise collectively contribute to the noise in the IR, a gel was imaged while applying varying potentials to maintain a set IR over many minutes. The gel was initiated at pH 7 and then potentials were applied using the PID loop to bring all the active electrodes to approximately pH 7.5 (state = -1, IR = 0.85). This experiment combines the noise contributions from the two previous experiments discussed above. The noise calculated from these experiments was comparable to the optical noise measurements, Table 2-2**.**

From these experiments, the noise in the optical measurements appears to be the biggest contributor to the overall experimental noise, with the largest standard deviations. To understand what effect this magnitude of noise has on the computational solving ability of the HCMC, we return to the previous number partitioning problem. When starting at Initial State III, convergence at a local minimum was observed. At Mode 1 with no *in silico* noise, the HCMC always converged on the local minimum. Switching to Mode 2, with an *in silico* noise value of 0.1, the frequency of local minimum convergence drops to only 20%. The computation was repeated at Mode 2 starting at Initial State III at varying *in silico* noise values (see Section 2.11). The HCMC needed at least an *in silico* noise value of 0.01 to find the global minima, however the success rate was fairly low, with only 26% of runs converging correctly on global minima and 74% converging on the local minimum. Increasing the *in silico* noise to 0.02, a similar magnitude as the experimental noise, the HCMC performance improves to 54% convergence at global minima. This supports that the experimental noise derived from the optical measurement is significant enough to benefit the HCMC's performance.

To establish the contribution from fluctuations in the molecular population above the electrode surfaces, the Poisson noise in the SNARF-1 population was estimated.[131] The number of SNARF-1 molecules present in the gel over a single electrode surface in the implemented HCMC is around 5x10^{13} molecules. With this number of molecules, the relative fluctuation in the number of SNARF-1 molecules in a particular protonation state would be around 1x10^{-7}, which is too low to impact the trajectory of the HCMC when starting at Initial State III. This estimation further supports that the major contributor to the experimental noise in this implementation of the HCMC is from the optical measurement itself.

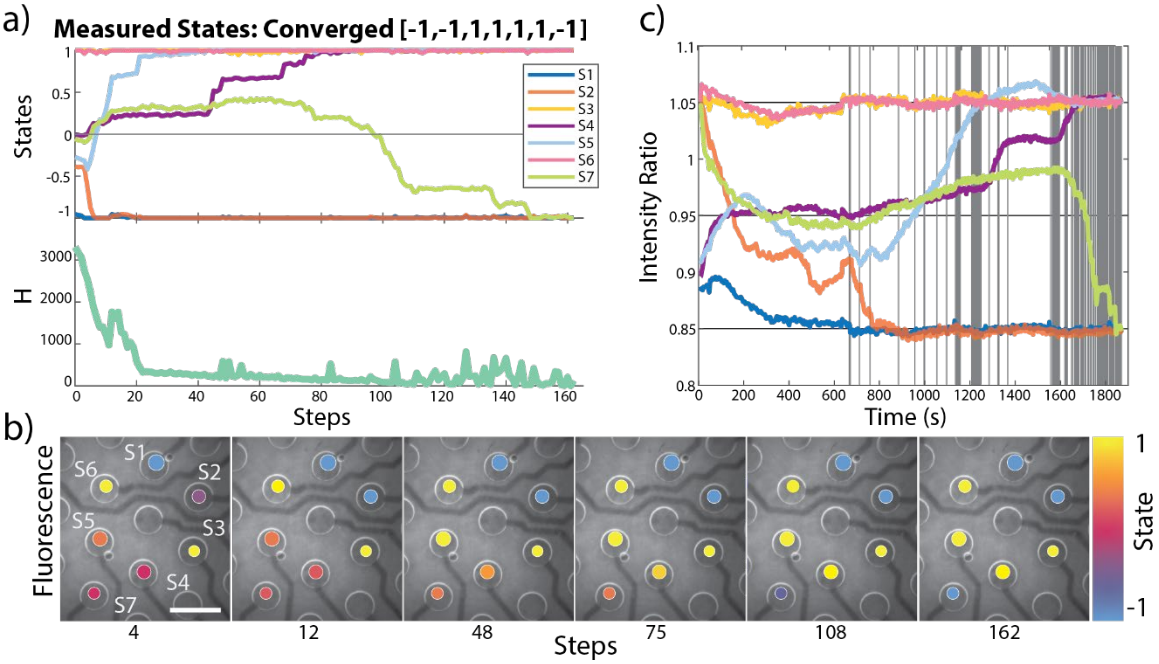

Figure 2-8. Progression of a computation by the hybrid classical-chemical computer solving a prime factorization problem with seven working electrodes.
a) Evolution of states throughout the computation, where S1-S7 represent the seven sites, and the value of the problem Hamiltonian (H) at each step. b) Fluorescence images of the reaction gel on the electrode chip with artificially colored circles depicting the state value at various steps, scale bar is 2 mm. c) The value of the intensity ratios over time during the computation, where vertical lines represent each step in the computation.

2.2.g 7 Electrode Computations and Beyond

A benefit of the HCMC platform is the ability to increase the number of variables easily and inexpensively. Scaling up the number of electrodes used allows the HCMC to tackle higher variable counts and more difficult computational problems. To explore this ability, we increased the number of working electrodes to seven to access new computational capabilities. For example, the HCMC at Mode 3, that is using measured states as the input, was used to solve 3-SAT problems with 7 variables with 28 clauses (shown in **Figure 2-12**). The 3-SAT problem is an NP-complete problem that asks whether a set of clauses in propositional logic is satisfiable. 3-SAT specifies that there are at most 3 variables within each clause. The HCMC has also successfully solved number factorization problems, as demonstrated by the decomposition of 91 into the prime factors 7 and 13 (**Figure 2-8**). Details about the generation of the problem Hamiltonian can be found in SI of manuscript. Prime factorization is a problem in the computational class NP, where given an integer (N) the goal is to find the two prime numbers whose product is N. This problem has two solutions, 7x13 and 13x7, which are expressed in binary numbers by the states. We ran this factorization problem to the point of convergence on the HCMC 10 times, with 8 out of the 10 runs resulting in convergence on a correct solution.

To continue to solve more complex and higher value problems, even more variables will be needed.[95] Scaling up to increased variable counts beyond those in the current work could be achieved straightforwardly using larger numbers of electrodes addressed within a larger optical field of view. Alternatively, the use of microelectrode arrays would allow for hundreds or thousands of electrodes to fit in an area even smaller than the active area in this work, allowing for increased complexity and computational power in the same form factor through miniaturization. In the limit of very small microdroplets of solution on these arrays, the HCMC could even retain high readout signal-to-noise while benefitting from Poisson noise among the now small molecular population as a new source of stochasticity as discussed above. In this regime, the Poisson noise, which is white and truly random, could be easily controlled by modulating the size and concentration of the microdroplets.[132] To achieve an HCMC state standard deviation of at least 0.02 from Poisson fluctuations of emissive molecules, a population of at most 2500 molecules would be needed, easily achievable and visible within microdroplets.

2.3 Conclusion

We have designed a programmable hybrid classical-molecular computer which maintains a set of state variables encoded both digitally and chemically. Digital information is stored conventionally *in silico* while the chemical information is encoded in a pH sensitive gel on top of an electrode array. Changes to the state variables can be communicated via a feedback loop between the digital and chemical variables. Spectroscopic monitoring of pH using a ratiometric dye transfers information from the chemical to the digital domain. Information then transfers from the digital to the chemical domain via electrochemical potentials applied by electrode array. Such an architecture enables chemical and digital operations in either domain to concurrently modify the state variables, enabling the execution of a single algorithm distributed across the two physical domains. The role of the intrinsic experimental noise within the HCMC was investigated and shown to be beneficial to solve classic NP-hard problems, without the need for *in silico* noise (pseudo random numbers) which is often used in combinatorial optimization problems. The modality of the HCMC system allows for inherent inexpensive scaling, easily increasing the number of variables and complexity of the possible problems by simply increasing the number of working electrodes. Additionally, our experiments demonstrate that the experimental noise within the measurement is sufficient to solve not only 4-variable number partitioning problems but also 7-variable problems, such as prime factorization and 3-SAT. Thus, this work demonstrates the use of key molecular subsystems as part of a functional HCMC. Thus, this demonstrative HCMC opens the way to more complex computational problems that take advantage of chemical behavior and development of more fully molecular implementations.

2.4 SI - Preparation of Chemical Reaction Solutions

A stock solution of 30% Pluronic F-127 (Sigma Aldrich) was made in Millipore ultrapure water. The solution was prepared at cold temperatures and stored in a 5°C fridge. Stock solutions of 100 mM p-

Benzoquinone (Sigma Aldrich) and 100 mM Hydroquinone (Sigma Aldrich) were prepared with 27% Pluronic F-127 solutions. 2 mM stock solution of SNARF (5-(and-6)-Carboxy-SNARF-1, ThermoFisher Scientific, Invitrogen) was made in Millipore water. Finally, for the buffer, 1 M stock solutions of potassium phosphate monobasic and dibasic potassium phosphate were made in Millipore water. These solutions were combined to create a 1 M pH 7 phosphate buffer.

The stock solutions above were used to make the reaction solution. The reaction solution was made by layering p-Benzoquinone (23 mM), then 30% Pluronic solution, Hydroquinone (23 mM), and then adding SNARF (180 µM) and phosphate buffer (9 mM). The reaction solution was kept cold on ice before using. 100 µL of the reaction was placed on the electrode chip for use in HCMC. The electrode chip and reaction solution were heated for 30-60 seconds at 30°C before placing a top coverslip on the sample and pressing the reaction solution to a thickness of 0.56 mm by using glass spacers.

2.5 SI - Optical Setup and Imaging Details

An open home-built epifluorescence microscope was used for the HCMC. The optical set up consists of a 40 mW 488 nm laser (Coherent Sapphire). The beam size is expanded 30x, and then sent through a lens for widefield excitation. A 505 nm dichroic is used to reflect the laser light onto the sample through a 1X air objective (Nikon, Plan UW, NA 0.04). The electrode chip sits on a metal stage within a 3D printed holder to ensure the sample position is reproducible for each implementation of the computer. The metal stage sits on a translation stage which controls the z-axis and allows the sample to be brought to focus. The fluorescence is collected via the 1X objective (Nikon), passes through the 505 nm dichroic (Semrock), and is directed towards the detection setup. The light is collimated, and the emission is spectrally isolated from the laser light and background fluorescence using a 532 nm long pass filter (Semrock) and 540 nm long pass filter (Semrock). The emission is then split into two channels using a 610 nm dichroic (Semrock), and then focused onto two separate cameras (Thorlabs). Image acquisition was done through a custom written LabView code. Images were taken sequentially at each camera with a 1 second exposure time.

2.6 SI - Electronic Components

2.6.a Electrode Array Design

A key portion of the HCMC is an array of electrodes that can interface with the electrochemical gel to transfer information between digital and chemical domains. For ease of simplicity and cost-effective design, we used larger electrodes (diameter 1 mm) such that the electrode arrays can be fabricated using standard PCB manufacturing. The electrodes were placed in a hexagonal grid to have higher nearest-neighbor connectivity, see **Figure 2-9a**. The region around the electrodes shown in the white circle is an active area and no connection vias were placed within the active circle to avoid short-circuiting. All the electrodes were gold-plated by the PCB manufacturer, and FFC connector was used for electrical contact with the electrodes. The PCB-based electrode arrays were designed using Altium Designer Ltd. An additional board called as Pin Expansion Board was also designed for the ease of interfacing the electrode array with the standard electronic power supply or potentiostats, where each FFC connector is mapped to standard pin headers, see **Figure 2-9b**. All the experiments in this work were performed using PCB-based electrode arrays.

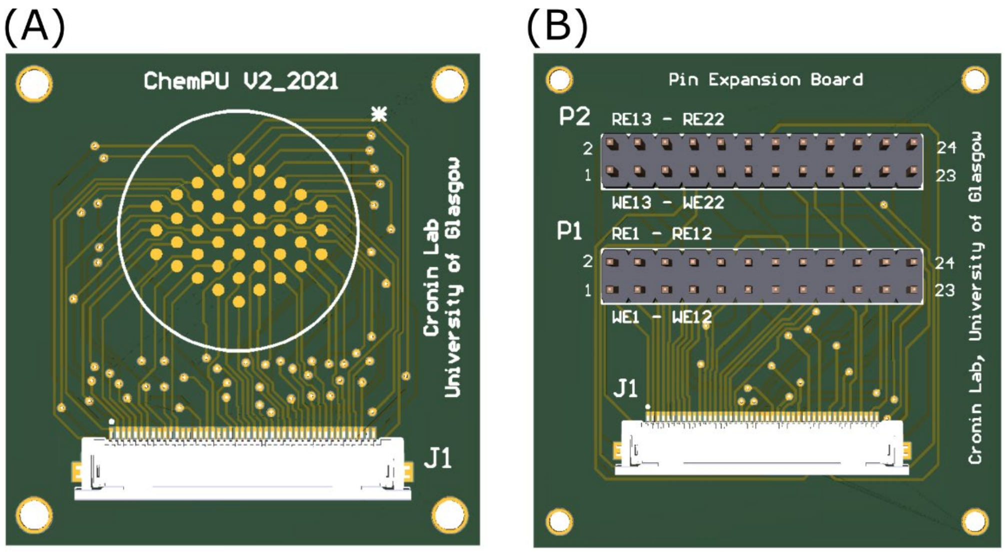

Figure 2-9. PCB-based electrode array and pin expansion board.
(a) shows the design of PCB based electrode array with a hexagonal network of gold electrodes. The active area is within the white circle without any vias within that region. The electrodes are interfaced with a FFC connector. (b) shows a pin expansion board which connects FFC connector to standard pin headers for all electrodes

2.6.b Potentiostat

The electrode chip is connected to a multi-channel potentiostat (Rodeostat, IO Rodeo), which had some minor alterations to the publicly available firmware; specifically, the multiplexed electrodes are not set back to ground and allowed to float during times when they are not directly controlled by the multiplexer, this gave a better regulation of pH than otherwise. For this implementation of the HCMC, the potentiostat is connected so that there are 7 working electrodes along with 7 counter electrodes. The reference and ground electrode are connected to each other in this implementation.

2.7 SI - pH Fluorescence Calibration

1 M stock solutions of dibasic potassium phosphate and potassium phosphate monobasic were used to make multiple solutions of pH values varying from 5.5 to 7.5. The pH was checked and confirmed using a pH probe (Mettler Toledo). Reaction solutions were made with each pH buffer. 100 µL of reaction

solution at a thickness of 0.56 mm was imaged for 100 seconds. The electrode chip was not connected to the potentiostat at this time, as no potential was applied. To calculate the intensity ratio corresponding to each pH, a region of interest was selected over each electrode. The intensity at each of these sites was measured and then the intensity at Camera 1 was divided by Camera 2 to obtain the intensity ratio. This was done at each electrode for each pH. Calibration curves of this information can be seen below in **Figure 2-10**. The pH range for the -1 to +1 states for each electrode are listed in **Table 2-3**.

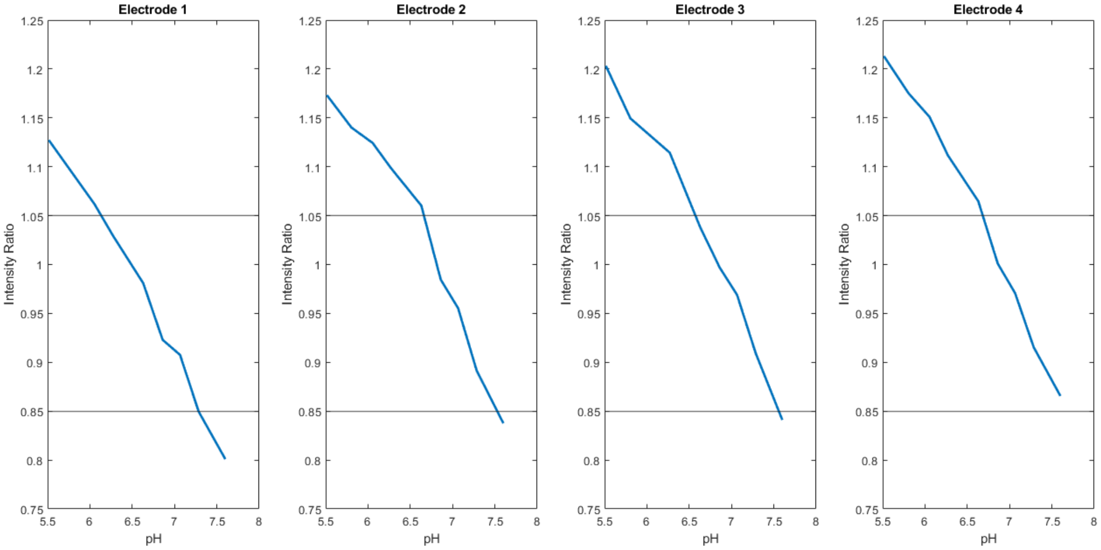

Electrode 1

Electrode 2

Electrode 3

Electrode 4

Figure 2-10. Calibration of pH to intensity ratio over the four electrodes used in the HCMC. Horizontal lines at IR values of 1.05 and 0.85 correspond to the intensity ratios for the +1 and -1 state values.

Table 2-3. pH values for each electrode

Electrode Number	pH for -1 State	pH for +1 State
1	6.13	7.28
2	6.66	7.53
3	6.57	7.56
4	6.68	7.7

2.8 SI – 2SAT 4 Electrode Computation

Before using the hybrid computer to solve number partitioning problems, a simpler 2SAT problem was explored to vet the ability of the system. The 2SAT problem chosen used 4 sites (variables) and 9 clauses.

The input 2SAT clauses are as follows:

[‘1 or 3’, ‘2 or not4’, ‘2 or 3’, ‘1 or not4’, ‘1 or 2’ ‘not1 or 2’, ‘3 or not4’, ‘not3 or 4’, ‘1 or 4’].

Expressed in conjunctive normal form:

$$(1 \vee 3) \wedge (2 \vee \neg 4) \wedge (2 \vee 3) \wedge (1 \vee \neg 4) \wedge (1 \vee 2) \wedge (\neg 1 \vee 2) \wedge (3 \vee \neg 4) \wedge (\neg 3 \vee 4) \wedge (1 \vee 4)$$

The Ising Hamiltonian for this problem is:

$$H = 2.25 - 0.75s_1 + 0.25s_1s_3 - 1s_2 + 0.25s_2s_3 - 0.25s_2s_4 - 0.5s_3 - 0.5s_3s_4 + 0.25s_4$$

$$H_0 = 2.25$$

$$H_1 = [-0.75 \quad -1 \quad -0.5 \quad 0.25]$$

$$H_2 = \begin{bmatrix} 0 & 0 & 0.125 & 0 \\ 0 & 0 & 0.125 & -0.125 \\ 0.125 & 0.125 & 0 & -0.25 \\ 0 & -0.125 & -0.25 & 0 \end{bmatrix}$$

This problem has two solutions: [1,1,-1,-1] and [1,1,1,1]. In this instance, a +1 represents a true value and -1 represents a false value, therefore for the first solution when variables (sites) 1 and 2 are true and variables (sites) 3 and 4 are false the 2SAT problem is satisfiable, as all the clauses are true. For the second solution, when all the variables are true then the 2SAT problem is satisfiable as well. An example of a completed run by the HCMC solving this 2SAT problem, at Mode 3, is shown below in **Figure 2-11**.

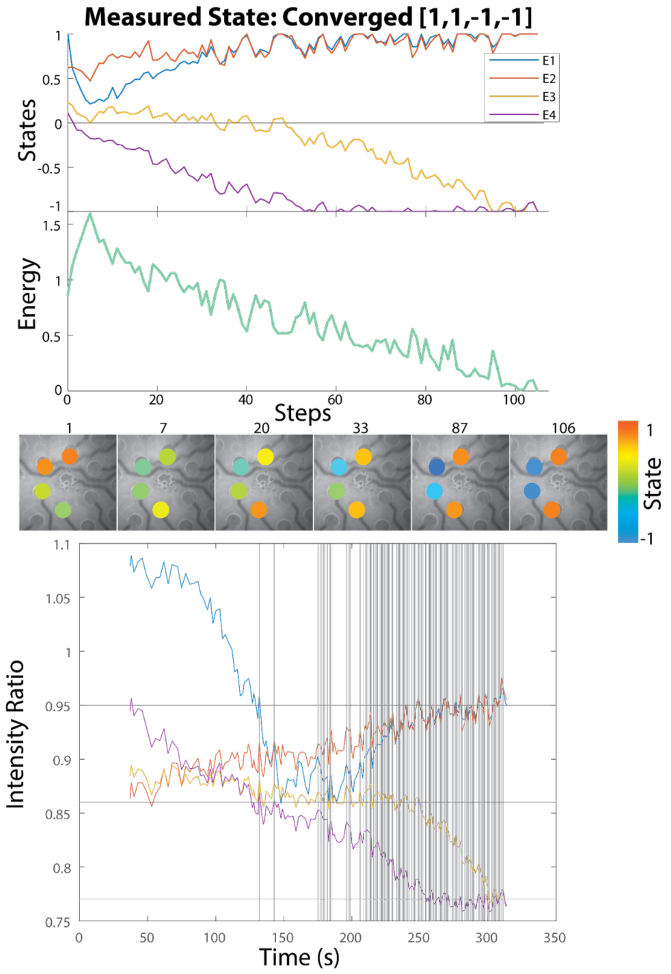

Figure 2-11. Progression of a computation by the hybrid classical-chemical computer solving a 2SAT problem. (Top) Evolution of states throughout the computation and energy of the Ising Hamiltonian at each step, where E1-E4 represent the four sites. (Center) Fluorescence images of the reaction gel on the electrode chip with artificially colored circles depicting the state value at various steps. (Bottom) The intensity ratios over time during the computation, vertical lines represent steps.

2.9 SI – 3SAT 7 Electrode Computation

The HCMC was also able to solve a 3SAT problem using 7 electrodes (variables) with 28 clauses at Mode 3, using measured states with no *in silico* noise. The possible solutions that make this problem satisfiable are: [1,-1,-1,-1,-1,-1,-1] and [1,-1,1,1,1,-1,-1]. A completed and correctly converged run of the HCMC at Mode 3 solving the 3SAT problem is shown in **Figure 2-12**.

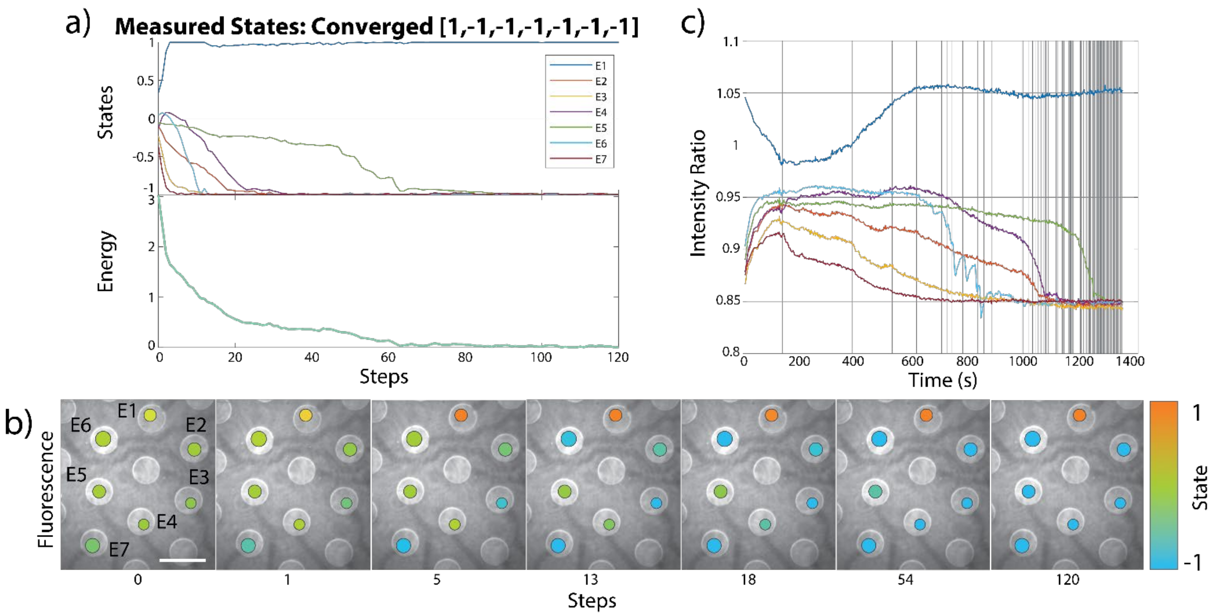

Figure 2-12. Progress of computation using the HCMC solving a 3SAT problem using 7 electrodes. (a) Evolution of states throughout the computation, where E1-E7 represent the 7 electrodes, and the Energy (Ising Hamiltonian scalar value). (b) Fluorescence image of the reaction gel on the electrode chip with artificially colored circles depicting the state value at various steps at each

2.10 SI – Noise Measurement Experimental Details

2.10.a Measurement of Noise in Applied Voltage

100 μL of reaction solution was placed onto the electrode chip, the solution is pressed to a thickness of 0.56 mm. To measure the potential, an external measure of the potential was performed using a National Instruments DAQ. Each electrode was measured individually by connected the DAQ to a single active working electrode along with the ground/counter electrodes. The potential was measured as each electrode was pulsed, applying a potential from 0V to -1V and then 0V to +1V. Additional measurements were performed where the potential was also pulsed at 0 to -1.4V and 0 to +2V. The potential measurement was acquired through LabView while simultaneously obtaining fluorescence images of the reaction gel. The measured potential was rebinned at 1 second intervals to be comparable to the HCMC settings. The signal after pulsing to +1 or -1V is taken and averaged. The standard deviation of the traces

is calculated and then the mean and standard deviation are used to calculate the percent deviation. The noise in applied potential was found to be insignificant relative to the noise added to the experiment from the optical measurement, with the percent standard deviation at 0.03%.

2.10.b Measurement of the Noise in the Current

After confirming that the applied potential is stable (as per the previous section), we then proceeded to perform controlled-potential chronoamperometry experiments. 100 µL of reaction solution was placed onto the electrode chip, the solution is pressed to a thickness of 0.56 mm. The potential was held first at 0V to establish a baseline, then stepped to +/- 1V, -1.4V, or +2.0V and held for 5 minutes while measuring the current. This was repeated for each electrode in turn to account for any variation among them. The current was measured using the same multi-channel potentiostat used for the HCMC. Meanwhile, the imaging setup was used to record intensity ratios at each electrode during these runs to monitor for any apparent changes in pH over the course of these experiments. Any noise observed in these current measurements will be influenced by noise in the potential applied, fluctuations in current caused by interactions at the electrode surface, and noise in the measurement of the current itself.

2.10.c Conversion of Current Noise to Fluctuations in Intensity Ratio

To compare the measured noise levels in the above section to the values from the optical noise measurements, the measured current was used to calculate a theoretical pH change over time. The fluctuations in this value could then be used to determine a theoretical IR noise value that would have resulted from any current fluctuations. This was done by assuming 100% Faradaic efficiency, such that any change in measured current corresponded to a change in quinone concentrations at the electrode surface, which would directly relate to gain or loss of protons. It is worth noting that this ignores any background current and any fluctuations that could arise from other sources. Though unrealistic, operating in this limit gives us a value for the maximum possible contribution from current noise to the overall measured noise in our computational runs.

To do this conversion, the current was converted to a net electron flow, which was converted directly into change or loss of proton concentration at the electrode surface (depletion of quinone at the surface was disregarded to get an upper limit on concentration changes). After accounting for buffering by our solution, this was converted to pH change over time (see **Figure 2-13**). Using our pH calibration, this could be directly converted to an intensity ratio (IR) as seen in our experiments. The noise in this IR trace is then directly comparable to the noise in the IR measured experimentally. As shown, the maximum possible contribution to experimental noise from current fluctuations is still insignificant relative to the imaging noise.

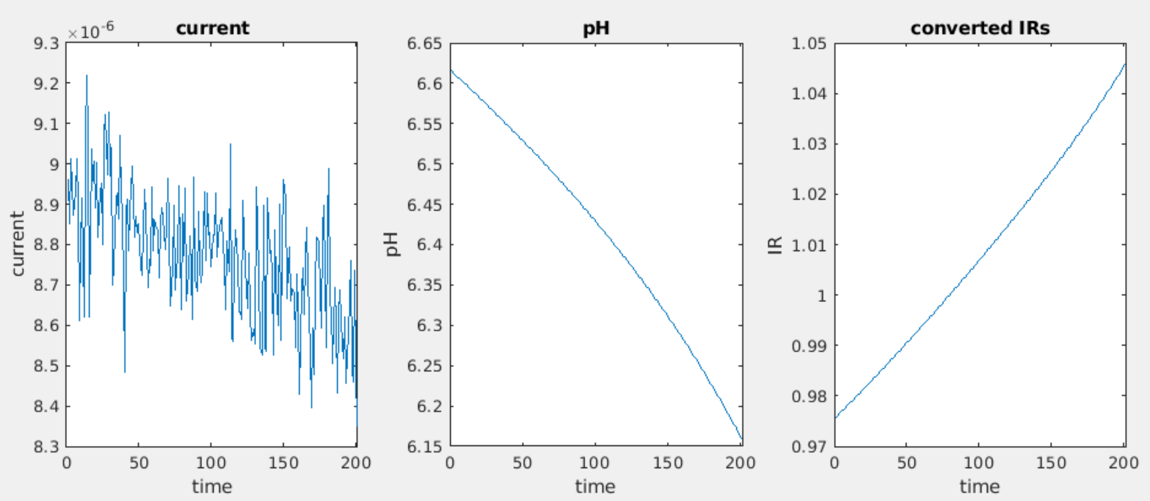

Figure 2-13. Current trace from noise measurement, corresponding pH values over time, and intensity ratios converted from these pH values.

2.10.d Measurement of Noise in Excitation Laser

A digital optical power meter (Thorlabs) was used to measure the noise within the excitation laser source. With all other additional lights turned off, the sensor was placed in the beam path of the excitation laser and data was collected in 1 second intervals for 300 seconds. The measured signal was averaged together, and standard deviation and percent deviation were calculated. The average power was 41.79 mW (0.02), with a percent standard deviation of 0.06%.

2.10.e Measurement of Noise from Optical Measurement

After confirming a stable laser excitation, we then measured the noise resulting from our optical measurement. These experiments were performed by imaging the reaction solution on the electrode chip without any applied potential. The sample was excited by the 40 mW 488 nm laser. Image acquisition was performed using the same settings as the HCMC experimental details. 300 images were collected at 1 second exposure, this was repeated 5 times. The fluorescence data was processed using MATLAB.

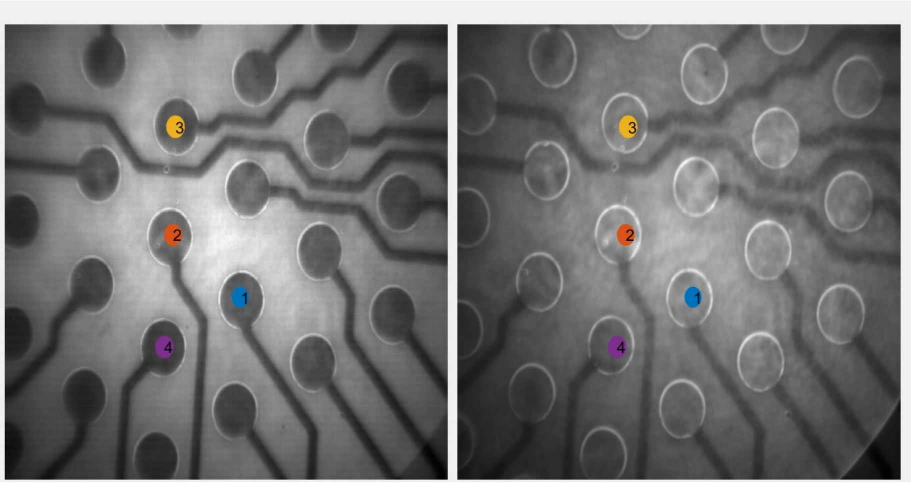

Figure 2-14. Fluorescence images of the reaction solution on an electrode chip.
(Left) Channel 1 and (Right) Channel 2, regions of interest (ROIs) in both channels are depicted by the colored circles over the electrodes, with the numbers labeling electrodes 1-4.

For each replicate the following was done, ROIs were selected at each site (over each active electrode) in both fluorescence channels, see **Figure 2-14**, and the intensity at each frame within the ROI was measured resulting in fluorescence intensity traces for each camera at each site. The fluorescence IR was calculated with Fluorescence Intensity Channel 1/Fluorescence Intensity Channel 2 for each frame, which generated an IR trace. See **Figure 2-15** for example of signal traces. The average, standard deviation, and percent standard deviation were determined for each signal (fluorescence traces and IR traces). The average intensity ratio over these experiments was 1.04, with a standard deviation of 0.002 and a percent standard deviation of 0.2%.

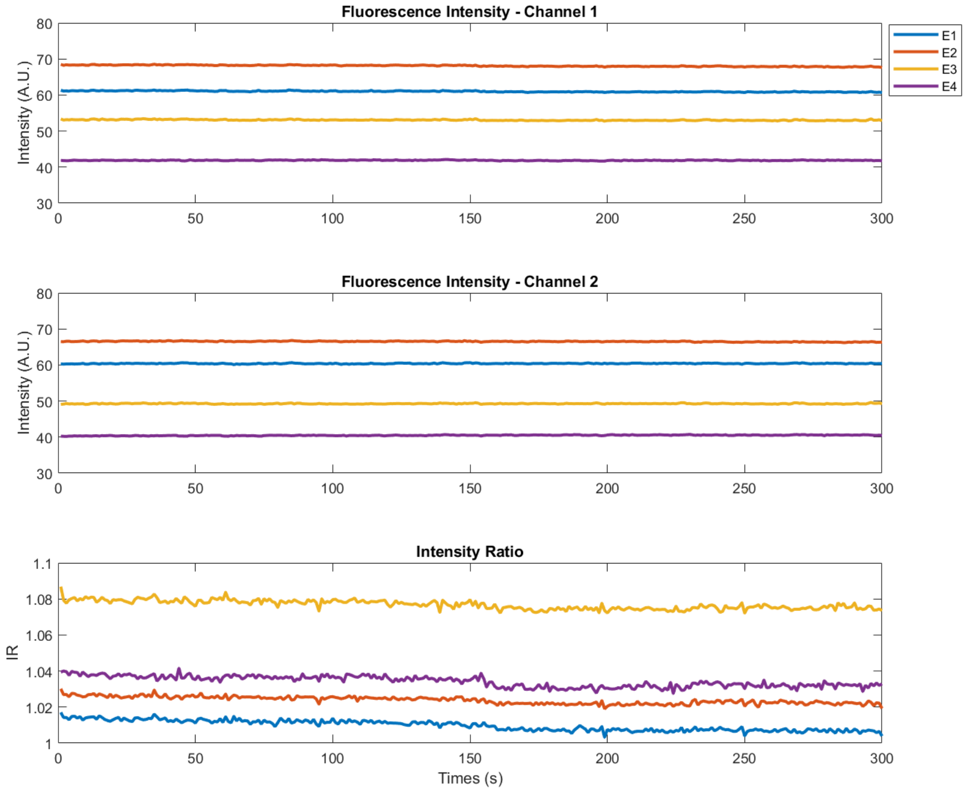

Figure 2-15. Plot of fluorescence intensity trace over time (s) for Channel 1 (top) and Channel 2 (middle). Plot of Intensity Ratio over time (s) (bottom).
Each color trace represents a site over a different electrode.

2.10.f Measurement of Noise from Complete Experimental Setup

The reaction solution was prepared as previously described and placed onto an electrode chip. The imaging acquisition is at the same settings previously stated. The reaction gel was imaged beginning at pH 7 and then potentials were applied (using the multiplexed potentiostat) bring each of the sites to a -1 state value, which corresponds to an IR of 0.85 and a more basic pH. The set IR was then maintained for

700 steps. This allows us to quantify the fluctuations from the full experimental set up under active PID conditions. For analysis, a section of the intensity trace after reaching the target IR was isolated (around 300 steps, see **Figure 2-16**) and used to calculate an average signal, standard deviation, and percent standard deviation. These experiments manipulated all 4 electrodes simultaneously. Additionally, the threshold for the PID was set to 0.01, which is the same value as the HCMC running at Mode 3.

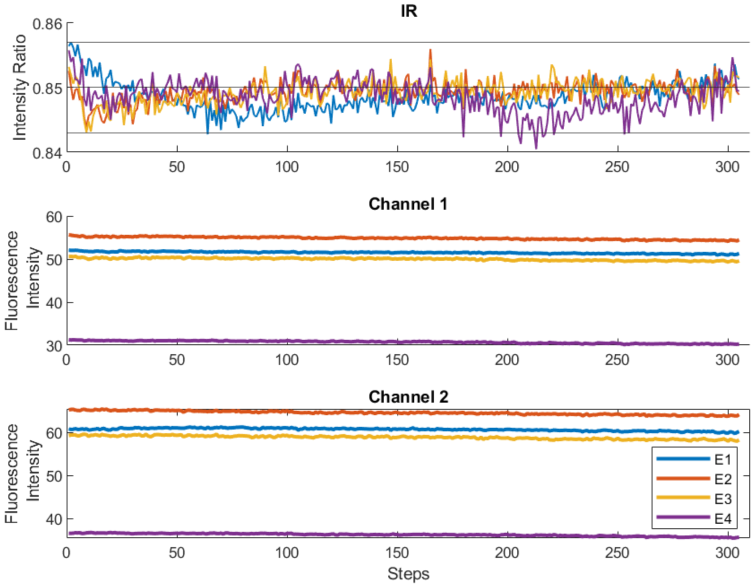

Figure 2-16. Plots of the IR (top) and fluorescence signals from Channels 1 (center) and 2 (bottom) while maintaining a set -1 state value using PID

2.11 SI – Calculating Minimum *in silico* Noise

The following experiments were performed to determine the minimum noise necessary to avoid a trajectory that converges on the local minima. The HCMC is solving the number partitioning Hamiltonian at Mode 2, completely *in silico*. The noise value (otherwise known as the standard deviation of normal Gaussian) varied by orders of magnitude from 0 (Mode 1 *in silico* noise value) to 0.1 (Mode 2 *in silico* noise value). Additional runs were performed at *in silico* noise values of 0.005 and 0.02 (matching the experimental noise values). The distribution of solutions the computer converged on are shown in **Figure 2-17**. Each run began at Initial State III and there were 100 repeats at each set of conditions. The HCMC starts to converge on correct solutions (A and B) at a noise setting of 0.005, but still majority convergence on the local minimum (3% correct, 97% LM). When getting to 0.02 noise, the frequency of convergence at the LM reduces to 46%, with correct solutions being at 54% (split 30% A, 24% B). Finally, at Mode 2, there is more Solution A convergence than LM at all. When the *in silico* noise value was set too high, the stochasticity would cause extreme hopping between states and convergence on various states, some that may be other local minima present within the energy landscape. Therefore, the *in silico* noise variable selected for Mode 2 was ideal to efficiently solve the number partitioning problem for these initial states.

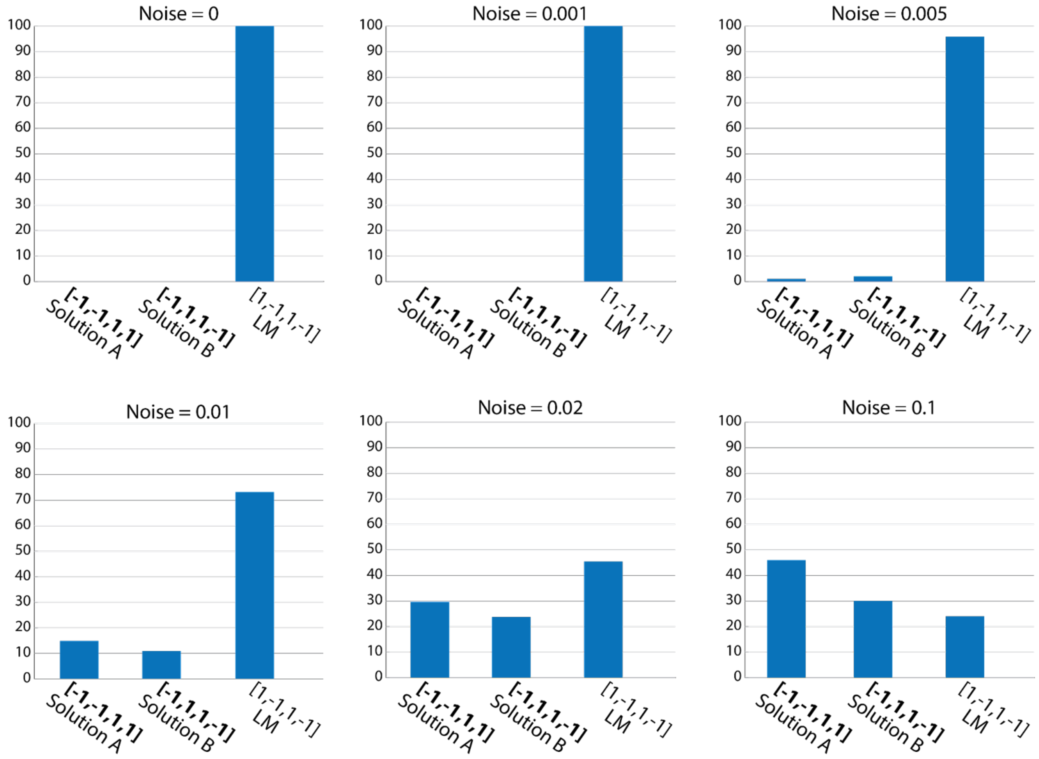

Figure 2-17. Bar graphs showing the propensity that a set of state values were converged on when running the HCMC at Mode 2) with varying *in silico* noise values (specified above each graph).

2.12 Acknowledgements

Andrew C. Cavell assisted with data collection, conversion of current noise to pH, wrote code to generate the Hamiltonian cost function landscapes, as well as assisted with gradient descent tests. Abhishek Sharma contributed PCB electrodes as well as simulations, which are featured in the submitted manuscript. Chris Forman contributed to the code for the HCMC, including the image processing, PID, and control over multiple electrodes featured in submitted manuscript. He also provided edits to the code to allow for solving of 7 electrode factorization problems. Si Yue Guo provided the problem Hamiltonians as well as plenty of helpful conversations. Evan Thomas Jensen, Mackinsey A. Smith, and Rachel Czerwinski all helped with sample preparation and data acquisition.

Chapter 3 Optical Monitoring of Polymerizations in Droplets with High Temporal Dynamic Range[ii]

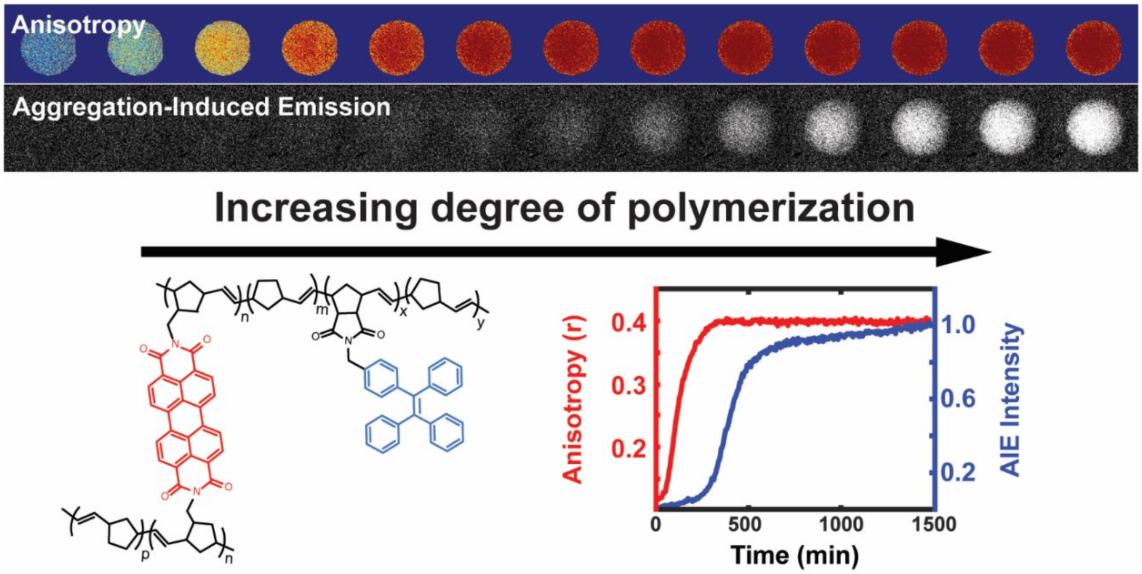

[ii] Authors: Andrew C. Cavell[a], Veronica K. Krasecki[a], Guoping Li[b], Abhishek Sharma[c], Hao Sun[b], Matthew P. Thompson[b], Christopher J Forman[b], Si Yue Guo[d], Riley J. Hickman[d], Katherine A. Parrish[a], Alán Aspuru-Guzik[d], Leroy Cronin[c], Nathan C. Gianneschi[b], Randall H. Goldsmith[a]
[a] Department of Chemistry, University of Wisconsin-Madison
[b] Department of Chemistry, Northwestern University
[c] School of Chemistry, University of Glasgow, UK
[d] Department of Chemistry, University of Toronto, Canada

The published version of this manuscript can be found at reference [124] (presented in this thesis with permission from the Royal Society of Chemistry). The formatting has been changed to fit the style of this thesis and omitted any sections that I did not provide a direct contribution.

VKK developed the surface functionalization for droplets immobilization. VKK acquired data for Figure 3-5, Figure 3-6, Figure 3-12 and Figure 3-13. VKK assisted ACC with data acquisition and processing for Figure 3-3 and Figure 3-4. AS designed robotic droplet platform, ACC and VKK built the robotic platform at UW-Madison. GL synthesized the AIE-NB compound. ACC synthesized the PDI-NB compound. ACC developed the distillation method for purifying toluene. HS and MPT performed GPC measurements.

Abstract:

The ability to optically monitor a chemical reaction and generate an *in situ* readout is an important enabling technology, with applications ranging from the monitoring of reactions in flow, to the critical assessment step for combinatorial screening, to mechanistic studies on single reactant and catalyst molecules. Ideally, such a method would be applicable to many polymers and not require only a specific monomer for readout. It should also be applicable if the reactions are carried out in microdroplet chemical reactors, which offer a route to massive scalability in combinatorial searches. We describe a convenient optical method for monitoring polymerization reactions, fluorescence polarization anisotropy monitoring, and show that it can be applied in a robotically generated microdroplet. Further, we compare our method to an established optical reaction monitoring scheme, the use of Aggregation-Induced Emission (AIE) dyes and find the two monitoring schemes offer sensitivity to different temporal regimes of the polymerization, meaning that the combination of the two provides a significantly increased temporal dynamic range. Anisotropy is sensitive at early times, suggesting it will be useful for detecting new polymerization "hits" in searches for new reactivity, while the AIE dye responds at longer times, suggesting it will be useful for detecting reactions capable of reaching higher molecular weights.

3.1 Introduction

Chemical transformations frequently entail complex mixtures of relevant chemical species. In catalyzed reactions, numerous intermediate states can be visited and catalyst speciation can contribute significantly to reaction dynamics.[133–137] Polymerization reactions are natural producers of chemical heterogeneity, as growing chains of varying length and functionality can result in diverse and dynamic chemical environments that may influence reaction pathways and rates.[58,138–140] As the number of processes developed for the synthesis of small molecules and polymeric materials continues to increase, so does the need for new, efficient techniques for gaining an understanding of their chemical composition and behavior. The monitoring of these systems under synthetically relevant conditions is essential for further insight and progress in the informed development of new reactions. In particular, optical methods have the benefit of allowing for monitoring of reactions in real-time, with minimal disruption to the natural dynamics of the reactions under study.[141–145] Photonic devices can act as multipliers for increasing sensitivity in optical spectroscopy of chemical reactions.[146,147] Advancements in fluorescence microscopy over the last few decades have allowed for remarkable strides to be made in the study of chemical reactions.[148–154] These techniques can even be employed at the single-molecule level to reveal unsynchronized dynamics of individual catalyst molecules.[52,60,150,151,155–158]At the other extreme, the inherent scalability of optical methods makes them attractive readouts for massively parallel, high-throughput combinatorial testing of reaction conditions.[159–164] Pairing this approach with machine-learning methods also enables accelerated discovery and screening of new functional materials.[165–168] Ideally, such combinatorial searches will occur in chemical environments that strongly resemble the conditions that would be used in an industrial setting.

Polymerization reactions performed in mixed phases and emulsions are used extensively in the industrial production of specialty materials.[169] There is much interest in studying polymerizations carried out in dispersed media, as these processes form a toolkit for the facile production of complex polymeric and hybrid materials on large scales.[170,171] Reactions in droplets are also highly relevant for microfluidic reactors, which can provide tight control of conditions in the continuous synthesis of complex structures,[172–174] high-throughput screening of reaction conditions,[174–176] and for applications in droplet-based assays.[174,177,178] However, the inherent complexity and transient nature of these droplet systems makes for some difficulty in understanding their dynamics and behavior.[179] For this reason, researchers have begun developing methods for *in situ* monitoring of this class of polymerizations.[38,180] Indeed, while the confinement of reactions to small droplets can sometimes alter the rate of the reaction,[181] it also plays to the advantage of optical monitoring strategies by allowing the application of microscopy.

Fluorescence-based methods are thus uniquely poised as powerful tools for the characterization and monitoring of polymerization catalysts *in situ* with high spatial resolution and signal to background.

One way of encoding useful chemical information into an optical signal is by relying on specific chemical transformations. Fluorogenic transformations rely on practically non-fluorescent reactants which yield strongly fluorescent products upon reaction and have been used to monitor a variety of chemical transformations.[51,52,55,155,182–186] Closely related to fluorogenic reactions, spectral shifts as a result of a change in functionality or extension of conjugation length have also been used to monitor chemical reactions.[187,188] These methods generally require the use of reagents that have been specifically engineered to provide the measured response. These reagents, however, may display different reactivity than the desired substrate and so may lack generality. A more versatile approach would entail the simple introduction of an additive at ppm concentrations to allow monitoring of arbitrary reactions. This more generally applicable strategy would be particularly powerful for applications in combinatorial searches for new reactivity.

Fluorescence polarization anisotropy, which quantifies the rotational time scale of a molecule, provides one avenue for the study of polymer reaction dynamics that satisfies this need. By doping in a small amount of tracer fluorophore, the rotational dynamics of the tracer molecule can be used to report on the chemical evolution of its environment. Measurements of fluorophore rotational dynamics via fluorescence anisotropy have been used to investigate a broad variety of polymeric systems, including measuring the mobility of grafted polymer chains in microgels,[189] observing the movement of small molecules in crosslinked polystyrene networks,[190] following production of silica gels,[191] studying the self-assembly of block copolymers in water,[192] quantifying distributions of conformers of intrinsically disordered proteins in solution,[17,193] and studying dynamics within supported polymer thin films and glasses.[194] There are very few studies that employ fluorescence polarization anisotropy measurements in droplets. One recent study measured the anisotropy of free rhodamine 6G dye molecules in microdroplets and examined the role of electrostatics at the droplet interface.[18] Another recent study successfully determined protein-peptide dissociation constants by measuring the anisotropy of a series of droplets with systematically varying composition in a flow cell.[195] To date, there are no examples of fluorescence anisotropy being used to monitor the progress of chemical reactions confined in droplets.

Another readout mode that satisfies this criterion, and can act through introduction of an additive, is aggregation-induced emission (AIE).[196] AIE dyes typically possess internal rotational degrees of freedom which allow the dye to relax non-radiatively to the ground state upon excitation. As viscosity increases or aggregation of the dye occurs, these rotations are limited and radiative modes of relaxation are favored, leading to an increase in fluorescence quantum yield and emission intensity. In this way, dyes that exhibit AIE or a viscosity-sensitive quantum yield can also be used to monitor the course of a polymerization reaction, either when the dye is covalently attached to a monomer[36,197] or simply added to the solution,[153,154] including in dispersed phase,[38] though this method has not been used at the level of single droplets. *A priori*, it is not evident whether AIE and fluorescence polarization anisotropy will reveal the same or complementary information about the polymerization.

Here, we demonstrate how fluorescence polarization anisotropy and AIE provide an information-rich readout of the state of a polymerization reaction in a single microdroplet. In particular, we show how an increase in fluorescence polarization anisotropy can be observed as a result of the incorporation of a fluorescent probe monomer into a growing polymer chain and demonstrate its use to track the course of a polymerization. We will also describe how fluorescence polarization anisotropy and AIE can be used simultaneously. As will be shown below, the dynamic ranges of fluorescence polarization anisotropy and AIE are distinct and complementary.

Ring-opening metathesis polymerization (ROMP) catalyzed by the ruthenium-based Grubbs Generation II (GG2) catalyst[198,199] was selected for the development of this monitoring strategy as it is relatively air and moisture-tolerant, easy to control, relatively well understood, and industrially relevant.[200,201] ROMP polymers and their derivatives are widely represented in both industrial catalysis and the development of specialized materials.[202] Diverse polymer morphologies and polyfunctional materials are now accessible via ROMP through reproducible means and under mild conditions.[203] Many thousands of tons of polynorbornene polymers are produced industrially each year.[200] Specifically, the ROMP of norbornene to form polynorbornene was chosen as the primary reaction under study to explore this readout method.

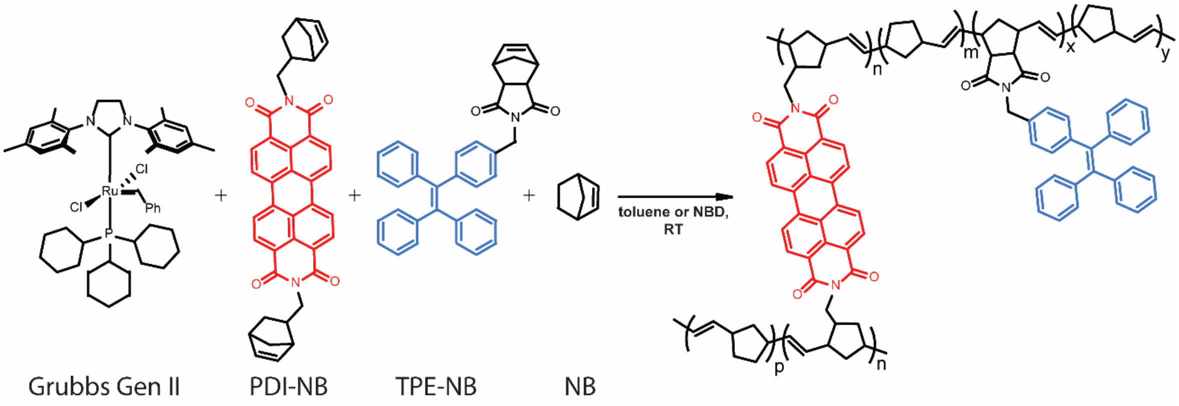

Scheme 3-1. Grubbs Gen II-catalyzed ROMP polymerization, with TPE and PDI-based norbornene monomers as fluorescent probes.
Probe monomers are present in low amounts (ppm for PDI and ppt for TPE) relative to unlabeled monomer (thus p, m, y >> n, x).

In our implementation, droplets of predefined compositions of organic reaction mixture are produced and deposited using a robotic platform, immobilized on fluorinated surfaces, and then monitored optically as the polymerization proceeds. The creation of large droplet arrays (from 2×2 up to 20×20 on a single coverslip) allows for investigation of multiple reaction conditions simultaneously. Rotational dynamics of a norbornene functionalized perylene diimide (PDI) dye[204–212] molecule are monitored using fluorescence polarization anisotropy (**Scheme 3-1**). Simultaneously, the intensity of emission from a tetraphenylethylene (TPE)-labelled norbornene monomer[213] which exhibits AIE is monitored. Together, these two methods provide a real-time readout of polymerization reaction progress with a greater temporal dynamic range than either method alone.

3.2 Results and Discussion

3.2.a Fluorous-Functionalized Surface for Droplet Immobilization

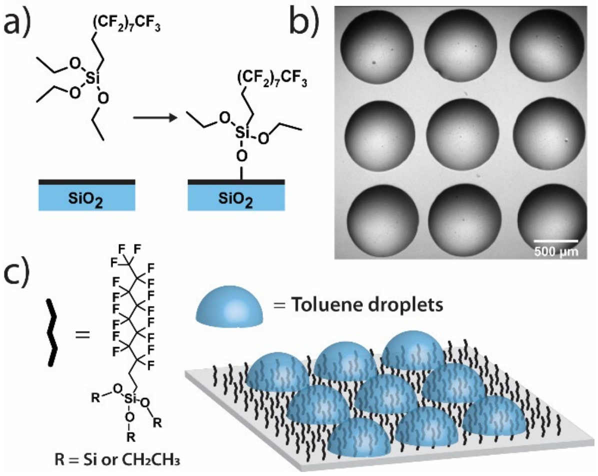

Figure 3-1. Surface functionalization for droplet immobilization.
a) Deposition of perfluorodecyltriethoxysilane. b) Bright field image of a 3x3 array of toluene droplets immobilized on a glass coverslip, surrounded by an aqueous continuous phase. c) The prepared hydrophobic fluorinated glass surface has a high relative affinity for organic solvent, allowing droplet array immobilization.

Measurements on individual reactions confined in droplets require that the droplets be immobilized for long-term imaging. We image through glass coverslips which are inherently hydrophilic, making it impractical to place an organic phase droplet onto the glass surface when water is present. A method was needed to functionalize the glass surfaces in a way that made them highly hydrophobic to repel the aqueous continuous phase but also lipophilic to immobilize the organic phase droplet. To this end, we functionalized pre-cleaned glass coverslips and all-glass reaction chambers[214] using a solution phase deposition of perfluorosilane, 1H,1H,2H,2H-perfluorodecyltriethoxysilane, to afford a hydrophobic and lipophilic fluorinated surface. Fluorinated surfaces are valuable as an immobilization technique,[215,216] with applications in molecular catalysis[217] and for immobilization of molecules in microarrays for biological assays.[218] While perfluorinated compounds are typically hydrophobic, certain fluorinated compounds are more lipophilic than others depending on fluorinated chain length.[219] By using a longer fluorinated chain to functionalize the glass surface, a surface is created where droplets of organic solvent placed in contact with these coverslips under an aqueous continuous phase will stick to the fluorinated surface and will stay immobilized (**Figure 3-1**). The surfaces are not readily wetted by the continuous phase and so the organic droplet phase stays in contact with the glass despite its low density relative to the surrounding water. Importantly, more typical alkylated hydrophobic/lipophilic surfaces (such as those made with octylsilane) did not result in as robust droplet phase immobilization as did the fluorinated surfaces.

3.2.b Droplet Placement with a Robotic Platform

A home-built robotic platform was constructed to allow for precise 2D placement of droplets of varying compositions.[220,221] The robot consists of 2 linear actuators mounted on rails above a sample preparation stage, topped with a stepper motor for precision z positioning of a custom 3D printed syringe module. The linear actuators allow for x-y control of the position of the syringe head, which can then be lowered to the sample stage for taking up each sample and placing droplets.[iii] The syringe head assembly contains a second stepper motor that controls the position of the syringe plunger to dispense small volumes of solution to create droplets. The configuration used for these experiments consisted of a 10 µL Hamilton Gastight syringe held by the stepper motor in a 3D-printed assembly allowing for precise actuation of the plunger down to sub-nanoliter steps. The syringe was fitted with a 27-gauge blunt-tip needle. The use of a blunt tip is essential, as the angled sharp tip on common laboratory needles allows for the organic phase reaction mixture to flow out the side of the needle aperture and float to the

---

[iii] It is important to not set the motors for the droplet robot too fast of speeds, setting the x-y-speed too high will result in issues with droplet placement and reproducibility.

surface of the continuous phase. A blunt needle forces the organic phase to contact the coverslip surface directly and stick in place. This computer-controlled robotic platform is modular in design, allowing for simple modification of the sample stage and easy interchange of different syringe types and volumes. While a simple syringe module was used for this work, the head could be swapped with a variety of alternate dispensing modules or microfluidic devices to scale droplet production and immobilization for the needs of future applications.

3.2.c Tracer Dye Design and Synthesis

Ensuring that polymerization will result in a measurable change in fluorescence polarization anisotropy necessitates the use of a fluorophore that changes its rotational dynamics significantly upon polymerization. To this end, we designed and synthesized a perylene diimide-based fluorescent crosslinking monomer (PDI-NB, **Scheme 3-1**), which is expected to experience a significant loss of rotational freedom upon incorporation into the growing polymer chain. The ability of this monomer to undergo a second incorporation (i.e. to cross-link) should additionally limit its rotation as the reaction proceeds, yielding a significant overall increase in the monomer's fluorescence anisotropy.

In addition to the rotational probe, a monomer labeled with tetraphenylethylene (TPE-NB, **Scheme 3-1**) was incorporated into the polymerizations for use in a complementary readout strategy. TPE exhibits AIE, wherein a restriction of intramolecular rotation yields an increase in fluorescence quantum yield. The chosen TPE-based ROMP monomer has been utilized previously in the synthesis of ion-and-pH-sensing fluorescent polymers[222,223] and in the preparation of fluorescent nano-objects.[213] Based on recent reports exploring the incorporation of TPE dyes in RAFT polymerizations,[36,197] we hypothesized that the fluorescence turn-on exhibited by the TPE-NB dye upon aggregation should also be observable during polymerization.

3.2.d Polymerization Reactions

The polymerization reactions in our experiments consist of a high concentration of unlabeled norbornene in toluene (typically 7 M unless otherwise noted) with lower concentrations of TPE-NB monomer (2 mM) and our PDI-NB monomer (~1 µM). The tracer dyes are kept at low concentrations to limit their effect on product polymer morphology and make any potential influence on reaction kinetics negligible. Use of low concentrations also prevents aggregation of the dyes, which would otherwise result in artificially low anisotropy values or high initial AIE intensities. Absorption spectra of PDI-NB taken in 7M norbornene confirm the presence of only the unaggregated form of the dye (see Fig. S15 in reference).[224]

Reactions were also explored using norbornadiene as a solvent and comonomer, with the unlabeled norbornene and norbornadiene present at 2 M and 7 M, respectively. Stock solutions of GG2 catalyst were freshly prepared before each experiment and added to each reaction mixture immediately before droplet production. The droplet arrays were assembled onto fluorinated surfaces underneath a continuous phase of water using the robotic platform described above. In experiments monitoring multiple reaction conditions simultaneously, the robot placed droplets of each composition in order, automatically rinsing the syringe in between samples. Immediately following droplet placement, these prepared arrays were placed on a fluorescence microscopy setup for imaging (**Figure 3-2**).

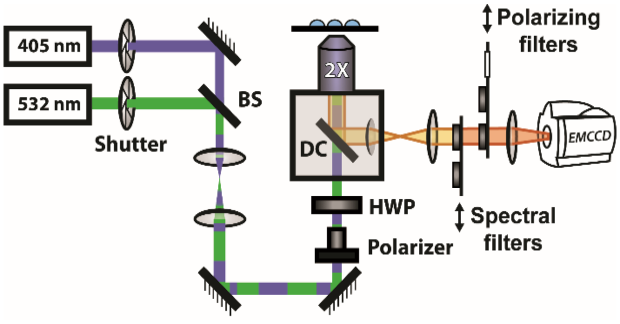

Figure 3-2. Optical Setup for fluorescence measurements.
Synchronized shutters and sliding mounts allow for alternating excitation with 405 nm and 532 nm light for the two probe monomers and collection through appropriate spectral and polarizing filters. BS: beamsplitter; HWP: half-wave plate; DC: dichroic.

3.2.e Fluorescence Anisotropy Measurements

The steady-state fluorescence anisotropy of the PDI-based fluorescent monomer was measured throughout each polymerization reaction using a home-built fluorescence microscopy setup (**Figure 3-2**). The droplets containing PDI dye were excited in a widefield geometry using a vertically polarized 532 nm laser. Emission from the PDI fluorophores was isolated from the excitation light via a multi-edge band-pass dichroic and subsequent 532 nm long-pass filter. Images of the parallel and perpendicular components ($I_{||}$ and $I_{\perp}$) of the emission from the PDI monomers were recorded sequentially every 5 minutes using a single camera (EMCCD, Andor Ixon) by taking alternating frames through two orthogonally oriented polarizing filters mounted in a computer-controlled sliding mount. The anisotropy (r) was calculated using equation 3.1:[3]

$$r = \frac{I_{\|} - GI_{\perp}}{I_{\|} + 2GI_{\perp}} \tag{3.1}$$

This anisotropy value (r) gives a measure of the depolarization of the emission relative to the excitation polarization. Said another way, this value relates the amount of rotational displacement over the emission lifetime of the dye. The calculated anisotropy should increase from $r \approx 0$ to $r \approx 0.4$ as the dye transitions from a state of fast rotation to one with highly limited rotation. This calculation was carried out for each pixel of interest in the recorded image. The constant G (the "G factor") is a correction factor to account for differences in collection efficiency between the parallel and perpendicular channels and was calculated and applied on a per-pixel basis (see refernce for details).[124] The anisotropy value reported for each droplet is an average taken over all pixels within the droplet. This value is recorded for every droplet in the array at every frame to produce plots of anisotropy over time (**Figure 3-3**), while the per-pixel anisotropy values are used to create color-scale images of the anisotropy across the droplet arrays at every frame (as in **Figure 3-4**). The use of larger arrays of droplets accelerates data acquisition by monitoring multiple reactions simultaneously, enabling a direct visual comparison between varied reaction conditions and internal controls in parallel. Movies of the monitoring of multiple droplets are available in the published supporting information.[124]

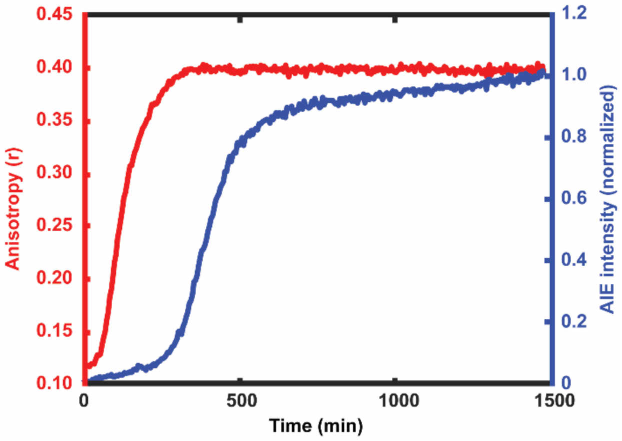

Figure 3-3. Average anisotropy vs time (red) and average AIE intensity vs time (blue), showing the additional dynamic range given by the offset response of the AIE signal relative to the increase in anisotropy.

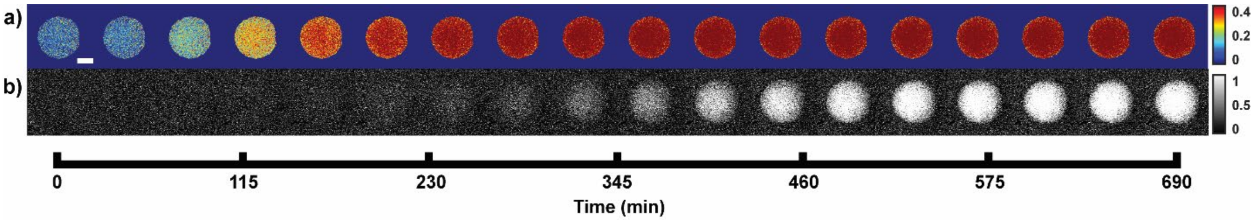

Figure 3-4. Monitoring the polymerization progress in a single droplet.
a) Color-scale image of anisotropy values in droplets over time. As the reaction progresses, the droplet increases in anisotropy. b) Emission intensity from the AIE monomer probe in a droplet over time. Droplet shown is the same as in the anisotropy images above. Each frame corresponds to the same timepoint as above (Scale bar 250 µm)

For every polymerization reaction, we observe an increase in the measured steady-state anisotropy of the reaction mixture droplet. A non-zero starting value of r≈0.1 is seen in each case, due to the relatively high initial viscosity of the unpolymerized reaction mixture as compared to toluene alone (where r=0.05, see Section 3.4.g). As the reactions continue, the anisotropy increases until at later times it saturates near the theoretical maximum value (r=0.4). Experiments with arrays containing varying catalyst concentrations show a shift in this response to later times for droplets with less catalyst, and earlier times for droplets with more catalyst, providing further evidence that the anisotropy increase depends on the rate of the polymerization reaction (**Figure 3-5**).

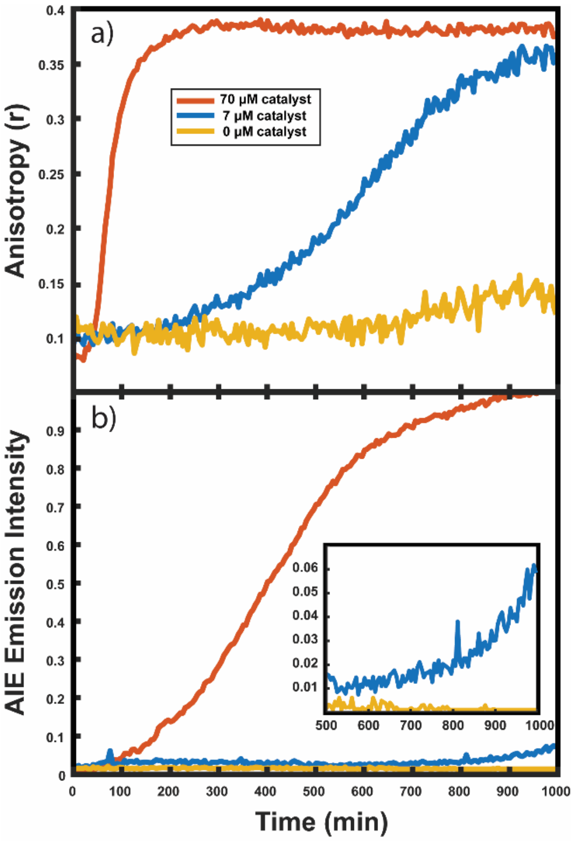

Figure 3-5. Monitoring norbornene/toluene droplets at different catalyst concentrations. a) Anisotropy response curves and b) AIE response curves in droplets containing 70 µM (red), 7 µM (blue), and 0 µM (yellow) Grubbs Gen II catalyst. Inset shows late time intensity dynamics.

Multiple competing phenomena could potentially contribute to a restricted degree of rotation for the fluorescent probe, potentially leading to an increase in fluorescence anisotropy that does not accurately track polymerization reaction progress. One potential cause of a false positive increase in anisotropy is lack of droplet stability resulting in loss of solvent to the surrounding continuous phase. If the droplet phase dissolves into the continuous phase too quickly, then an observed increase in anisotropy could be due to changes in freedom of motion resulting from a decrease in droplet volume (and consequent change in viscosity). In our experiments, we see that the immobilized droplets are stable over long periods of time, preventing this effect from being dominant on the timescale of the polymerizations. Still, some droplet contraction is seen at longer times, causing the slight rise seen in the yellow trace in **Figure 3-5**, and when left for many hours, the organic droplets are observed to disappear entirely, eventually dissolving into the surrounding aqueous continuous phase. Notably, the droplets containing polymer are more stable at these later times and are seen to shrink much more slowly than the catalyst-free droplets. Our attempts to use various surfactants to increase their stability led to an even faster contraction of the droplets, likely due to the solubilizing effect of the surfactants. Control experiments comparing droplets with and without catalyst present show that the anisotropy increases observed in droplets containing active polymerizations occur well before any changes in anisotropy occur due to solvent loss in inactive droplets (see Section 3.4.g).

3.2.f Aggregation-Induced Emission Measurements

In addition to the anisotropy measurements described above, emission intensity from an aggregation-induced emission dye, TPE-NB, was measured as a complementary readout of reaction progress. With progressing polymerization, the measured fluorescence from the TPE dye should increase both from incorporation into the growing polymer and consequent steric hindrance, as well as from increasing viscosity of the surrounding chemical environment. These effects will both contribute to a restriction of intramolecular rotation, suppressing non-radiative decay from the excited state, and thereby increasing its emission intensity. The TPE-NB monomer was excited at 405 nm for the AIE measurements. These measurements were made at the same time as the anisotropy measurements described above. The 405 nm laser necessary for the AIE readout was coaligned with the 532 nm anisotropy beam (**Figure 3-2**), and computer-controlled shutters and sliding mounts were used to excite and collect the fluorescence from each probe monomer individually at each timepoint (additional details in Section 3.4.d). In this way, time-lapse videos were created of the changing emission from each of the droplets.

3.2.g Complementary Measurements

The collected AIE videos reveal increases in emission intensity over time for the polymerizing droplets, followed by eventual saturation of the response. As with the anisotropy experiments, the time at which the increases occur is sensitive to different reaction conditions and tracks with changes in catalyst concentration. Importantly, the AIE response is seen to occur after the anisotropy response in all cases. The onset of the AIE response is delayed relative to the onset of the anisotropy increase, and it continues to increase well after the anisotropy measurement has saturated at its highest value. This separation reveals the ongoing polymerization continuing for hours after the anisotropy response has run out of dynamic range. At the same time, the anisotropy response is sensitive to the developing polymerization at shorter timescales that the AIE measurement misses. The combination of these two readout methods yields a significant extension to their temporal dynamic range, as the measurement of fluorescence anisotropy adds the ability to observe polymerization reactions at much earlier times (and lower Mw) than the AIE response would allow for on its own. Fluorescence polarization anisotropy may be better suited for assessing if a polymerization has occurred at all (i.e. for differentiating a small amount of polymerization from no polymerization), as would be valuable in identifying a “hit” in a combinatorial screen, while AIE may be more suited to determine if a large molecule weight has been reached (though it may be insensitive to small degrees of polymer formation).

This separation of observed dynamic ranges is not entirely unexpected, as these different measurements are probing different phenomena. Previous work examining the AIE of growing polymers shows that, for some reaction conditions, there is not an appreciable increase in AIE until a critical molecular weight has been reached, after which the emission intensity scales with increasing conversion.[36] The difference in observed dynamic ranges can be explained by the different mechanisms that give rise to each observed increase – in the anisotropy measurement, the rotational correlation time of the fluorescent monomer must only be slowed relative to its emission lifetime to see an increase in r. As the PDI dye is incorporated into the large polymer chain, its rotation is slowed dramatically. Though the TPE dye's global rotation is also slowing at these earlier timepoints (as it is also being incorporated), it is the intramolecular rotations of the phenyl rotors that must be slowed to turn on the AIE response. Judging from the observed separation in time scales, this process requires more time to reach a much higher effective solution viscosity before increased emission intensity can be observed. In some cases, it may be that intermolecular interactions between multiple TPE molecules or TPE molecules with other π-systems may be required to reduce these internal degrees of freedom.[196]

3.2.h Experiments in Neat Monomer

Many important polymerizations are carried out in neat monomer. To investigate the influence of the presence of solvent on our reaction readout, we performed experiments in which we replaced the toluene component of the reaction mixture with norbornadiene (NBD). Norbornadiene may also act as a monomer in the polymerization along with norbornene, but is a liquid at room temperature, allowing for its use as a solvent for the polymerization reaction. Importantly, norbornadiene's reactivity differs slightly from that of norbornene due to differences in ring strain energies of the two monomers, and it may undergo some crosslinking as the second double bond is opened, though this second ring opening is relatively unfavorable.[225,226]

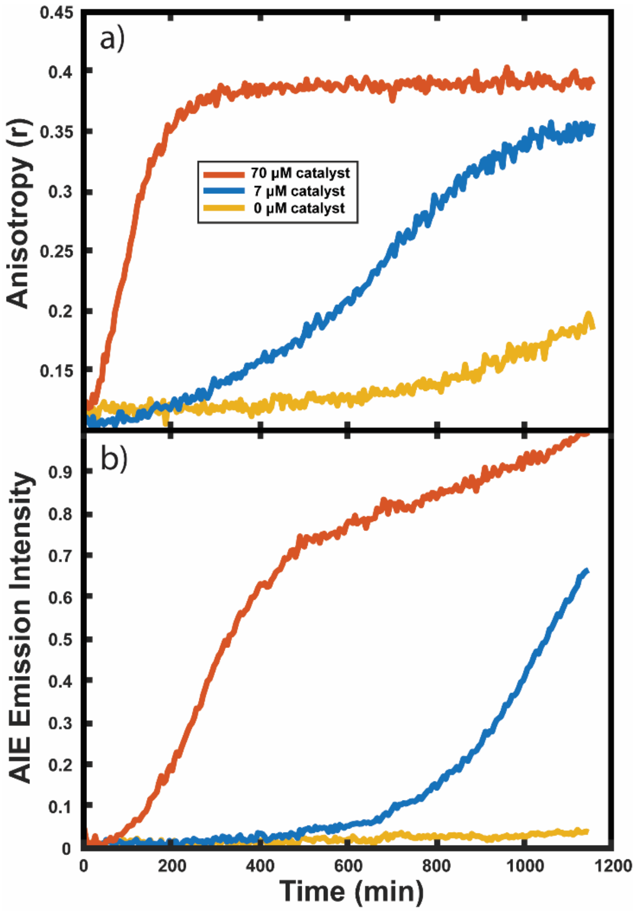

Figure 3-6. Monitoring norbornene/norbornadiene droplets at different catalyst concentrations. a) Anisotropy response curves and b) AIE response curves in droplets containing 70 µM (red), 7 µM (blue), and 0 µM (yellow) Grubbs Gen II catalyst.

Fluorescence anisotropy and AIE were used to monitor the progression of the ring opening metathesis polymerization of NB/NBD to form a statistical copolymer of polynorbornene with lightly crosslinked norbornadiene units. The data collected from droplets under these conditions show increases in anisotropy and AIE as before (**Figure 3-6**). These experiments showed that both the anisotropy and the AIE readout methods are capable of tracking polymerizations in reactions of neat monomer, a common condition for industrial polymerizations.

3.2.i Calibration of Readout with Molecular Weight

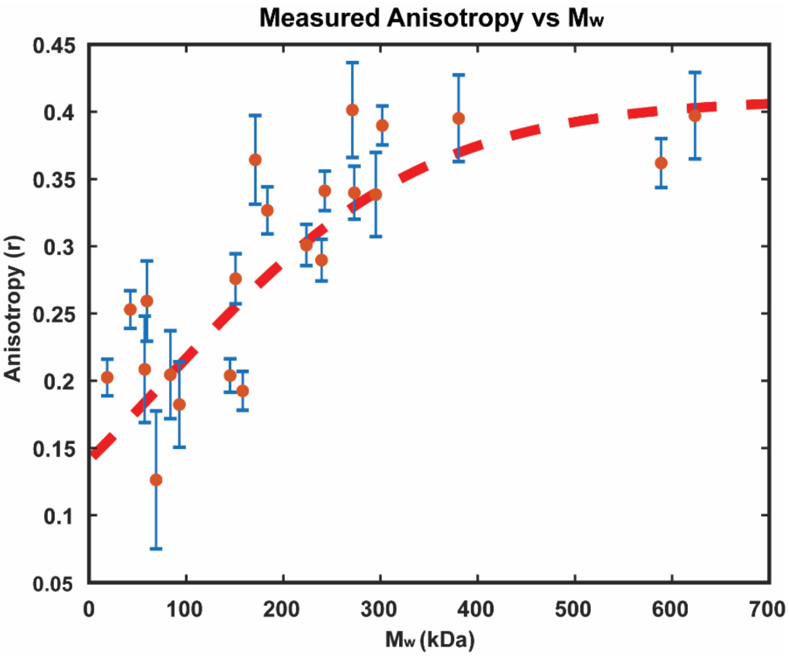

Figure 3-7. Calibration of measured anisotropy values with molecular weight, as measured by GPC-MALS. A correlation of measured anisotropy is seen with increasing molecular weight until the maximum value of 0.4 is reached. Red dashed line is a sigmoidal fit of the data added as a visual guide and is not meant as a quantitative model.

In order to confirm that the observed increases in anisotropy correspond to increasing polymer molecular weight in our reactions, SEC-MALS measurements were taken of various polymers formed in reactions in immobilized droplet arrays. To accomplish this, larger scale experiments (consisting of>1000 droplets each) were performed under the same conditions as those detailed above. For each run, a smaller droplet array was produced as usual for optical monitoring, while 3 additional 20×20 arrays were left to polymerize simultaneously. We carried out these reactions with 25 µM GG2 and ended them at varying times from 30-1200 minutes. At the desired end timepoint, the anisotropy value was recorded and the reactions in the larger arrays were quenched by addition of ethyl vinyl ether. The polymer left on the surface was then collected and placed under vacuum overnight in order to remove any remaining solvent and unreacted monomer. In this way, large enough samples could be produced for SEC-MALS without altering the reaction conditions used in earlier optical experiments.

The resulting relationship between Mw and steady state anisotropy, shown in **Figure 3-7**, reveals that the shorter timescale reactions which produced smaller molecular weight polymers correspond to lower measured anisotropy values, while the samples which consisted of higher molecular weight polymers are those which measured high anisotropy values, as expected. This relationship saturates at around r=0.4, the maximum possible steady state anisotropy value, and so it appears that for this reaction system all polymers greater than ~300 kDa would be expected to yield this limiting anisotropy value. The scatter in the data shown could result from variability in how quickly the polymerization was quenched after measuring each sample's anisotropy, as well as from changes in the optical setup that may not have been fully corrected for by the g-factor calibration. This observed correlation of anisotropy with molecular weight further confirms the viability of this measurement technique for tracking polymerization reactions *in situ.*

3.3 Conclusions

We have demonstrated a method for optical monitoring of polymerization reaction progress in single droplets based on two complementary approaches. As the reaction progresses, increases in molecular weight of the growing ROMP polymers are accompanied by an increase in the fluorescence polarization anisotropy of a PDI tracer molecule is observed. This method is informative at early reaction times for polymerizations of varying compositions and morphologies, suggesting utility for combinatorial searches for new polymerization reactions. Following the saturation of the anisotropy response, the fluorescence intensity of an AIEgen-based monomer is seen to increase at later times, suggesting utility for monitoring production of high molecule weight polymers. The combination of these two optically orthogonal readouts allows for a larger temporal dynamic range than either of the methods could provide on its own. Both methods can be used to monitor the reactions in droplets at the single-droplet level, with a fluorous surface providing convenient immobilization. Confinement of the reactions under study to precisely positioned sub-mm droplets of organic phase, coupled with the use of widefield fluorescence microscopy to monitor their optical response, allows for measurement of many reaction conditions in parallel, with simple incorporation of simultaneous internal controls with many replicates. The advantages afforded by a computer-controlled robotic platform for precision droplet placement lays the groundwork for the future development of multi-droplet computing paradigms.[227] Simple scaling to larger droplet arrays (>20×20) and the use of automated image processing opens a path to massively high throughput, combinatorial testing of reaction chemistries.

3.4 Methods

3.4.a SI - Solvent and Reagent Purification

Toluene (Optima™ Grade, Fisher) was used as solvent for most reactions. Notably, even this grade of solvent contained fluorescent impurities significant enough to measure on our microscopy setup. To remove these impurities, the toluene was purified by vacuum transfer at room temperature. Liquid N_2 was used to cool the receiving flask and condense toluene from the vapor phase. All glassware used in this process was first rinsed thoroughly with HPLC solvent, dried, and then cleaned in a plasma etcher for 5 minutes at 300W to remove potential organic fluorescent impurities from the glassware as well. Fractions of purified toluene were kept sealed immediately after collection in clean round bottom flasks until use.

Norbornene (bicyclo[2.2.1]hept-2-ene, Sigma Aldrich) was also seen to have significant fluorescent impurities. The monomer was purified by sublimation at room temperature onto a cold finger cooled with dry ice/acetone.

Norbornadiene (bicyclo[2.2.1]hepta-2,5-diene, Sigma Aldrich) was used as received, without further purification. All other materials were purchased commercially and used as provided, except where noted.

3.4.b SI - Surface Functionalization of Glass Reaction Chambers

Perfluoroalkylated glass chambers were constructed to facilitate droplet immobilization and imaging over long timescales. Unfunctionalized glass chambers were constructed first by the following procedure: Coverslips (25x25mm, Fisherbrand™) and micro slide rings (Thomas®, 3x15mm and 5x18mm) were rinsed with HPLC grade methanol and ultrapure water, dried under nitrogen, and then O_2 plasma cleaned (300 W, 5 minutes). The rings were bonded to the coverslips with sodium silicate as described previously.

To functionalize the glass chambers, each chamber or coverslip was first rinsed with HPLC methanol and ultrapure water. The chambers were dried under nitrogen and then O_2 plasma cleaned in a plasma etcher at 300W for 5 min. A 5% solution of 1H,1H,2H,2H-perfluorodecyltriethoxysilane in 2-propanol was prepared and placed in the cleaned chambers for 1 hour to allow the silane to physisorb to the surface. After 1 hour, the solution was removed, and the chambers were again dried under nitrogen before heating at 110°C for 10 minutes in order to create a covalent bond to the surface.[iv] They were then allowed to cool down to room temperature before finally rinsing with 2-propanol. Functionalized chambers were made in batches and could be stored and used for droplet immobilization long after their initial preparation.

[iv] There is a potential for residual perfluorinated solution to be vaporized when heated. Therefore, in the interest of chemical safety, the thermal annealing step for any future functionalization should be done either in a vacuum oven or as an alternative, on hot plate inside of a fume hood.

3.4.c SI - Sample Preparation

Stock solutions of PDI-NB and TPE-NB in purified toluene were prepared in cleaned scintillation vials and used immediately or stored sealed in light-tight containers. Purified norbornene was kept as a saturated solution in either purified toluene (~8 M) or norbornadiene (~6 M). Reaction mixtures were prepared by dilution of the above samples into purified toluene (or norbornadiene, where appropriate), to afford 80% of the saturated concentration of monomer, 2 mM TPE-NB, and ~1 µM PDI-NB in solution. Stock solutions of Grubbs Generation II catalyst (GG2) were prepared in purified toluene immediately prior to use, as degradation of the catalyst occurs too quickly to store these over long periods of time.

Prior to imaging, the chambers were rinsed, then filled with ultrapure water to act as a continuous phase surrounding the organic droplet phase before being placed on the robotic droplet production platform.

3.4.d SI - Fluorescence Microscopy Setup and Timelapse Imaging:

Microscopy was performed on an inverted microscope (Nikon Ti-U), with excitation provided by a 532 nm laser (Coherent Sapphire FP, 80 mW) for the PDI dye, and excitation provided by a 405 nm laser (Cobolt MLD, 120 mW) for excitation of the TPE dye. Each laser was attenuated with ND filters, then coaligned through a telescope to expand the beams until their diameters were slightly larger than the back aperture of the objective (Nikon 2x, 0.1 NA, Plan Apo). The excitation beam passed through a polarizer (Thorlabs PBS251) and half-wave plate (Thorlabs WPH10M-532) to afford a linearly polarized 532 nm beam for fluorescence polarization anisotropy experiments. Electronic shutters (Uniblitz) at the beginning of each beam path were used to keep the sample from being exposed to excitation light until images were taken (thus preventing excessive photobleaching). Emission from the sample was passed through a multi-edge dichroic mirror (Semrock Di01-R405/488/532/635-25x36) and directed to the collection optics. Computer controlled sliding mounts (Thorlabs ELL6K, ELL9K) were used to automatically select the appropriate spectral filters and polarization filters for each image. During excitation with the 532 nm laser, a 532 nm long pass filter (Semrock LP03-532RU-25) was in place, and during 405 nm excitation, the sliding mount switched to a 470/100 band pass filter (Semrock FF02-470/100-25) which was used to isolate the emission of the AIE dye. A second 4 position sliding mount was used to switch between two orthogonally oriented polarizing filters (Thorlabs LPVISE100-A) for acquisition of the parallel and perpendicular fluorescence polarization images at each timepoint. During acquisition of the TPE emission images, this sliding mount moved to a third empty position to allow all emitted light through regardless of polarization. Emission was collected and recorded on an EM-CCD camera (Andor, Ixon 897). Custom LabVIEW code interfaced with the camera and synchronized the shutters, sliding mounts, and camera exposures times to ensure all three images were automatically collected at each timepoint. The shutters were closed in between exposures to minimize photobleaching. Unless stated otherwise, each timelapse experiment used a 100 ms exposure time with 300 EM gain. The CCD was cooled to -80C during data acquisition. Frames were taken 5 minutes apart for up to 300 repetitions maximum (i.e. up to 1500 min or 25 hours).

3.4.e SI - Droplet Stabilization and Surfactant Tests

As toluene droplets are unstable in aqueous environment, we sought to stabilize them using typical surfactants (listed below). In our hands, any of the various surfactants tried had either no discernible benefit or accelerated droplet contraction and disappearance (**Figure 3-8**). We hypothesize that this is due to a solubilizing effect of the surfactants on the toluene/monomer organic phase. Switching back to only ultrapure water as the continuous phase resulted in longer droplet stability (see **Figure 3-9** and **Figure 3-10**). All droplets shown in **Figure 3-8**, **Figure 3-9**, and **Figure 3-10** contain norbornene monomer in toluene, but with no catalyst added.

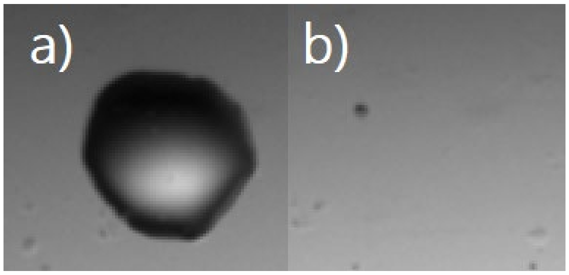

Figure 3-8. Droplet surrounded by aqueous continuous phase with TWEEN surfactant.
Bright field image. a) t = 0 minutes b) t = 890 minutes

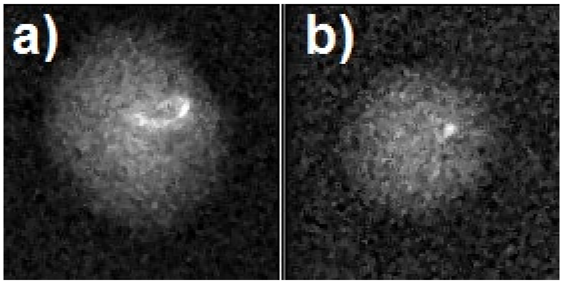

Figure 3-9. Droplet surrounded by pure water (fluorescence emission).
a) t = 0 minutes b) t = 890 minutes

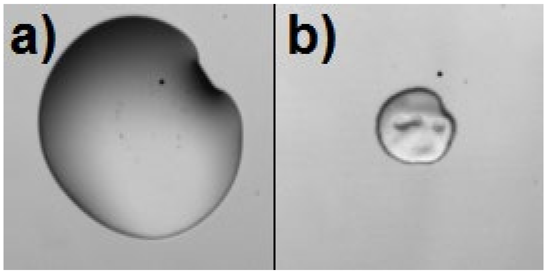

Figure 3-10. Droplet surround by pure water after 24 hours.
a) t = 0 hours. b) t = 24 hours

Surfactants tested include TWEEN 20, TWEEN 80, Sodium dodecyl sulfate, Triton X-100, MTAB, CTAB, CA 720, and CO 720. Interestingly, the production of polymer itself seems to slow droplet contraction, regardless of the contents of the surrounding continuous phase (See **Figure 3-11**).

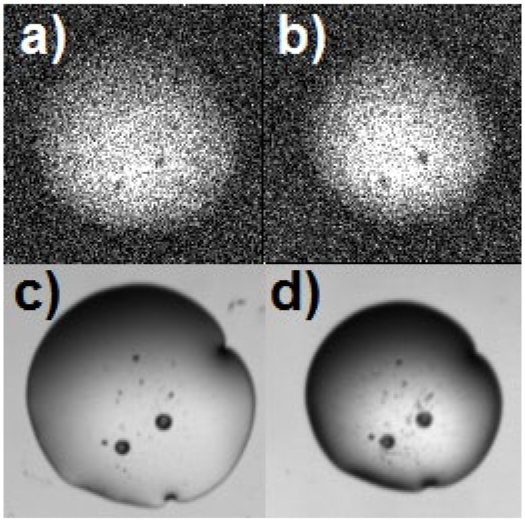

Figure 3-11. Droplets containing catalyst (and thus active polymerizations) shrink much less over the course of 24 hours.
a) Fluorescence image at t = 0 min. b) Fluorescence image at t= 890 min. c) Bright field image at t= 0 min. d) Bright Field image at t= 24 hours.

3.4.f SI - Unaveraged Traces of NB/NBD Reactions in a 3x3 Array:

Typically, we track at least 3 droplets with the same conditions in each experiment. In the main text, we average the responses of the droplets together for clarity to produce the plots shown. In **Figure 3-12**, we show the un-averaged traces (Each trace shown is still the average of many points within each droplet). Despite some inter-droplet variability, droplet behavior and response times are largely the same. Likely sources of this slight variability are imperfections in G factor and differences in background and noise coming from inhomogeneous excitation.

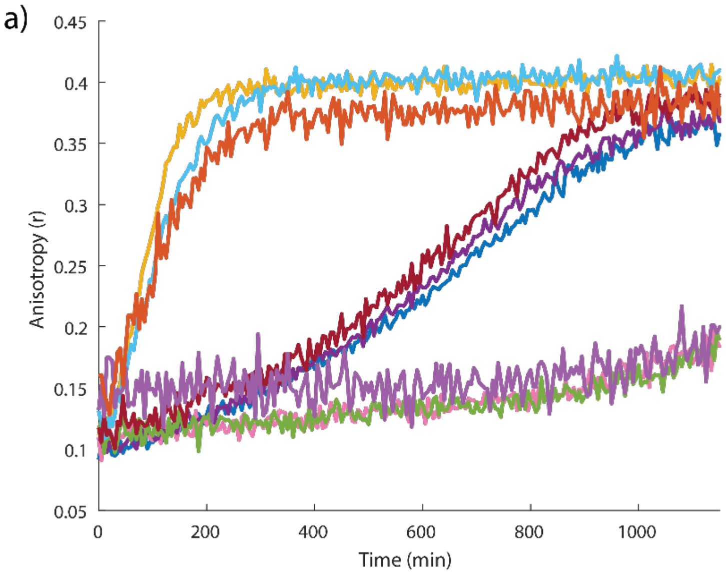

Figure 3-12. Norbornene/norbornadiene reaction mixtures.
Each trace is from a single droplet in a 3x3 array (three replicates per condition). This data was used for the NB/NBD figure in the main text, with each set of 3 droplets averaged together for clarity. Some small variation is seen between droplets, due most likely to their differing positions in the beam and an imperfect G factor correction.

3.4.g SI - Control Reaction

In analogy to the above plot, **Figure 3-13** shows 2 sets of 3 droplets where one row contains catalyst and one row does not. Again, the behavior and timescale are similar between all 3 droplets in each set. The long scale fluctuations seen centered around 200 frames are due to changes in background.

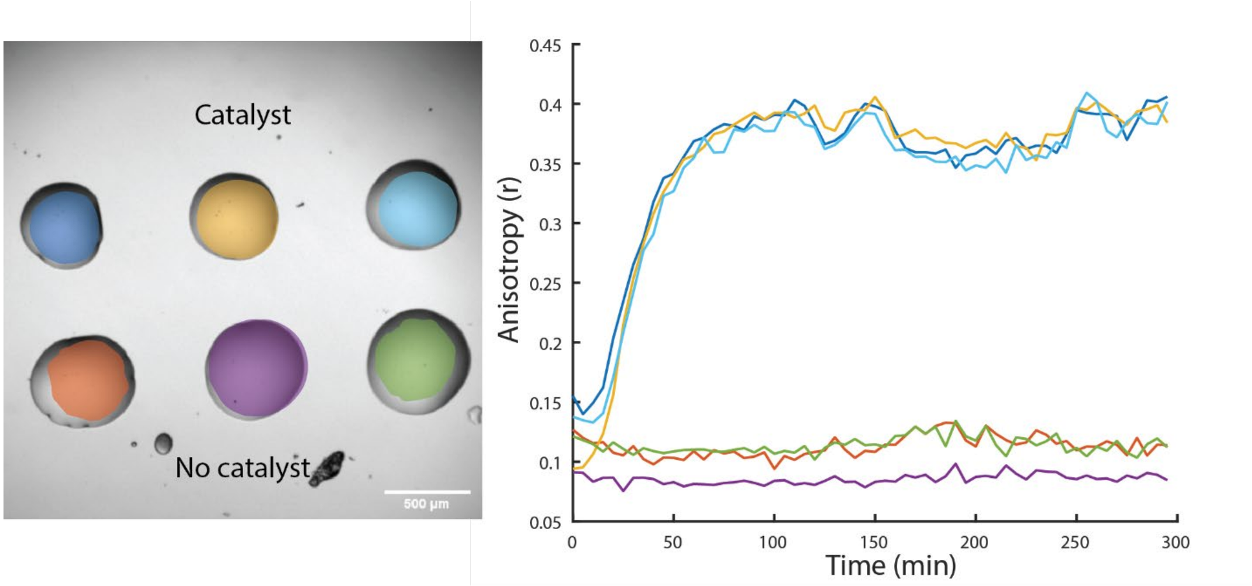

Figure 3-13. Control reaction comparing droplets with and without catalyst present.
A rise in anisotropy is seen concurrent with polymerization in the droplets containing catalyst (top row, false color overlay matched to traces on right). Droplets without catalyst do not display any increase on this timescale, instead maintaining their initial values (bottom row).

Chapter 4 Optical Monitoring of Polymerization within Attodroplets using Single-Molecule Fluorescence Anisotropy

4.1 Introduction

In this chapter we aim to take the anisotropy monitoring technique developed in the previous chapter and utilize it to investigate and monitor polymerizations at the single-molecule level. Single-molecule techniques, in particular single-molecule spectroscopy and fluorescence microscopy can be particularly powerful tools for identifying and understanding unsynchronized molecular dynamics observed under reaction conditions.[52,60,150,156] However, utilizing single-molecule techniques is not trivial. To transition from the experiments of the previous chapter to this one required the development of new methods for droplet production, improvements to the optical set up, as well as new data processing methods. With all these requirements, we are left with the question, *why investigate single molecule dynamics?*

Chemical reactions consist of combinations of molecules undergoing complex transformations. Understanding these reactions requires uncovering mechanistic information, particularly in the case of catalyst species. Typically, mechanistic information is acquired *via* bulk measurements, which inherently includes ensemble averaging. Ensemble averaged measurements can fail to identify unsynchronized events or heterogeneity present during a reaction. This can impede gaining a full mechanistic understanding of a catalyzed reaction. During a catalytic cycle, catalysts can form short-lived reactive intermediates which can affect catalyst rate and selectivity or even introduce competing pathways.[134–136]

However, these intermediates are very difficult to identify using ensemble measurements as they do not reach detectable steady-state populations. Single-molecule measurements can allow direct observation of unsynchronized behavior, as measurements are made on each molecule individually.

Single-molecule fluorescence experiments have been critical for mechanistic studies of enzymes and other biological molecules.[151,228–230] Advancements in fluorescence microscopy techniques has allowed greater understanding of biological processes including protein folding,[231,232] and cellular division mechanisms.[233] While SM fluorescence has been traditionally applied to biology, it has more recently been used to probe chemical reactions, with applications in both heterogeneous[49,54,230,234–237] and molecular catalysis.[57,60,238,239]

One great advantage of single-molecule measurements is that they can uncover heterogeneity across a molecular population. Bulk measurements, such as measurement of an averaged rate constant for a catalyst, fail to capture how each catalyst has contributed to that rate constant. It is unlikely that each catalyst is contributing to the reaction identically. There can be a distribution of catalytic behavior, i.e., some catalysts with high activity, some that are completely inactive, and some that reside in the middle. This type of distribution describes *static* heterogeneity, which is the differences between individual molecules. A second type of heterogeneity that can be present is *dynamic* heterogeneity, which describes how the behavior of an individual molecule can change with time, such as fluctuations in the catalytic rate constant for a single molecule due to a catalyst changing between inactive to active states. Xu *et al.* used single-molecule fluorescence to observe single turnover events for a heterogeneous catalyst, revealing different subpopulations of catalytic nanoparticles with varying reactivity.[52] Liu *et al.* investigated the dynamics of single-atom platinum catalysts using single-molecule fluorescence, identifying that structural restructuring induces fluctuations in activity between various catalysts, resulting in both static and dynamic heterogeneity.[240] To gain a full insight into a catalytic reaction, it is beneficial to develop and utilize single-molecule based methods.

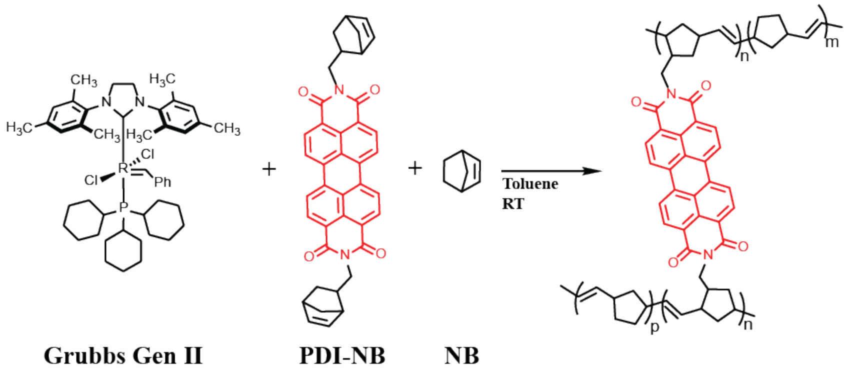

Scheme 4-1. Polymerization of Norbornene (NB) to polynorbornene, with fluorescently labeled perylene diimide norbornene (PDI-NB) catalyzed by Grubbs Generation II catalyst.

This work returns to the same ring-opening metathesis polymerization (ROMP) that was featured in the previous chapter; of norbornene (NB) to polynorbornene catalyzed by Grubbs Generation II (GG2),[198,199] **Scheme 4-1**. The reaction is relatively air and moisture-stable, relatively well understood, and industrially relevant but also, has featured interesting dynamics when investigated using single-molecule experiments. Easter *et al.* have observed abrupt changes in catalytic reactivity within polymer aggregates using fluorescence microscopy.[157] Eivgi and Blum investigated polymer growth kinetics using fluorescence lifetime imaging microscopy and deduced that increases in microviscosity due to crosslinking is correlated to a reduced turnover rate of the molecular Grubbs catalyst.[241] Liu *et al.* monitored the chain-growth of single polymers using magnetic tweezers. Interestingly, it was observed that the polymerization did not increase continuously, rather in “wait-and-jump steps”, where it is hypothesized that the growing polymer entangles and unravels during the polymerization.[58] The goal of this work is to monitor the polymer growth from a single catalyst using fluorescence anisotropy within droplets that are smaller than the diffraction limit of light. Encapsulating the reaction within droplets eliminated the need to synthetically attach molecules to the surface, while also maintaining extended observation times. Additionally, these single-molecule fluorescence anisotropy experiments can provide additional context of polymer growth and entanglement beyond techniques that force polymer extensions.

By encapsulating the reaction within droplets smaller than the diffraction limit of light (~250 nm), there is a large increase in the signal-to-background of our measurement, with all the emission localized within an individual droplet. These droplets are produced from nanoemulsions, which feature organic droplets within an aqueous continuous phase. One of the first single-molecule fluorescence experiments investigated the activity of single β-D-Galactosidase molecules within droplets *via* a fluorogenic reaction.[242] Since then, droplets have been implemented as a means of confinement for single-molecule experiments,[243,244] including measurement of single-molecule fluorescence resonance energy transfer within and between droplets,[245,246] dynamics of biological molecules within nanovesicles[247–249] and catalytic activity within nanopores.[250,251]

Each droplet should contain only one catalyst molecule, to determine the average concentration of catalyst within a droplet we use the following equation:

$$n = v\,x \tag{4.1}$$

Where x is the number of molecules within a solution, v is the volume of the droplets made of that solution and n is the average number of molecules. However, there are statistical fluctuations that will result in variation from droplet to droplet so that not every droplet has exactly n molecules. To further confirm the likelihood that a single catalyst is within a specific size of droplet, Poisson statistics are used.[242] The probability of finding a specific number of molecules (r) within a droplet can be determined by Equation 4.2.

$$p(r) = \left({n^r e^{-n}}/{r!} \right) \tag{4.2}$$

Using these two equations it can be determined that the smaller the droplet size, the more concentrated the total solution can be while still maintaining a probability that less than one catalyst is within a droplet.

It is possible to monitor the polymerization progress by an increase in fluorescence anisotropy in large droplets through the use of a perylene diimide-labeled norbornene (PDI-NB) monomer, **Scheme 4-1**.[124] In addition to our previous experiments in large droplets, perylene diimide dyes have also been utilized for single-molecule investigation of radical polymerization.[252] Fluorescence anisotropy provides a measured of the rotational behavior of the PDI-NB monomer by the polarization of its emission. It is calculated with Equation 4.3.

$$r = \frac{I_{\parallel} - GI_{\perp}}{I_{\parallel} + 2GI_{\perp}} \tag{4.3}$$

$I_{\parallel}, I_{\perp}$ are the intensities in the parallel and perpendicular channels respectively and G, known as the G factor, is a correction factor for the optical set up. Details regarding fluorescence anisotropy and its previous applications beyond our own can be found in Chapter 1. As the PDI-NB monomers are incorporated into the polymer, there should be a rise in anisotropy. If there is a reorganization of the polymer, either by entangling or unraveling, this would cause fluctuations in the anisotropy, as opposed to the continual rise observed with only incorporation events.

4.2 Functionalized Surfaces for Droplet Immobilization

Alkylsilane specifically triethoxyoctylsilane (TEOS) is used to functionalize glass surfaces to immobilize droplets for the duration of the experiments, **Figure 4-1**. TEOS results in a more hydrophobic surface than non-functionalized glass, allowing for the immobilization of toluene droplets to the surface with the presence of an aqueous continuous phase to prevent evaporation.

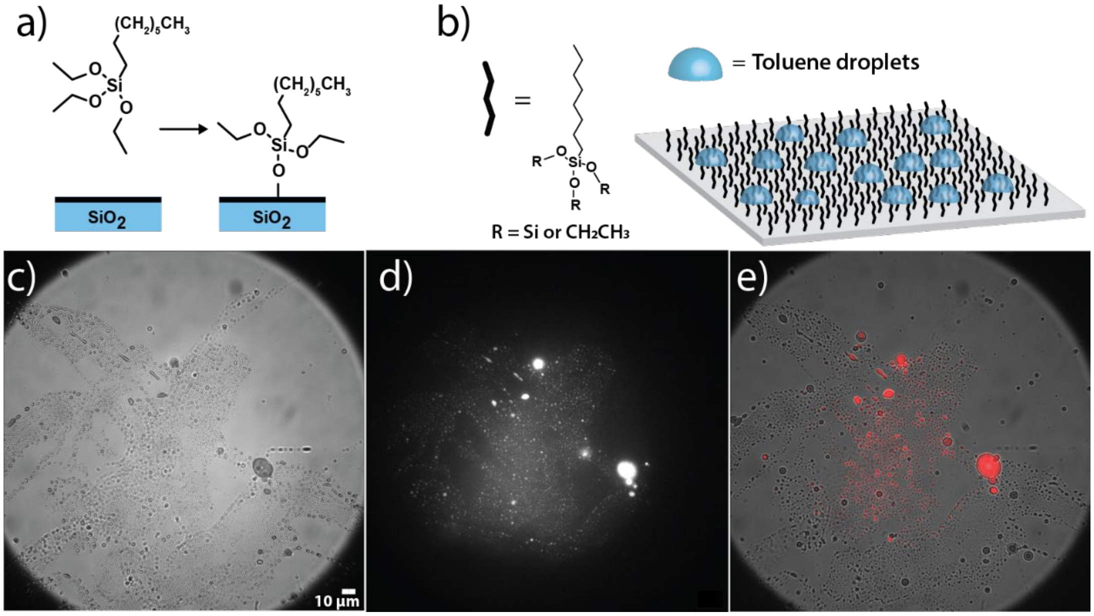

Figure 4-1. Surface functionalization with TEOS.
(a-b) Illustrations regarding the functionalization of glass surfaces with TEOS. c) Toluene droplets immobilized onto TEOS surface c) illuminated by white light, d) fluorescence emission, e) overlay of c and d with false color for fluorescence (red). 10 µm scale bar.

In the previous chapter, perfluorosilane compounds were found to produce hydrophobic surfaces that provided a robust immobilization method for the organic droplets. When transitioning from a large scale (0.5 mm) droplet down to the single catalyst, diffraction-limited droplet, a hydrophobic surface is still required to obtain droplet immobilization. Additionally, a surface free of fluorescent impurities is also required. When imaging fluorous-functionalized surfaces without any fluorophores deposited, an inconsistency in the fluorescence impurities present is observed, resulting in some coverslips being relatively clean and others covered with fluorescent impurities, see **Figure 4-2**.

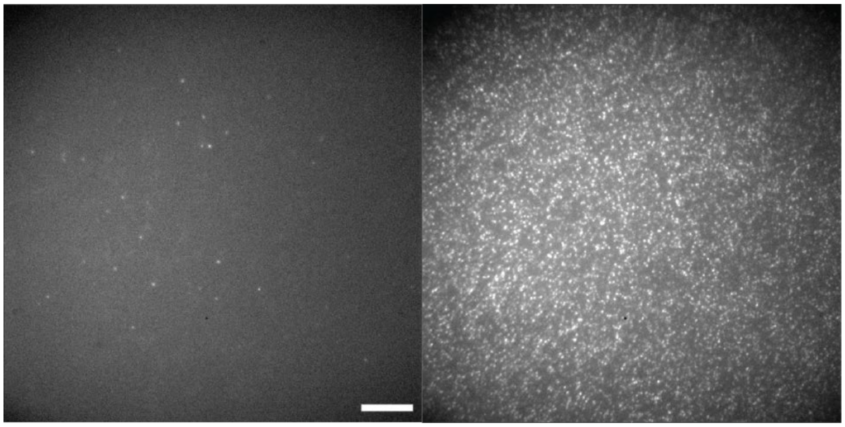

Figure 4-2. Inconsistency in fluorescent impurities on perfluorinated surface excited by 532 nm light. 10 µm scale bar.

With diligent cleaning procedures it can be possible to generate a fluorous-functionalized surface that is free of fluorescent impurities. However, this inconsistency motivated the switch from a perfluorosilane to an alkylsilane-functionalized surface, specifically using TEOS for surface functionalization. While the TEOS-surface was not ideal for the larger microdroplets, it resulted in comparable immobilization of attodroplets to the perfluorosilane surface. Along with long-term droplet immobilization, TEOS consistently produced a fluorescent impurity-free surface when exciting at 532 nm, ideal for single-molecule experiments. Details regarding surface functionalization are found in Section 4.7.a.

4.3 Diffraction-Limited Droplets

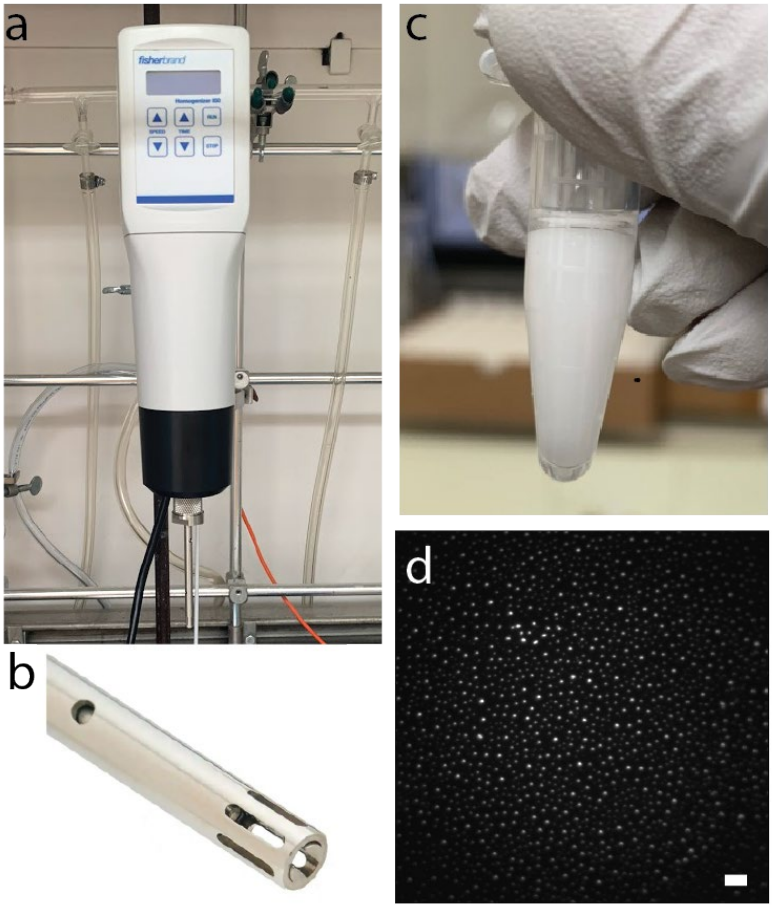

Figure 4-3. (a) Homogenizer (b) close up of homogenizer flat bottom probe (c) emulsion in Eppendorf and (d) fluorescence image of toluene droplets with PDI-labeled norbornene on a 1% TEOS functionalized glass surface, 5 µm scale bar.

To investigate the dynamics of single catalysts required the production of monodisperse diffraction limited droplets. These droplets, referred to as 'attodroplets', as they are on the volume scale of hundreds of attoliters, provide the best signal-to-background while also allowing for µM concentration of catalyst. A homogenizer is used to produce the attodroplets. A homogenizer is a device that is used to create homogenous mixtures, where particles of one solution are evenly dispersed and remain uniform among the second solution. Homogenizers are used to create emulsions for industry applications such as pharmaceutical sciences, personal care products, as well as food science. Homogenizers can be broadly classified by the process of how they break down solutions into small particles.[253] Mechanical homogenizers use a blade or rotor moved through the liquid at high speeds using shear forces to form and break particles in solution.[254] A benefit of utilizing a homogenizer is its ability to work with small volumes (total emulsion volume 0.2 to 5 mL). Attodroplets are made using a rotor-stator homogenizer (Fisherbrand 850) with a flat bottom probe to create nanoemulsions of organic reaction solution and water, **Figure 4-3**, with experimental details found in Section 4.7.b.

4.4 Fluorescence Optical Setup

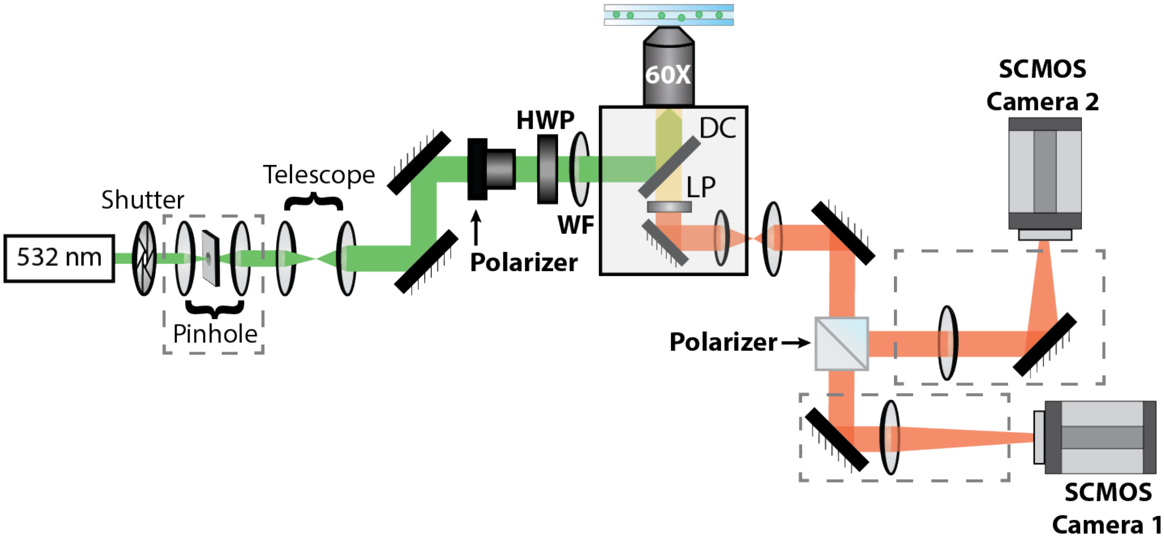

Figure 4-4. Optical Set Up for Small Droplet Anisotropy.
150 µm pinhole, HWP = Half Waveplate, DC = Multi-edge Dichroic Beamsplitter. Polarizer = Polarizing Beamsplitter. The area encased in the squares with dashed lines indicate where optical cage systems are used. Camera 1 is the parallel channel, while Camera 2 is the perpendicular channel.

A diagram depicting the optical microscopy setup is seen in **Figure 4-4**. Microscopy experiments were performed on an inverted microscopy (Nikon Eclipse, Ti-E, with perfect focus system) with excitation from a 532 nm laser (LaserTack, 80 mW). The laser is attenuated with neutral density (ND) filters, and then focused through a 150 µm pinhole[v] using 25 mm and 50 mm lenses which are aligned within an optical cage system. The beam is then expanded 10× using 50 mm – 500 mm plano-convex lenses. The beam is directed to the back of the microscope, passed through a polarizing beamsplitter (Thorlabs PBS251) and half-wave plate (Thorlabs WPH10M-532) to generate linearly polarized light. The light is expanded through a widefield lens and then reflected by a multi-edge dichroic filter (Semrock Di01-R405/488/532/635-25x36) onto the back aperture of the 60× oil immersion objective (Nikon, TIRF 1.49NA), which collimates the excitation light and collects the fluorescence. The fluorescence is isolated from any residual excitation light using a 532 nm long pass filter (Semrock LP03-532RU-25). The fluorescence is passed through a second polarizing beamsplitter (Thorlabs PBS251), separating the fluorescence into two linearly polarized emission channels. The emission was collected and recorded onto two sCMOS cameras (Andor, SONA 4.2B-11). Optical cage systems are used for the 300 mm lenses within the detection path. This is to maintain the identical focal points for both cameras with the relay optics, which is critical when imaging diffraction-limited spots.

A custom LabVIEW code synced the two cameras and laser shutter for extended optical experiments. Cameras were cooled to -45°C during acquisition. Images were taken at 100 ms exposure time.

4.5 Preliminary Anisotropy Results and Discussion

For microscopy experiments, the nanoemulsion (5 µL) is placed onto a TEOS functionalized coverslip. Water (15 µL) is layered on top, covered with a second coverslip (unfunctionalized, clean), and sealed

---

[v] This is a relatively large pinhole for this beam; however, the purpose of this pinhole was to remove extreme spatial aberrations seen in the beam profile during alignment. Prior to incorporating this pinhole, the beam was uneven, and it was very difficult to identify where the center of the beam was. Therefore, a larger pinhole was chosen to keep most of the laser power but remove high angle scattering.

with clear nail polish to create a coverslip ‘sandwich.’ It is important that the sample not be pressed or squished together in the center. Previous observations show that pressing on the sample encouraged larger droplets to appear on the surface, resulting in difficulties obtaining signal from attodroplets.

Initial experiments monitoring anisotropy changes were taken over the course of 6 hours, with images acquired every 5 minutes at a catalyst concentration of 3 µM, similar to the experiments in Chapter 3. With these experiments, decreases in anisotropy were observed, **Figure 4-5**. Along with decreases in anisotropy, photobleaching within the droplets and focal drift were also observed. Focal drift can be compensated with the perfect focus system present within the microscope. It is important to note that if the continuous phase within the coverslip sandwich dries out it will cause the perfect focus system to fail.

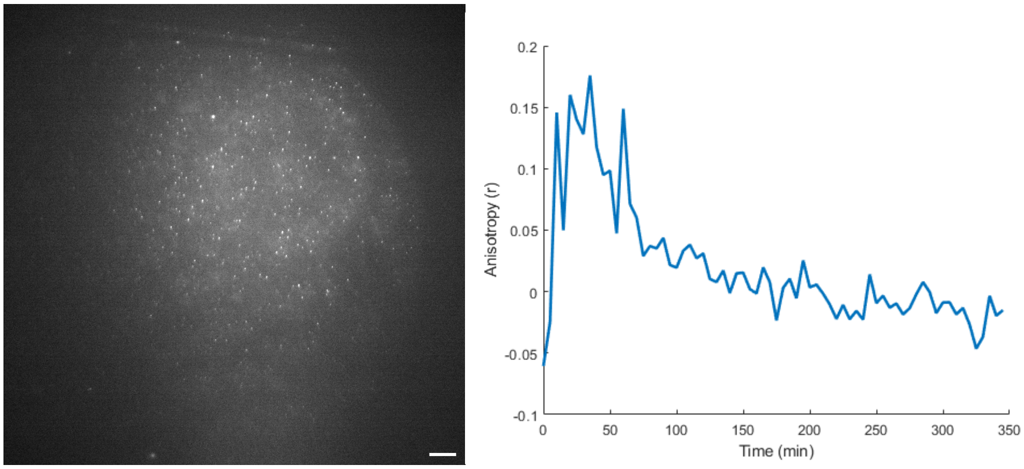

Figure 4-5. (left) Fluorescence image of reaction droplets and (right) anisotropy plot of 3 µM GG2, showing a steady decline in anisotropy.

The next set of experiments featured an increase in catalyst concentration while decreasing the image acquisition frequency. The catalyst concentration was increased by an order of magnitude to 60 µM. This concentration results in thousands of catalyst molecules per droplet, ensuring polymerization to occur within the majority of droplets. Additionally, the reduction in number of images taken was to ensure that full dynamics were captured, essentially limiting our measurement to only measure the start and end of the polymerization. This allowed for confirmation that not only high anisotropy values could be measured, but that also a change in anisotropy values could be observed.

The following data was taken over 6 hours, with images acquired at 30 minutes, 140 minutes and 356 minutes. By manually calculating anisotropy of user-selected spots, increases in anisotropy were observed between the 30 minute time point to the 140 minute time point. By 356 minutes, the continuous phase for the coverslip sandwich had evaporated and was no longer usable. However, by the 140 minute mark, anisotropy values of approximately 0.4 (the theoretical maximum) were observed. Therefore, by 140 minutes with 60 µM GG2 and 73 nM PDI-labeled norbornene monomer, the polymerization has reached an end-point, seen in **Figure 4-6**, with anisotropy values provided in **Table 4-1**. This exciting result provides a temporal range for the polymerization at 60 µM GG2, as well as confirms that high anisotropy values are measurable and that changes in anisotropy (low to high) are observable.

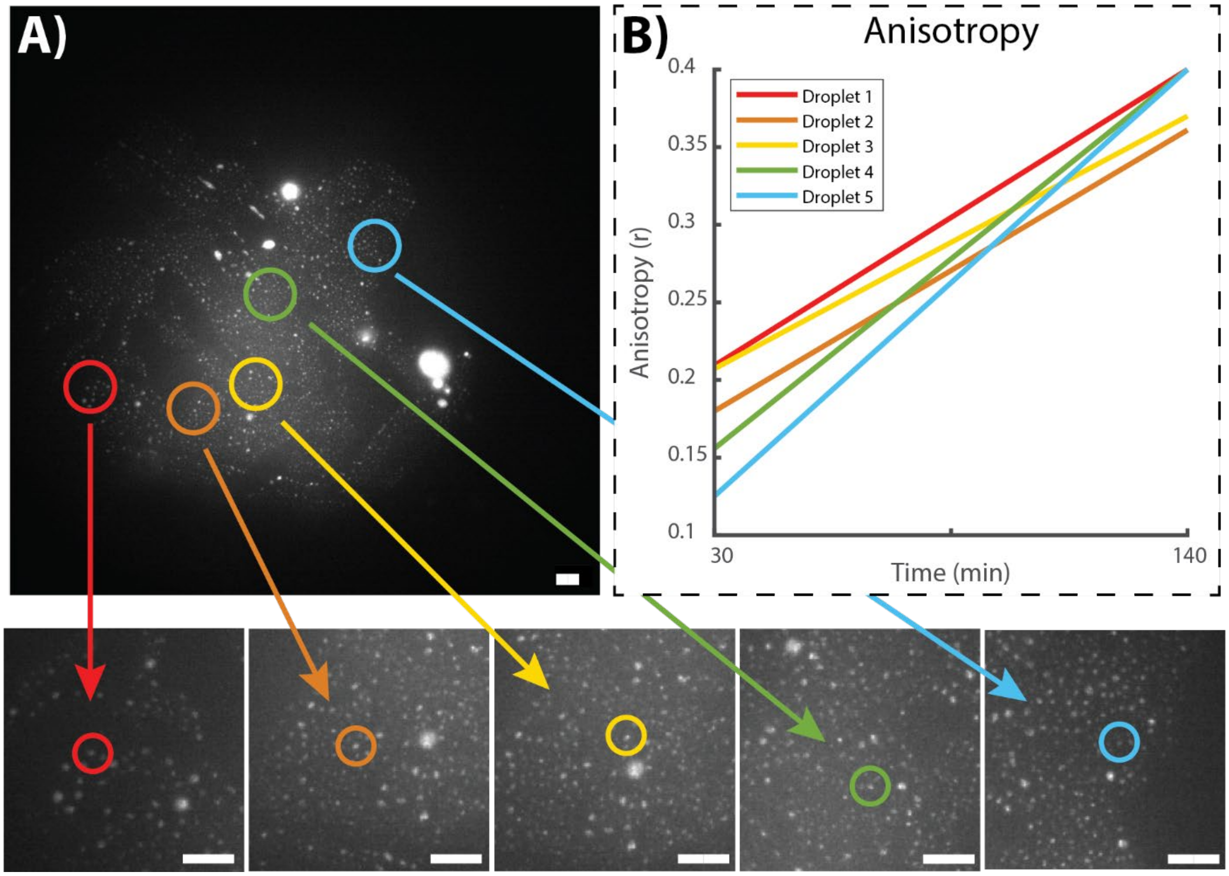

Figure 4-6. a) Fluorescence images of <1 µm diameter organic droplets made with 60 µM GG2 catalyst with labeled droplets that produced b) Anisotropy changes from 30 min. to 140 min. 10 µm scalebar.

Table 4-1. Anisotropy values for droplets containing 60 µM GG2.

Droplet #	***r* (t = 33 min)**	***r* (t = 144 min)**
1	0.21	0.40
2	0.18	0.36
3	0.21	0.37
4	0.16	0.40
5	0.12	0.40

After confirming that anisotropy changes were possible within a 2 hour timeframe, experiments were repeated with images acquired every 5 minutes over the course of 2 hours. These experiments aimed to provide data points between the 30 and 140 minutes observed in the experiment above. Catalyst concentration was within an order of magnitude of the previous experiment (30 µM), therefore similar dynamics are expected. Issues with data acquisition persisted, with samples drying out over the course of the acquisition resulting in focal drift that rendered the signal after drying unmeasurable. However, one set of experiments showed promising results prior to the focal drift, with one droplet identified that showed a promising increase in anisotropy, **Figure 4-7**.

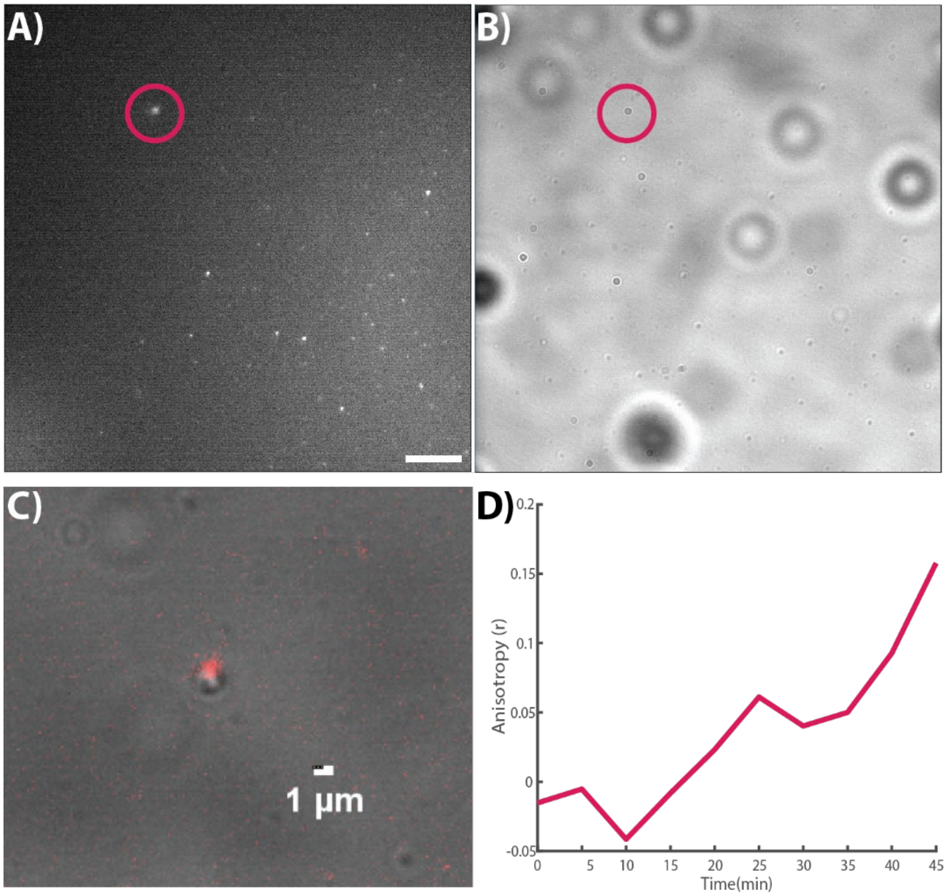

Figure 4-7. Changes in anisotropy for 1 µm diameter droplet with 30 µM GG2.
a) Fluorescence image of droplets on surface, b) white light illumination, c) overlayed false color fluorescence with white light illumination, and d) measured anisotropy increase.

By manually selecting and calculating anisotropy, one droplet persisted over the course of 45 minutes and showed an increase from r = -0.1 to r = 0.15, seen in **Figure 4-7**. This data showed that it was possible to monitor anisotropy increases over the course of 45 minutes with images acquired at least every 5 minutes. Previous attempts at 5 minute time points always resulted in decreases in anisotropy **Figure 4-5**, therefore, this observable increase shows promise that anisotropy can be measured within attodroplets.

4.6 Conclusions and Next Steps

Initial results show the promising increases of anisotropy in droplets less than 1 µm in diameter with bulk concentrations of catalyst (60 µM). As these are preliminary results, there are many controls that still need to be performed, including repeating these experiments with no catalyst added. In those experiments, it is expected that the anisotropy should stay constant at a low ($r < 0.2$) value. Additionally, the anisotropy value obtained from the control experiments without catalyst can be compared to the early time points from the catalyst droplets, identifying if early dynamics are being lost during the time it takes to make the emulsion and begin data collection.

The next major challenge in this project is making consistent and stable attodroplets, subdiffraction-limited in size. After that, it will be fine tuning the concentration of catalyst and dye so that the anisotropy changes from a single catalyst are measurable. The data shown in this chapter features droplets on the order of 1 µm in diameter, which is around a volume of 2.7×10^{-16} L. At the concentrations of catalyst that were used in the emulsions (30-60 µM), the droplets are expected to have between 5,000-10,000 GG2 molecules, still many orders of magnitude above 1 catalyst per droplet. With these preliminary results, I see this project as a promising direction for single-molecule investigations of molecular catalysts.

4.7 Methods

4.7.a Functionalizing TEOS Surfaces

This process should be performed in a fume hood. Surfaces were prepared based on the protocol previously published.[61] To functionalize glass surfaces, coverslips (Fisher Finest #1) held in a Teflon boat and a beaker (150 mL, depending on number of coverslips) are rinsed 3x each with HPLC methanol from a plastic bottle, Millipore water from a plastic bottle and then finally with HPLC methanol from a glass bottle. All glassware is then dried with nitrogen and plasma etched for 5 minutes. Plasma etching will not only remove organic impurities present on the coverslips, but it will also prepare the glass surface for functionalization. The deposition of TEOS occured immediately after plasma etching, as the surface composition can change within hours after a plasma etch has been performed. The Teflon boat of coverslips is placed into the beaker and a solution of TEOS in HPLC isopropanol (IPA) is added. A watch glass or petri dish is used to cap the beaker to reduce evaporation. TEOS is deposited onto the coverslips for 1 hour, then dried with nitrogen before being thermally annealed at 110°C within a single-molecule clean oven. After thermal anneal, coverslips are rinsed with IPA, methanol, and water, then dried with nitrogen. Long-term storage should be under vacuum, as functionalization can degrade over time (months) when exposed to moisture in the air.

4.7.b Generating Diffraction-Limited Droplets

Toluene (Optima Grade, Fisher) is used as the solvent for the stock solutions used in these experiments. Fluorescent impurities were removed using vacuum transfer at room temperature. Norbornene (bicyclo[2.2.1]hept-2-ene, Sigma Aldrich) does not fluoresce when excited with 532 nm light, however it was observed to contain fluorescent impurities. Therefore, it was purified via sublimation at room temperature onto a cold finger cooled with dry ice/acetone. Further details can be found in the Section

3.4.a. All other starting materials for these experiments are used without further purification. Synthesis of perylene diimide-labeled norbornene (PDI-NB) can be found in the supporting information of reference 124.[124]

All stock solutions were prepared in cleaned scintillation vials and stored sealed in light-tight containers. A saturated solution of sublimed norbornene was prepared in distilled toluene (8M) and used in the reaction solutions for the emulsions. Grubbs Generation II catalyst (Millipore Sigma) stock solutions were prepared immediately prior to use. The catalyst degrades quickly when stored in solution over long periods of time.[vi] The catalyst stock can be kept on ice prior to use.

Emulsions are made in 1 mL Eppendorf tubes, **Figure 4-3(d)**. A 95:5 ratio of Millipore water: organic reaction solution is used. Emulsions were made by layering solutions in the following order: aqueous continuous phase, unlabeled norbornene (5.47 M), then the PDI-labeled NB (60 nM), and finally the Grubb's catalyst (30 or 60 μM) within a 1 mL Eppendorf tube. The emulsion is kept on ice during the homogenization. The catalyst can be initiated by heat (20-50°C),[199] therefore, the reaction is cooled to slow the polymerization until the microscopy experiment can begin. Homogenization is done at 25,000 RPM for 1 minute.[vii] During homogenization, the Eppendorf should be moved around to encourage further mixing. The finished emulsion appeared cloudy and opaque (**Figure 4-3**c). After forming the emulsion, the homogenizer is rinsed with the following solvents to remove the fluorophores, organic molecules, and any polymer from the probe. This consists of running the homogenizer with large volumes (10 mL) of HPLC grade solvents, in the following order: toluene, isopropanol, methanol, and water.

[vi] You can see the color of the stock solution of catalyst change to a much darker purple as it degrades.

[vii] I suggest doing this in a fume hood with the sashes closed as much as possible as the homogenizer produces a very loud sound when running.

4.7.b.1 Surfactant Use

The properties of the attodroplets, such as composition, size and stability, depend in part on the ratio of the two phases used as well as the speed and duration of the homogenization. Droplet stability also depends on the presence and identity of a surfactant, which are molecules commonly used to stabilize emulsions.[255,256] For the purposes of these experiments, surfactants were omitted. Inclusions of surfactants in the emulsion production resulted in a wide disparity of droplet sizes. There have been a variety of routes to form toluene-in-water emulsions reported in the literature,[257–260] these can be used as resources to tune future parameters for droplet production.

4.7.b.2 Characterization of Droplet Size via Dynamic Light Scattering

Droplet size can be characterized using dynamic light scattering (DLS).[261] DLS works by combining the diffusion of particles in solution with fluctuations in scattered light to obtain the hydrodynamic radii of those particles. DLS measurements work best to describe stable, primarily monodisperse samples.

Particles in solution are subject to random forces due to constant collisions with solvent molecules, this results in particles moving about in a "random walk" which is referred to as Brownian motion. When placed in a DLS instrument, the laser light interacts with diffusing molecules scattering incident light and resulting in constructive and destructive interference. This results in fluctuations in collected intensity, the magnitude of which can reveal information regarding the diffusive behavior of particles. DLS instruments then correlate the diffusion coefficient for a particle to calculate the hydrodynamic radius of the particles present, using the Stokes-Einstein equation[262,263] (Equation 4.7).

$$R_h = \frac{k_B T}{6\pi n D_t} \tag{4.7}$$

Where k_B is the Boltzmann constant, T is absolute temperature (in Kelvin), n is the viscosity of the solution, D_t is the translational diffusion coefficient.

DLS measurements were attempted on initial emulsions, however they resulted in large disparity of sizes due to instability of the overall emulsion. The average size of droplets measured varied greatly from 300 nm (±150 nm) during one measurement and 1000 nm (±400 nm) during a second measurement, **Figure 4-8**. As the droplets used for fluorescence experiments are immobilized onto glass surfaces, the stability in bulk solution is not critical. Droplet size can instead be determined *via* fluorescence.

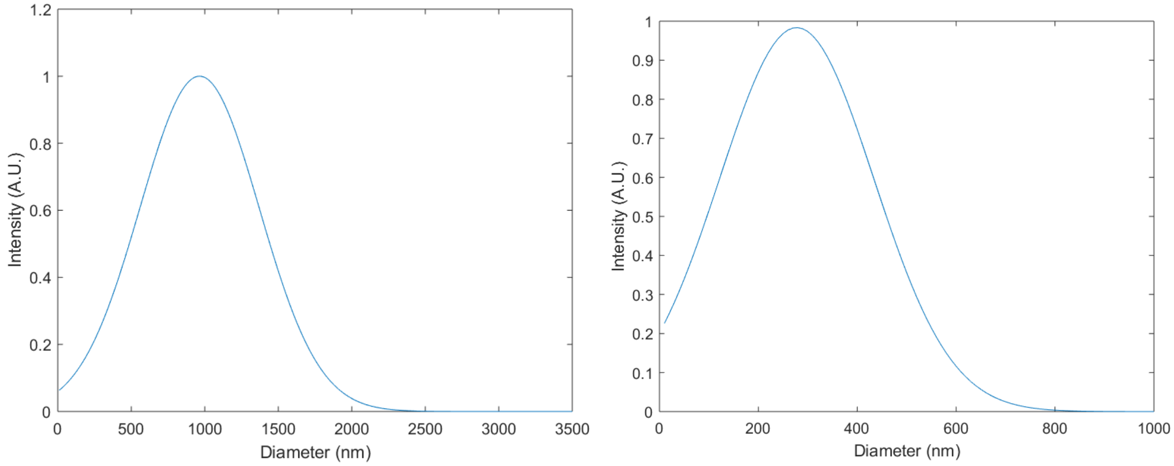

Figure 4-8. DLS Data
90:10 5% Tween 80/Water: Toluene emulsions. (left) 100 µL emulsion in 3 mL of water, mean diameter = 964 nm (406 nm). (right) 60 µL of emulsion diluted in 3 mL of water, mean diameter = 278 nm (156 nm)

4.7.c Data Acquisition and Processing

4.7.c.1 Dual-Camera Data Acquisition

Fluorescence images were acquired by two sCMOS cameras (Andor, SONA 4.2B-11). Time lapse videos were recorded using a custom LabVIEW code,[viii] which synchronized the laser shutter (Uniblitz) with

---

[viii] The Andor SONA software guide as well as the Andor SDK3 should be referred to for any assistance or additional explanations needed, at the time of this thesis writing, it located in the Catalysis subfolder of the LabVIEW VIs on databackup.

acquisition of images from both cameras sequentially. The code (**Figure 4-9**) allows for a user defined wait time (the time between acquired images), as well as user specified number of images acquired, allowing for overnight timelapse experiments. Additionally, images may also be taken manually using this code. The shutter driver is connected via the National Instruments data acquisition system (NI-DAQ) to allow control through LabVIEW. Captured images are saved as *.tif* files using IMAQ provided from the NI Vision Development Module.

During acquisition, the cameras are cooled to -45°C. If lab temperatures exceed 70°F, use cameras only at -25°C operating temperatures. Images are taken at 100 ms exposure times, with 16-bit depth.

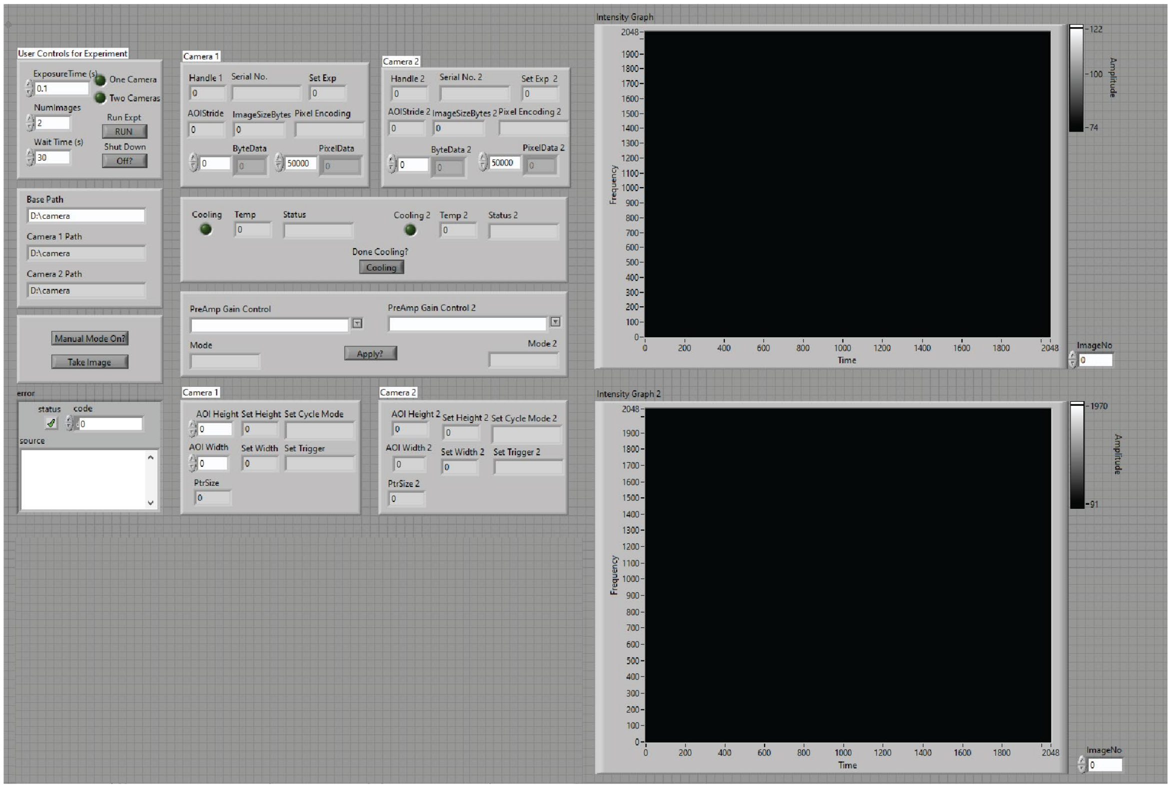

User Controls for Experiment
ExposureTime (s): 0.1
NumImages: 2
Wait Time (s): 30

Base Path: D:\camera
Camera 1 Path: D:\camera
Camera 2 Path: D:\camera

Camera 1
Handle 1: 0
Set Exp: 0
AOIStride: 0
ImageSizeBytes: 0
ByteData: 0
PixelData: 50000

Camera 2
Handle 2: 0
Set Exp 2: 0
AOIStride 2: 0
ImageSizeBytes 2: 0
ByteData 2: 0
PixelData 2: 50000

Temp: 0
Temp 2: 0

error
code: 0

Camera 1
AOI Height: 0
Set Height: 0
AOI Width: 0
Set Width: 0
PtrSize: 0

Camera 2
AOI Height 2: 0
Set Height 2: 0
AOI Width 2: 0
Set Width 2: 0
PtrSize 2: 0

ImageNo: 0
ImageNo: 0

Figure 4-9. LabVIEW code interface for two camera image acquisition.

4.7.c.2 Data Processing within ImageJ and MATLAB

Data processing is done in part with ImageJ plugins and MATLAB. ImageJ plugin, StackReg[264,265] is used to correct X- and Y-axial drift. Droplet identification is performed using TrackMate.[42,43] Regions of interest (ROIs) that correspond to the fluorescent droplets within an image are identified and labeled. A .csv file of labeled positions is output and can be used within a custom-written MATLAB code for further processing and anisotropy calculations.

MATLAB image processing includes calculating and applying a registration to transform the perpendicular channel to match the parallel channel. When working with diffraction-limited spots, it is imperative that an accurate registration is applied, as the difference in one pixel can drastically change the anisotropy value. Spatially resolved images of fluorescent beads or fluorescent nanodiamonds can be used to determine the registration needed to match the pixels positions of the two emission channels. To calculate the registration transform, the Registration Estimator App in MATLAB (‘registrationEstimator’) is used. This provided more accurate registrations than previous techniques used, and details about previous registration techniques can be found in reference.[124]

After identifying ROIs and registering images, the intensities within the ROIs are determined and used to calculate the average anisotropy (Equation 4.3) within a droplet at that frame. A local background subtraction can be applied to each ROI allowing for correction of the intensity measured prior to calculation of anisotropy.

4.7.c.3 G Factor Calculations

A correction factor is applied to the anisotropy calculation, known as the G factor, which corrects for instances where an artificially high or low anisotropy value is measured due to differences in the optical paths. The G factor is generated by using images taken of a standard solution of oxazine-170 perchlorate (Sigma Aldrich), following a modified version of a previously published method.[17] Oxazine-170 solutions are prepared in water and sonicated for a minimum of 1 hour to allow dye to fully dissolve. Oxazine-170 solutions should appear pale blue in color.[ix] Solutions are imaged within a silicone well (Grace Bio-labs) adhered to a glass coverslip. It is critical that no aggregates or single molecules appear on the surface, as those will produce inaccurate measurements due to impaired rotational dynamics.

$$r = \frac{r_0}{\left(1 + {}^{\tau}\!/_{\theta}\right)} \tag{4.4}$$

$$G = \frac{(1 - r)I_{\parallel}}{(2r + 1)I_{\perp}} \tag{4.5}$$

Using the known rotational correlation time (θ), fluorescence lifetime (τ), and fundamental anisotropy (r_0) for oxazine in water,[266] the steady state anisotropy (r) of oxazine is determined using Equation 4.4. The steady state anisotropy can then be used to calculate the G factor using Equation 4.5. The G factor can then be calculated either as an average value of the whole field of view for the camera or for each pixel individually.

4.7.c.4 Considerations for Future Data Processing

Future improvements should consider integrating localization software aimed for super-resolution single-molecule data. One method that allows super-resolution is single-molecule localization microscopy (SMLM).[267–273] SMLM methods use widefield excitation and achieves super-resolution by localizing individual molecules with spatially resolved point-spread functions (PSFs) to Gaussian-shaped spots. The software developed for SMLM can be used to identify and confirm the presence of diffraction limited droplets. There is a variety of software available for use[274–276] and one specific set of ImageJ plugins that

---

[ix] You need very little oxazine to make a stock solution, the *dusting* on a glass pipette is more than enough to result in a concentrated solution for these purposes. Wait until after sonication to add more solid if the solution does not appear pale blue.

can be used is the GDSC Single Molecule Light Microscopy ImageJ Plugin.[277] These plugins can be used for droplet localization and fitting of a 2D Gaussian (Equation 4.6) to determine the full-width at half-maximum (FWHM) of the emission from the droplet. It is important to consider the effects of nanoscale drift present in videos which can cause spreading of the PSF providing inaccuracies in calculation of the FWHM.[278]

$$f(x,y) = Aexp\left(-\left(\frac{(x-x_0)^2}{2{\sigma_x}^2}+\frac{(y-y_0)^2}{2\sigma_y^2}\right)\right) \tag{4.6}$$

In Equation 4.6, A is the amplitude of the Gaussian, x_0, y_0 are the centers of the Gaussian, and σ_x, σ_y are the widths of the Gaussian. Droplets that are diffraction-limited in size will appear similar to fluorescent single molecules on the microscope. As opposed to a single fluorophore, the droplets contain many fluorophores and therefore will not “blink” or bleach in single steps. Photobleaching of droplets will follow an exponential decay. If the droplets are below the diffraction limit in size, then the FWHM measured should be equal to the theoretical diffraction limit for the emission of a PDI molecule.

Chapter 5 Investigation of Noncovalent Fluorous Interactions using Single-Molecule Fluorescence

5.1 Introduction

Single-molecule investigations of chemical reactions or biological systems require immobilizing the molecule of interest within the excitation volume of the laser. The immobilization technique should be stable and robust for the timescales of the experiment, and most importantly the technique should not impact the activity of the immobilized molecule.

Passivation of surfaces is a common technique used to immobilize molecules. Common passivation techniques for single-molecule studies of biological molecules includes coupling fluorophores or molecules of interest to a surface using polyethylene glycol (PEG)-biotin[279] and/or biotin-streptavidin complexes.[280,281] Other routes include encapsulating fluorophores and molecules within vesicles which are then immobilized onto the surface.[282,283] In Chapters 3 and 4, we use this concept for monitoring polymerizations within organic droplets. Molecules can also be covalently attached to surfaces using click chemistry and formation of disulfide-bridges.[284] In catalysis, molecular catalysts are covalently attached to surfaces and nanoparticles, thereby "heterogenizing" them. These surface-supported catalysts can maintain or even see increased catalytic activity while obtaining benefits such as minimal catalyst leaching, ease of recyclability, as well as recovery of catalyst species.[285–288] However, there are instances when covalent attachments of catalysts to surfaces can fail based on reaction conditions, as shown in the investigation of initiation dynamics of single surface-supported Pd-PEPPSI catalyst.[60]

An alternative route for immobilizing catalysts can be through non-covalent interactions between a fluorine-passivated surface and a fluorine-labeled molecule. The concept of this technique is based on biphasic catalysis, where perfluoro-tagged catalysts are separated from organic products easily using fluorous solvents.[289,290] Fluorous-surfaces or supports, such as fluorous reversed-phase silica gel,[291] have been developed as alternatives for perfluorinated solvents. This allows for the ease of separation and recovery of catalysts without the use of perfluorinated solvents which have environmental concerns. This technique has been used for the immobilization of palladium complexes on fluorous reverse-phase silica gel, resulting in comparable catalyst activity, minimal catalyst leaching and ease of recyclability of the catalyst.[217] Additionally, there has been development of various other fluorous-tagged catalysts, including platinum,[292] nickel,[293] ruthenium complexes,[294] and other palladium complexes.[295,296] This concept has also been used to create carbohydrate or protein microarrays, indicating that fluorous-tagged molecules strongly adhere to fluorous-specific sites on glass surfaces.[218,297–300] Despite the many uses of this immobilization technique, it is not clear whether the fluorous-tagged molecule is truly immobile within the fluorous-surface, specifically whether the interactions between the molecule and surface would render the molecule embedded or diffusive throughout the fluorous-surface. Any immobilization technique can potentially affect the dynamics of an immobilized molecule,[280,301] therefore a full understanding of the interactions at these surfaces is necessary to confidently use this fluorous-based immobilization method for either catalysis or biological microarrays.

Fluorescence microscopy is one method to investigate the dynamics at these surfaces. As it offers a real time *in situ* measurement to investigate the immobilization or diffusion of fluorous-fluorophores within a fluorous-glass surface. Preliminary investigations of the interactions between fluorous-molecules and fluorous-surfaces were conducted via two different optical measurements, which probe the diffusion dynamics of fluorous-fluorophores within a fluorous-surface. Fluorescence recovery after photobleaching (FRAP) and single particle tracking (SPT) were attempted to monitor the diffusion of two novel fluorous-tagged 4,4-difluoro-4-bora-3a,4a-diaza-s-indacene (BODIPY) compounds with a glass surface functionalized with 1H,1H,2H,2H-perfluorodecyltriethoxysilane (PFDS), **Figure 5-1**. The fluorous-green BODIPY (2G) is used for FRAP experiments, while the fluorous-red BODIPY (2F) is used for SPT experiments. The diffusion of these fluorophores will indicate the rigidity of the fluorous interactions.

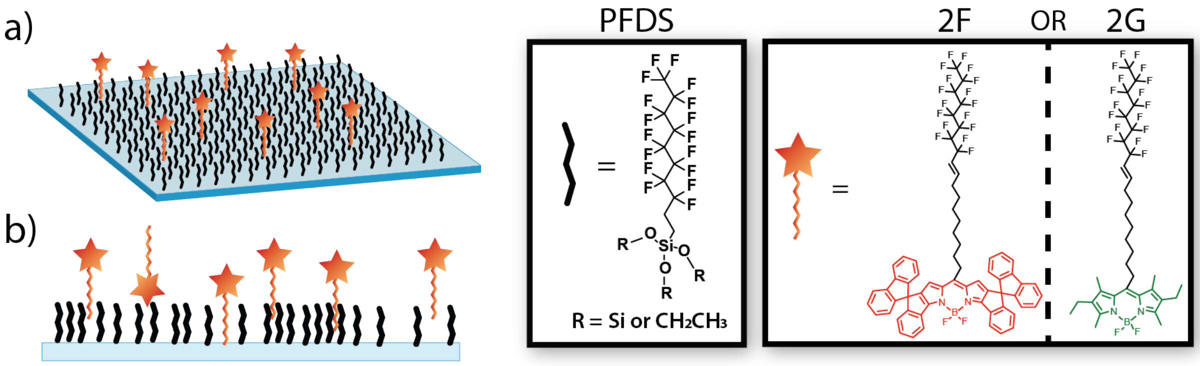

Figure 5-1. Illustration of interaction between fluorinated BODIPY molecules and perfluorinated surface (a) Top view and (b) side view.

The random movement of particles within a solution is described as Brownian motion. This movement is caused by collisions and interactions with other molecules in solution. Cases where the motion of molecules deviate from Brownian motion is referred to as anomalous diffusion, of which there are two types: superdiffusion or subdiffusion. This can also be referred to as confined or directed motion. One way to describe or quantify these different types of diffusion is through calculating the mean-squared displacement (MSD), which is the average displacement or change in position of a molecule. It is defined by the following equation, where $x_0$is original position and x is the position after some time:

$$MSD = < (x - x_0)^2 > \tag{5.1}$$

You can relate the MSD to the 2D diffusion coefficient of a molecule by equation 2.

$$MSD = 4Dt^a \tag{5.2}$$

where D is the diffusion coefficient and t is the time. The constant a changes depending on the type of diffusion. For Brownian motion a is 1, resulting in a linear relationship between MSD and time. For instances of directed motion, such as active transport, $a > 1$. In instances where the diffusion of molecules is impeded, such as crowded environments, $a < 1$.[302] 3D diffusion is defined by $6Dt^{a}$.

FRAP, as introduced in Chapter 1, determines the diffusion of molecules using a layer of fluorescent molecules. A spot within that layer is photobleached with a high intensity laser. The sample is then monitored optically to observe the recovery of fluorescence within the photobleached area as the photobleached molecules diffuse away and still-fluorescent molecules diffuse in. The rate of recovery in fluorescence is correlated to diffusion coefficients and this can be calculated using various programs.[303,304]

To further understand the interactions between the fluorous-molecules and surface, we employ single particle tracking (SPT), also introduced in Chapter 1. It is a fluorescence microscopy technique that captures images or videos of single molecules over extended periods of time. Molecules are then identified, localized and then their positions are connected throughout the video or series of images to create trajectories. These trajectories then can be related to the diffusion coefficient of the molecule using MSD curves. This can be accomplished either with self-written code or using open-source programs available for ImageJ.[42,43] Both techniques can be used to elucidate valuable information regarding the strength of fluorous-interactions for immobilization.

5.2 Fluorous-Fluorophores

A BODIPY fluorophore was chosen for the experiments above, partly because they exhibit strong photostability. There are established synthesis procedures within the group for both green and red BODIPY derivatives. To create the fluorous-tagged versions, **Schemes 1 and 2**, the BODIPY-moieties undergo a cross-coupling reaction catalyzed by Grubbs Generation II catalyst (GG2).[305,306] The red BODIPY has been chosen for the single particle tracking experiments as the excitation and collection wavelengths allow for less fluorescent impurities, often excited by blue/green wavelengths of light. The $–(CF_2)_7CF_3$ tail is comparable to the fluorous-labels used in the fluorous-based microarrays as well as the Pd-catalysis immobilization.[217,218,298] Therefore, these fluorophores should be good test molecules to investigate fluorous-interactions.

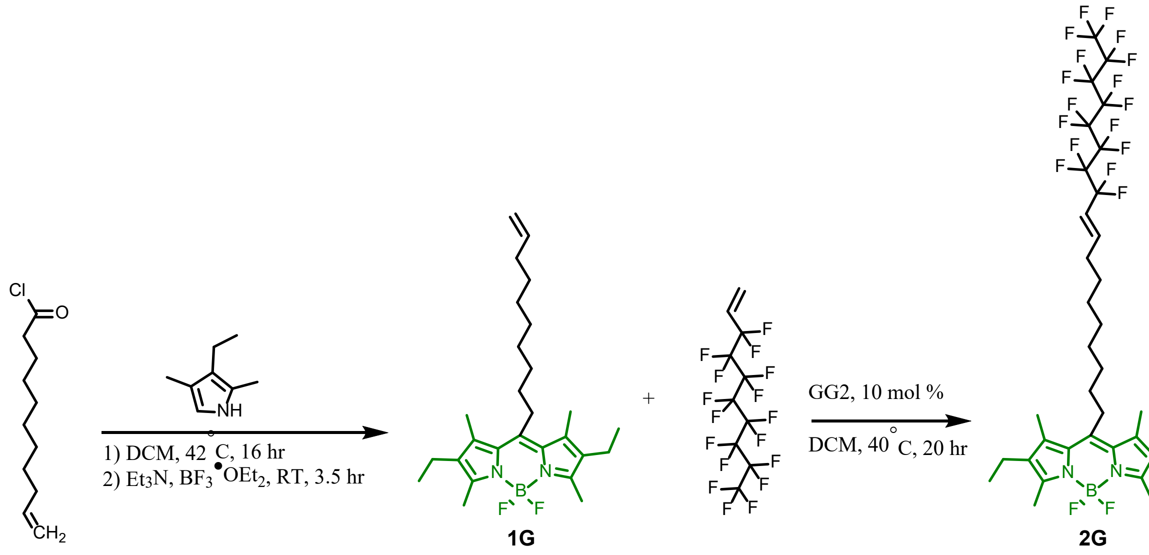

Scheme 5-1. Synthesis of green fluorous-BODIPY, 2G.

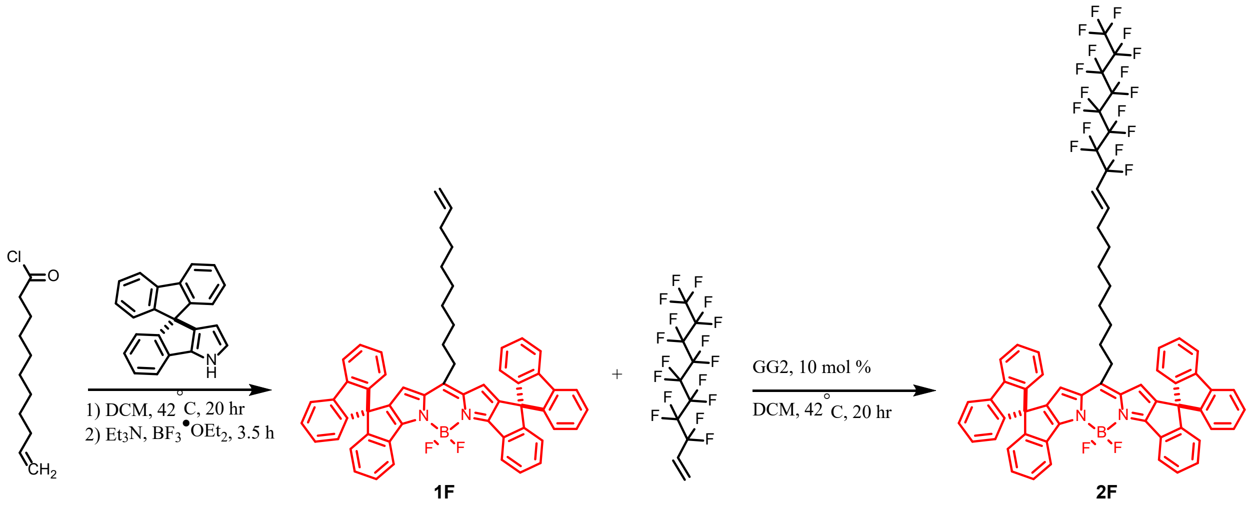

Scheme 5-2. Synthesis of fluorous-BODIPY, 2F.

5.3 Fluorous-functionalized Surface

There are many versions of fluorous-functionalized surfaces with various substrates and fluorous-component combinations. Transparent surfaces are necessary for fluorescence experiments, particularly with those in solution, therefore initial experiments have been done on functionalized glass surfaces, i.e. coverslips, which can be functionalized using silanization. This type of chemistry been used previously in the Goldsmith group to investigate the heterogeneity of binding at silica surfaces.[61] Silanization uses a molecule with silicon bound to either methoxy-, ethoxy-, or chloro-groups which can attach to glass through condensation reactions that occur with the surface. This chemistry depends on the presence and availability of silanol (SiOH) groups of the glass, which can vary depending on preparation, but typically features 4-5 hydroxyl groups per nm^2.[307] The use of aggressive cleaning procedures, such as a Piranha etch, allows access and formation of the silanol groups prior to functionalization. After cleaning, the surfaces are then exposed to the silane for functionalization. Finally, surfaces are thermally annealed to cause adhered silanes to condense and form covalent surface linkages.

Our glass surfaces are functionalized with PFDS, **Figure 5-1**. PFDS has a comparable fluorine concentration to the fluorous-surfaces used in the literature,[217,218] making it a relevant surface for fluorous-interactions. Formation of a PFDS monolayer on a glass surface has proven difficult, with various functionalization procedures attempted, listed in Section 5.8.a. Both coverslips and coverslip-chambers have been functionalized with PFDS.[x] While functionalization of the surface with PFDS has confidently been performed, the generation of a homogeneous surface has not yet been achieved.

5.4 Optical Set Up

5.4.a FRAP with 2G

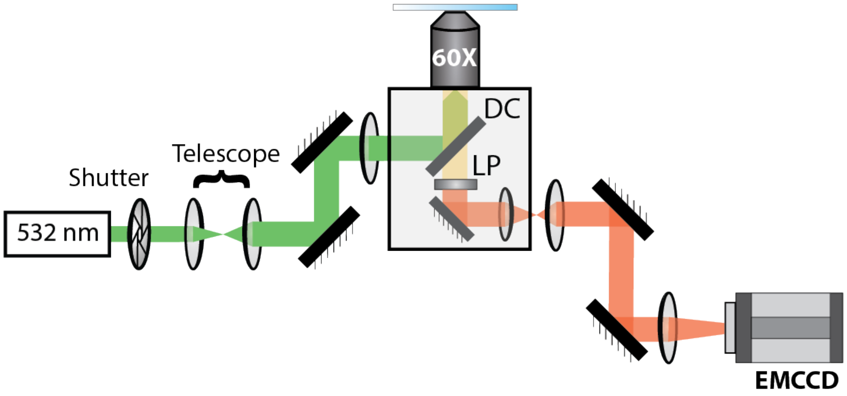

Figure 5-2. Optical microscopy setup for FRAP experiments.
60X Oil TIRF objective, DC = 532 nm dichroic, LP = 532 nm long pass filter.

Imaging and bleaching of sample were performed using a 532 nm laser (Coherent, 80 mW). Imaging was done using a widefield lens while bleaching was performed using the focused beam at full power. Light was guided to the sample using a Nikon 60x Apo TIRF 1.49 oil-immersion objective on a Nikon Eclipse Ti inverted microscope. The fluorescence is collected through the same objective, passed through a 532 nm dichroic mirror (Semrock, RazorEdge) and a 532 nm long pass filter (Semrock LP03-532RU-25). The

---

[x] Details on chamber creation can be found in Section 3.4.b.

fluorescence was focused onto an Andor iXon EMCCD camera. Sample illumination was controlled using a Uniblitz shutter. Images were taken at 100 ms exposure times, with gain set to 300 using Andor Solis software.

5.4.b SPT with 2F

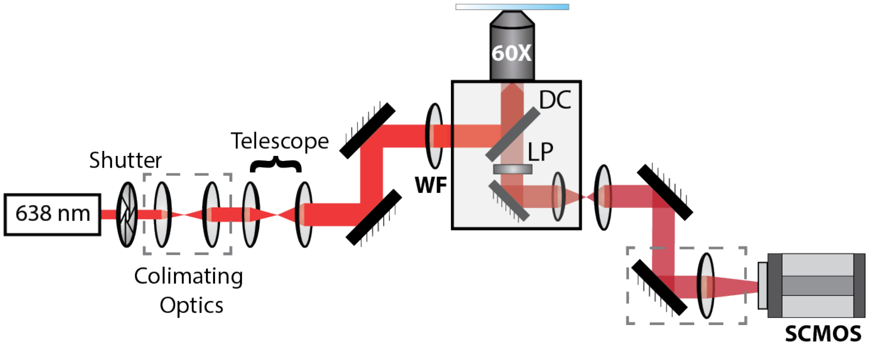

Figure 5-3. Optical microscope set up for SPT experiments.
60x TIRF oil objective, WF = widefield lens, DC = multi-edge dichroic, LP = 635 long pass filter.

Single particle tracking imaging was performed using the optical set up in **Figure 5-3**, with a 638 nm laser excitation source (LaserTack, 50 mW). Additional lenses are introduced in the beam path to collimate the beam prior to expansion with telescope lenses. Widefield excitation is used. Light is directed to the sample using a 60x oil immersion objective (Nikon, TIRF 1.49NA) on a Nikon Eclipse Ti-E inverted microscope with perfect focus system. Fluorescence is collected by the same objective and passed through a multi-edge dichroic (Semrock Di01-R405/488/532/635-25x36), and a 635 nm long pass filter (Semrock, EdgeBasic). The light is then focused onto an Andor SONA sCMOS camera. Laser illumination is controlled by a Uniblitz shutter. Images are taken at exposure times varying from 30 to 50 ms using Andor Solis software.

5.5 Preliminary Results of Diffusion Experiments

5.5.a FRAP Results

For FRAP experiments, 300 µL of 0.5 mM 2G solution in HPLC isopropanol (IPA) was deposited into PFDS chambers (Made with 30 mM PFDS/IPA, see Section 5.8.a for specific details regarding functionalization). The 2G solution was then removed and the chamber was rinsed 6x with HPLC IPA. Chambers were imaged with 200 µL of HPLC IPA.

Preliminary FRAP experiments were performed. Some experiments showed overall photobleaching of the entire area while other experiments showed recovery of fluorescence. One experiment shows some recovery of fluorescence over 40 minutes, **Figure 5-4**. However, there were issues with focal drift which caused fluctuations in the fluorescence signal as well as prevented collection of longer time points. The focal drift issues can be alleviated with the new optical set up present for the SPT experiments, as switching to the Nikon Eclipse Ti-E microscope with a perfect focus system keeps the sample within the focal plane of the objective indefinitely. As these experiments were preliminary, it is difficult make definitive conclusions regarding the diffusion of 2G, however these initial results do suggest that diffusion is present on the PFDS surface.

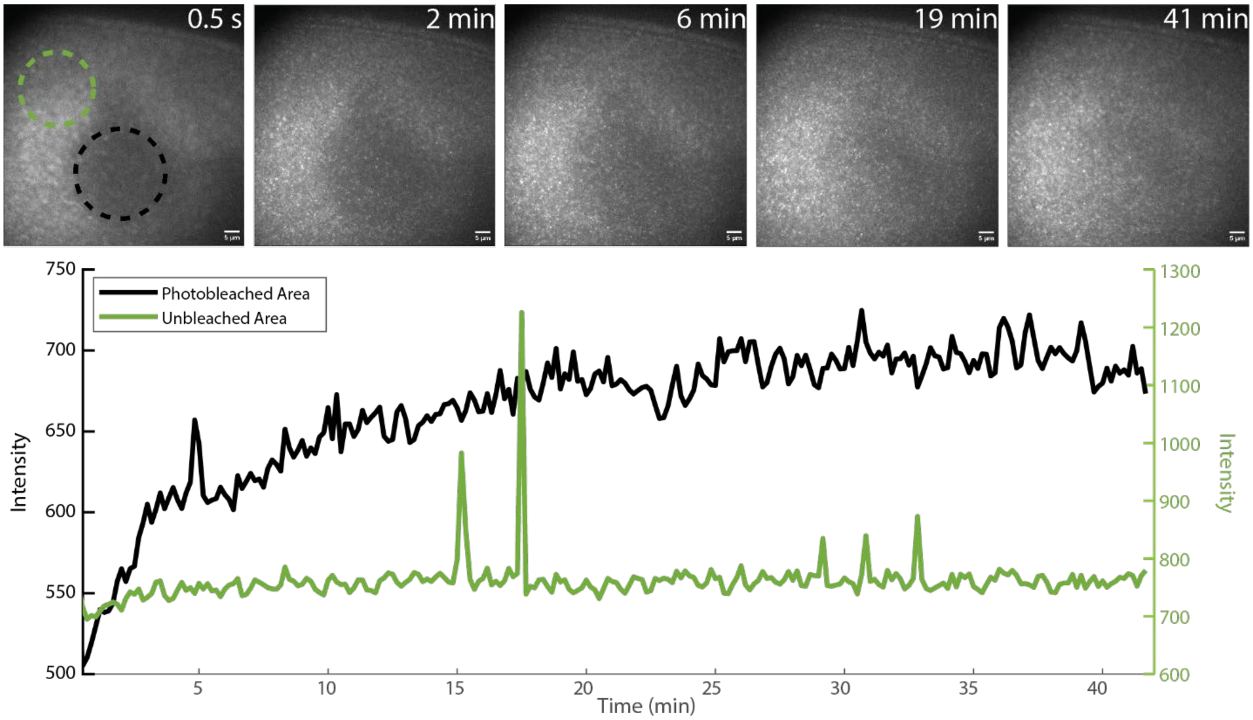

Figure 5-4. FRAP experiment with 2G.
(top) Fluorescence images after photobleaching at various time points (bottom) Intensity traces of photobleached are (black) compared to adjacent non-photobleached area (green) over 40 min.

5.5.b SPT Results

For SPT experiments, 600 µL of 8 nM 2F solution in distilled toluene (Optima) was deposited into the SPT chambers (2 mM PFDS). BODIPY solution was removed, and the chambers were rinsed and then 600 µL of distilled Optima toluene was used for imaging. (Toluene distillation is described in Chapter 3).

Preliminary SPT experiments were conducted, which showed fluorophores on surface, with varying dynamics. Some spots appeared stationary and immobilized on the surface, while others moved across. In **Figure 5-5**, we see both of these dynamics, with an immobilized fluorophore at the top of the image, and a diffusing fluorophore at the bottom in the red box. These images were taken at 100 ms exposure, which is too slow to capture dynamics of free diffusion. Therefore, the fluorophore moving at the bottom must interact with the surface in some way that causes sticking at certain points, but not rigid enough to cause full immobilization.

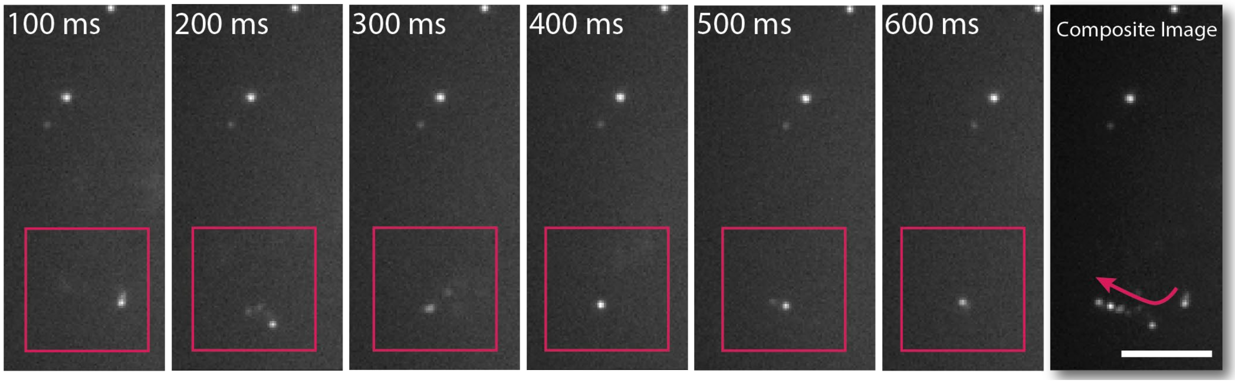

Figure 5-5. Fluorescence images of diffusion of single 2F BODIPY on 30 mM PFDS/IPA surface over 600 ms, 5 µm scale bar. Composite image of the combined previous frames shows the trajectory of the single molecule.

Single particle tracking is not possible at this exposure time (100 ms) as blurring of the point spread function (PSF) is observed (**Figure 5-5**, t = 200ms, 300ms, and 500ms). Therefore, the experiment was repeated at faster exposure times (45 ms). This change reduced the blurring significantly and allowed for the trajectory of some spots to be determined using TrackMate, **Figure 5-6**. Calculating the diffusion constant or mean-squared displacement was not possible at this time. 45 ms is still significantly slower exposure time compared to what is used for free diffusion, around 10 ms. However, these initial experiments show that there are some fluorous-fluorophore which are able to move around and interact with the surface while others stay immobilized in one spot.

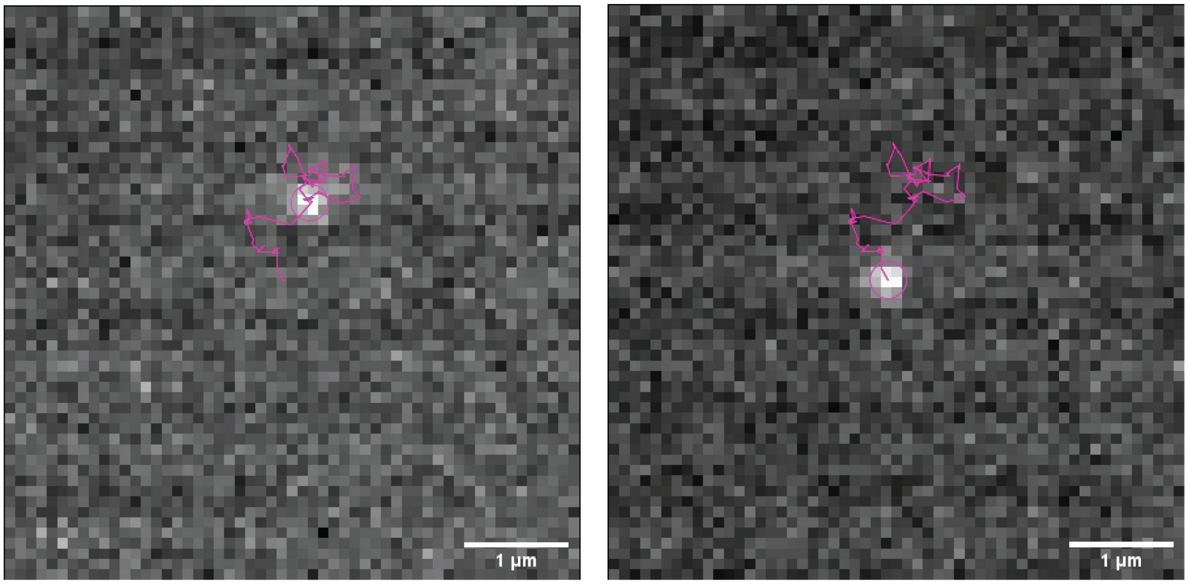

Figure 5-6. Trajectory of single 2F molecule on PFDS surface.
Fluorescence image of single 2F molecule on PFDS surface at beginning (left) and end (right) of a trajectory as determined by TrackMate software (pink line).

A few control experiments were performed to investigate the difference in behavior observed. The first was to investigate if the differences in dynamics were caused by the fluorous-tag in 2F. This was first attempted by comparing the deposition of 1F (precursor to 2F) and 2F BODIPY compounds on a PFDS surface, **Figure 5-9**. The concentration of both BODIPY compounds should be on the nM scale in these experiments, although exact concentrations are unknown. The precursor BODIPY 1F seems to adhere and stick to the surface better through the washing steps than the 2F BODIPY, as there is a greater density of fluorescent objects observed on the surface with 1F deposited. It should be noted that as the exact concentration is not known, it is not possible to conclusively say that the density is greater due to surface interactions. In these samples, 1F and 2F both exhibit mixes of diffusion and sticking. As these are preliminary experiments, the difference in diffusion between them has not been quantified. Further investigation is needed to confirm that both molecules show the same exact diffusion.

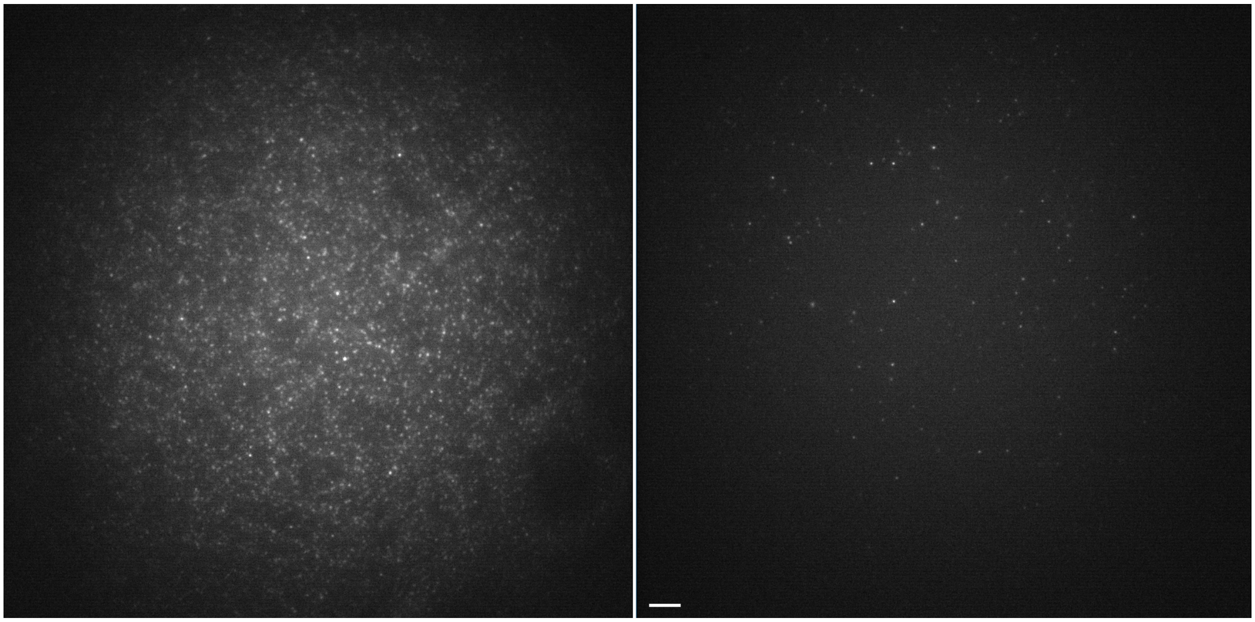

Figure 5-7. Fluorescence Images of 1F BODIPY (right) vs 2F BODIPY (left) on 30 mM PFDS/IPA surface.

To further complicate the above measurement, the 1F BODIPY core features 2 fluorine atoms. It was unsure if those F-atoms would be enough to cause a propensity for the BODIPY to adhere or interact with the surface. Additionally, it was not clear if having two separate fluorine sites in the 2F BODIPY could cause differences in the diffusion dynamics. To investigate this, 2 additional BODIPY molecules were synthesized in the group by Dr. Michael Aristov, which featured propyl groups replacing the fluorine atoms in the BODIPY cores. The structures and deposition of these molecules is shown in **Figure 5-8**. The protected analogue of the 1F BODIPY is labeled 1, while the protected analogue of the 2F BODIPY is labeled 2. The concentrations of all solutions were estimated to be around 100 nM, though bulk fluorescence experiments should be conducted to confirm and determine exact concentration. This initial experiment showed sticking of all BODIPY molecules, with the density of molecules varying with each structure. As with previous experiments, combinations of sticking and diffusion were observed. Without additional replicates is not possible to determine any conclusive statements regarding dynamics. However, the sticking of all the BODIPY molecules does indicate either an issue with deposition of the dye or an issue with surface composition.

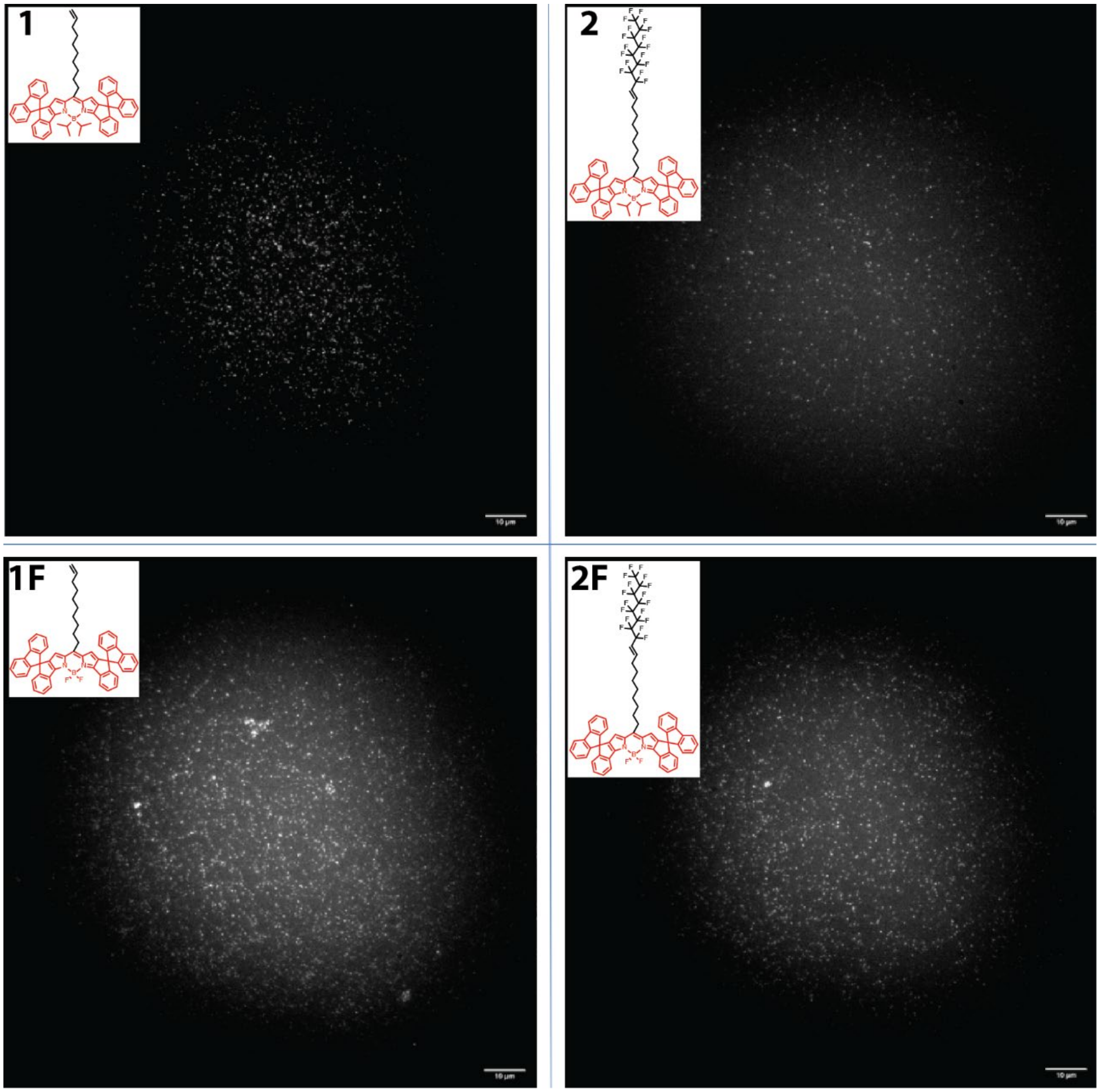

Figure 5-8. Fluorescence images of various BODIPY molecules on 1 mM PFDS/Toluene surface (Piranha Etch). BODIPY compounds 1 and 2 feature protected BODIPY cores, where F-atoms are replaced with propyl-groups. They are also analogues of 1F and 2F BODIPY compounds respectively.

To further explore if the initial results are a cause of BODIPY deposition or surface functionalization, BODIPY 2F was imaged on a non-functionalized surface and compared to a PFDS surface, **Figure 5-9**. It was observed that while the same concentration of 2F was deposited in both, the non-functionalized plain chamber seemed to have more objects adhered to the surface. This is strange as the 2F BODIPY is expected to have a higher affinity to the PFDS surface as compared to just the glass surface. Additionally, it was observed that both surfaces showed molecules sticking and possible diffusion.

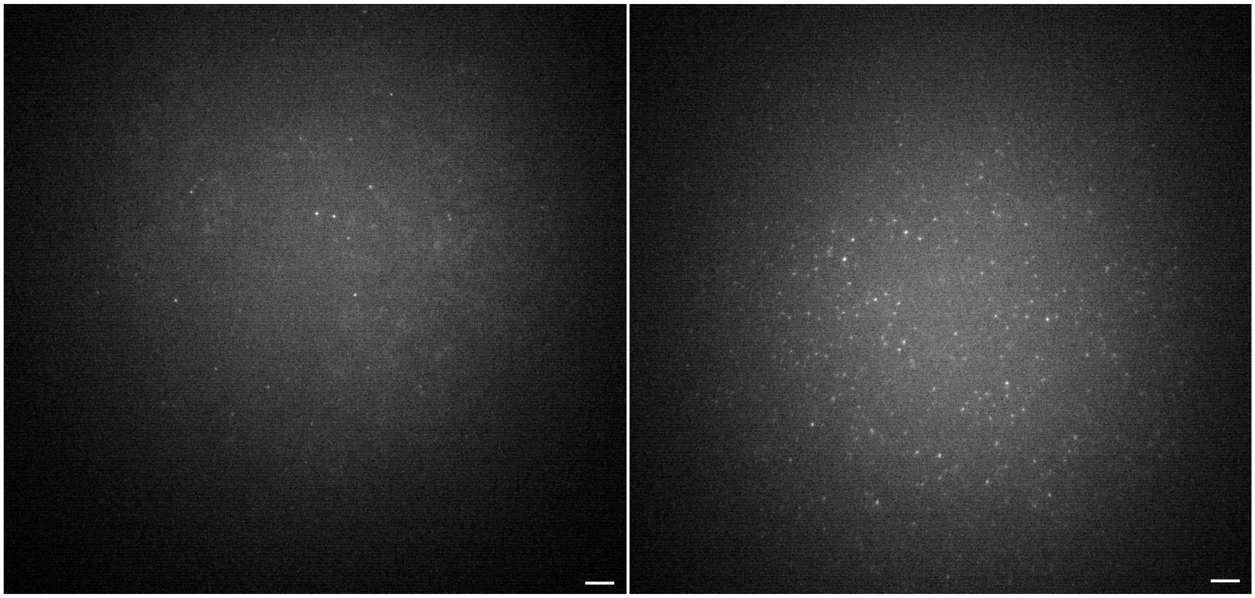

Figure 5-9. Comparison of 1 µM 2F deposition on 30 mM PFDS/IPA chamber (left) vs Plasma Cleaned plain chamber (right).
Scale bar 5 um.

Given the resulted listed above, it was clear that more characterization was required for the PFDS surfaces, to confirm the creation of a homogenous and uniform surface. A strange phenomenon which was observed on the PFDS surfaces when illuminated with white light (bright field) is the presence of small circular objects that appeared similar to small droplets generated in Chapter 4, **Figure 5-10** and **Figure 5-11**. These objects appeared only on PFDS surfaces and would vary in size and shape, and they were present regardless of functionalization procedure followed. To further understand the surface and these objects we turned to surface characterization techniques such as contact angle measurements and Atomic Force Microscopy (AFM).

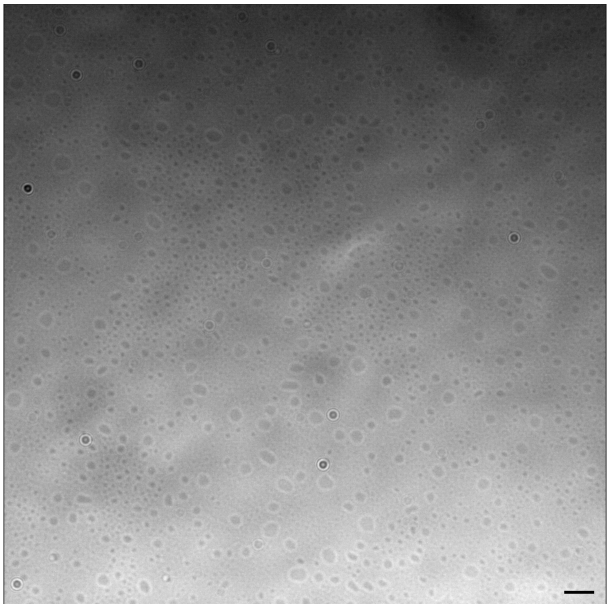

Figure 5-10. Droplet-like objects on 2 mM PFDS surface. White light illumination, 5 µm scale bar.

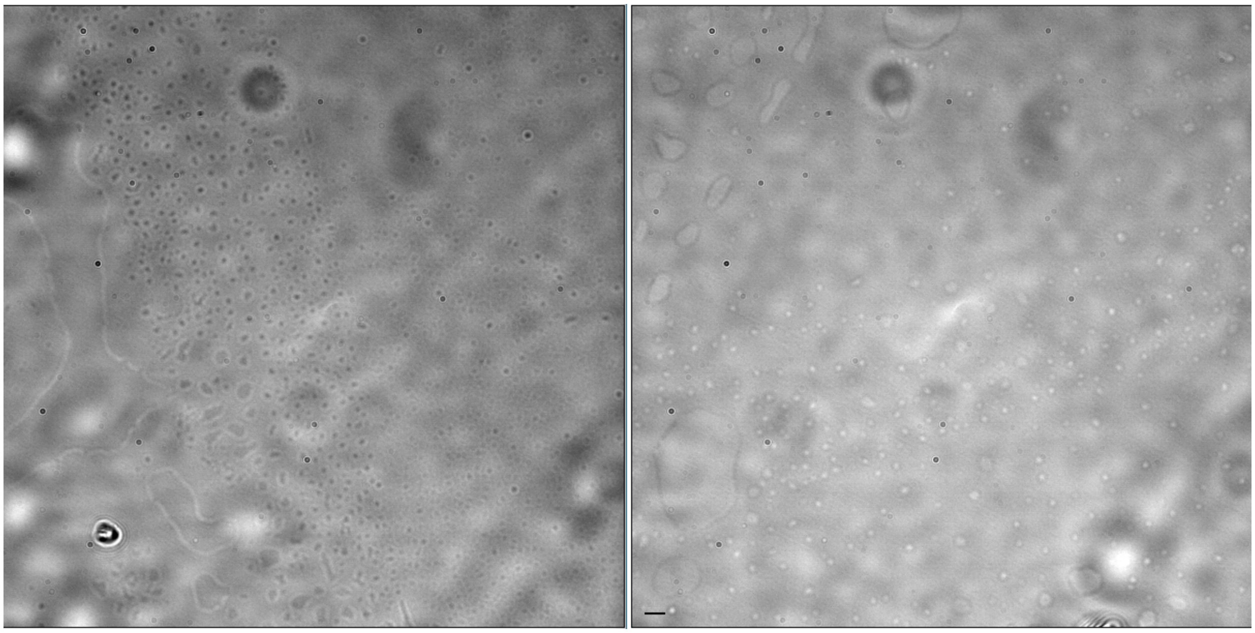

Figure 5-11. Droplet-like objects on 30 mM PFDS surface. White light illumination, 5 µm scale bar.

5.6 Characterization of Fluorous Surfaces

Surface characterization techniques, such as contact angle and AFM, can be used to confirm the formation of a fluorous-functionalized surface. Contact angle measurements are commonly used to confirm the formation of a functionalized surface. A contact angle, or wetting angle, is the angle of curvature of a liquid drop that is placed on a surface. The surface tension of the liquid in relation to the surface causes changes in the angle indicating the strength of the interactions between the liquid and surface. Multiple measurements are performed on one surface to confirm an even functionalization. The expected contact angle (θ) can determined using the Young equation:[308]

$$\gamma_{AB} + \gamma_B \cos\theta = \gamma_A \tag{5.3}$$

In this equation, γ_{AB} is the interfacial tension between the surface and liquid, γ_A is the energy of the surface, and γ_B is the surface tension of the liquid (in this case water). Using known literature values for water and fluorocarbon-monolayers, one can calculate the expected contact angle for our surfaces to be 115°.[308–310] Fluorous surfaces are generally highly hydrophobic, resulting in high contact angles for water droplets. When comparing the PFDS surfaces to unfunctionalized surfaces, we observed higher contact angles on PFDS surfaces. We also observe an increase in contact angle with PFDS deposition solution concentration, **Figure 5-12**. While the contact angles are higher for lower concentration solutions of PFDS, the only concentration that reaches close to the theoretical maxima is the 10 mM PFDS surface, however the 1 mM also seems well functionalized. However, there are inconsistencies in replicates of contact angle measurements, with some 1 mM surfaces showing low contact angles. This indicates there may need to be a careful analysis of the deposition/functionalization process of the PFDS coverslips.

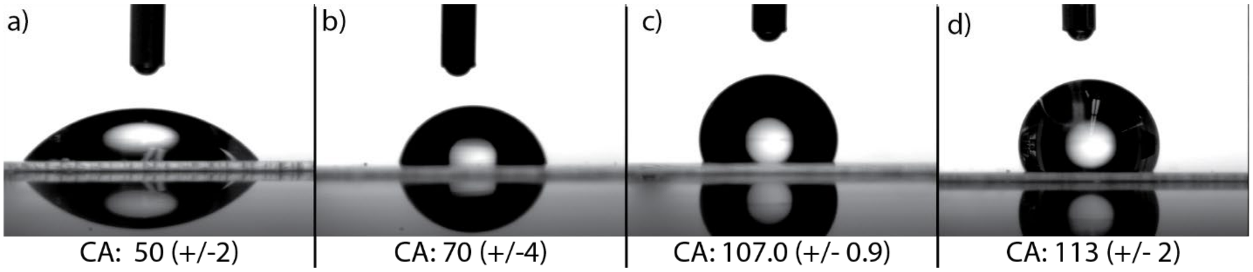

Figure 5-12. Images of 10 µL water droplet on various surfaces with calculated contact angle below. a) Plain glass, b) 10 µM PFDS with plasma cleaning, c) 1 mM PFDS with piranha etching, and d) 10 mM PFDS with piranha etching.

While this contact angle can confirm the hydrophobicity of the surface it cannot discern finer details, like the presence of a homogenous monolayer. To investigate the dynamics between the fluorous-molecule and surface it is imperative to understand the composition of the surface, i.e., monolayer *vs.* aggregates *vs.* films. More sensitive surface characterization techniques are required to identify the presence of a homogeneous monolayer, such as atomic force microscopy (AFM), x-ray photoelectron spectroscopy (XPS) and ellipsometry. However, these measurements are often performed on thick or opaque samples, such silicon wafers. This poses an inherent challenge to investigating the state of the PFDS on the glass coverslips. Ellipsometry itself is impractical to perform on thin transparent substrates, with the signal from the monolayer distorted by back reflections within the glass substrate, though it may be possible to create an opaque surface on one side of the sample to suppress back reflections using tape.[311] XPS also has difficulties isolating the signal from the functionalized-layer Si-O groups and the bulk surface Si-O groups in instances with thin films and thin substrates.

AFM was used to characterize the PFDS surfaces. AFM often is used to identify the height of a film to confirm presence of a monolayer, however using the glass coverslips makes establishing a natural contrast difficult. Therefore, surface characterization is done instead by determining the surface roughness. Roughness is the averages of the absolute values of the surface height deviations measured within a plane and is expressed by equation 3.

$$R_a = \frac{1}{N}\sum_{j=1}^{N}\left|Z_j\right| \tag{5.4}$$

In the literature roughness is usually reported as the root mean square average of the height deviations (standard deviation), expressed by equation 4.

$$R_q = \sqrt{\frac{\sum Z_i^2}{N}} \tag{5.5}$$

Homogeneous monolayers exhibit low surface roughness (R_q < 1 nm).[312] In **Figure 5-13**, AFM images of a blank coverslip are compared to two different areas from the same 1 mM PFDS surface. In these AFM images of PFDS surfaces, there are a significant number of objects on PFDS surfaces. The surface roughness varies greatly not only between different deposition techniques but even within the same coverslip.

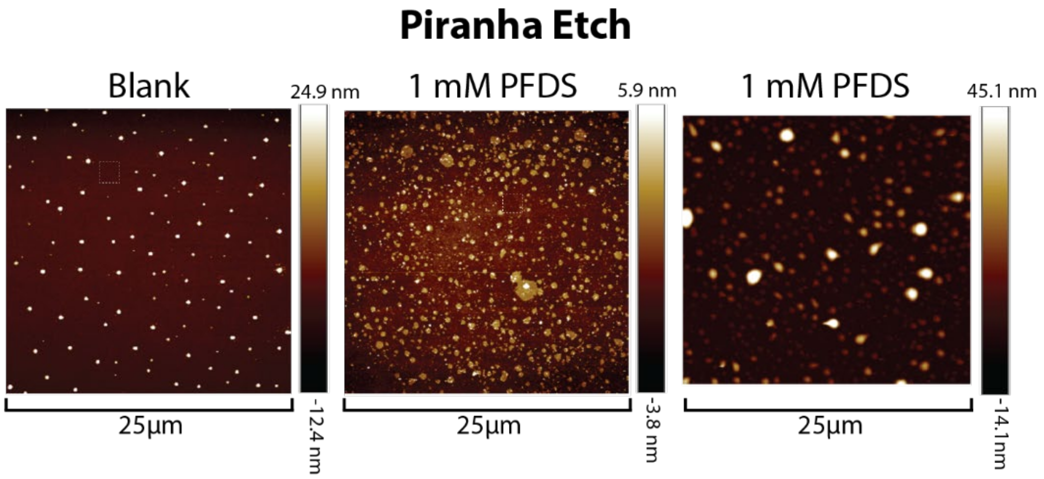

Figure 5-13. AFM measurements of (right) nonfunctionalized glass coverslip, (center, left) 1 mM PFDS surfaces. All surfaces were cleaned with piranha etch before functionalization.

Droplet-like objects are once again observed on the functionalized coverslips, similar to what was observed using optical microscopy. These objects are called “islands” in the literature, which can form on surfaces as the result of varying deposition times and potentially thermal annealing.[313,314] Varying deposition times resulted in changes in contact angle, **Figure 5-14**, however still showed droplet-like objects on the surfaces using AFM.

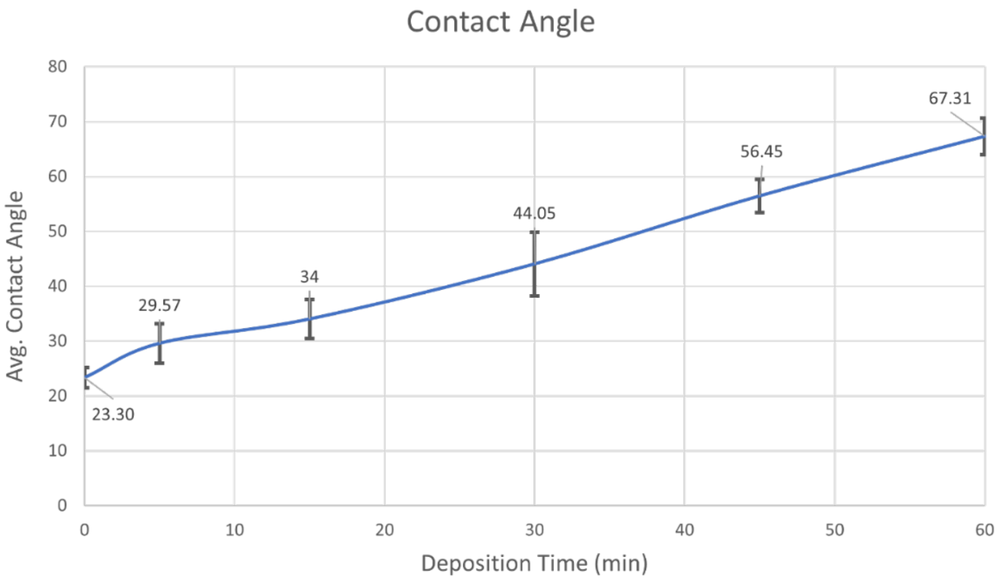

Figure 5-14. Change in Contact Angle of 1 mM PFDS coverslips (piranha cleaned) based on deposition time (0-60 min, in 15 min intervals).

There are reports of droplet-like objects on fluorous-functionalized Si-wafer surfaces in the literature, though they worked with a perfluoro-trichlorosilane compound as opposed to the triethoxysilane compound used in these experiments.[310,315] However, work done by Bunker *et al.* shows that these "droplets" may be micelles or vesicles of fluorous-silane/deposition solvent. Using AFM, they observed the formation of these droplets on surfaces at the same time scale that nucleation was observed in solution using light scattering measurements.[310] Silane degradation can occur through hydrolysis in solution, resulting in aggregates that cause solutions to appear cloudy. The amount of water present during deposition can greatly change the functionalization of a surface, along with deposition times and temperatures of thermal annealing. Bunker provides very general guidance for production of their monolayers.[310] With the inconsistencies in contact angle measurements and the observation of droplet-like aggregates on the surfaces, it is clear that a more rigorous deposition and functionalization process needs to be developed before further microscopy experiments can be performed. The heterogeneity of the surface is too large to be able to perform conclusive microscopy experiments. It may also be the reason that the same dynamics are observed regardless of which fluorophore is deposited onto the surface.

5.7 Conclusion, Future Directions and Considerations

The design and synthesis of fluorous-labeled BODIPY molecules (2F and 2G) was accomplished with a relatively straightforward cross-coupling synthesis catalyzed by Grubbs Gen. II catalyst. Preliminary investigations of fluorous-interactions between a PFDS surface and fluorous-labeled BODIPY molecules (2F and 2G) were performed. While initial experiments showed both sticking and diffusion across surfaces, more data is needed for any conclusions. High contact angle measurements support the formation of at least a partially functionalized PFDS surface. However, AFM measurements show droplet-like aggregates on the surface. Therefore, proper investigation into the dynamics between molecules and surfaces is not possible at this time due to the heterogeneity of the surface functionalization. Next steps would include tuning deposition settings to result in an even and homogenous PFDS layer on the glass surface, which could potentially include a second short heating step at high temperatures (250-300°C), as suggested by Bunker *et al*.[310] It is critical that future deposition protocols strictly control the water concentration, with minimal water content in solvents and the atmosphere. Additionally, it may be worth considering keeping samples under vacuum when not in use, to prevent interaction with atmospheric water. After confirming the production of homogeneous surfaces, then the fluorescence measurements can be repeated more rigorously to provide a full picture of any diffusion on the surface.

5.8 Experimental Details

5.8.a Functionalization of Perfluorinated Surfaces

Surfaces were functionalized with 1H,1H,2H,2H-perfluorodecyltriethoxysilane (PFDS). The general procedure consists of cleaning and preparing solution for functionalization, exposing the surface to a solution of PFDS for some time, thermal annealing at high temperatures to cause a condensation reaction at the surface and covalently attach silanes to the surface. Details regarding the various steps are listed below and a comprehensive list of deposition conditions is found in **Table 5-1**. Note that droplet formation was visible with all of these conditions.

Table 5-1. Comprehensive list of PFDS deposition conditions *Denotes surface conditions for FRAP experiments.

Etch	Concentration/Solvent	Deposition Time, Atmosphere	Sonication	Thermal Anneal (Temperature and Time)
Plasma	2 mM PFDS / IPA	1 Hour, Air	N/A	110°C, 10 min
Plasma	22 mM PFDS / IPA	1 Hour, Air	N/A	110°C, 10 min
*Plasma	30 mM PFDS / IPA	1 Hour, Air	N/A	110°C, 10 min
Plasma	75 mM PFDS / IPA	1 Hour, Air	N/A	110°C, 10 min
Plasma	Spuncoat PFDS	Air	N/A	N/A
Plasma	22 mM PFS / IPA	1 hour, Air	N/A	110°C, 20 min
Plasma	22 mM PFS / Toluene	1 hour, Air	N/A	110°C, 20 min
Piranha	10 mM PFS / Toluene	15 min, N_2	5 min – IPA	150°C, 1 hour
Piranha	1 mM PFS / Toluene	15 min, N_2	5 min – IPA	150°C, 1 hour
NaOH	2 mM PFS/ Toluene	30 min, Air	5 min – IPA	150°C, 30 min

5.8.a.1 Cleaning and Preparing Surfaces

Surfaces have been cleaned with various techniques. Regardless of which procedure is used, coverslips should be used immediately after cleaning. The first is using plasma, which is produced in our lab using atmosphere (air) as opposed to pure oxygen plasma. Plasma cleaning removes organic material on the surface, which should produce a more hydrophilic glass surface than an uncleaned coverslip. Coverslips are rinsed with HPLC methanol from a plastic bottle, Millipore water from a plastic bottle, and then HPLC methanol from a glass bottle. Coverslips are then dried with nitrogen before being placed in the plasma cleaner for 5 minutes.

The second method consists of cleaning surfaces with a Piranha solution (or piranha etch). Piranha solution is a mixture of 3:1 sulfuric acid and hydrogen peroxide. It is a strong oxidizing agent, highly acidic, and will decompose most organic molecules, and thereby cleaning surfaces from organic residue. The process also can form silanol groups on the surface of the glass, resulting in a more hydrophilic surface than prior to cleaning. It is very important to use the correct ratio of sulfuric acid to hydrogen peroxide, as an excess of hydrogen peroxide can result in an explosion. Additionally, the piranha solution will react violently with any organic solutions, possibly resulting in an explosion as well. Coverslips are cleaned in the 3:1 piranha solution for 30 minutes at 80°C, then removed and rinsed with copious amounts of Millipore water. The standard operating procedure should be followed when performing a Piranha etch.

The last cleaning process is a sodium hydroxide (NaOH) etch, performed following the procedure detailed in the reference.[218]

5.8.a.2 Functionalization and Thermal Annealing of PFDS

PFDS surfaces are formed using a solution deposition. In this step, the PFDS molecules will interact with surface silanol groups forming weak connections. The concentration of PFDS has varied from 0.1 mM to 75 mM in two different solvents, HPLC isopropanol (IPA) and dry toluene. Deposition times have varied from 5 minutes up to 1 hour. There are two main deposition procedures that have been used. The first includes dunking coverslips (sitting in a Teflon boat) into a solution of PFDS in HPLC IPA for 1 hour. The solution is exposed to air during this, which can introduce impurities. The second technique is performed within a deposition chamber, **Figure 5-15**. Coverslips (within the Teflon boat) are placed within a beaker than is inside of the deposition chamber. Vacuum is pulled and then a nitrogen atmosphere is introduced. A PFDS solution in dry toluene is syringed into the chamber and allowed to sit for 15 minutes. Afterwards the coverslips are removed and sonicated in HPLC IPA for 5 minutes.

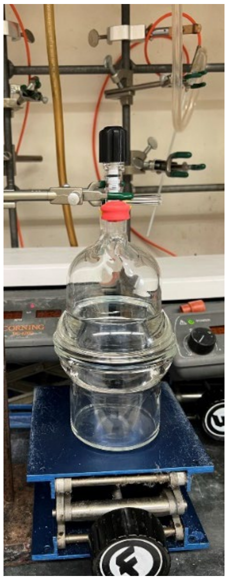

Figure 5-15. Photo of deposition chamber.
A 100 mL beaker is placed within to hold the Teflon boat with coverslips and PFDS solution for deposition.

5.8.a.3 Thermal Annealing

Thermal annealing is the last step of the functionalization process. At this step the surface is heated above 100°C causing a condensation reaction and resulting in a strong bond forming between the PFDS solution and the surface. Thermal annealing originally occurred within a 110°C oven for 10 minutes, however this is no longer suggested due to safety concerns. If the coverslip surface has not been fully dried before placing in the oven, PFDS can potentially vaporize from the surface and be a safety hazard to anyone working in the lab. Therefore, it is instead suggested to heat the surfaces on a hot plate within a fume hood. The thermal anneal step has varied from 10 min all the way to 1 hour. The most common times were 10 minutes within a 110°C oven and 1 hour on at 150°C hot plate.

5.8.b Surface Characterization

5.8.b.1 Contact Angle

Contact angle measurements were taken at the Soft Materials Characterization Lab at UW-Madison, on the Dataphysics OCA 15 Plus instrument. A 5-10 µL droplet of water is placed onto the surface by an automated syringe. An image is taken of the droplet and then processed to determine the contact angle. A list of the contact angles measured from various surfaces is found in **Table 5-2**. It is important to note that all the coverslips which underwent a PFDS deposition exhibited higher contact angles than the corresponding non-functionalized coverslips. Plain coverslips are non-functionalized coverslips that were cleaned in the same process as the functionalized coverslips prior to deposition.

Table 5-2. Contact Angle Measurements of Various Concentrations PFDS surfaces

Surface	Contact Angle (std)
Plain Coverslip – Plasma Cleaned	37° (±1)
1 µM PFDS – Plasma Cleaned	68.4° (±4)
10 µM PFDS – Plasma Cleaned	71° (±4)
2 mM PFDS – Plasma Cleaned	56.1° (±0.4)
Plain coverslip – Piranha Cleaned	50° (±2)
1 mM PFDS – Piranha Cleaned	107.0° (±0.9)
10 mM PFDS – Piranha Cleaned	113° (±2)
Plain Coverslip – NaOH Etch	34° (±4)
2 mM PFDS – NaOH Etch	76° (±16)

5.8.b.2 Atomic Force Microscopy

Atomic force microscopy (AFM) measurements were performed at the Nanoscale Imaging and Analysis Center at UW Madison a Bruker Dimension Icon AFM. Images were taken in air tapping mode using a TESPA-V2 tip probe.

Table 5-3. Roughness (R_a and R_q) for various surfaces determined from AFM

Surface	**R_a**	**R_q**
Plasma Etch – Blank	0.274 nm	0.405 nm
Plasma Etch – 1 µM PFDS	4.20 nm	7.19 nm
Plasma Etch 10 µM PFDS	1.17 nm	2.05 nm
Plasma Etch 2 mM PFDS	0.272 nm	0.213 nm
Piranha Etch – Blank	1.69 nm	4.26 nm
Piranha Etch – 1 mM	0.937 nm	1.43 nm
Piranha Etch – 1 mM	4.14 nm	7.44 nm
NaOH Etch – Blank	0.472 nm	0.870 nm
NaOH Etch – 2 mM	4.61 nm	7.66 nm

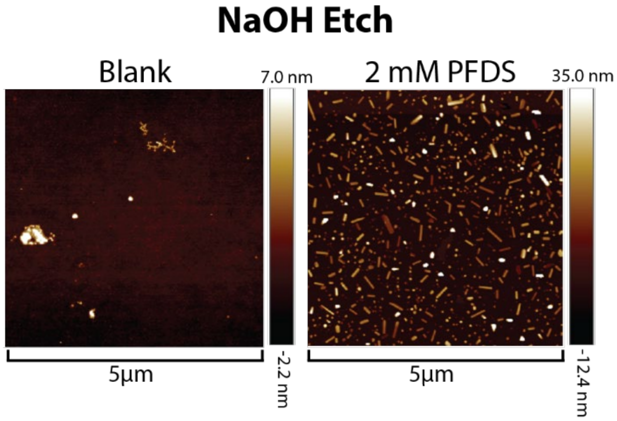

Figure 5-16. AFM measurements of (left) nonfunctionalized glass coverslip, (right) 2 mM PFDS surfaces. All surfaces were cleaned with NaOH etch.

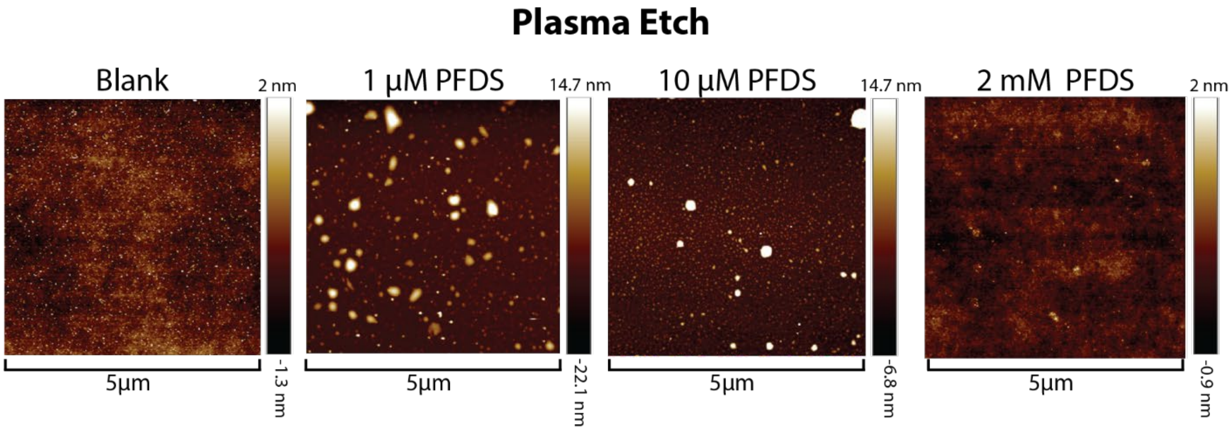

Figure 5-17. AFM measurements of nonfunctionalized coverslip, 1 µM PFDS surface, 10 µM PFDS surface, and 2 mM PFDS surfaces. All surfaces were cleaned with plasma etch.

5.8.c PFDS-Surface Stability with Base

To test the stability of the PFDS surface, plain glass coverslips as well as PFDS coverslips were both dunked into 4 mM solutions of potassium tert-butoxide (KOtBu). A qualitative measurement was performed by placing 10 µL droplets of Millipore water on both surfaces. The water droplets balled up on the PFDS surfaces prior to dunking, indicating a hydrophobic surface. On the non-functionalized coverslip, the water droplets would spread, wetting the surface and indicating that the surface was hydrophilic. The fluorous surface maintained bulk level hydrophobicity even after being in the solution for over an hour. Qualitatively, PFDS seems to resist etching by KOtBu. However, more experiments, such as quantitative contact angle measurements, as well as AFM investigation of the surface changes, are needed to confirm that the film has not been destroyed by base.

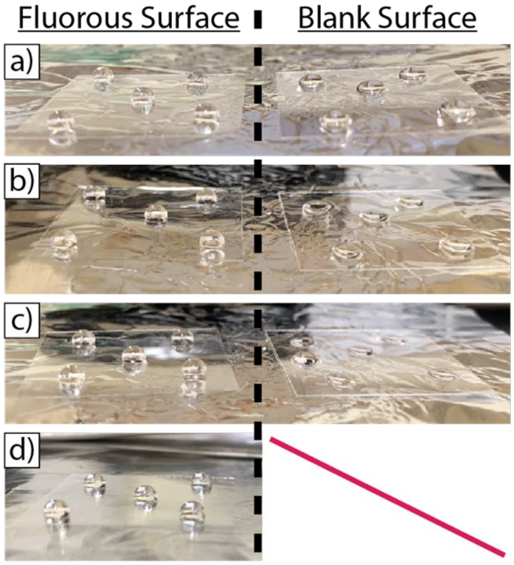

Figure 5-18. Testing stability of 5% PFDS hydrophobic surface after treatment with base.
10 µL droplets of Millipore water on fluorous coverslip (right) and unfunctionalized clean coverslip (right). a) Before placing coverslips in 4 mM solution of KOtBu and after being in the solution for b) a few seconds, c) 5 minutes, and d) 1 hour.

5.8.d Fluorescence Impurities from Deposition Process

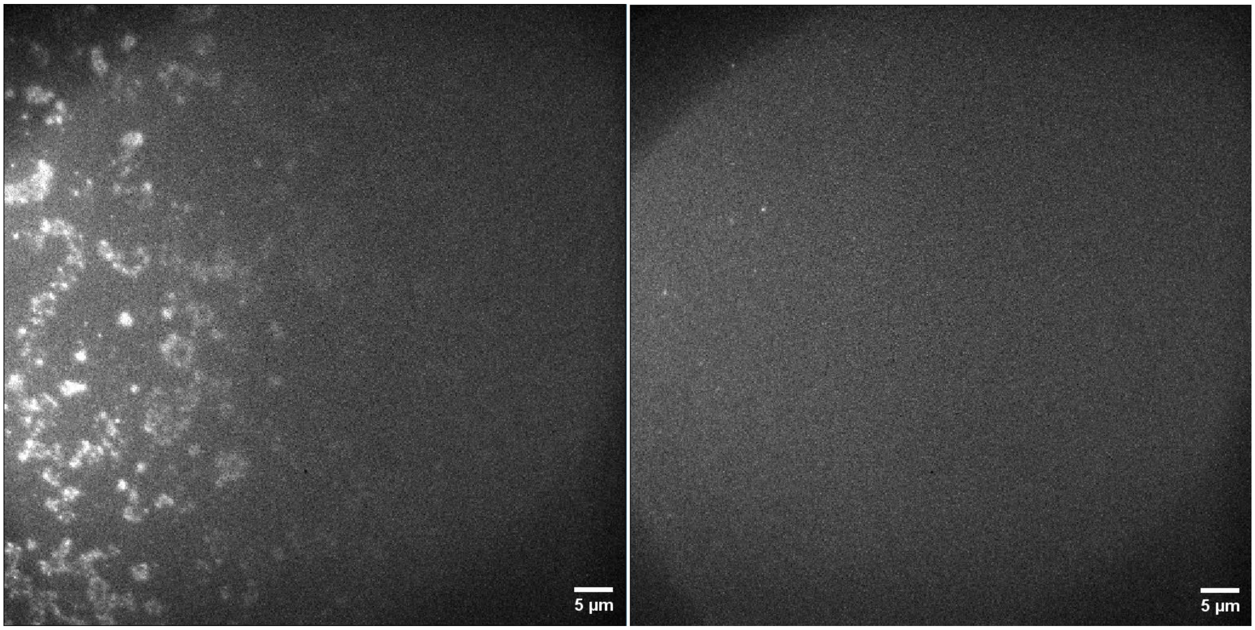

Figure 5-19. Comparison of PFDS surfaces with functionalization at elevated temperatures (40°C, left) and at room temperature (right) using fluorescence emission, 532 nm excitation.

Initial deposition of PFDS attempted heating to 40°C while the coverslips were dipped in the PFDS solution. This resulted in many fluorescence impurities appear on the surface, see **Figure 5-19**. This sample was excited by 532 nm light which will show the most fluorescence impurities. When comparing a coverslip that was functionalized in the same way except at room temperature, the same fluorescent impurities are not observed. By switching to redder excitation and collection wavelengths (>630 nm) and diligent cleaning procedures, PFDS surfaces without fluorescent impurities can be produced, **Figure 5-20**.

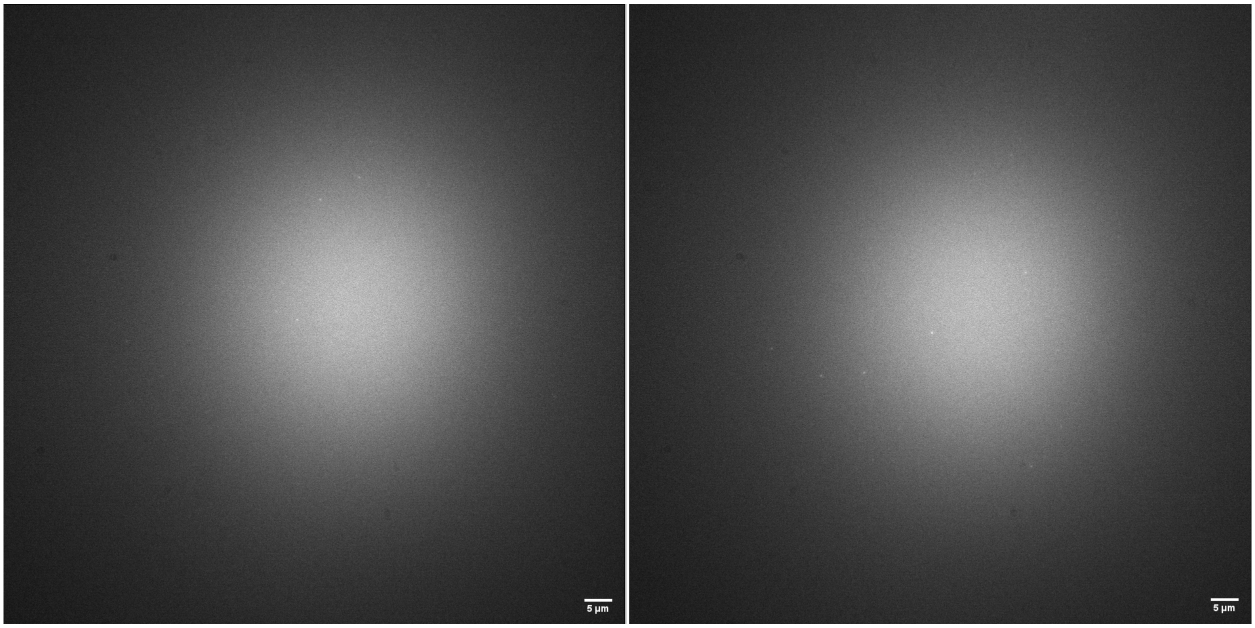

Figure 5-20. Fluorescence blank images (left) nonfunctionalized coverslip (right) PFDS surface, 638 nm excitation.

5.9 Synthetic Details

5.9.a Fluorine Labeled Green BODIPY

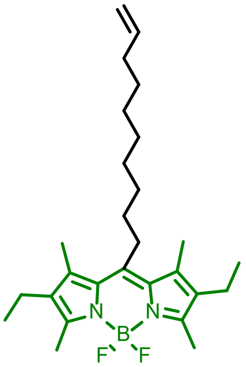

1G

Synthesis of compound 1G: Synthesized from procedure a modified procedure. This reaction was performed in an oven-dried 2-neck 250 mL round bottom flask. 3-ethyl-2,4-dimethyl pyrrole (4.9 mmol, 0.59 g) and 10-undecenoyl chloride (2.4 mmol, 0.49 g) were dissolved in dry dichloromethane (DCM, 60 mL) and refluxed under N_2 atmosphere for 15 hours. The solution was cranberry pink in color. The solution then was then cooled to room temperature. Triethylamine (Et_3N, 2 mL) was added and allowed to stir for 15 minutes; at this time the solution was yellow/brown in color. Then, $BF_3{\cdot}OEt_2$ (4 mL) was added slowly dropwise and stirred for an additional 3.5 hours still under N_2 at room temperature. The solution returned to a cranberry pink color. After 3.5 hours, solvent was evaporated using nitrogen, and the crude product was purified via column chromatography (10:1 acetone/ hexanes) to give pure product **G1** (95.7 mg, 9% yield). This reaction is a modified from procedures in references.[316,317] ^1H NMR (400 MHz, $CDCl_3$) δ 5.81 (ddt, *J* = 16.9, 10.2, 6.7 Hz, 1H), 5.05 – 4.88 (m, 2H), 3.04 – 2.91 (m, 1H), 2.49 (s, 2H), 2.39 (p, *J* = 7.6 Hz, 3H), 2.33 (s, 2H), 2.20 (s, 2H), 1.80 – 1.24 (m, 14H), 1.05 (t, *J* = 7.5 Hz, 4H).

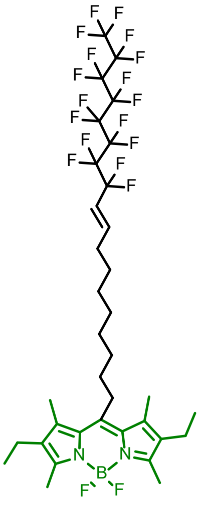

2G

Synthesis of Compound 2G: This synthesis was done in an oven-dried 2-neck 25 mL round bottom flask. Compound **G1** (0.17 mmol, 75 mg) was dissolved with 1H,1H,2H-perfluoro-1-decene (0.85 mmol, 225 µL) in dry dichloromethane (DCM, 10 mL) and kept under an N_2 atmosphere. Grubbs Generation II catalyst (10 mol %, 14 mg) was added and the solution was refluxed for 20 hours. Solvent was evaporated under N_2, and the crude product was purified with silica gel column chromatography (3:7 Hexane/DCM[xi]). TLC showed three spots, leading with the desired product (G2), followed by the starting material (G1) and tailing is assumed to be the homo-coupled BODIPY. ^{1}H NMR (400 MHz, $CDCl_3$) δ 6.42 (dd, *J* = 15.8, 6.8 Hz, 1H), 5.66 – 5.53 (m, 1H), 3.01 – 2.94 (m, 2H), 2.49 (s, 5H), 2.43 – 2.34 (m, 4H), 2.33 (s, 5H), 2.24 – 2.16 (m, 2H), 1.69 – 1.19 (m, 16H), 1.05 (t, *J* = 7.6 Hz, 5H).

[xi] This solvent mixture can easily get cracks and air bubbles in the silica.

5.9.b Fluorine Labeled Red BODIPY

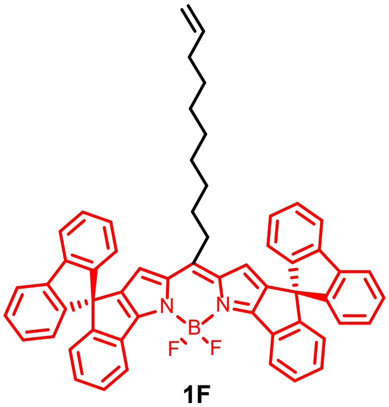

1F

Synthesis of 1F:[xii] Synthesis done in at oven dried 250 mL two neck round bottom flask. Spiro[fluorene-9,4’(1’*H*)-indeno[1,2,-*b*]pyrrole] (1.9 mmol, 596 mg) and 10-undecenoyl chloride (2.2 mmol, 480 µL)[xiii] were refluxed in dry dichloromethane (DCM, 60 mL) under nitrogen for 20 hours. The solution is blue in color. The reaction was brought to room temperature. Triethylamine (Et_3N, 2 mL) was added and stirred for 15 minutes; the solution turned a red color. Then $BF_3{\cdot}OEt_2$ (4 mL) was added slowly dropwise and stirred under nitrogen for 3.5 hours. The solution turned back to a blue color. Solvent was evaporated with nitrogen, leaving an oily crude product. The crude product was purified via silica column chromatography (2:3 hexanes/DCM). ^{1}H NMR (400 MHz, $CDCl_3$) δ 8.44 (d, *J* = 7.7 Hz, 1H), 7.84 (d, *J* = 7.6 Hz, 3H), 7.48 (t, *J* = 7.5 Hz, 1H), 7.40 (t, *J* = 7.6 Hz, 2H), 7.19 (t, *J* = 7.0 Hz, 4H), 6.98 (d, *J* = 7.6 Hz, 2H), 6.64 (d, *J* = 7.7 Hz, 1H), 6.58 (d, *J* = 10.6 Hz, 1H), 5.73 (d, *J* = 6.8 Hz, 1H), 5.00 – 4.80 (m, 2H), 2.57 (t, *J* = 8.2 Hz, 1H), 1.44 – 1.08 (m, 13H).

[xii] This is different than the traditional red BODIPY synthesis route that is used in the group.

[xiii] There was a calculation error that resulted in the addition of the wrong amount of acyl chloride experimentally. There should be a 2.1:1 equivalence of pyrrole: acyl chloride, for 1.9 mmol of pyrrole, one would use 0.9 mmol of acyl chloride.

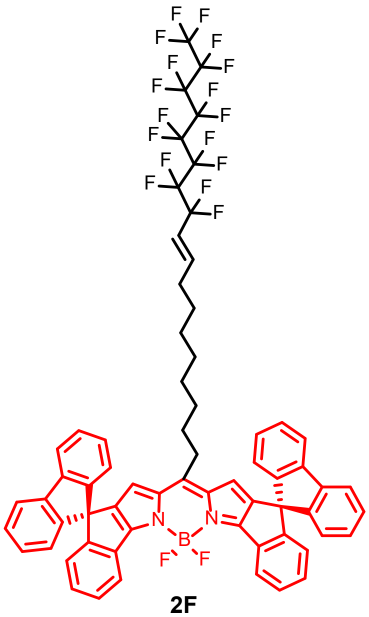

2F

Synthesis of 2F: A oven dried 50 mL round bottom flask is used for this synthesis. Compound **1F** (92 µmol, 75 mg) and 1H,1H,2H-perfluoro-1-decene (0.8 mmol, 220 µL) were added to dichloromethane (DCM, 10 mL) under nitrogen. Grubbs Generation II catalyst (GG2, 18 mol %, 14 mg) The solution was refluxed for 20 hours. Solvent was removed in *vacuo*. Crude product was purified by silica column chromatography (3:7 hexanes/DCM). (15.6 mg, 14%) ^{1}H NMR (400 MHz, $CDCl_3$) δ 8.44 (d, *J* = 7.6 Hz, 2H), 7.84 (d, *J* = 7.7 Hz, 5H), 7.48 (t, *J* = 7.6 Hz, 2H), 7.40 (t, *J* = 7.6 Hz, 4H), 7.19 (t, *J* = 7.5 Hz, 7H), 6.98 (d, *J* = 7.7 Hz, 5H), 6.64 (d, *J* = 7.7 Hz, 2H), 6.56 (s, 2H), 6.35 (s, 1H), 5.53 (d, *J* = 13.8 Hz, 1H), 2.57 (t, *J* = 8.0 Hz, 2H), 1.35 – 1.09 (m, 19H).

References

(1) Moerner, W. E.; Fromm, D. P. Methods of Single-Molecule Fluorescence Spectroscopy and Microscopy. *Review of Scientific Instruments* **2003**, *74* (8), 3597–3619.

(2) Möckl, L.; Moerner, W. E. Super-Resolution Microscopy with Single Molecules in Biology and Beyond–Essentials, Current Trends, and Future Challenges. *J. Am. Chem. Soc.* **2020**, *142* (42), 17828–17844.

(3) *Principles of Fluorescence Spectroscopy*; Lakowicz, J. R., Ed.; Springer US: Boston, MA, 2006.

(4) Magde, D.; Wong, R.; Seybold, P. G. Fluorescence Quantum Yields and Their Relation to Lifetimes of Rhodamine 6G and Fluorescein in Nine Solvents: Improved Absolute Standards for Quantum Yields¶. *Photochemistry and Photobiology* **2002**, *75* (4), 327–334.

(5) Berezin, M. Y.; Achilefu, S. Fluorescence Lifetime Measurements and Biological Imaging. *Chem. Rev.* **2010**, *110* (5), 2641–2684.

(6) Boens, N.; Qin, W.; Basarić, N.; Hofkens, J.; Ameloot, M.; Pouget, J.; Lefèvre, J.-P.; Valeur, B.; Gratton, E.; vandeVen, M.; Silva, N. D.; Engelborghs, Y.; Willaert, K.; Sillen, A.; Rumbles, G.; Phillips, D.; Visser, A. J. W. G.; van Hoek, A.; Lakowicz, J. R.; Malak, H.; Gryczynski, I.; Szabo, A. G.; Krajcarski, D. T.; Tamai, N.; Miura, A. Fluorescence Lifetime Standards for Time and Frequency Domain Fluorescence Spectroscopy. *Anal. Chem.* **2007**, *79* (5), 2137–2149.

(7) 1 Ratiometric Fluorescence Microscopy. In *Methods in Microbiology*; Academic Press, 2002; Vol. 31, pp 1–18.

(8) Han, J.; Burgess, K. Fluorescent Indicators for Intracellular PH. *Chem. Rev.* **2010**, *110* (5), 2709–2728.

(9) Hurst, T. K.; Wang, D.; Thompson, R. B.; Fierke, C. A. Carbonic Anhydrase II-Based Metal Ion Sensing: Advances and New Perspectives. *Biochimica et Biophysica Acta (BBA) - Proteins and Proteomics* **2010**, *1804* (2), 393–403.

(10) Marimuthu, P.; Ramu, A. A Ratiometric Fluorescence Chemosensor for Mg2+ Ion and Its Live Cell Imaging. *Sensors and Actuators B: Chemical* **2018**, *266*, 384–391.

(11) Buckler, K. J.; Vaughan-Jones, R. D. Application of a New PH-Sensitive Fluoroprobe (Carboxy-SNARF-1) for Intracellular PH Measurement in Small, Isolated Cells. *Pflugers Arch.* **1990**, *417* (2), 234–239.

(12) Seksek, O.; Henry-Toulmé, N.; Sureau, F.; Bolard, J. SNARF-1 as an Intracellular PH Indicator in Laser Microspectrofluorometry: A Critical Assessment. *Analytical Biochemistry* **1991**, *193* (1), 49–54.

(13) Van Erp, P. E. J.; Jansen, M. J. J. M.; De Jongh, G. J.; Boezeman, J. B. M.; Schalkwijk, J. Ratiometric Measurement of Intracellular PH in Cultured Human Keratinocytes Using Carboxy-SNARF-1 and Flow Cytometry. *Cytometry* **1991**, *12* (2), 127–132.

(14) Wieder, E. D.; Hang, H.; Fox, M. H. Measurement of Intracellular PH Using Flow Cytometry with Carboxy-SNARF-1. *Cytometry* **1993**, *14* (8), 916–921.

(15) Bassnett, S.; Reinisch, L.; Beebe, D. C. Intracellular PH Measurement Using Single Excitation-Dual Emission Fluorescence Ratios. *American Journal of Physiology-Cell Physiology* **1990**.

(16) C. Gradinaru, C.; O. Marushchak, D.; Samim, M.; J. Krull, U. Fluorescence Anisotropy : From Single Molecules to Live Cells. *Analyst* **2010**, *135* (3), 452–459.

(17) Manger, L. H.; Foote, A. K.; Wood, S. L.; Holden, M. R.; Heylman, K. D.; Margittai, M.; Goldsmith, R. H. Revealing Conformational Variants of Solution-Phase Intrinsically Disordered Tau Protein at the Single-Molecule Level. *Angew Chem Int Ed Engl* **2017**, *56* (49), 15584–15588.

(18) Zhou, Z.; Yan, X.; Lai, Y.-H.; Zare, R. N. Fluorescence Polarization Anisotropy in Microdroplets. *J. Phys. Chem. Lett.* **2018**, *9* (11), 2928–2932.

(19) Zhu, C.; Kwok, R. T. K.; Lam, J. W. Y.; Tang, B. Z. Aggregation-Induced Emission: A Trailblazing Journey to the Field of Biomedicine. *ACS Appl. Bio Mater.* **2018**, *1* (6), 1768–1786.

(20) Zhao, Z.; Zhang, H.; Lam, J. W. Y.; Tang, B. Z. Aggregation-Induced Emission: New Vistas at the Aggregate Level. *Angewandte Chemie International Edition* **2020**, *59* (25), 9888–9907.

(21) Wu, W.; Liu, B. Aggregation-Induced Emission: Challenges and Opportunities. *National Science Review* **2021**, *8* (6), nwaa222.

(22) Tian, X.; Murfin, L. C.; Wu, L.; Lewis, S. E.; James, T. D. Fluorescent Small Organic Probes for Biosensing. *Chem Sci 12* (10), 3406–3426.

(23) Wang, M.; Zhang, D.; Zhang, G.; Tang, Y.; Wang, S.; Zhu, D. Fluorescence Turn-On Detection of DNA and Label-Free Fluorescence Nuclease Assay Based on the Aggregation-Induced Emission of Silole. *Anal. Chem.* **2008**, *80* (16), 6443–6448.

(24) Hong, Y.; Häußler, M.; Lam, J. W. Y.; Li, Z.; Sin, K. K.; Dong, Y.; Tong, H.; Liu, J.; Qin, A.; Renneberg, R.; Tang, B. Z. Label-Free Fluorescent Probing of G-Quadruplex Formation and Real-Time Monitoring of DNA Folding by a Quaternized Tetraphenylethene Salt with Aggregation-Induced Emission Characteristics. *Chemistry – A European Journal* **2008**, *14* (21), 6428–6437.

(25) Tong, H.; Hong, Y.; Dong, Y.; Häußler, M.; Lam, J. W. Y.; Li, Z.; Guo, Z.; Guo, Z.; Tang, B. Z. Fluorescent “Light-up” Bioprobes Based on Tetraphenylethylene Derivatives with Aggregation-Induced Emission Characteristics. *Chem. Commun.* **2006**, No. 35, 3705–3707.

(26) Ding, A.-X.; Tang, Q.; Gao, Y.-G.; Shi, Y.-D.; Uzair, A.; Lu, Z.-L. [12]AneN3 Modified Tetraphenylethene Molecules as High-Performance Sensing, Condensing, and Delivering Agents toward DNAs. *ACS Appl. Mater. Interfaces* **2016**, *8* (23), 14367–14378.

(27) Wen, X.; Wang, Q.; Fan, Z. An Active Fluorescent Probe Based on Aggregation-Induced Emission for Intracellular Bioimaging of Zn2+ and Tracking of Interactions with Single-Stranded DNA. *Analytica Chimica Acta* **2018**, *1013*, 79–86.

(28) Wang, Z.; Gu, Y.; Liu, J.; Cheng, X.; Zhi Sun, J.; Qin, A.; Zhong Tang, B. A Novel Pyridinium Modified Tetraphenylethene: AIE-Activity, Mechanochromism, DNA Detection and Mitochondrial Imaging. *Journal of Materials Chemistry B* **2018**, *6* (8), 1279–1285.

(29) Wang, M.; Gu, X.; Zhang, G.; Zhang, D.; Zhu, D. Convenient and Continuous Fluorometric Assay Method for Acetylcholinesterase and Inhibitor Screening Based on the Aggregation-Induced Emission. *Anal. Chem.* **2009**, *81* (11), 4444–4449.

(30) Tong, H.; Hong, Y.; Dong, Y.; Häussler, M.; Li, Z.; Lam, J. W. Y.; Dong, Y.; Sung, H. H.-Y.; Williams, I. D.; Tang, B. Z. Protein Detection and Quantitation by Tetraphenylethene-Based Fluorescent Probes with Aggregation-Induced Emission Characteristics. *J. Phys. Chem. B* **2007**, *111* (40), 11817–11823.

(31) Gu, X.; Zhao, E.; Zhao, T.; Kang, M.; Gui, C.; Lam, J. W. Y.; Du, S.; Loy, M. M. T.; Tang, B. Z. A Mitochondrion-Specific Photoactivatable Fluorescence Turn-On AIE-Based Bioprobe for Localization Super-Resolution Microscope. *Advanced Materials* **2016**, *28* (25), 5064–5071.

(32) Hu, R.; Kang, Y.; Tang, B. Z. Recent Advances in AIE Polymers. *Polym J* **2016**, *48* (4), 359–370.

(33) Zhan, R.; Pan, Y.; Manghnani, P. N.; Liu, B. AIE Polymers: Synthesis, Properties, and Biological Applications. *Macromolecular Bioscience* **2017**, *17* (5), 1600433.

(34) Qiu, Z.; Liu, X.; Lam, J. W. Y.; Tang, B. Z. The Marriage of Aggregation-Induced Emission with Polymer Science. *Macromolecular Rapid Communications* **2019**, *40* (1), 1800568.

(35) Hu, R.; Qin, A.; Tang, B. Z. AIE Polymers: Synthesis and Applications. *Progress in Polymer Science* **2020**, *100*, 101176.

(36) Liu, S.; Cheng, Y.; Zhang, H.; Qiu, Z.; Kwok, R. T. K.; Lam, J. W. Y.; Tang, B. Z. In Situ Monitoring of RAFT Polymerization by Tetraphenylethylene-Containing Agents with Aggregation-Induced Emission Characteristics. *Angewandte Chemie International Edition* **2018**, *57* (21), 6274–6278.

(37) Liu, L.; Wang, M.; Guo, L.-X.; Sun, Y.; Zhang, X.-Q.; Lin, B.-P.; Yang, H. Aggregation-Induced Emission Luminogen-Functionalized Liquid Crystal Elastomer Soft Actuators. *Macromolecules* **2018**, *51* (12), 4516–4524.

(38) Qiao, X. G.; Ma, H. H.; Zhou, Z.; Shi, Y. L.; Pang, X. C.; Zhou, S. Z. New Sight for Old Polymerization Technique Based on Aggregation-Induced Emission: Mechanism Analysis for Conventional Emulsion Polymerization. *Dyes and Pigments* **2020**, *172*, 107796.

(39) Iasilli, G.; Battisti, A.; Tantussi, F.; Fuso, F.; Allegrini, M.; Ruggeri, G.; Pucci, A. Aggregation-Induced Emission of Tetraphenylethylene in Styrene-Based Polymers. *Macromolecular Chemistry and Physics* **2014**, *215* (6), 499–506.

(40) Rayan, G.; Guet, J.-E.; Taulier, N.; Pincet, F.; Urbach, W. Recent Applications of Fluorescence Recovery after Photobleaching (FRAP) to Membrane Bio-Macromolecules. *Sensors* **2010**, *10* (6), 5927–5948.

(41) Cai, N.; Lai, A. C.-K.; Liao, K.; Corridon, P. R.; Graves, D. J.; Chan, V. Recent Advances in Fluorescence Recovery after Photobleaching for Decoupling Transport and Kinetics of Biomacromolecules in Cellular Physiology. *Polymers* **2022**, *14* (9), 1913.

(42) Ershov, D.; Phan, M.-S.; Pylvänäinen, J. W.; Rigaud, S. U.; Le Blanc, L.; Charles-Orszag, A.; Conway, J. R. W.; Laine, R. F.; Roy, N. H.; Bonazzi, D.; Duménil, G.; Jacquemet, G.; Tinevez, J.-Y. TrackMate 7:

Integrating State-of-the-Art Segmentation Algorithms into Tracking Pipelines. *Nat Methods* **2022**, *19* (7), 829–832.

(43) Tinevez, J.-Y.; Perry, N.; Schindelin, J.; Hoopes, G. M.; Reynolds, G. D.; Laplantine, E.; Bednarek, S. Y.; Shorte, S. L.; Eliceiri, K. W. TrackMate: An Open and Extensible Platform for Single-Particle Tracking. *Methods* **2017**, *115*, 80–90.

(44) Lee, B. H.; Park, H. Y. HybTrack: A Hybrid Single Particle Tracking Software Using Manual and Automatic Detection of Dim Signals. *Sci Rep* **2018**, *8* (1), 212.

(45) Shuang, B.; Chen, J.; Kisley, L.; F. Landes, C. Troika of Single Particle Tracking Programing: SNR Enhancement, Particle Identification, and Mapping. *Physical Chemistry Chemical Physics* **2014**, *16* (2), 624–634.

(46) van Heerden, B.; Vickers, N. A.; Krüger, T. P. J.; Andersson, S. B. Real-Time Feedback-Driven Single-Particle Tracking: A Survey and Perspective. *Small* **2022**, *18* (29), 2107024.

(47) Manzo, C.; Garcia-Parajo, M. F. A Review of Progress in Single Particle Tracking: From Methods to Biophysical Insights. *Rep. Prog. Phys.* **2015**, *78* (12), 124601.

(48) Shen, H.; Tauzin, L. J.; Baiyasi, R.; Wang, W.; Moringo, N.; Shuang, B.; Landes, C. F. Single Particle Tracking: From Theory to Biophysical Applications. *Chem. Rev.* **2017**, *117* (11), 7331–7376.

(49) Chen, Y.; Li, Z.; Huang, X.; Lu, G.; Huang, W. Single-Molecule Mapping of Catalytic Reactions on Heterostructures. *Nano Today* **2020**, *34*, 100957.

(50) Dong, B.; Mansour, N.; Huang, T.-X.; Huang, W.; Fang, N. Single Molecule Fluorescence Imaging of Nanoconfinement in Porous Materials. *Chem. Soc. Rev.* **2021**, *50* (11), 6483–6506.

(51) Roeffaers, M. B. J.; Sels, B. F.; Uji-i, H.; De Schryver, F. C.; Jacobs, P. A.; De Vos, D. E.; Hofkens, J. Spatially Resolved Observation of Crystal-Face-Dependent Catalysis by Single Turnover Counting. *Nature* **2006**, *439* (7076), 572–575.

(52) Xu, W.; Kong, J. S.; Yeh, Y.-T. E.; Chen, P. Single-Molecule Nanocatalysis Reveals Heterogeneous Reaction Pathways and Catalytic Dynamics. *Nature Mater* **2008**, *7* (12), 992–996.

(53) Chen, P.; Xu, W.; Zhou, X.; Panda, D.; Kalininskiy, A. Single-Nanoparticle Catalysis at Single-Turnover Resolution. *Chemical Physics Letters* **2009**, *470* (4), 151–157.

(54) Xu, W.; S. Kong, J.; Chen, P. Probing the Catalytic Activity and Heterogeneity of Au-Nanoparticles at the Single-Molecule Level. *Physical Chemistry Chemical Physics* **2009**, *11* (15), 2767–2778.

(55) Zhou, X.; Xu, W.; Liu, G.; Panda, D.; Chen, P. Size-Dependent Catalytic Activity and Dynamics of Gold Nanoparticles at the Single-Molecule Level. *J. Am. Chem. Soc.* **2010**, *132* (1), 138–146.

(56) Xu, W.; Shen, H.; Kim, Y. J.; Zhou, X.; Liu, G.; Park, J.; Chen, P. Single-Molecule Electrocatalysis by Single-Walled Carbon Nanotubes. *Nano Lett.* **2009**, *9* (12), 3968–3973.

(57) Cordes, T.; Blum, S. A. Opportunities and Challenges in Single-Molecule and Single-Particle Fluorescence Microscopy for Mechanistic Studies of Chemical Reactions. *Nature Chem* **2013**, *5* (12), 993–999.

(58) Liu, C.; Kubo, K.; Wang, E.; Han, K.-S.; Yang, F.; Chen, G.; Escobedo, F. A.; Coates, G. W.; Chen, P. Single Polymer Growth Dynamics. *Science* **2017**, *358* (6361), 352–355.

(59) Garcia IV, A.; Saluga, S. J.; Dibble, D. J.; López, P. A.; Saito, N.; Blum, S. A. Does Selectivity of Molecular Catalysts Change with Time? Polymerization Imaged by Single-Molecule Spectroscopy. *Angewandte Chemie International Edition* **2021**, *60* (3), 1550–1555.

(60) Ng, J. D.; Upadhyay, S. P.; Marquard, A. N.; Lupo, K. M.; Hinton, D. A.; Padilla, N. A.; Bates, D. M.; Goldsmith, R. H. Single-Molecule Investigation of Initiation Dynamics of an Organometallic Catalyst. *J. Am. Chem. Soc.* **2016**, *138* (11), 3876–3883.

(61) Lupo, K. M.; Hinton, D. A.; Ng, J. D.; Padilla, N. A.; Goldsmith, R. H. Probing Heterogeneity and Bonding at Silica Surfaces through Single-Molecule Investigation of Base-Mediated Linkage Failure. *Langmuir* **2016**, *32* (36), 9171–9179.

(62) Loudet, A.; Burgess, K. BODIPY Dyes and Their Derivatives: Syntheses and Spectroscopic Properties. *Chem. Rev.* **2007**, *107* (11), 4891–4932.

(63) Kowada, T.; Yamaguchi, S.; Ohe, K. Highly Fluorescent BODIPY Dyes Modulated with Spirofluorene Moieties. *Org. Lett.* **2010**, *12* (2), 296–299.

(64) Pop, E.; Sinha, S.; Goodson, K. E. Heat Generation and Transport in Nanometer-Scale Transistors. *Proceedings of the IEEE* **2006**, *94* (8), 1587–1601.

(65) Taylor, M. B. Is Dark Silicon Useful?: Harnessing the Four Horsemen of the Coming Dark Silicon Apocalypse. In *Proceedings of the 49th Annual Design Automation Conference*; ACM: San Francisco California, 2012; pp 1131–1136.

(66) Ye, P.; Ernst, T.; Khare, M. V. The Last Silicon Transistor: Nanosheet Devices Could Be the Final Evolutionary Step for Moore’s Law. *IEEE Spectrum* **2019**, *56* (8), 30–35.

(67) Leiserson, C. E.; Thompson, N. C.; Emer, J. S.; Kuszmaul, B. C.; Lampson, B. W.; Sanchez, D.; Schardl, T. B. There’s Plenty of Room at the Top: What Will Drive Computer Performance after Moore’s Law? *Science* **2020**, *368* (6495), eaam9744.

(68) Adamatzky, A.; Costello, B. D. L.; Asai, T. *Reaction-Diffusion Computers*; Elsevier, 2005.

(69) Kaminaga, A.; Vanag, V. K.; Epstein, I. R. A Reaction–Diffusion Memory Device. *Angewandte Chemie International Edition* **2006**, *45* (19), 3087–3089.

(70) Toiya, M.; Vanag, V. K.; Epstein, I. R. Diffusively Coupled Chemical Oscillators in a Microfluidic Assembly. *Angew. Chem. Int. Ed.* **2008**, *47* (40), 7753–7755.

(71) Gorecki, J.; Gizynski, K.; Guzowski, J.; Gorecka, J. N.; Garstecki, P.; Gruenert, G.; Dittrich, P. Chemical Computing with Reaction–Diffusion Processes. *Philosophical Transactions of the Royal Society A: Mathematical, Physical and Engineering Sciences* **2015**, *373* (2046), 20140219.

(72) Vodenicarevic, D.; Locatelli, N.; Abreu Araujo, F.; Grollier, J.; Querlioz, D. A Nanotechnology-Ready Computing Scheme Based on a Weakly Coupled Oscillator Network. *Sci Rep* **2017**, *7* (1), 44772.

(73) Dueñas-Díez, M.; Pérez-Mercader, J. How Chemistry Computes: Language Recognition by Non-Biochemical Chemical Automata. From Finite Automata to Turing Machines. *iScience* **2019**, *19*, 514–526.

(74) Parrilla-Gutierrez, J. M.; Sharma, A.; Tsuda, S.; Cooper, G. J. T.; Aragon-Camarasa, G.; Donkers, K.; Cronin, L. A Programmable Chemical Computer with Memory and Pattern Recognition. *Nat Commun* **2020**, *11* (1), 1442.

(75) Sharma, A.; Ng, M. T.-K.; Gutierrez, J. M. P.; Jiang, Y.; Cronin, L. A Probabilistic Chemical Programmable Computer. arXiv April 28, 2022. http://arxiv.org/abs/2204.13493 (accessed 2023-04-24).

(76) Adleman, L. M. Molecular Computation of Solutions to Combinatorial Problems. *Science* **1994**, *266* (5187), 1021–1024.

(77) Seelig, G.; Soloveichik, D.; Zhang, D. Y.; Winfree, E. Enzyme-Free Nucleic Acid Logic Circuits. *Science* **2006**, *314* (5805), 1585–1588.

(78) Prokup, A.; Hemphill, J.; Deiters, A. DNA Computation: A Photochemically Controlled AND Gate. *J. Am. Chem. Soc.* **2012**, *134* (8), 3810–3815.

(79) Siuti, P.; Yazbek, J.; Lu, T. K. Engineering Genetic Circuits That Compute and Remember. *Nat Protoc* **2014**, *9* (6), 1292–1300.

(80) Yu, W.; Liu, Y.; Gong, L.; Tian, M.; Tu, L. Double-Image Encryption Based on Spatiotemporal Chaos and DNA Operations. *Multimed Tools Appl* **2019**, *78* (14), 20037–20064.

(81) Moerner, W. E. Molecular Electronics for Frequency Domain Optical Storage. Persistent Spectral Hole-Burning. A Review. *J. Molec. Electr.* **1985**, *1*, 55–71.

(82) Cafferty, B. J.; Ten, A. S.; Fink, M. J.; Morey, S.; Preston, D. J.; Mrksich, M.; Whitesides, G. M. Storage of Information Using Small Organic Molecules. *ACS Cent. Sci.* **2019**, *5* (5), 911–916.

(83) Rosenstein, J. K.; Rose, C.; Reda, S.; Weber, P. M.; Kim, E.; Sello, J.; Geiser, J.; Kennedy, E.; Arcadia, C.; Dombroski, A.; Oakley, K.; Chen, S. L.; Tann, H.; Rubenstein, B. M. Principles of Information Storage in Small-Molecule Mixtures. *IEEE Transactions on NanoBioscience* **2020**, *19* (3), 378–384.

(84) Arcadia, C. E.; Kennedy, E.; Geiser, J.; Dombroski, A.; Oakley, K.; Chen, S.-L.; Sprague, L.; Ozmen, M.; Sello, J.; Weber, P. M.; Reda, S.; Rose, C.; Kim, E.; Rubenstein, B. M.; Rosenstein, J. K. Multicomponent Molecular Memory. *Nat Commun* **2020**, *11* (1), 691.

(85) Nagarkar, A. A.; Root, S. E.; Fink, M. J.; Ten, A. S.; Cafferty, B. J.; Richardson, D. S.; Mrksich, M.; Whitesides, G. M. Storing and Reading Information in Mixtures of Fluorescent Molecules. *ACS Cent. Sci.* **2021**, *7* (10), 1728–1735.

(86) Bohn, P.; Weisel, M. P.; Wolfs, J.; Meier, M. A. R. Molecular Data Storage with Zero Synthetic Effort and Simple Read-Out. *Sci Rep* **2022**, *12* (1), 13878.

(87) Dombroski, A.; Oakley, K.; Arcadia, C.; Nouraei, F.; Chen, S. L.; Rose, C.; Rubenstein, B.; Rosenstein, J.; Reda, S.; Kim, E. Implementing Parallel Arithmetic via Acetylation and Its Application to Chemical Image Processing. *Proceedings of the Royal Society A: Mathematical, Physical and Engineering Sciences* **2021**, *477* (2248), 20200899.

(88) E. Arcadia, C.; Dombroski, A.; Oakley, K.; Ling Chen, S.; Tann, H.; Rose, C.; Kim, E.; Reda, S.; M. Rubenstein, B.; K. Rosenstein, J. Leveraging Autocatalytic Reactions for Chemical Domain Image Classification. *Chemical Science* **2021**, *12* (15), 5464–5472.

(89) Agiza, A. A.; Oakley, K.; Rosenstein, J. K.; Rubenstein, B. M.; Kim, E.; Riedel, M.; Reda, S. Digital Circuits and Neural Networks Based on Acid-Base Chemistry Implemented by Robotic Fluid Handling. *Nat Commun* **2023**, *14* (1), 496.

(90) de Silva, P. A.; Gunaratne, N. H. Q.; McCoy, C. P. A Molecular Photoionic AND Gate Based on Fluorescent Signalling. *Nature* **1993**, *364* (6432), 42–44.

(91) Tóth, Á.; Showalter, K. Logic Gates in Excitable Media. *The Journal of Chemical Physics* **1995**, *103* (6), 2058–2066.

(92) Adamatzky, A.; De Lacy Costello, B. Experimental Logical Gates in a Reaction-Diffusion Medium: The XOR Gate and Beyond. *Phys. Rev. E* **2002**, *66* (4), 046112.

(93) De Silva; Prasanna, A. A Layer of Logic. *Nature* **2008**, *454* (7203), 417–418.

(94) G, U. R.; Axthelm, J.; Hoffmann, P.; Taye, N.; Gläser, S.; Görls, H.; Hopkins, S. L.; Plass, W.; Neugebauer, U.; Bonnet, S.; Schiller, A. Co-Registered Molecular Logic Gate with a CO-Releasing Molecule Triggered by Light and Peroxide. *J. Am. Chem. Soc.* **2017**, *139* (14), 4991–4994.

(95) Guo, S. Y.; Friederich, P.; Cao, Y.; Wu, T. C.; Forman, C. J.; Mendoza, D.; Degroote, M.; Cavell, A.; Krasecki, V.; Hickman, R. J.; Sharma, A.; Cronin, L.; Gianneschi, N.; Goldsmith, R. H.; Aspuru-Guzik, A. A Molecular Computing Approach to Solving Optimization Problems via Programmable Microdroplet Arrays. *Matter* **2021**, *4* (4), 1107–1124.

(96) Stepney, S.; Abramsky, S.; Bechmann, M.; Gorecki, J.; Kendon, V.; Naughton, T. J.; Perez-Jimenez, M. J.; Romero-Campero, F. J.; Sebald, A. Heterotic Computing Examples with Optics, Bacteria, and Chemicals. In *Unconventional Computation and Natural Computation*; Durand-Lose, J., Jonoska, N., Eds.; Lecture Notes in Computer Science; Springer: Berlin, Heidelberg, 2012; pp 198–209.

(97) Kendon, V.; Sebald, A.; Stepney, S. Heterotic Computing: Exploiting Hybrid Computational Devices. *Philosophical Transactions of the Royal Society A: Mathematical, Physical and Engineering Sciences* **2015**, *373* (2046), 20150091.

(98) Henson, A.; Gutierrez, J. M. P.; Hinkley, T.; Tsuda, S.; Cronin, L. Towards Heterotic Computing with Droplets in a Fully Automated Droplet-Maker Platform. *Philosophical Transactions of the Royal Society A: Mathematical, Physical and Engineering Sciences* **2015**, *373* (2046), 20140221.

(99) Horsman, C.; Stepney, S.; Wagner, R. C.; Kendon, V. When Does a Physical System Compute? *Proc. R. Soc. A.* **2014**, *470* (2169), 20140182.

(100) Lucas, A. Ising Formulations of Many NP Problems. *Frontiers in Physics* **2014**, *2*.

(101) Lobanov, M. Y.; Galzitskaya, O. V. The Ising Model for Prediction of Disordered Residues from Protein Sequence Alone. *Phys. Biol.* **2011**, *8* (3), 035004.

(102) Weber, M.; Buceta, J. The Cellular Ising Model: A Framework for Phase Transitions in Multicellular Environments. *J. R. Soc. Interface.* **2016**, *13* (119), 20151092.

(103) Okamoto, Y. Finding a Maximum Common Subgraph from Molecular Structural Formulas through the Maximum Clique Approach Combined with the Ising Model. *ACS Omega* **2020**, *5* (22), 13064–13068.

(104) Li, Y.; Zhao, P.; Guo, B.; Zhao, C.; Liu, X.; He, S.; Guo, D. Design of Combinational Digital Circuits Optimized with Ising Model and PSO Algorithm. In *2021 IEEE 15th International Conference on Anti-counterfeiting, Security, and Identification (ASID)*; 2021; pp 31–35.

(105) Carrasquilla, J.; Melko, R. G. Machine Learning Phases of Matter. *Nature Phys* **2017**, *13* (5), 431–434.

(106) Efthymiou, S.; Beach, M. J. S.; Melko, R. G. Super-Resolving the Ising Model with Convolutional Neural Networks. *Phys. Rev. B* **2019**, *99* (7), 075113.

(107) Dutta, S.; Khanna, A.; Assoa, A. S.; Paik, H.; Schlom, D. G.; Toroczkai, Z.; Raychowdhury, A.; Datta, S. An Ising Hamiltonian Solver Based on Coupled Stochastic Phase-Transition Nano-Oscillators. *Nat Electron* **2021**, *4* (7), 502–512.

(108) Aramon, M.; Rosenberg, G.; Valiante, E.; Miyazawa, T.; Tamura, H.; Katzgraber, H. G. Physics-Inspired Optimization for Quadratic Unconstrained Problems Using a Digital Annealer. *Frontiers in Physics* **2019**, *7*.

(109) McMahon, P. L.; Marandi, A.; Haribara, Y.; Hamerly, R.; Langrock, C.; Tamate, S.; Inagaki, T.; Takesue, H.; Utsunomiya, S.; Aihara, K.; Byer, R. L.; Fejer, M. M.; Mabuchi, H.; Yamamoto, Y. A Fully Programmable 100-Spin Coherent Ising Machine with All-to-All Connections. *Science* **2016**, *354* (6312), 614–617.

(110) Pierangeli, D.; Marcucci, G.; Conti, C. Large-Scale Photonic Ising Machine by Spatial Light Modulation. *Phys. Rev. Lett.* **2019**, *122* (21), 213902.

(111) Borders, W. A.; Pervaiz, A. Z.; Fukami, S.; Camsari, K. Y.; Ohno, H.; Datta, S. Integer Factorization Using Stochastic Magnetic Tunnel Junctions. *Nature* **2019**, *573* (7774), 390–393.

(112) Inagaki, T.; Haribara, Y.; Igarashi, K.; Sonobe, T.; Tamate, S.; Honjo, T.; Marandi, A.; McMahon, P. L.; Umeki, T.; Enbutsu, K.; Tadanaga, O.; Takenouchi, H.; Aihara, K.; Kawarabayashi, K.; Inoue, K.; Utsunomiya, S.; Takesue, H. A Coherent Ising Machine for 2000-Node Optimization Problems. *Science* **2016**, *354* (6312), 603–606.

(113) Dutta, S.; Khanna, A.; Paik, H.; Schlom, D.; Raychowdhury, A.; Toroczkai, Z.; Datta, S. *An Ising Hamiltonian Solver Using Stochastic Phase-Transition Nano-Oscillators*; preprint; In Review, 2020. https://www.researchsquare.com/article/rs-93438/v1 (accessed 2022-08-01).

(114) Chou, J.; Bramhavar, S.; Ghosh, S.; Herzog, W. Analog Coupled Oscillator Based Weighted Ising Machine. *Sci Rep* **2019**, *9* (1), 14786.

(115) Thomson, W. V. Mechanical Integration of the Linear Differential Equations of the Second Order with Variable Coefficients. *Proceedings of the Royal Society of London* **1997**, *24* (164–170), 269–271.

(116) Thomson, W. VI. Mechanical Integration of the General Linear Differential Equation of Any Order with Variable Coefficients. *Proceedings of the Royal Society of London* **1997**, *24* (164–170), 271–275.

(117) He, Y. Chaotic Simulated Annealing with Decaying Chaotic Noise. *IEEE Transactions on Neural Networks* **2002**, *13* (6), 1526–1531.

(118) Wang, T.; Roychowdhury, J. Oscillator-Based Ising Machine. arXiv October 12, 2017. http://arxiv.org/abs/1709.08102 (accessed 2022-08-17).

(119) Wang, T.; Roychowdhury, J. OIM: Oscillator-Based Ising Machines for Solving Combinatorial Optimisation Problems. arXiv March 17, 2019. http://arxiv.org/abs/1903.07163 (accessed 2022-08-17).

(120) Cai, F.; Kumar, S.; Van Vaerenbergh, T.; Sheng, X.; Liu, R.; Li, C.; Liu, Z.; Foltin, M.; Yu, S.; Xia, Q.; Yang, J. J.; Beausoleil, R.; Lu, W. D.; Strachan, J. P. Power-Efficient Combinatorial Optimization Using Intrinsic Noise in Memristor Hopfield Neural Networks. *Nat Electron* **2020**, *3* (7), 409–418.

(121) Rodriguez, S. R. K. Enhancing the Speed and Sensitivity of a Nonlinear Optical Sensor with Noise. *Phys. Rev. Applied* **2020**, *13* (2), 024032.

(122) Rebentrost, P.; Mohseni, M.; Kassal, I.; Lloyd, S.; Aspuru-Guzik, A. Environment-Assisted Quantum Transport. *New J. Phys.* **2009**, *11* (3), 033003.

(123) S. Minero, G. A.; F. Wagler, P.; A. Oughli, A.; S. McCaskill, J. Electronic PH Switching of DNA Triplex Reactions. *RSC Advances* **2015**, *5* (35), 27313–27325.

(124) Cavell, A. C.; Krasecki, V. K.; Li, G.; Sharma, A.; Sun, H.; Thompson, M. P.; Forman, C. J.; Guo, S. Y.; Hickman, R. J.; Parrish, K. A.; Aspuru-Guzik, A.; Cronin, L.; Gianneschi, N. C.; Goldsmith, R. H. Optical Monitoring of Polymerizations in Droplets with High Temporal Dynamic Range. *Chem. Sci.* **2020**, *11* (10), 2647–2656.

(125) Szmacinski, H.; Lakowicz, J. R. Optical Measurements of PH Using Fluorescence Lifetimes and Phase-Modulation Fluorometry. *Anal Chem* **1993**, *65* (13), 1668–1674.

(126) *pH Indicators—Chapter 20 - US*. https://www.thermofisher.com/us/en/home/references/molecular-probes-the-handbook/ph-indicators.html (accessed 2022-08-01).

(127) Balut, C.; vandeVen, M.; Despa, S.; Lambrichts, I.; Ameloot, M.; Steels, P.; Smets, I. Measurement of Cytosolic and Mitochondrial PH in Living Cells during Reversible Metabolic Inhibition. *Kidney International* **2008**, *73* (2), 226–232.

(128) Whitaker, J. E.; Haugland, R. P.; Prendergast, F. G. Spectral and Photophysical Studies of Benzo[c]Xanthene Dyes: Dual Emission PH Sensors. *Analytical Biochemistry* **1991**, *194* (2), 330–344.

(129) Meyer, F. Color Image Segmentation. In *1992 International Conference on Image Processing and its Applications*; 1992; pp 303–306.

(130) Mertens, S. The Easiest Hard Problem: Number Partitioning. In *Computational Complexity and Statistical Physics*; Oxford University Press, 2005.

(131) Moerner, W. E.; Carter, T. P. Statistical Fine Structure of Inhomogeneously Broadened Absorption Lines. *Phys. Rev. Lett.* **1987**, *59* (23), 2705–2708.

(132) Shon, M. J.; Cohen, A. E. Mass Action at the Single-Molecule Level. *J. Am. Chem. Soc.* **2012**, *134* (35), 14618–14623.

(133) Eremin, D. B.; Ananikov, V. P. Understanding Active Species in Catalytic Transformations: From Molecular Catalysis to Nanoparticles, Leaching, "Cocktails" of Catalysts and Dynamic Systems. *Coordination Chemistry Reviews* **2017**, *346*, 2–19.

(134) Shekhar, S.; Ryberg, P.; Hartwig, J. F.; Mathew, J. S.; Blackmond, D. G.; Strieter, E. R.; Buchwald, S. L. Reevaluation of the Mechanism of the Amination of Aryl Halides Catalyzed by BINAP-Ligated Palladium Complexes. *J. Am. Chem. Soc.* **2006**, *128* (11), 3584–3591.

(135) Reetz, M. T.; Westermann, E. Phosphane-Free Palladium-Catalyzed Coupling Reactions: The Decisive Role of Pd Nanoparticles. *Angewandte Chemie International Edition* **2000**, *39* (1), 165–168.

(136) Phan, N. T. S.; Van Der Sluys, M.; Jones, C. W. On the Nature of the Active Species in Palladium Catalyzed Mizoroki–Heck and Suzuki–Miyaura Couplings – Homogeneous or Heterogeneous Catalysis, A Critical Review. *Advanced Synthesis & Catalysis* **2006**, *348* (6), 609–679.

(137) Sullivan, K. P.; Wieliczko, M.; Kim, M.; Yin, Q.; Collins-Wildman, D. L.; Mehta, A. K.; Bacsa, J.; Lu, X.; Geletii, Y. V.; Hill, C. L. Speciation and Dynamics in the [Co4V2W18O68]10–/Co(II)Aq/CoOx Catalytic Water Oxidation System. *ACS Catal.* **2018**, *8* (12), 11952–11959.

(138) Easter, Q. T.; Trauschke, V.; Blum, S. A. Catalyst Inefficiencies: Supported Ring-Opening Metathesis Polymerization Catalyst Yields Its Ensemble Rate from a Small Number of Molecular Active Sites. *ACS Catal.* **2015**, *5* (4), 2290–2295.

(139) Pandey, A.; Champouret, Y.; Rastogi, S. Heterogeneity in the Distribution of Entanglement Density during Polymerization in Disentangled Ultrahigh Molecular Weight Polyethylene. *Macromolecules* **2011**, *44* (12), 4952–4960.

(140) Sanford, M. S.; Love, J. A.; Grubbs, R. H. Mechanism and Activity of Ruthenium Olefin Metathesis Catalysts. *J. Am. Chem. Soc.* **2001**, *123* (27), 6543–6554.

(141) Bañares, M. A. Operando Spectroscopy: The Knowledge Bridge to Assessing Structure–Performance Relationships in Catalyst Nanoparticles. *Advanced Materials* **2011**, *23* (44), 5293–5301.

(142) Tinnemans, S. J.; Mesu, J. G.; Kervinen, K.; Visser, T.; Nijhuis, T. A.; Beale, A. M.; Keller, D. E.; van der Eerden, A. M. J.; Weckhuysen, B. M. Combining Operando Techniques in One Spectroscopic-Reaction Cell: New Opportunities for Elucidating the Active Site and Related Reaction Mechanism in Catalysis. *Catalysis Today* **2006**, *113* (1), 3–15.

(143) M. Weckhuysen, B. Determining the Active Site in a Catalytic Process: Operando Spectroscopy Is More than a Buzzword. *Physical Chemistry Chemical Physics* **2003**, *5* (20), 4351–4360.

(144) Müller, P.; Burt, S. P.; Love, A. M.; McDermott, W. P.; Wolf, P.; Hermans, I. Mechanistic Study on the Lewis Acid Catalyzed Synthesis of 1,3-Butadiene over Ta-BEA Using Modulated Operando DRIFTS-MS. *ACS Catal.* **2016**, *6* (10), 6823–6832.

(145) Müller, P.; Hermans, I. Applications of Modulation Excitation Spectroscopy in Heterogeneous Catalysis. *Ind. Eng. Chem. Res.* **2017**, *56* (5), 1123–1136.

(146) Heylman, K. D.; Knapper, K. A.; Horak, E. H.; Rea, M. T.; Vanga, S. K.; Goldsmith, R. H. Optical Microresonators for Sensing and Transduction: A Materials Perspective. *Advanced Materials* **2017**, *29* (30), 1700037.

(147) M. Cubillas, A.; Unterkofler, S.; G. Euser, T.; M. Etzold, B. J.; C. Jones, A.; J. Sadler, P.; Wasserscheid, P.; St.J. Russell, P. Photonic Crystal Fibres for Chemical Sensing and Photochemistry. *Chemical Society Reviews* **2013**, *42* (22), 8629–8648.

(148) Roeffaers, M. B. J.; Hofkens, J.; De Cremer, G.; De Schryver, F. C.; Jacobs, P. A.; De Vos, D. E.; Sels, B. F. Fluorescence Microscopy: Bridging the Phase Gap in Catalysis. *Catalysis Today* **2007**, *126* (1), 44–53.

(149) Cremer, G. D.; F. Sels, B.; Vos, D. E. D.; Hofkens, J.; J. Roeffaers, M. B. Fluorescence Micro(Spectro)Scopy as a Tool to Study Catalytic Materials in Action. *Chemical Society Reviews* **2010**, *39* (12), 4703–4717.

(150) Kitagawa, K.; Blum, S. A. Structure–Reactivity Studies of Intermediates for Mechanistic Information by Subensemble Fluorescence Microscopy. *ACS Catal.* **2017**, *7* (6), 3786–3791.

(151) Roeffaers, M. B. J.; De Cremer, G.; Uji-i, H.; Muls, B.; Sels, B. F.; Jacobs, P. A.; De Schryver, F. C.; De Vos, D. E.; Hofkens, J. Single-Molecule Fluorescence Spectroscopy in (Bio)Catalysis. *Proc Natl Acad Sci U S A* **2007**, *104* (31), 12603–12609.

(152) Valdes-Aguilera, O.; Pathak, C. P.; Neckers, D. C. Pyrene as a Fluorescent Probe for Monitoring Polymerization Rates. **1990**, *23* (2).

(153) Mikeš, F.; González-Benito, F.; Serrano, B.; Bravo, J.; Baselga, J. Fluorescence Monitoring of Polymerization Reaction. A New Method for Treating Fluorescence Experimental Data. *Polymer* **2002**, *43* (16), 4331–4339.

(154) Loutfy, R. O. Fluorescence Probes for Polymerization Reactions: Bulk Polymerization of Styrene, n-Butyl Methacrylate, Ethyl Methacrylate, and Ethyl Acrylate. *Journal of Polymer Science: Polymer Physics Edition* **1982**, *20* (5), 825–835.

(155) English, B. P.; Min, W.; van Oijen, A. M.; Lee, K. T.; Luo, G.; Sun, H.; Cherayil, B. J.; Kou, S. C.; Xie, X. S. Ever-Fluctuating Single Enzyme Molecules: Michaelis-Menten Equation Revisited. *Nat Chem Biol* **2006**, *2* (2), 87–94.

(156) Easter, Q. T.; Garcia, A. I.; Blum, S. A. Single-Polymer–Particle Growth Kinetics with Molecular Catalyst Speciation and Single-Turnover Imaging. *ACS Catal.* **2019**, *9* (4), 3375–3383.

(157) Easter, Q. T.; Blum, S. A. Evidence for Dynamic Chemical Kinetics at Individual Molecular Ruthenium Catalysts. *Angewandte Chemie International Edition* **2018**, *57* (6), 1572–1575.

(158) Easter, Q. T.; Blum, S. A. Single Turnover at Molecular Polymerization Catalysts Reveals Spatiotemporally Resolved Reactions. *Angewandte Chemie International Edition* **2017**, *56* (44), 13772–13775.

(159) T. Allen, Z.; R. Sackey-Addo, J.; P. Hopps, M.; Tahseen, D.; T. Anderson, J.; A. Graf, T.; B. Cooley, C. Fluorogenic Atom Transfer Radical Polymerization in Aqueous Media as a Strategy for Detection. *Chemical Science* **2019**, *10* (4), 1017–1022.

(160) Hopkinson, M. N.; Gómez-Suárez, A.; Teders, M.; Sahoo, B.; Glorius, F. Accelerated Discovery in Photocatalysis Using a Mechanism-Based Screening Method. *Angewandte Chemie International Edition* **2016**, *55* (13), 4361–4366.

(161) Friest, J. A.; Broussy, S.; Chung, W. J.; Berkowitz, D. B. Combinatorial Catalysis Employing a Visible Enzymatic Beacon in Real Time: Synthetically Versatile (Pseudo)Halometalation/Carbocyclizations. *Angewandte Chemie International Edition* **2011**, *50* (38), 8895–8899.

(162) Herrera, B. T.; Moor, S. R.; McVeigh, M.; Roesner, E. K.; Marini, F.; Anslyn, E. V. Rapid Optical Determination of Enantiomeric Excess, Diastereomeric Excess, and Total Concentration Using Dynamic-Covalent Assemblies: A Demonstration Using 2-Aminocyclohexanol and Chemometrics. *J. Am. Chem. Soc.* **2019**, *141* (28), 11151–11160.

(163) Stambuli, J. P.; Stauffer, S. R.; Shaughnessy, K. H.; Hartwig, J. F. Screening of Homogeneous Catalysts by Fluorescence Resonance Energy Transfer. Identification of Catalysts for Room-Temperature Heck Reactions. *J. Am. Chem. Soc.* **2001**, *123* (11), 2677–2678.

(164) Stauffer, S. R.; Hartwig, J. F. Fluorescence Resonance Energy Transfer (FRET) as a High-Throughput Assay for Coupling Reactions. Arylation of Amines as a Case Study. *J. Am. Chem. Soc.* **2003**, *125* (23), 6977–6985.

(165) Dragone, V.; Sans, V.; Henson, A. B.; Granda, J. M.; Cronin, L. An Autonomous Organic Reaction Search Engine for Chemical Reactivity. *Nat Commun* **2017**, *8*, 15733.

(166) Gromski, P. S.; Henson, A. B.; Granda, J. M.; Cronin, L. How to Explore Chemical Space Using Algorithms and Automation. *Nat Rev Chem* **2019**, *3* (2), 119–128.

(167) Gómez-Bombarelli, R.; Aguilera-Iparraguirre, J.; Hirzel, T. D.; Duvenaud, D.; Maclaurin, D.; Blood-Forsythe, M. A.; Chae, H. S.; Einzinger, M.; Ha, D.-G.; Wu, T.; Markopoulos, G.; Jeon, S.; Kang, H.; Miyazaki, H.; Numata, M.; Kim, S.; Huang, W.; Hong, S. I.; Baldo, M.; Adams, R. P.; Aspuru-Guzik, A. Design of Efficient Molecular Organic Light-Emitting Diodes by a High-Throughput Virtual Screening and Experimental Approach. *Nature Mater* **2016**, *15* (10), 1120–1127.

(168) Tabor, D. P.; Roch, L. M.; Saikin, S. K.; Kreisbeck, C.; Sheberla, D.; Montoya, J. H.; Dwaraknath, S.; Aykol, M.; Ortiz, C.; Tribukait, H.; Amador-Bedolla, C.; Brabec, C. J.; Maruyama, B.; Persson, K. A.; Aspuru-Guzik, A. Accelerating the Discovery of Materials for Clean Energy in the Era of Smart Automation. *Nat Rev Mater* **2018**, *3* (5), 5–20.

(169) Asua, J. M. Challenges in Polymerization in Dispersed Media. In *Polymer Reaction Engineering of Dispersed Systems: Volume II*; Pauer, W., Ed.; Advances in Polymer Science; Springer International Publishing: Cham, 2018; pp 1–22.

(170) Landfester, K. Miniemulsion Polymerization and the Structure of Polymer and Hybrid Nanoparticles. *Angewandte Chemie International Edition* **2009**, *48* (25), 4488–4507.

(171) Thickett, S. C.; Teo, G. H. Recent Advances in Colloidal Nanocomposite Design via Heterogeneous Polymerization Techniques. *Polym. Chem.* **2019**, *10* (23), 2906–2924.

(172) Jeong, W. J.; Kim, J. Y.; Choo, J.; Lee, E. K.; Han, C. S.; Beebe, D. J.; Seong, G. H.; Lee, S. H. Continuous Fabrication of Biocatalyst Immobilized Microparticles Using Photopolymerization and Immiscible Liquids in Microfluidic Systems. *Langmuir* **2005**, *21* (9), 3738–3741.

(173) Brugarolas, T.; Tu, F.; Lee, D. Directed Assembly of Particles Using Microfluidic Droplets and Bubbles. *Soft Matter* **2013**, *9* (38), 9046–9058.

(174) Mashaghi, S.; Abbaspourrad, A.; Weitz, D. A.; van Oijen, A. M. Droplet Microfluidics: A Tool for Biology, Chemistry and Nanotechnology. *TrAC Trends in Analytical Chemistry* **2016**, *82*, 118–125.

(175) Du, G.; Fang, Q.; den Toonder, J. M. J. Microfluidics for Cell-Based High Throughput Screening Platforms—A Review. *Analytica Chimica Acta* **2016**, *903*, 36–50.

(176) Churski, K.; Korczyk, P.; Garstecki, P. High-Throughput Automated Droplet Microfluidic System for Screening of Reaction Conditions. *Lab Chip* **2010**, *10* (7), 816–818.

(177) Brouzes, E.; Medkova, M.; Savenelli, N.; Marran, D.; Twardowski, M.; Hutchison, J. B.; Rothberg, J. M.; Link, D. R.; Perrimon, N.; Samuels, M. L. Droplet Microfluidic Technology for Single-Cell High-Throughput Screening. *Proceedings of the National Academy of Sciences* **2009**, *106* (34), 14195–14200.

(178) Churski, K.; Kaminski, T. S.; Jakiela, S.; Kamysz, W.; Baranska-Rybak, W.; Weibel, D. B.; Garstecki, P. Rapid Screening of Antibiotic Toxicity in an Automated Microdroplet System. *Lab Chip* **2012**, *12* (9), 1629–1637.

(179) Thickett, S. C.; Gilbert, R. G. Emulsion Polymerization: State of the Art in Kinetics and Mechanisms. *Polymer* **2007**, *48* (24), 6965–6991.

(180) Frochot, C.; Mascherin, M.; Haumont, A.; Viriot, M.-L.; Marie, E. Fluorescence Spectroscopy as a Non Invasive Tool to Follow in Situ the Polymerization in Miniemulsion. *Journal of Applied Polymer Science* **2011**, *119* (1), 219–224.

(181) Crans, D. C.; Baruah, B.; Ross, A.; Levinger, N. E. Impact of Confinement and Interfaces on Coordination Chemistry: Using Oxovanadate Reactions and Proton Transfer Reactions as Probes in Reverse Micelles. *Coordination Chemistry Reviews* **2009**, *253* (17), 2178–2185.

(182) Rotman, B.; Papermaster, B. W. Membrane Properties of Living Mammalian Cells as Studied by Enzymatic Hydrolysis of Fluorogenic Esters. *Proceedings of the National Academy of Sciences* **1966**, *55* (1), 134–141.

(183) Rozhkov, R. V.; Davisson, V. J.; Bergstrom, D. E. Fluorogenic Transformations Based on Formation of C⍰C Bonds Catalyzed by Palladium: An Efficient Approach for High Throughput Optimizations and Kinetic Studies. *Advanced Synthesis & Catalysis* **2008**, *350* (1), 71–75.

(184) Greene, L. E.; Lincoln, R.; Krumova, K.; Cosa, G. Development of a Fluorogenic Reactivity Palette for the Study of Nucleophilic Addition Reactions Based on Meso-Formyl BODIPY Dyes. *ACS Omega* **2017**, *2* (12), 8618–8624.

(185) Sambur, J. B.; Chen, T.-Y.; Choudhary, E.; Chen, G.; Nissen, E. J.; Thomas, E. M.; Zou, N.; Chen, P. Sub-Particle Reaction and Photocurrent Mapping to Optimize Catalyst-Modified Photoanodes. *Nature* **2016**, *530* (7588), 77–80.

(186) Lu, H. P.; Xun, L.; Xie, X. S. Single-Molecule Enzymatic Dynamics. *Science* **1998**, *282* (5395), 1877–1882.

(187) Rybina, A.; Lang, C.; Wirtz, M.; Grußmayer, K.; Kurz, A.; Maier, F.; Schmitt, A.; Trapp, O.; Jung, G.; Herten, D.-P. Distinguishing Alternative Reaction Pathways by Single-Molecule Fluorescence Spectroscopy. *Angewandte Chemie International Edition* **2013**, *52* (24), 6322–6325.

(188) De Cremer, G.; Roeffaers, M. B. J.; Bartholomeeusen, E.; Lin, K.; Dedecker, P.; Pescarmona, P. P.; Jacobs, P. A.; De Vos, D. E.; Hofkens, J.; Sels, B. F. High-Resolution Single-Turnover Mapping Reveals Intraparticle Diffusion Limitation in Ti-MCM-41-Catalyzed Epoxidation. *Angewandte Chemie International Edition* **2010**, *49* (5), 908–911.

(189) Chen, Y.; Sun, P.; Zhang, Y.; Ye, Y. Fluorescence Anisotropy Analysis of Comb-Type Grafted Poly(N,N-Diethylacrylamide-Co-Acrylic Acid)-g-Poly(N,N-Diethylacrylamide) Microgels Labeled by Acenaphthylene. *Journal of Applied Polymer Science* **2018**, *135* (46), 46742.

(190) Levitus, M.; Bourdelande, J. L.; Marqués, G.; Aramendía, P. F. Fluorescence Anisotropy of Dyes Included in Crosslinked Polystyrene. *Journal of Photochemistry and Photobiology A: Chemistry* **1999**, *126* (1), 77–82.

(191) Geddes, C. D.; Karolin, J.; Birch, D. J. S. 1- and 2-Photon Fluorescence Anisotropy Decay in Silicon Alkoxide Sol−Gels: Interpretation in Terms of Self-Assembled Nanoparticles. *J. Phys. Chem. B* **2002**, *106* (15), 3835–3841.

(192) Beija, M.; Fedorov, A.; Charreyre, M.-T.; Martinho, J. M. G. Fluorescence Anisotropy of Hydrophobic Probes in Poly(N-Decylacrylamide)-Block-Poly(N,N-Diethylacrylamide) Block Copolymer Aqueous Solutions: Evidence of Premicellar Aggregates. *J. Phys. Chem. B* **2010**, *114* (31), 9977–9986.

(193) Foote, A. K.; Manger, L. H.; Holden, M. R.; Margittai, M.; Goldsmith, R. H. Time-Resolved Multirotational Dynamics of Single Solution-Phase Tau Proteins Reveals Details of Conformational Variation. *Phys. Chem. Chem. Phys.* **2019**, *21* (4), 1863–1871.

(194) Paeng, K.; Richert, R.; Ediger, M. D. Molecular Mobility in Supported Thin Films of Polystyrene, Poly(Methyl Methacrylate), and Poly(2-Vinyl Pyridine) Probed by Dye Reorientation. *Soft Matter* **2011**, *8* (3), 819–826.

(195) Gielen, F.; Butz, M.; Rees, E. J.; Erdelyi, M.; Moschetti, T.; Hyvönen, M.; Edel, J. B.; Kaminski, C. F.; Hollfelder, F. Quantitative Affinity Determination by Fluorescence Anisotropy Measurements of Individual Nanoliter Droplets. *Anal. Chem.* **2017**, *89* (2), 1092–1101.

(196) Mei, J.; Leung, N. L. C.; Kwok, R. T. K.; Lam, J. W. Y.; Tang, B. Z. Aggregation-Induced Emission: Together We Shine, United We Soar! *Chem. Rev.* **2015**, *115* (21), 11718–11940.

(197) Ma, C.; Ling, Q.; Xu, S.; Zhu, H.; Zhang, G.; Zhou, X.; Chi, Z.; Liu, S.; Zhang, Y.; Xu, J. Preparation of Biocompatible Aggregation-Induced Emission Homopolymeric Nanoparticles for Cell Imaging. *Macromolecular Bioscience* **2014**, *14* (2), 235–243.

(198) Scholl, M.; Ding, S.; Lee, C. W.; Grubbs, R. H. Synthesis and Activity of a New Generation of Ruthenium-Based Olefin Metathesis Catalysts Coordinated with 1,3-Dimesityl-4,5-Dihydroimidazol-2-Ylidene Ligands. *Org. Lett.* **1999**, *1* (6), 953–956.

(199) Bielawski, C. W.; Grubbs, R. H. Highly Efficient Ring-Opening Metathesis Polymerization (ROMP) Using New Ruthenium Catalysts Containing N-Heterocyclic Carbene Ligands. *Angewandte Chemie International Edition* **2000**, *39* (16), 2903–2906.

(200) Delaude, L.; Noels, A. F. Metathesis. In *Kirk-Othmer Encyclopedia of Chemical Technology*; John Wiley & Sons, Ltd, 2005.

(201) Pariya, C.; Jayaprakash, K. N.; Sarkar, A. Alkene Metathesis: New Developments in Catalyst Design and Application. *Coordination Chemistry Reviews* **1998**, *168*, 1–48.

(202) Leitgeb, A.; Wappel, J.; Slugovc, C. The ROMP Toolbox Upgraded. *Polymer* **2010**, *51* (14), 2927–2946.

(203) Wright, D. B.; Touve, M. A.; Thompson, M. P.; Gianneschi, N. C. Aqueous-Phase Ring-Opening Metathesis Polymerization-Induced Self-Assembly. *ACS Macro Lett.* **2018**, *7* (4), 401–405.

(204) Huang, C.; Barlow, S.; Marder, S. R. Perylene-3,4,9,10-Tetracarboxylic Acid Diimides: Synthesis, Physical Properties, and Use in Organic Electronics. *J. Org. Chem.* **2011**, *76* (8), 2386–2407.

(205) Langhals, H.; Krotz, O.; Polborn, K.; Mayer, P. A Novel Fluorescent Dye with Strong, Anisotropic Solid-State Fluorescence, Small Stokes Shift, and High Photostability. *Angewandte Chemie International Edition* **2005**, *44* (16), 2427–2428.

(206) Zhan, X.; Facchetti, A.; Barlow, S.; Marks, T. J.; Ratner, M. A.; Wasielewski, M. R.; Marder, S. R. Rylene and Related Diimides for Organic Electronics. *Advanced Materials* **2011**, *23* (2), 268–284.

(207) Goldsmith, R. H.; Sinks, L. E.; Kelley, R. F.; Betzen, L. J.; Liu, W.; Weiss, E. A.; Ratner, M. A.; Wasielewski, M. R. Wire-like Charge Transport at near Constant Bridge Energy through Fluorene Oligomers. *Proceedings of the National Academy of Sciences* **2005**, *102* (10), 3540–3545.

(208) Ahrens, M. J.; Sinks, L. E.; Rybtchinski, B.; Liu, W.; Jones, B. A.; Giaimo, J. M.; Gusev, A. V.; Goshe, A. J.; Tiede, D. M.; Wasielewski, M. R. Self-Assembly of Supramolecular Light-Harvesting Arrays from Covalent Multi-Chromophore Perylene-3,4:9,10-Bis(Dicarboximide) Building Blocks. *J. Am. Chem. Soc.* **2004**, *126* (26), 8284–8294.

(209) Weiss, E. A.; Ahrens, M. J.; Sinks, L. E.; Gusev, A. V.; Ratner, M. A.; Wasielewski, M. R. Making a Molecular Wire: Charge and Spin Transport through Para-Phenylene Oligomers. *J. Am. Chem. Soc.* **2004**, *126* (17), 5577–5584.

(210) Wasielewski, M. R. Self-Assembly Strategies for Integrating Light Harvesting and Charge Separation in Artificial Photosynthetic Systems. *Acc. Chem. Res.* **2009**, *42* (12), 1910–1921.

(211) Rybtchinski, B.; Sinks, L. E.; Wasielewski, M. R. Combining Light-Harvesting and Charge Separation in a Self-Assembled Artificial Photosynthetic System Based on Perylenediimide Chromophores. *J. Am. Chem. Soc.* **2004**, *126* (39), 12268–12269.

(212) Yagai, S.; Seki, T.; Karatsu, T.; Kitamura, A.; Würthner, F. Transformation from H- to J-Aggregated Perylene Bisimide Dyes by Complexation with Cyanurates. *Angewandte Chemie International Edition* **2008**, *47* (18), 3367–3371.

(213) Zhao, Y.; Wu, Y.; Yan, G.; Zhang, K. Aggregation-Induced Emission Block Copolymers Based on Ring-Opening Metathesis Polymerization. *RSC Adv.* **2014**, *4* (93), 51194–51200.

(214) Upadhyay, S. P.; Lupo, K. M.; Marquard, A. N.; Ng, J. D.; Bates, D. M.; Goldsmith, R. H. Fluorescent Dendrimeric Molecular Catalysts Demonstrate Unusual Scaling Behavior at the Single-Molecule Level. *J. Phys. Chem. C* **2015**, *119* (34), 19703–19714.

(215) Santos, C. M.; Kumar, A.; Zhang, W.; Cai, C. Functionalization of Fluorous Thin Films via “Click” Chemistry. *Chem. Commun.* **2009**, No. 20, 2854–2856.

(216) Vincent, J.-M. Recent Advances of Fluorous Chemistry in Material Sciences. *Chem. Commun.* **2012**, *48* (93), 11382–11391.

(217) Tzschucke, C. C.; Markert, C.; Glatz, H.; Bannwarth, W. Fluorous Biphasic Catalysis without Perfluorinated Solvents: Application to Pd-Mediated Suzuki and Sonogashira Couplings. *Angewandte Chemie International Edition* **2002**, *41* (23), 4500–4503.

(218) Ko, K.-S.; Jaipuri, F. A.; Pohl, N. L. Fluorous-Based Carbohydrate Microarrays. *J. Am. Chem. Soc.* **2005**, *127* (38), 13162–13163.

(219) Darmanin, T.; Guittard, F. Superoleophobic Surfaces with Short Fluorinated Chains? *Soft Matter* **2013**, *9* (25), 5982–5990.

(220) Gutierrez, J. M. P.; Hinkley, T.; Taylor, J. W.; Yanev, K.; Cronin, L. Evolution of Oil Droplets in a Chemorobotic Platform. *Nat Commun* **2014**, *5* (1), 5571.

(221) Grizou, J.; Points, L. J.; Sharma, A.; Cronin, L. Exploration of Self-Propelling Droplets Using a Curiosity Driven Robotic Assistant. arXiv April 22, 2019. http://arxiv.org/abs/1904.12635 (accessed 2023-05-10).

(222) Zhao, Y.; Zhu, W.; Ren, L.; Zhang, K. Aggregation-Induced Emission Polymer Nanoparticles with PH-Responsive Fluorescence. *Polym. Chem.* **2016**, *7* (34), 5386–5395.

(223) Zhao, Y.; Zhu, W.; Wu, Y.; Qu, L.; Liu, Z.; Zhang, K. An Aggregation-Induced Emission Star Polymer with PH and Metal Ion Responsive Fluorescence. *Polym. Chem.* **2016**, *7* (42), 6513–6520.

(224) Ahrens, M. J.; Kelley, R. F.; Dance, Z. E. X.; Wasielewski, M. R. Photoinduced Charge Separation in Self-Assembled Cofacial Pentamers of Zinc-5,10,15,20-Tetrakis(Perylenediimide)Porphyrin. *Phys. Chem. Chem. Phys.* **2007**, *9* (12), 1469–1478.

(225) Howell, J.; Goddard, J. D.; Tam, W. A Relative Approach for Determining Ring Strain Energies of Heterobicyclic Alkenes. *Tetrahedron* **2009**, *65* (23), 4562–4568.

(226) Khoury, P. R.; Goddard, J. D.; Tam, W. Ring Strain Energies: Substituted Rings, Norbornanes, Norbornenes and Norbornadienes. *Tetrahedron* **2004**, *60* (37), 8103–8112.

(227) Escuela, G.; Gruenert, G.; Dittrich, P. Symbol Representations and Signal Dynamics in Evolving Droplet Computers. *Nat Comput* **2014**, *13* (2), 247–256.

(228) Blank, K.; De Cremer, G.; Hofkens, J. Fluorescence-Based Analysis of Enzymes at the Single-Molecule Level. *Biotechnology Journal* **2009**, *4* (4), 465–479.

(229) Claessen, V. I.; Engelkamp, H.; Christianen, P. C. M.; Maan, J. C.; Nolte, R. J. M.; Blank, K.; Rowan, A. E. Single-Biomolecule Kinetics: The Art of Studying a Single Enzyme. *Annual Review of Analytical Chemistry* **2010**, *3* (1), 319–340.

(230) F. Janssen, K. P.; Cremer, G. D.; K. Neely, R.; V. Kubarev, A.; Loon, J. V.; A. Martens, J.; Vos, D. E. D.; J. Roeffaers, M. B.; Hofkens, J. Single Molecule Methods for the Study of Catalysis: From Enzymes to Heterogeneous Catalysts. *Chemical Society Reviews* **2014**, *43* (4), 990–1006.

(231) Talaga, D. S.; Lau, W. L.; Roder, H.; Tang, J.; Jia, Y.; DeGrado, W. F.; Hochstrasser, R. M. Dynamics and Folding of Single Two-Stranded Coiled-Coil Peptides Studied by Fluorescent Energy Transfer Confocal Microscopy. *Proc Natl Acad Sci U S A* **2000**, *97* (24), 13021–13026.

(232) Jia, Y.; Talaga, D. S.; Lau, W. L.; Lu, H. S. M.; DeGrado, W. F.; Hochstrasser, R. M. Folding Dynamics of Single GCN-4 Peptides by Fluorescence Resonant Energy Transfer Confocal Microscopy. *Chemical Physics* **1999**, *247* (1), 69–83.

(233) Squyres, G. R.; Holmes, M. J.; Barger, S. R.; Pennycook, B. R.; Ryan, J.; Yan, V. T.; Garner, E. C. Single-Molecule Imaging Reveals That Z-Ring Condensation Is Essential for Cell Division in Bacillus Subtilis. *Nat Microbiol* **2021**, *6* (5), 553–562.

(234) Shen, H.; Zhou, X.; Zou, N.; Chen, P. Single-Molecule Kinetics Reveals a Hidden Surface Reaction Intermediate in Single-Nanoparticle Catalysis. *J. Phys. Chem. C* **2014**, *118* (46), 26902–26911.

(235) Zhou, X.; Andoy, N. M.; Liu, G.; Choudhary, E.; Han, K.-S.; Shen, H.; Chen, P. Quantitative Super-Resolution Imaging Uncovers Reactivity Patterns on Single Nanocatalysts. *Nature Nanotech* **2012**, *7* (4), 237–241.

(236) Wang, W. Imaging the Chemical Activity of Single Nanoparticles with Optical Microscopy. *Chemical Society Reviews* **2018**, *47* (7), 2485–2508.

(237) Naito, K.; Tachikawa, T.; Fujitsuka, M.; Majima, T. Real-Time Single-Molecule Imaging of the Spatial and Temporal Distribution of Reactive Oxygen Species with Fluorescent Probes: Applications to TiO2 Photocatalysts. *J. Phys. Chem. C* **2008**, *112* (4), 1048–1059.

(238) Canham, S. M.; Bass, J. Y.; Navarro, O.; Lim, S.-G.; Das, N.; Blum, S. A. Toward the Single-Molecule Investigation of Organometallic Reaction Mechanisms: Single-Molecule Imaging of Fluorophore-Tagged Palladium(II) Complexes. *Organometallics* **2008**, *27* (10), 2172–2175.

(239) Menges, J. A.; Grandjean, A.; Clasen, A.; Jung, G. Kinetics of Palladium(0)-Allyl Interactions in the Tsuji-Trost Reaction, Derived from Single-Molecule Fluorescence Microscopy. *ChemCatChem* **2020**, *12* (9), 2630–2637.

(240) Liu, X.; Ge, X.; Cao, J.; Xiao, Y.; Wang, Y.; Zhang, W.; Song, P.; Xu, W. Revealing the Catalytic Kinetics and Dynamics of Individual Pt Atoms at the Single-Molecule Level. *Proceedings of the National Academy of Sciences* **2022**, *119* (14), e2114639119.

(241) Eivgi, O.; Blum, S. A. Real-Time Polymer Viscosity–Catalytic Activity Relationships on the Microscale. *J. Am. Chem. Soc.* **2022**, *144* (30), 13574–13585.

(242) Rotman, B. MEASUREMENT OF ACTIVITY OF SINGLE MOLECULES OF β-D-GALACTOSIDASE*. *Proceedings of the National Academy of Sciences* **1961**, *47* (12), 1981–1991.

(243) Goldner, L. S.; Jofre, A. M.; Tang, J. Chapter 5 - Droplet Confinement and Fluorescence Measurement of Single Molecules. In *Methods in Enzymology*; Walter, N. G., Ed.; Single Molecule Tools: Fluorescence Based Approaches, Part A; Academic Press, 2010; Vol. 472, pp 61–88.

(244) Weinmeister, R.; Freeman, E.; Eperon, I. C.; Stuart, A. M.; Hudson, A. J. Single-Fluorophore Detection in Femtoliter Droplets Generated by Flow Focusing. *ACS Nano* **2015**, *9* (10), 9718–9730.

(245) Rahmanseresht, S.; Milas, P.; Ramos, K. P.; Gamari, B. D.; Goldner, L. S. Single-Molecule-Sensitive Fluorescence Resonance Energy Transfer in Freely-Diffusing Attoliter Droplets. *Applied Physics Letters* **2015**, *106* (19), 194107.

(246) Reiner, J. E.; Crawford, A. M.; Kishore, R. B.; Goldner, L. S.; Helmerson, K.; Gilson, M. K. Optically Trapped Aqueous Droplets for Single Molecule Studies. *Applied Physics Letters* **2006**, *89* (1), 013904.

(247) Rhoades, E.; Gussakovsky, E.; Haran, G. Watching Proteins Fold One Molecule at a Time. *Proceedings of the National Academy of Sciences* **2003**, *100* (6), 3197–3202.

(248) Cisse, I.; Okumus, B.; Joo, C.; Ha, T. Fueling Protein–DNA Interactions inside Porous Nanocontainers. *Proceedings of the National Academy of Sciences* **2007**, *104* (31), 12646–12650.

(249) Benítez, J. J.; Keller, A. M.; Ochieng, P.; Yatsunyk, L. A.; Huffman, D. L.; Rosenzweig, A. C.; Chen, P. Probing Transient Copper Chaperone−Wilson Disease Protein Interactions at the Single-Molecule Level with Nanovesicle Trapping. *J. Am. Chem. Soc.* **2008**, *130* (8), 2446–2447.

(250) Dong, B.; Pei, Y.; Zhao, F.; Goh, T. W.; Qi, Z.; Xiao, C.; Chen, K.; Huang, W.; Fang, N. In Situ Quantitative Single-Molecule Study of Dynamic Catalytic Processes in Nanoconfinement. *Nat Catal* **2018**, *1* (2), 135–140.

(251) Dong, B.; Pei, Y.; Mansour, N.; Lu, X.; Yang, K.; Huang, W.; Fang, N. Deciphering Nanoconfinement Effects on Molecular Orientation and Reaction Intermediate by Single Molecule Imaging. *Nat Commun* **2019**, *10*, 4815.

(252) Wöll, D.; Uji-i, H.; Schnitzler, T.; Hotta, J.; Dedecker, P.; Herrmann, A.; De Schryver, F. C.; Müllen, K.; Hofkens, J. Radical Polymerization Tracked by Single Molecule Spectroscopy. *Angewandte Chemie International Edition* **2008**, *47* (4), 783–787.

(253) Dhankhar, P. Homogenization Fundamentals. *IOSRJEN* **2014**, *4* (5), 01–08.

(254) Maa, Y.-F.; Hsu, C. Liquid-Liquid Emulsification by Rotor/Stator Homogenization. *Journal of Controlled Release* **1996**, *38* (2–3), 219–228.

(255) Zembyla, M.; Murray, B. S.; Sarkar, A. Water-in-Oil Emulsions Stabilized by Surfactants, Biopolymers and/or Particles: A Review. *Trends in Food Science & Technology* **2020**, *104*, 49–59.

(256) Porras, M.; Solans, C.; González, C.; Martínez, A.; Guinart, A.; Gutiérrez, J. M. Studies of Formation of W/O Nano-Emulsions. *Colloids and Surfaces A: Physicochemical and Engineering Aspects* **2004**, *249* (1), 115–118.

(257) Wojciechowski, K.; Bitner, A.; Warszyński, P.; Żubrowska, M. The Hofmeister Effect in Zeta Potentials of CTAB-Stabilised Toluene-in-Water Emulsions. *Colloids and Surfaces A: Physicochemical and Engineering Aspects* **2011**, *376* (1), 122–126.

(258) Stamkulov, N. Sh.; Mussabekov, K. B.; Aidarova, S. B.; Luckham, P. F. Stabilisation of Emulsions by Using a Combination of an Oil Soluble Ionic Surfactant and Water Soluble Polyelectrolytes. I: Emulsion Stabilisation and Interfacial Tension Measurements. *Colloids and Surfaces A: Physicochemical and Engineering Aspects* **2009**, *335* (1), 103–106.

(259) Liang, F.; Liu, J.; Zhang, C.; Qu, X.; Li, J.; Yang, Z. Janus Hollow Spheres by Emulsion Interfacial Self-Assembled Sol–Gel Process. *Chemical Communications* **2011**, *47* (4), 1231–1233.

(260) S. Sander, J.; Isa, L.; A. Rühs, P.; Fischer, P.; R. Studart, A. Stabilization Mechanism of Double Emulsions Made by Microfluidics. *Soft Matter* **2012**, *8* (45), 11471–11477.

(261) McClements, D. J. Emulsion Droplet Size Determination. *Current Protocols in Food Analytical Chemistry* **2001**, *00* (1), D3.3.1-D3.3.9.

(262) Stetefeld, J.; McKenna, S. A.; Patel, T. R. Dynamic Light Scattering: A Practical Guide and Applications in Biomedical Sciences. *Biophys Rev* **2016**, *8* (4), 409–427.

(263) *DLS*. Wyatt Technology. https://www.wyatt.com/library/theory/dynamic-light-scattering-theory.html (accessed 2023-05-01).

(264) Thevenaz, P.; Ruttimann, U. E.; Unser, M. A Pyramid Approach to Subpixel Registration Based on Intensity. *IEEE Transactions on Image Processing* **1998**, *7* (1), 27–41.

(265) *StackReg*. http://bigwww.epfl.ch/thevenaz/stackreg/ (accessed 2023-05-01).

(266) Dutt, G. B.; Doraiswamy, S.; Periasamy, N.; Venkataraman, B. Rotational Reorientation Dynamics of Polar Dye Molecular Probes by Picosecond Laser Spectroscopic Technique. *The Journal of Chemical Physics* **1990**, *93* (12), 8498–8513.

(267) Lelek, M.; Gyparaki, M. T.; Beliu, G.; Schueder, F.; Griffié, J.; Manley, S.; Jungmann, R.; Sauer, M.; Lakadamyali, M.; Zimmer, C. Single-Molecule Localization Microscopy. *Nat Rev Methods Primers* **2021**, *1* (1), 1–27.

(268) Chang, Y.; Kim, D.-H.; Zhou, K.; Jeong, M. G.; Park, S.; Kwon, Y.; Hong, T. M.; Noh, J.; Ryu, S. H. Improved Resolution in Single-Molecule Localization Microscopy Using QD-PAINT. *Exp Mol Med* **2021**, *53* (3), 384–392.

(269) Chozinski, T. J.; Gagnon, L. A.; Vaughan, J. C. Twinkle, Twinkle Little Star: Photoswitchable Fluorophores for Super-Resolution Imaging. *FEBS Lett* **2014**, *588* (19), 3603–3612.

(270) Zwettler, F. U.; Reinhard, S.; Gambarotto, D.; Bell, T. D. M.; Hamel, V.; Guichard, P.; Sauer, M. Molecular Resolution Imaging by Post-Labeling Expansion Single-Molecule Localization Microscopy (Ex-SMLM). *Nat Commun* **2020**, *11* (1), 3388.

(271) Henriques, R.; Griffiths, C.; Hesper Rego, E.; Mhlanga, M. M. PALM and STORM: Unlocking Live-Cell Super-Resolution. *Biopolymers* **2011**, *95* (5), 322–331.

(272) Nieves, D. J.; Gaus, K.; Baker, M. A. B. DNA-Based Super-Resolution Microscopy: DNA-PAINT. *Genes* **2018**, *9* (12), 621.

(273) Stein, J.; Stehr, F.; Schueler, P.; Blumhardt, P.; Schueder, F.; Mücksch, J.; Jungmann, R.; Schwille, P. Toward Absolute Molecular Numbers in DNA-PAINT. *Nano Lett.* **2019**, *19* (11), 8182–8190.

(274) Sage, D.; Pham, T.-A.; Babcock, H.; Lukes, T.; Pengo, T.; Chao, J.; Velmurugan, R.; Herbert, A.; Agrawal, A.; Colabrese, S.; Wheeler, A.; Archetti, A.; Rieger, B.; Ober, R.; Hagen, G. M.; Sibarita, J.-B.; Ries, J.; Henriques, R.; Unser, M.; Holden, S. Super-Resolution Fight Club: Assessment of 2D and 3D Single-Molecule Localization Microscopy Software. *Nat Methods* **2019**, *16* (5), 387–395.

(275) Mortensen, K. I.; Churchman, L. S.; Spudich, J. A.; Flyvbjerg, H. Optimized Localization-Analysis for Single-Molecule Tracking and Super-Resolution Microscopy. *Nat Methods* **2010**, *7* (5), 377–381.

(276) McEvoy, A. L.; Greenfield, D.; Bates, M.; Liphardt, J. Q&A: Single-Molecule Localization Microscopy for Biological Imaging. *BMC Biol* **2010**, *8*, 106.

(277) *GDSC SMLM: Single-molecule localisation ... | Wellcome Open Research*. https://wellcomeopenresearch.org/articles/7-241/v1 (accessed 2023-05-11).

(278) Stallinga, S.; Rieger, B. Accuracy of the Gaussian Point Spread Function Model in 2D Localization Microscopy. *Opt. Express, OE* **2010**, *18* (24), 24461–24476.

(279) Ha, T.; Rasnik, I.; Cheng, W.; Babcock, H. P.; Gauss, G. H.; Lohman, T. M.; Chu, S. Initiation and Re-Initiation of DNA Unwinding by the Escherichia Coli Rep Helicase. *Nature* **2002**, *419* (6907), 638–641.

(280) Zhuang, X.; Bartley, L. E.; Babcock, H. P.; Russell, R.; Ha, T.; Herschlag, D.; Chu, S. A Single-Molecule Study of RNA Catalysis and Folding. *Science* **2000**, *288* (5473), 2048–2051.

(281) Zhuang, X.; Kim, H.; Pereira, M. J. B.; Babcock, H. P.; Walter, N. G.; Chu, S. Correlating Structural Dynamics and Function in Single Ribozyme Molecules. *Science* **2002**, *296* (5572), 1473–1476.

(282) Liu, B.; Mazouchi, A.; Gradinaru, C. C. Trapping Single Molecules in Liposomes: Surface Interactions and Freeze−Thaw Effects. *J. Phys. Chem. B* **2010**, *114* (46), 15191–15198.

(283) Boukobza, E.; Sonnenfeld, A.; Haran, G. Immobilization in Surface-Tethered Lipid Vesicles as a New Tool for Single Biomolecule Spectroscopy. *J. Phys. Chem. B* **2001**, *105* (48), 12165–12170.

(284) Alemán, E. A.; Pedini, H. S.; Rueda, D. Covalent-Bond-Based Immobilization Approaches for Single-Molecule Fluorescence. *ChemBioChem* **2009**, *10* (18), 2862–2866.

(285) Price, G. A.; Bogdan, A. R.; Aguirre, A. L.; Iwai, T.; Djuric, S. W.; Organ, M. G. Continuous Flow Negishi Cross-Couplings Employing Silica-Supported Pd-PEPPSI–IPr Precatalyst. *Catal. Sci. Technol.* **2016**, *6* (13), 4733–4742.

(286) Çetinkaya, B.; Gürbüz, N.; Seçkin, T.; Özdemir, I. Synthesis and Immobilization of N-Heterocyclic Carbene Complexes of Ru(II): Catalytic Activity and Recyclability for the Furan Formation. *Journal of Molecular Catalysis A: Chemical* **2002**, *184* (1–2), 31–38.

(287) Notestein, J. M.; Katz, A. Enhancing Heterogeneous Catalysis through Cooperative Hybrid Organic–Inorganic Interfaces. *Chemistry – A European Journal* **2006**, *12* (15), 3954–3965.

(288) Jutz, F.; Grunwaldt, J.-D.; Baiker, A. Mn(III)(Salen)-Catalyzed Synthesis of Cyclic Organic Carbonates from Propylene and Styrene Oxide in “Supercritical” CO2. *Journal of Molecular Catalysis A: Chemical* **2008**, *279* (1), 94–103.

(289) Hope, E. G.; Stuart, A. M. Fluorous Biphase Catalysis. *Journal of Fluorine Chemistry* **1999**, *100* (1), 75–83.

(290) Horváth, I. T.; Rábai, J. Facile Catalyst Separation Without Water: Fluorous Biphase Hydroformylation of Olefins. *Science* **1994**, *266* (5182), 72–75.

(291) Curran, D. P. Fluorous Reverse Phase Silia Gel. A New Tool for Preparative Separations in Synthetic Organic and Organofluorine Chemistry. *Synlett* **2001**, *2001* (9), 1488–1496.

(292) Zhang, Q.; Luo, Z.; Curran, D. P. Separation of “Light Fluorous” Reagents and Catalysts by Fluorous Solid-Phase Extraction: Synthesis and Study of a Family of Triarylphosphines Bearing Linear and Branched Fluorous Tags. *J. Org. Chem.* **2000**, *65* (26), 8866–8873.

(293) Croxtall, B.; G. Hope, E.; M. Stuart, A. Separation, Recovery and Recycling of a Fluorous-Tagged Nickel Catalyst Using Fluorous Solid-Phase Extraction. *Chemical Communications* **2003**, *0* (19), 2430–2431.

(294) Matsugi, M.; Curran, D. P. Synthesis, Reaction, and Recycle of Light Fluorous Grubbs−Hoveyda Catalysts for Alkene Metathesis. *J. Org. Chem.* **2005**, *70* (5), 1636–1642.

(295) Curran, D. P.; Fischer, K.; Moura-Letts, G. A Soluble Fluorous Palladium Complex That Promotes Heck Reactions and Can Be Recovered and Reused. *Synlett* **2004**, *2004* (8), 1379–1382.

(296) Bernini, R.; Cacchi, S.; Fabrizi, G.; Forte, G.; Niembro, S.; Petrucci, F.; Pleixats, R.; Prastaro, A.; Sebastián, R. M.; Soler, R.; Tristany, M.; Vallribera, A. Phosphine-Free Perfluoro-Tagged Palladium Nanoparticles Supported on Fluorous Silica Gel: Application to the Heck Reaction. *Org. Lett.* **2008**, *10* (4), 561–564.

(297) Mamidyala, S. K.; Ko, K.-S.; Jaipuri, F. A.; Park, G.; Pohl, N. L. Noncovalent Fluorous Interactions for the Synthesis of Carbohydrate Microarrays. *Journal of Fluorine Chemistry* **2006**, *127* (4), 571–579.

(298) Nicholson, R. L.; Ladlow, M. L.; Spring, D. R. Fluorous Tagged Small Molecule Microarrays. *Chem. Commun.* **2007**, No. 38, 3906.

(299) Collet, B. Y. M.; Nagashima, T.; Yu, M. S.; Pohl, N. L. B. Fluorous-Based Peptide Microarrays for Protease Screening. *Journal of Fluorine Chemistry* **2009**, *130* (11), 1042–1048.

(300) Li, B.-Y.; Juang, D. S.; Adak, A. K.; Hwang, K.-C.; Lin, C.-C. Fabrication of a Protein Microarray by Fluorous-Fluorous Interactions. *Sci Rep* **2017**, *7* (1), 7053.

(301) Nelson, K. E.; Gamble, L.; Jung, L. S.; Boeckl, M. S.; Naeemi, E.; Golledge, S. L.; Sasaki, T.; Castner, D. G.; Campbell, C. T.; Stayton, P. S. Surface Characterization of Mixed Self-Assembled Monolayers Designed for Streptavidin Immobilization. *Langmuir* **2001**, *17* (9), 2807–2816.

(302) Alves, S. B.; de Oliveira, G. F.; de Oliveira, L. C.; Passerat de Silans, T.; Chevrollier, M.; Oriá, M.; de S. Cavalcante, H. L. D. Characterization of Diffusion Processes: Normal and Anomalous Regimes. *Physica A: Statistical Mechanics and its Applications* **2016**, *447*, 392–401.

(303) Blumenthal, D.; Goldstien, L.; Edidin, M.; Gheber, L. A. Universal Approach to FRAP Analysis of Arbitrary Bleaching Patterns. *Sci Rep* **2015**, *5* (1), 11655.

(304) Kang, M.; Day, C. A.; Kenworthy, A. K.; DiBenedetto, E. Simplified Equation to Extract Diffusion Coefficients from Confocal FRAP Data. *Traffic* **2012**, *13* (12), 1589–1600.

(305) Hensle, E. M.; Esfandiari, N. M.; Lim, S.-G.; Blum, S. A. BODIPY Fluorophore Toolkit for Probing Chemical Reactivity and for Tagging Reactive Functional Groups. *European Journal of Organic Chemistry* **2014**, *2014* (16), 3347–3354.

(306) Eignerová, B.; Slavíková, B.; Buděšínský, M.; Dračínský, M.; Klepetářová, B.; Šťastná, E.; Kotora, M. Synthesis of Fluorinated Brassinosteroids Based on Alkene Cross-Metathesis and Preliminary Biological Assessment. *J. Med. Chem.* **2009**, *52* (18), 5753–5757.

(307) Jal, P. K.; Patel, S.; Mishra, B. K. Chemical Modification of Silica Surface by Immobilization of Functional Groups for Extractive Concentration of Metal Ions. *Talanta* **2004**, *62* (5), 1005–1028.

(308) Israelachvili, J. N. *Intermolecular and Surface Forces*; Elsevier Science & Technology: Saint Louis, UNITED STATES, 2010.

(309) Drummond, C. J.; Georgaklis, G.; Chan, D. Y. C. Fluorocarbons: Surface Free Energies and van Der Waals Interaction. *Langmuir* **1996**, *12* (11), 2617–2621.

(310) Bunker, B. C.; Carpick, R. W.; Assink, R. A.; Thomas, M. L.; Hankins, M. G.; Voigt, J. A.; Sipola, D.; de Boer, M. P.; Gulley, G. L. The Impact of Solution Agglomeration on the Deposition of Self-Assembled Monolayers. *Langmuir* **2000**, *16* (20), 7742–7751.

(311) Synowicki, R. A. Suppression of Backside Reflections from Transparent Substrates. *physica status solidi c* **2008**, *5* (5), 1085–1088.

(312) Fan, Z.; Zhi, C.; Wu, L.; Zhang, P.; Feng, C.; Deng, L.; Yu, B.; Qian, L. UV/Ozone-Assisted Rapid Formation of High-Quality Tribological Self-Assembled Monolayer. *Coatings* **2019**, *9* (11), 762.

(313) Xu, G. Formation of OTS Self-Assembled Monolayer on Glass Surface Investigated by AFM. *JZUS* **2000**, *1* (2), 162.

(314) Hasan, A.; Pandey, L. M. Kinetic Studies of Attachment and Re-Orientation of Octyltriethoxysilane for Formation of Self-Assembled Monolayer on a Silica Substrate. *Materials Science and Engineering: C* **2016**, *68*, 423–429.

(315) Pellerite, M. J.; Wood, E. J.; Jones, V. W. Dynamic Contact Angle Studies of Self-Assembled Thin Films from Fluorinated Alkyltrichlorosilanes. *J. Phys. Chem. B* **2002**, *106* (18), 4746–4754.

(316) Coskun, A.; Akkaya, E. U. Signal Ratio Amplification via Modulation of Resonance Energy Transfer: Proof of Principle in an Emission Ratiometric Hg(II) Sensor. *J. Am. Chem. Soc.* **2006**, *128* (45), 14474–14475.

(317) Hinton, D. A. Enabling Single Molecule Fluorescence Microscopy Investigations of Chemical Reactions Using a Spiroconjugated BODIPY Fluorophore. Ph.D., The University of Wisconsin - Madison, United States -- Wisconsin. https://www.proquest.com/docview/2166833227/abstract/ED736F6231C3402APQ/1 (accessed 2023-05-11).

NMR Spectra

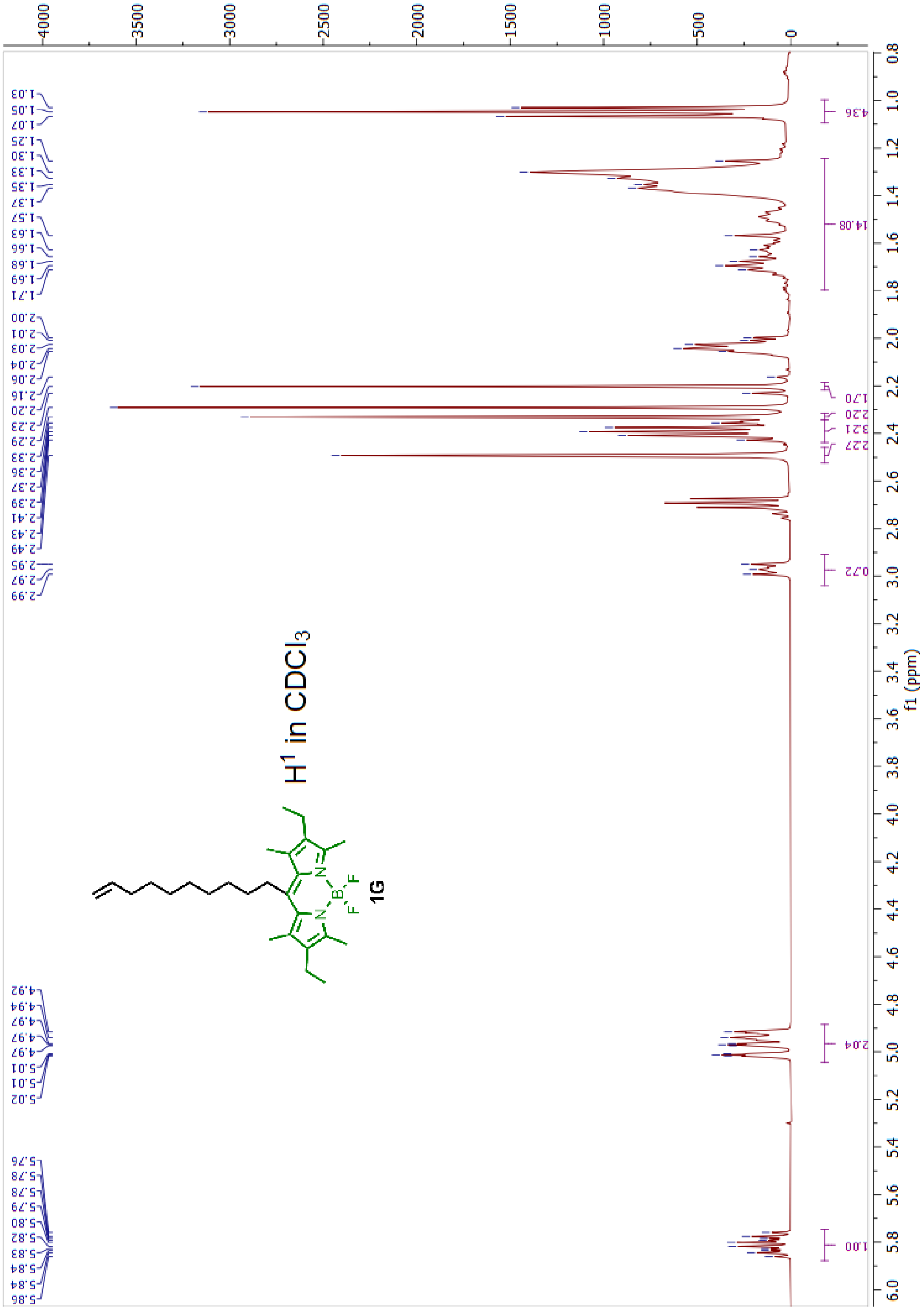
H1 in CDCl3
1G
B
N
N
F
F
1.03
1.05
1.07
1.25
1.30
1.33
1.35
1.37
1.57
1.63
1.66
1.68
1.69
1.71
2.00
2.01
2.03
2.04
2.06
2.16
2.20
2.23
2.29
2.33
2.36
2.37
2.39
2.41
2.43
2.49
2.95
2.97
2.99
4.92
4.94
4.97
4.97
4.97
5.01
5.01
5.02
5.76
5.78
5.78
5.79
5.80
5.82
5.83
5.84
5.84
5.86
4.36
14.08
1.70
2.20
3.21
2.27
0.72
2.04
1.00
4000
3500
3000
2500
2000
1500
1000
500
0
0.8
1.0
1.2
1.4
1.6
1.8
2.0
2.2
2.4
2.6
2.8
3.0
3.2
3.4
3.6
3.8
4.0
4.2
4.4
4.6
4.8
5.0
5.2
5.4
5.6
5.8
6.0
f1 (ppm)

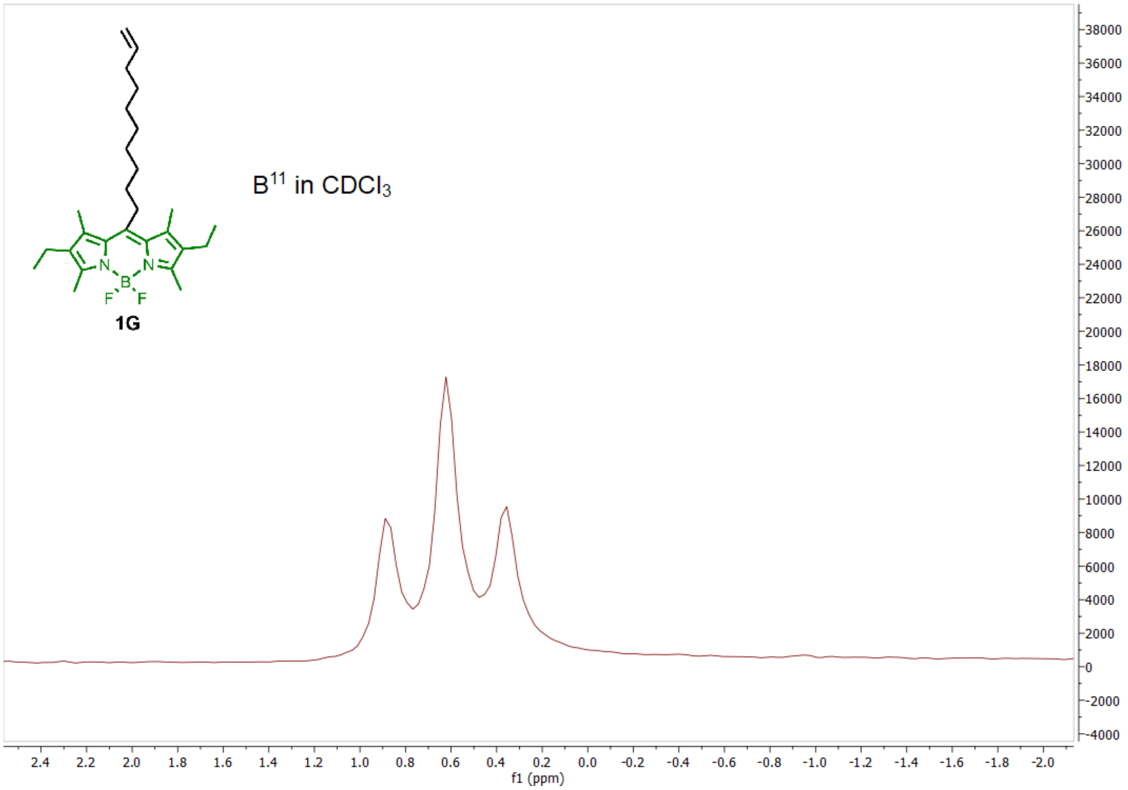
B11 in CDCl3
N
B
N
F
F
1G
38000
36000
34000
32000
30000
28000
26000
24000
22000
20000
18000
16000
14000
12000
10000
8000
6000
4000
2000
0
-2000
-4000
2.4
2.2
2.0
1.8
1.6
1.4
1.2
1.0
0.8
0.6
0.4
0.2
0.0
-0.2
-0.4
-0.6
-0.8
-1.0
-1.2
-1.4
-1.6
-1.8
-2.0
f1 (ppm)

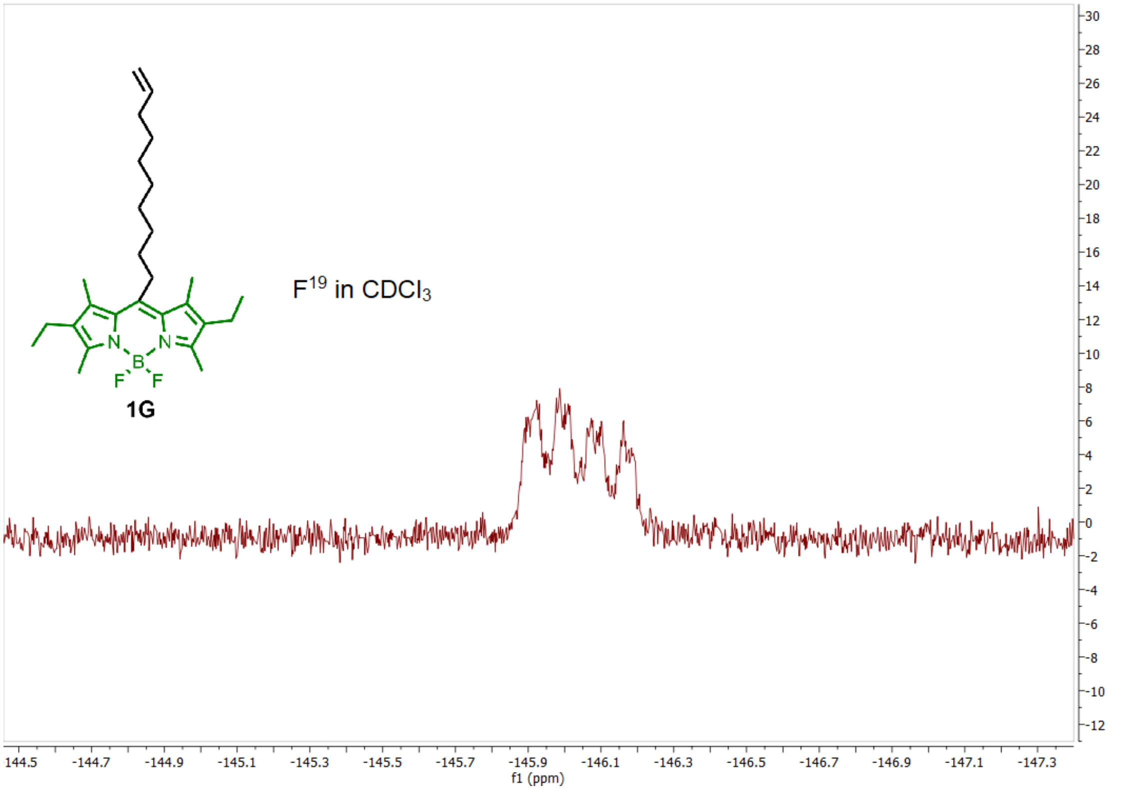
F19 in CDCl3
N
B
N
F
F
1G
30
28
26
24
22
20
18
16
14
12
10
8
6
4
2
0
-2
-4
-6
-8
-10
-12
144.5
-144.7
-144.9
-145.1
-145.3
-145.5
-145.7
-145.9
-146.1
-146.3
-146.5
-146.7
-146.9
-147.1
-147.3
f1 (ppm)

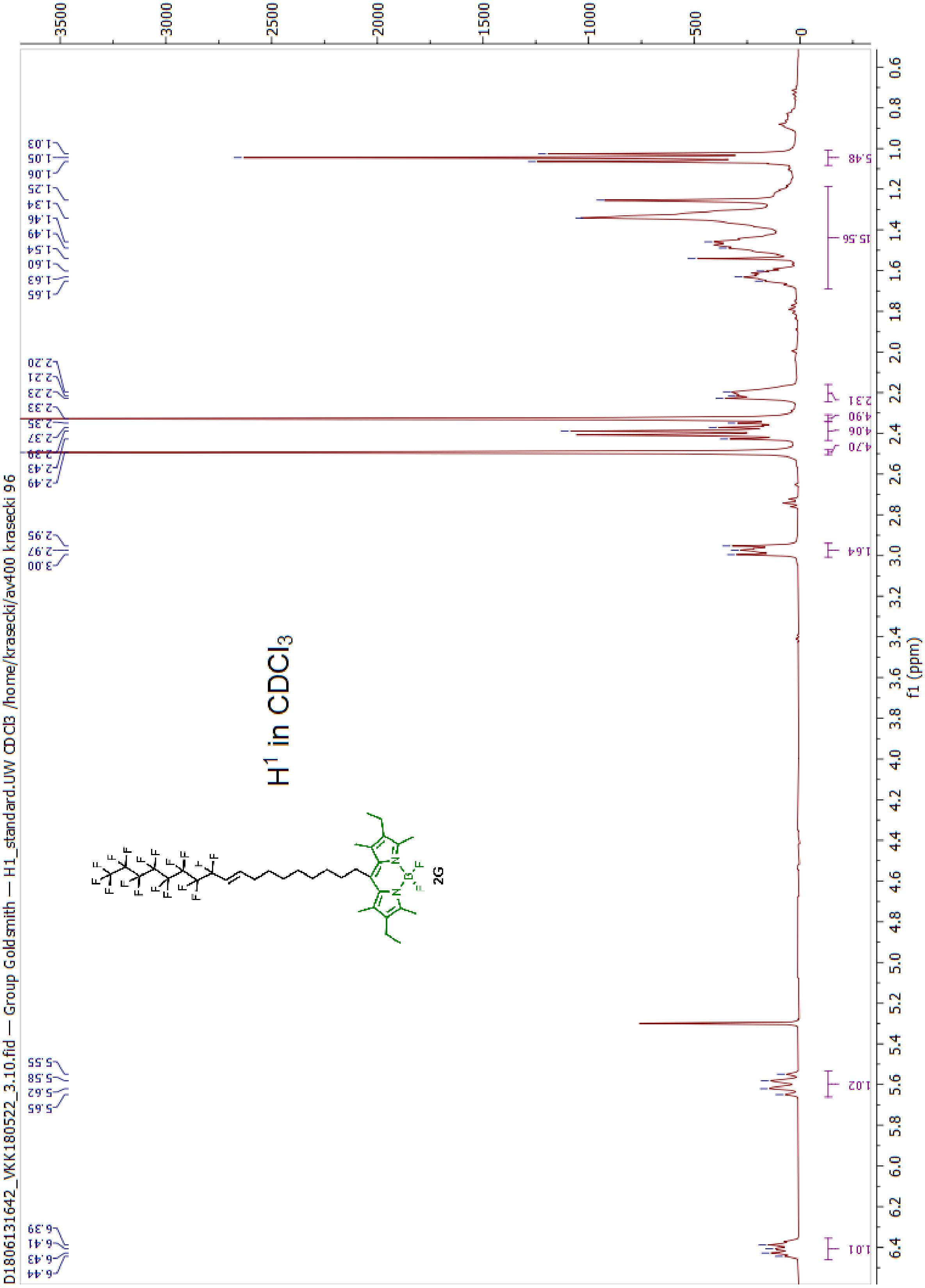
D1806131642_VKK180522_3.10.fid — Group Goldsmith — H1_standard.UW CDCl3 /home/krasecki/av400 krasecki 96
1.03
1.05
1.06
1.25
1.34
1.46
1.49
1.54
1.60
1.63
1.65
2.20
2.21
2.23
2.33
2.35
2.37
2.39
2.43
2.49
2.95
2.97
3.00
5.55
5.58
5.62
5.65
6.39
6.41
6.43
6.44
H1 in CDCl3
F
N
B
2G
5.48
15.56
2.31
4.90
4.06
4.70
1.64
1.02
1.01
3500
3000
2500
2000
1500
1000
500
0
0.6
0.8
1.0
1.2
1.4
1.6
1.8
2.0
2.2
2.4
2.6
2.8
3.0
3.2
3.4
3.6
3.8
4.0
4.2
4.4
4.6
4.8
5.0
5.2
5.4
5.6
5.8
6.0
6.2
6.4
f1 (ppm)

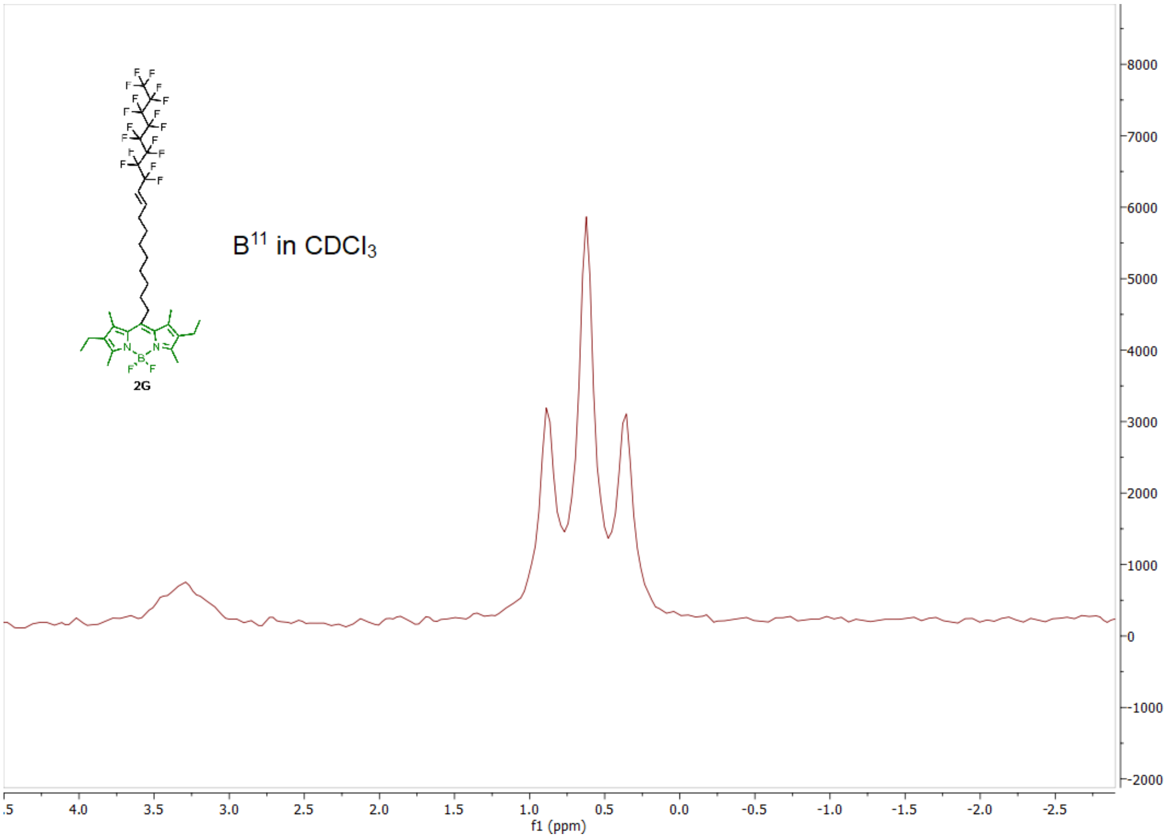
B11 in CDCl3
2G
N
B
F
8000
7000
6000
5000
4000
3000
2000
1000
0
-1000
-2000
.5
4.0
3.5
3.0
2.5
2.0
1.5
1.0
0.5
0.0
-0.5
-1.0
-1.5
-2.0
-2.5
f1 (ppm)

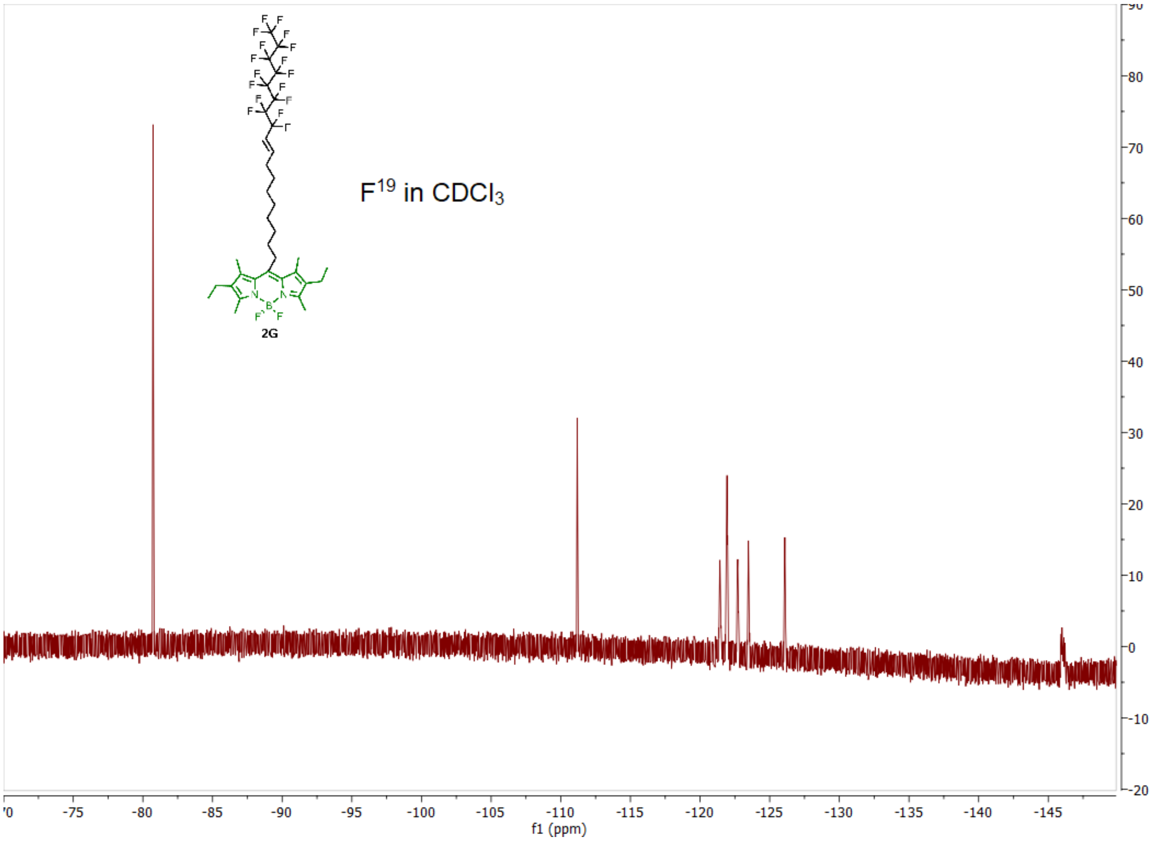
F19 in CDCl3
2G
N
B
F
80
70
60
50
40
30
20
10
0
-10
-20
-75
-80
-85
-90
-95
-100
-105
-110
-115
-120
-125
-130
-135
-140
-145
f1 (ppm)

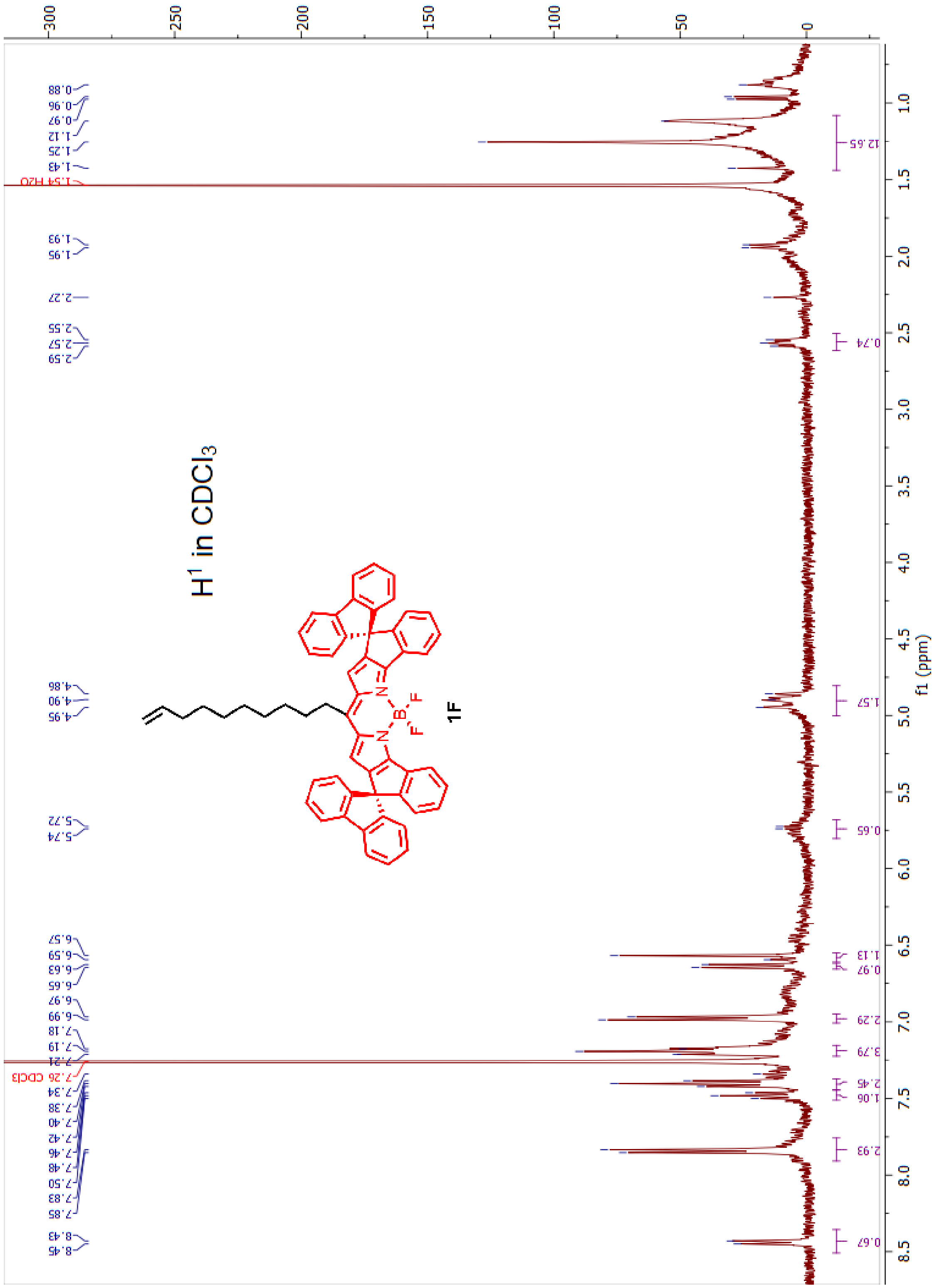
H1 in CDCl3
1F
N
N
B
F
F
0.88
0.96
0.97
1.12
1.25
1.43
1.54 H2O
1.93
1.95
2.27
2.55
2.57
2.59
4.86
4.90
4.95
5.72
5.74
6.57
6.59
6.63
6.65
6.97
6.99
7.18
7.19
7.21
7.26 CDCl3
7.34
7.38
7.40
7.42
7.46
7.48
7.50
7.83
7.85
8.43
8.45
12.65
0.74
1.57
0.65
1.13
0.97
2.29
3.79
2.45
1.06
2.93
0.67
300
250
200
150
100
50
0
1.0
1.5
2.0
2.5
3.0
3.5
4.0
4.5
5.0
5.5
6.0
6.5
7.0
7.5
8.0
8.5
f1 (ppm)

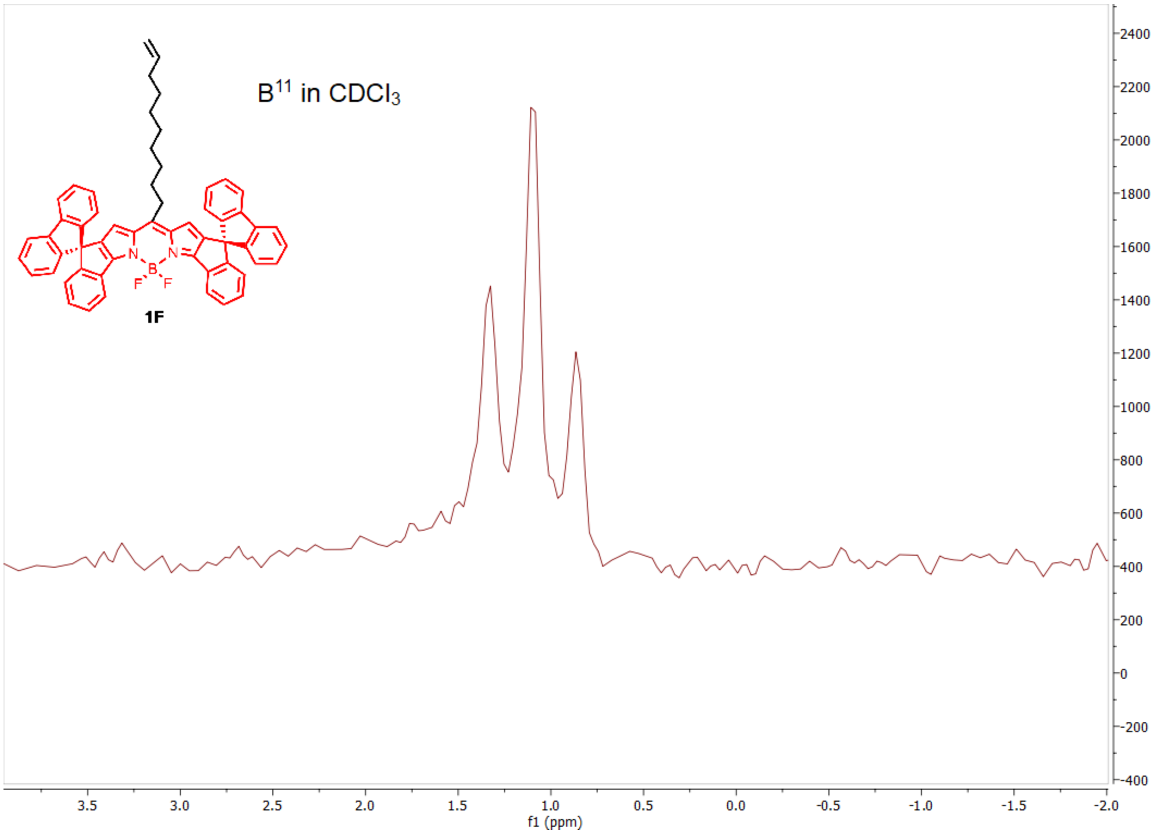
B11 in CDCl3
1F
N
B
N
F
F
2400
2200
2000
1800
1600
1400
1200
1000
800
600
400
200
0
-200
-400
3.5
3.0
2.5
2.0
1.5
1.0
0.5
0.0
-0.5
-1.0
-1.5
-2.0
f1 (ppm)

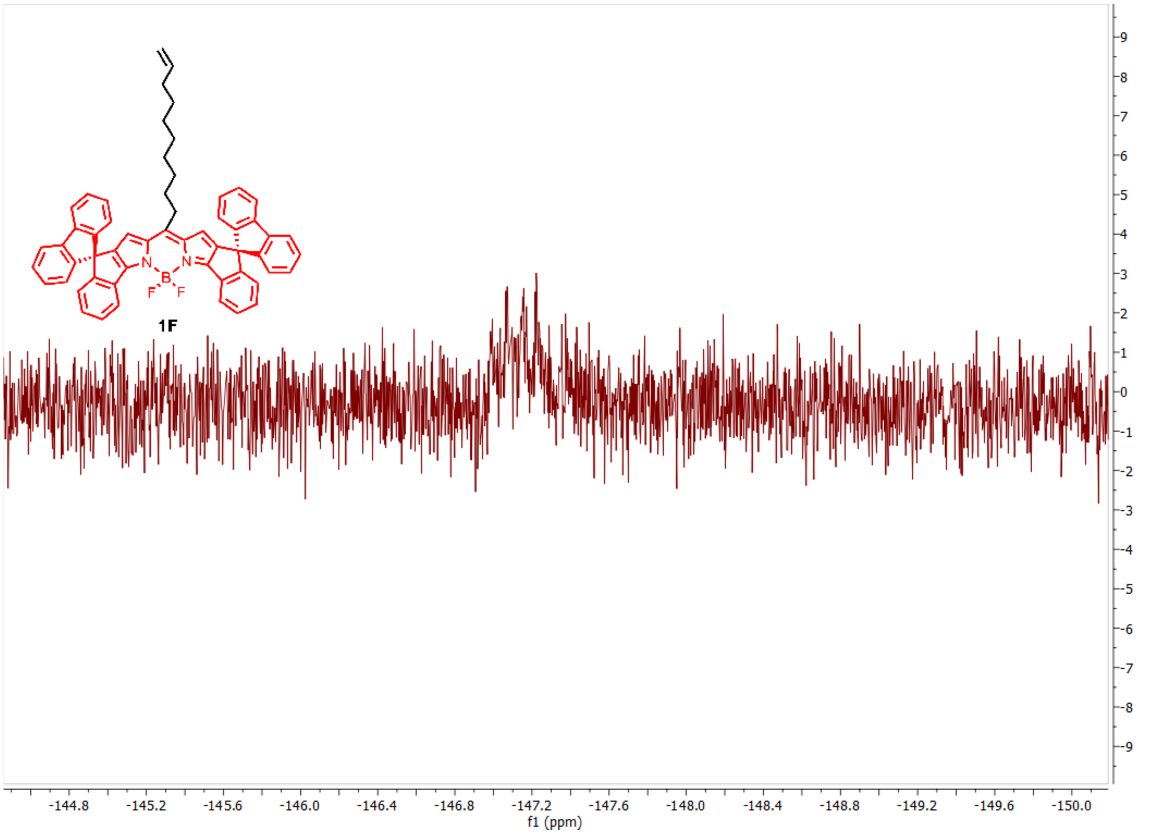
1F
N
B
N
F
F
9
8
7
6
5
4
3
2
1
0
-1
-2
-3
-4
-5
-6
-7
-8
-9
-144.8
-145.2
-145.6
-146.0
-146.4
-146.8
-147.2
-147.6
-148.0
-148.4
-148.8
-149.2
-149.6
-150.0
f1 (ppm)

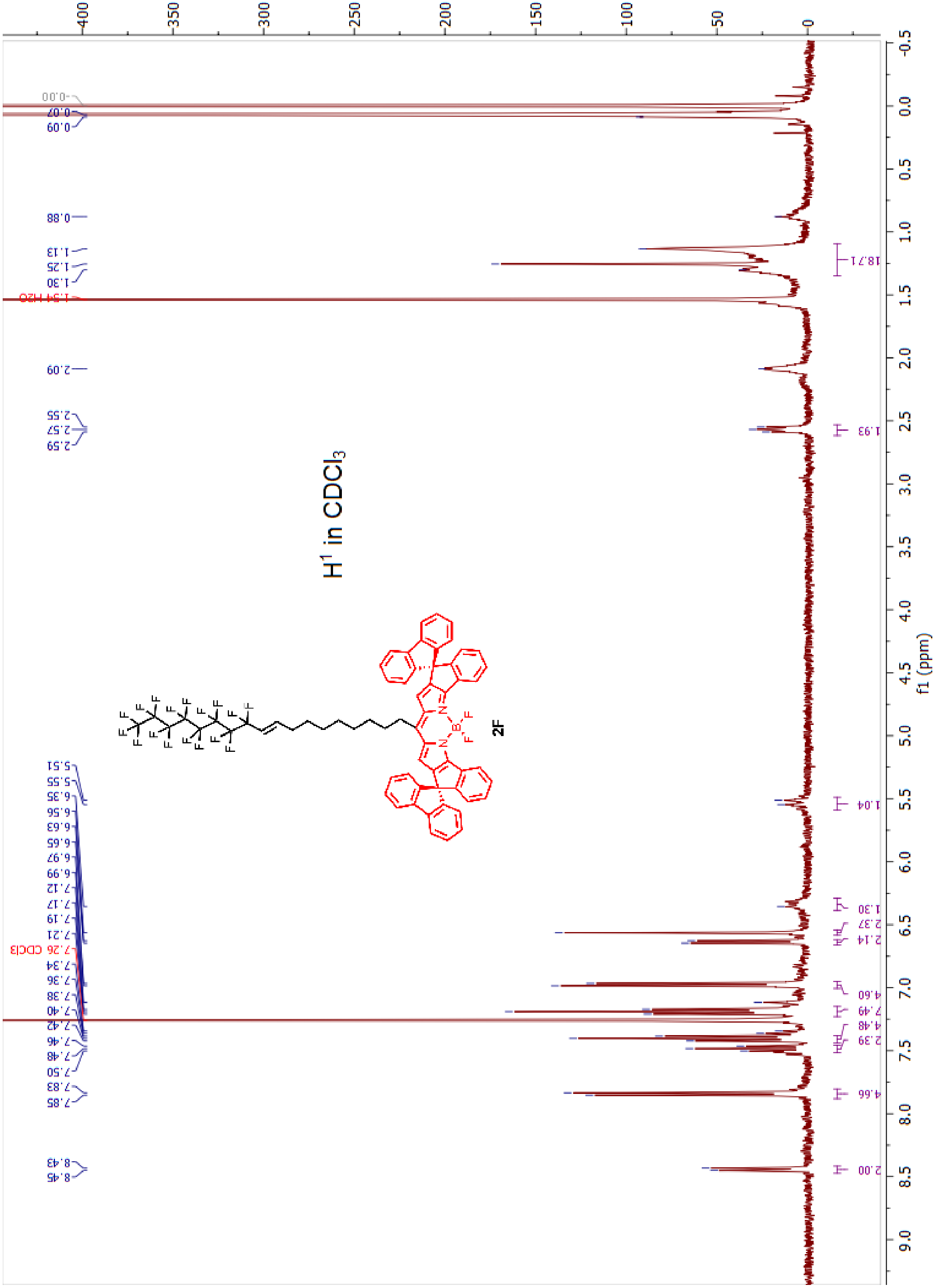
H1 in CDCl3
2F
f1 (ppm)
-0.5
0.0
0.5
1.0
1.5
2.0
2.5
3.0
3.5
4.0
4.5
5.0
5.5
6.0
6.5
7.0
7.5
8.0
8.5
9.0
0
50
100
150
200
250
300
350
400
0.00
0.07
0.09
0.88
1.13
1.25
1.30
1.54 H2O
2.09
2.55
2.57
2.59
5.51
5.55
6.35
6.56
6.63
6.65
6.97
6.99
7.12
7.17
7.19
7.21
7.26 CDCl3
7.34
7.36
7.38
7.40
7.42
7.46
7.48
7.50
7.83
7.85
8.43
8.45
18.71
1.93
1.04
1.30
2.37
2.14
4.60
7.49
4.48
2.39
4.66
2.00
F
N
B

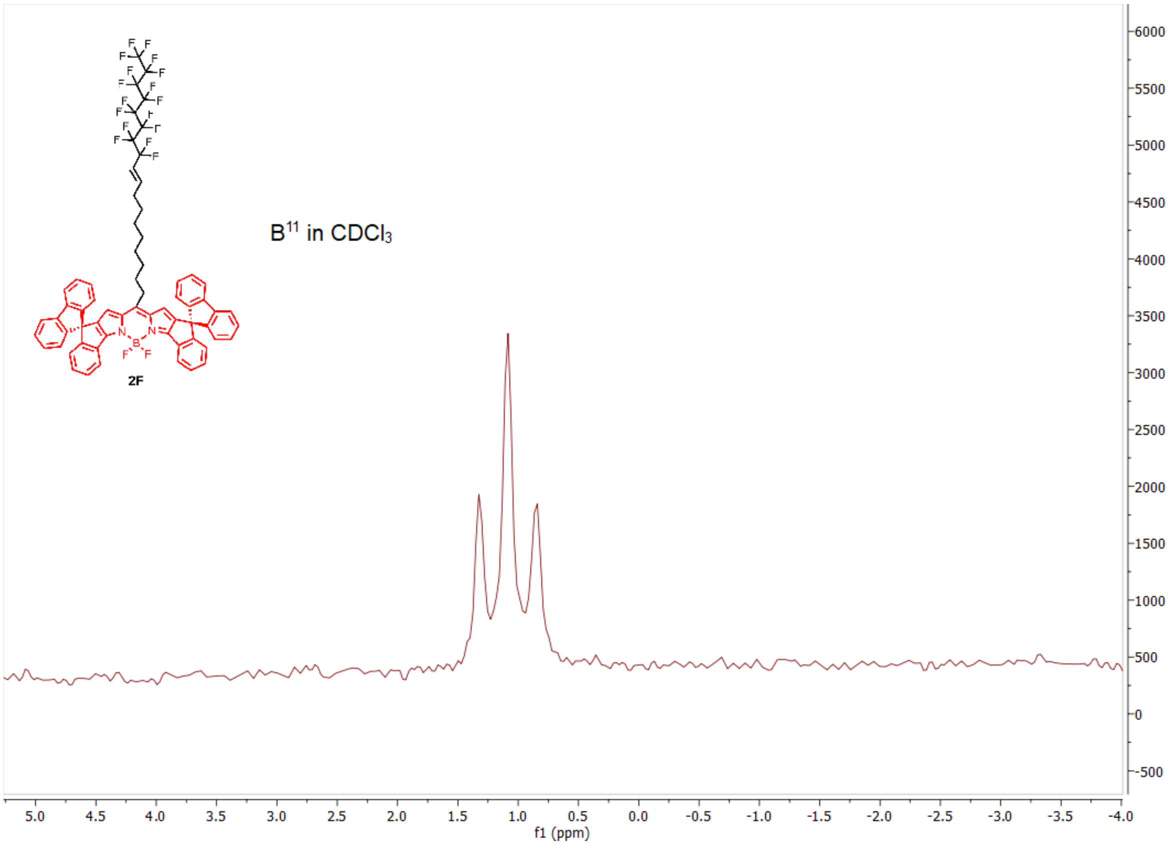
B11 in CDCl3
2F
6000
5500
5000
4500
4000
3500
3000
2500
2000
1500
1000
500
0
-500
5.0
4.5
4.0
3.5
3.0
2.5
2.0
1.5
1.0
0.5
0.0
-0.5
-1.0
-1.5
-2.0
-2.5
-3.0
-3.5
-4.0
f1 (ppm)

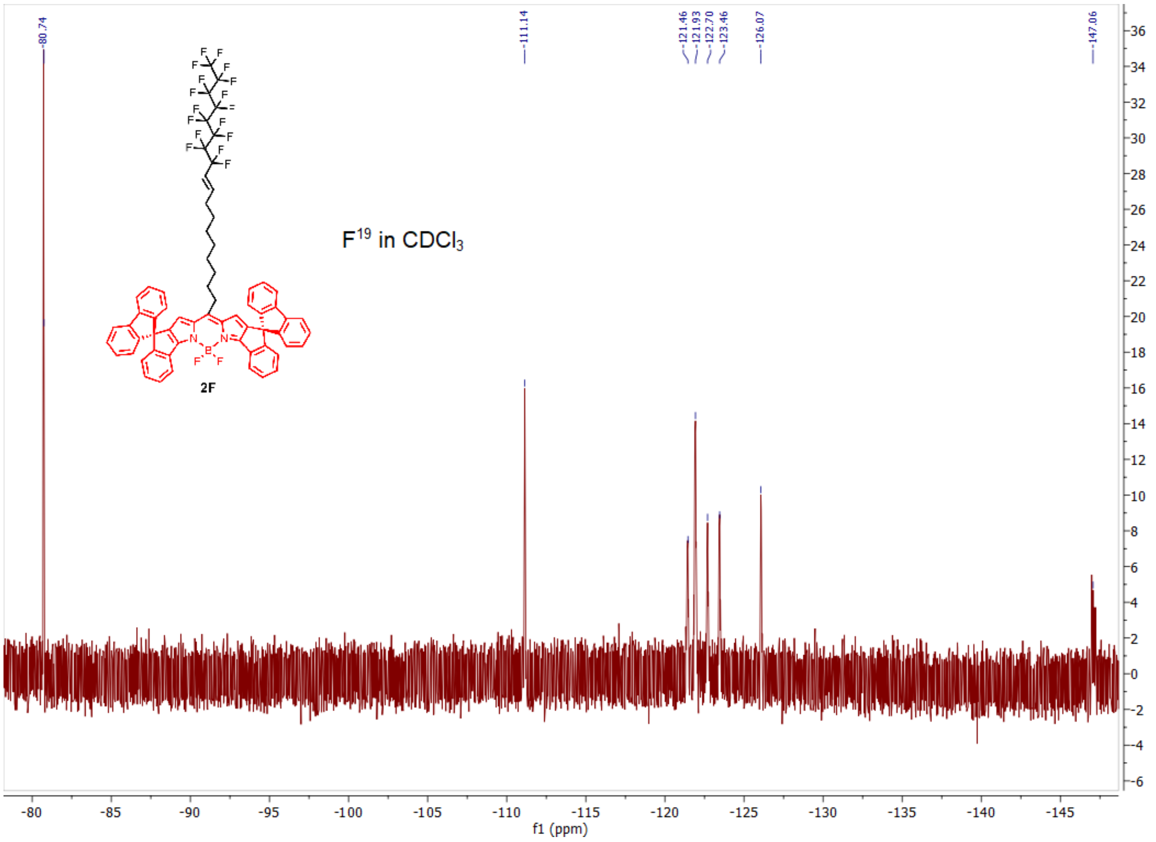
-80.74
-111.14
-121.46
-121.93
-122.70
-123.46
-126.07
-147.06
F19 in CDCl3
2F
36
34
32
30
28
26
24
22
20
18
16
14
12
10
8
6
4
2
0
-2
-4
-6
-80
-85
-90
-95
-100
-105
-110
-115
-120
-125
-130
-135
-140
-145
f1 (ppm)